University of Sussex

The NOAO-XCS Survey

&

The Optical to X-ray Scaling Relations of Galaxy Clusters

Nicola Mehrtens

Submitted for the degree of Doctor of Philosophy

University of Sussex

April 2010

Declaration

I hereby declare that this thesis has not been and will not be submitted in whole or in part to another University for the award of any other degree.

Signature:

Nicola Mehrtens

UNIVERSITY OF SUSSEX

Nicola Mehrtens, Doctor of Philosophy

The NOAO-XCS Survey
&
The Optical to X-ray Scaling Relations of Galaxy Clusters

Summary

In this thesis we present the NOAO-XMM Cluster Survey (NXS). NXS has provided optical follow-up of X-ray cluster candidates serendipitously detected by the XMM Cluster Survey (XCS). We report details on the execution, data reduction and analysis of 154 wide-field MOSAIC images containing 630 XCS cluster candidates.

We present a redshift algorithm, based on the 'red-sequence technique', designed to confirm cluster identifications and extract photometric cluster redshifts from NXS data. This algorithm exploits the homogeneity of elliptical cluster galaxies to provide simultaneous redshift and optical richness estimates. In addition, we apply this redshift algorithm to the Sloan Digital Sky Survey public data releases SDSS DR7 and SDSS Stripe 82.

The resulting catalogue of $\sim$500 optically confirmed XCS clusters with red-sequence redshifts is presented, spanning the redshift range $0.1<z<1.0$. This sample will enable a future XCS measurement of the cosmological parameters Ω_m and σ_8, as well as a self-consistent measure of the cluster X-ray luminosity to temperature scaling relation.

Furthermore, for clusters with measured X-ray temperatures or luminosities, we measure the optical richness of red-sequence galaxies within the cluster virial radius (R_{200}). Using these measurements, we investigate the optical halo-mass scaling relation. Understanding cluster optical scaling relations, in particular the optical-light to halo-mass relation, is key for surveys hoping to measure cosmological parameters using optically detected clusters alone. By combining the optical NXS and SDSS data sets with X-ray information from XCS, this thesis provides much needed optical to X-ray scaling relations for future optical cluster surveys.

Acknowledgements

"Lets see what's out there." – Captain Jean-Luc Picard.

This PhD would not have been possible without funding from PPARC/STFC. I would also like to thank the University of Sussex and my supervisor, Kathy Romer, for taking me on as a PhD student. Thanks to Matt Hilton for his extensive help regarding the NXS. Thanks to Chris Wegg for his support and valuable discussions, and without whom I would not have applied for a PhD. Thanks to Mark Hosmer, my 'brother in arms', and to Ed Lloyd-Davies for their input into this thesis regarding the XCS. Thanks to Ben Hoyle for his help with XCS-Zoo. Thanks to Isaac Roseboom for valuable discussions, particularly those relating to the Optical–X-ray scaling relations of this work, and for proof-reading numerous sections of this thesis.

My time at Sussex would have been considerably more dull and lonely without the following people, whom I love dearly: Mark and Sarah Hosmer, Laura Valkonen, Mike MacIntyre, Alex Dunford, Mark Frost, James Karamath, David Parkinson, Matt Thomson, Leon Baruah, Owain Young, Leonidas Christodoulou, Bruno Henriques, and Isaac Roseboom. Thanks for your support and for many fun times.

I would also like to thank my family for their continuing support, and in particular, my Grandmother, to whom I dedicate this thesis.

Contents

List of Tables

List of Figures

Chapter 1

Introduction

Galaxy clusters are the largest gravitationally bound objects in the universe. This makes them a useful probe of cosmological parameters as they form from the largest perturbations of the primordial density field that exists prior to recombination and structure formation. In addition, they provide independent and complementary constraints to other cosmological probes *e.g.* supernovae and the CMB. In order to use galaxy clusters as a cosmological probe, one must compile large samples of galaxy clusters, ideally selected in a uniform manner with a well known selection function. By studying the distribution of cluster mass with redshift one can then infer these cosmological parameters.

To date, cluster mass estimates have been best obtained using their X-ray properties emanating from the hot intracluster gas. Gaining masses from X-ray data (*e.g.* T_X or L_X) is a more efficient and reliable method than gaining cluster mass estimates from their optical properties (*e.g.* N_{gal} or σ_v). The latest generation of X-ray satellites, the XMM-Newton[1] and Chandra[2] space telescopes, have provided imaging data that have been exploited to both detect clusters and measure mass proxies. The next generation of X-ray satellite, IXO[3], providing increased sensitivity, thus detecting clusters at smaller masses and improving errors on T_X and L_X, won't be realised until after 2020. Therefore current emphasis is being placed on the optical detection of clusters and the optical scaling relations that bias their selection. In particular, understanding the optical light-halo mass relation is key for surveys hoping to measure cosmological parameters using optically detected clusters alone. These surveys need external optical scaling relations with which to calibrate their data, which can be obtained by studying clusters with both optical and X-ray data. By combining both optical and X-ray data this thesis will provide such

[1] http://xmm.esac.esa.int/

[2] http://www.nasa.gov/mission_pages/chandra/main/index.html

[3] http://ixo.gsfc.nasa.gov/

relations.

This thesis uses an X-ray selected galaxy cluster catalog produced by the XMM Cluster Survey (XCS; Romer et al. (2001)). XCS is a serendipitous survey exploiting the archival database of the XMM-Newton telescope, with the joint goals of measuring the cosmological parameters and cluster X-ray scaling relations. The primary work of this thesis is the production of the NOAO-XCS Survey (NXS). NXS is the optical follow-up survey to XCS providing photometric redshifts via a modified version of the red sequence technique (Gladders and Yee, 2000a). This thesis further supplements the XCS optical follow-up by using publicly available optical data from the Sloan Digital Sky Survey (SDSS). These optical and X-ray data sets are then used to measure cluster optical-X-ray scaling relations.

Hence the goal of this thesis is two-fold; *i*) providing a list of optically confirmed XCS cluster candidates with redshift estimates to enable an XCS measurement of cosmological parameters and cluster X-ray scaling relations; and *ii*) measuring optical to X-ray scaling relations to aid future optical cluster surveys.

Chapter 1 provides an introduction to the work in this thesis. Chapter 2 reviews the XMM-Cluster Survey (XCS) and defines our X-ray selected cluster sample. Chapters 3 and 4 describe the strategy, execution and data products of the NOAO-XCS Survey (NXS). The development of a red sequence redshift algorithm to extract cluster photometric redshifts from NXS data, along with its results, is presented in Chapter 5. Chapter 6 describes the adaptation of this redshift algorithm for use on SDSS data and presents its results. Chapter 7 determines a method for measuring optical cluster mass estimates, and presents optical to X-ray scaling relations using the NXS, SDSS and XCS data sets.

1.1 The current ΛCDM Paradigm

The Friedmann Equation (Equation 1.1) describes the expansion of the universe and derives from the equations of general relativity. It assumes energy conservation in the universe and relies upon the assumptions of the cosmological principle, which states that the universe is homogeneous and isotropic.

$$H^2 = \left(\frac{\dot{a}}{a}\right)^2 = \frac{8\pi G}{3}\rho \ - \frac{kc^2}{a^2} + \frac{\Lambda c^2}{3}, \tag{1.1}$$

In this equation, H, the Hubble parameter is expressed in terms of co-moving coordinates which is given by the *scale factor* of the universe $a(t)$, with a present day value of a_0=1. The time derivative of a is $\dot{a}$. The density of the universe, ρ, is spatially invariant

but evolves with time. The constant k corresponds to the geometry of the universe, taking the values -1,0,1 for a closed, flat, and open universe respectively.

As the universe is effectively homogeneous (*i.e.* smooth on large scales), the energy density of the universe can be thought of as a fluid, and thus can be represented by a fluid equation (that derives from the laws of thermodynamics). The fluid equation describes how the energy density of the universe evolves with time.

$$\rho + 3\frac{\dot{a}}{a}\left(\rho + \frac{p}{c^2}\right) = 0, \tag{1.2}$$

where p is pressure and c is the speed of light.

By combining the Friedmann and Fluid equations, the Friedmann acceleration equation can be derived, which describes the acceleration of the expansion of the universe.

$$\frac{\ddot{a}}{a} = -\frac{4\pi G}{3}\left(\rho + \frac{3p}{c^2}\right) \tag{1.3}$$

The pressure p in the universe is related to its density ρ using the equation of state: $p = w\rho c^2$. This implies that the density is related to the scale factor by the equation of state as $\rho \propto a^{-3(1+w)}$, leading to Equation 1.4

$$\dot{a}^2 = \frac{8\pi G}{3}\rho_0 a^{-(1+3w)} + constant \tag{1.4}$$

The energy density of the universe is typically expressed by the density parameter Ω (defined as $\Omega = \rho/\rho_{crit}$) which relates the energy density, ρ, to the critical density, ρ_{crit} (given by $\rho_{crit} = 3H^2/8\pi G$, the density needed for a flat universe).

In addition, the scale factor is related to the cosmological redshift z (§1.2) of distant objects by $a = (1+z)^{-1}$. This allows us to express the expansion of the universe in terms of its total energy density Ω, given by Equation 1.5.

$$H^2 = \left(\frac{\dot{a}}{a}\right)^2 = H_0^2[\Omega(1+z)^{3(1+w)} + (1-\Omega)(1+z)^2] \tag{1.5}$$

The density parameter Ω is often broken down into its component parts; Ω_m, Ω_r and Ω_Λ representing the matter, radiation, and dark energy density of the universe required for a closed universe.

We can therefore express the Friedmann equation in terms of the energy density parameters, leading to the dynamical description of the universe given by Equation 1.6, where H_0 is the present day Hubble parameter:

$$H^2(z) = \left(\frac{\dot{a}}{a}\right)^2 = (H_0)^2[\Omega_m(1+z)^3 + \Omega_r(1+z)^4 + \Omega_\Lambda + (1-\Omega_{total})(1+z)^2] \quad (1.6)$$

Therefore by measuring values for the components of the density parameter Ω_m, Ω_r and Ω_Λ, we can understand the expansion of the universe.

This dynamical model of the universe has been known for the last 100 years, however it is only since the 1980's that we have been able to measure these cosmological parameters to any precision. This era of *precision cosmology* has given rise to a consensus on the values of the cosmological parameters and to the so called *concordance cosmology*.

Powerful constraints on cosmological parameters have come from the NASA Wilkinson Microwave Anisotropy Probe (WMAP) (Jarosik et al., 2010), which measures the cosmic microwave background (CMB) radiation. These CMB photons are relics of the hot dense state of the universe that existed shortly after the Big Bang. As the universe cooled, electrons combined with protons (known as *Recombination*), allowing photons to decouple from matter and free-stream throughout the universe to the present day. It is these photons that are detected by WMAP. Anisotropies within the map are measured to be one part in 10^5, thus demonstrating the homogeneity of the early universe. The WMAP seven-year data (the fourth WMAP data release), in conjunction results from the Hubble Space Telescope (HST) Key project (Riess et al., 2009), and from Baryon Acoustic Oscillations (Percival et al., 2009), have produced the latest set of parameter values, measured to be: $H_0 = 70.4^{+1.3}_{-1.4}$ kms^{-1}Mpc^{-1}; $\Omega_\Lambda = 0.728^{+0.015}_{-0.016}$; Ω_m is made up of Baryonic and non-baryonic components measured to be $\Omega_{Baryons} = 0.0456 \pm 0.0016$ and $\Omega_{DM} = 0.227 \pm 0.014$ respectively (Jarosik et al., 2010), hereafter WMAP7. In addition, WMAP7 measures the universe to be spatially flat today, $k_0 = 0.002$ *i.e* parallel lines remain parallel.

Studies of galaxy rotation curves, galaxy cluster mass, weak lensing, and WMAP7 *etc.*, have all inferred that only a small fraction of the matter density is made up of baryonic matter. The remaining matter is thought to exist in a form which is non-relativistic (*i.e.* cold), only acts through gravitational interaction (*i.e.* collisionless) and does not emit electromagnetic radiation (*i.e.* non-emitting). This has given rise to the term Cold Dark Matter (CDM). Indeed, direct empirical proof for the existence of dark matter has come from a study of the Bullet Cluster (Clowe et al., 2006).

Furthermore, studies of distant supernovae have shown that not only is the universe expanding, but that it is accelerating in its expansion (Perlmutter et al., 1999). Given the mechanism by which Type Ia supernova are produced, it is a fair assumption that the light given off by a Type Ia supernova explosion is constant, regardless of the supernova. This

allows us to use them as *standard candles* (§1.2). Perlmutter et al. (1999) discovered that the light from distant ($z\sim1$) supernovae were fainter than expected given their redshift. Leading to the conclusion that space is expanding at a more rapid rate for these distant supernova. This accelerated expansion has been attributed to a force known as Dark Energy (or vacuum energy). Although we do not know the mechanism by which it acts, it is believed to be a property inherant to space itself. Dark Energy is often parameterised as Ω_Λ and w, with w_0 being the value today.

In summary, the current cosmological paradigm is of a flat universe, dominated by cold dark matter with a majority dark energy component that is accelerating the expansion of the universe. This paradigm has been encapsulated by the term 'ΛCDM'.

1.2 Cosmological distances

In this section we will briefly state some considerations that must be taken into account when measuring cosmological distances and sizes.

Redshift. The expansion of the universe causes galaxies to recede from our position. As a consequence, the light emitted from galaxies is shifted to redder wavelengths caused by their line of sight recession velocity. The distances to galaxies can be measured via this *redshift*, by comparing the shift of spectral features at known wavelengths in a galaxy spectrum to their observed wavelengths. Redshift is a dimensionless quantity and is given by Equation 1.7:

$$z = \frac{\lambda_{obs} - \lambda_{em}}{\lambda_{em}}, \tag{1.7}$$

where λ_{em} is the known wavelength of a specific spectral feature and λ_{obs} is its observed wavelength.

Luminosity distance. The flux (S) received from a galaxy is proportional to its luminosity (L, the energy emitted per second per solid angle), and inversely proportional to the square of its luminosity distance d_L. Due to the expansion of the universe, this luminosity distance is increased by a factor of $(1+z)$ over the proper distance, thus reducing the flux received from a galaxy by a factor of $1/(1+z)^2$.

If one knows the luminosity of a galaxy, its luminosity distance (d_L) can be calculated by measuring its flux using Equation 1.8.

$$d_L = \sqrt{\frac{L}{4\pi S}}, \tag{1.8}$$

In this manner, objects with known luminosities, known as *standard candles*, such as Type Ia Supernovae are used to measure cosmological distances.

Angular-diameter distance. The angular-diameter distance (d_A) is a measure of how large an object appears on the sky. Assuming a static universe, the angular-diameter distance (d_A) is defined by Equation 1.9:

$$d_A = \frac{l}{\sin\theta} \sim \frac{l}{\theta}, \tag{1.9}$$

Therefore, if one knows the physical (or proper) size of an object (l), the distance to the object can be calculated using its angular size (θ) on the sky. In this manner, objects or phenomena (*e.g.* BAO) with known sizes, known as *standard rulers*, are used to measure cosmological distances.

Like d_L, d_A is also affected by the expansion and geometry of the universe. The relation between d_L and d_A is given by Equation 1.10:

$$d_L = (1+z)^2 d_A, \tag{1.10}$$

1.3 Cosmological Mass Function

The current scenario explaining the growth of structure in the universe is via *hierarchical structure formation*. In this scenario, the large scale structure seen in the present day universe arises from the initial density perturbations (*i.e.* over-densities) in the primordial density field at recombination.

Cold Dark Matter, unaffected by processes other than gravitational interaction, collapse to form *dark matter haloes*. These haloes then merge, through gravitational attraction, to form larger and larger haloes. Baryonic matter, attracted to the gravitational potential well of the halo, subsequently falls into these dark matter haloes. As hierarchical structure formation is an ongoing process, dark matter haloes are continually undergoing mass mergers and their effects are apparent in the evolution of the galaxies contained within them.

A natural consequence of this hierarchical structure formation scenario is a universe containing dark matter haloes with a range of masses. This distribution of mass is known as the Cosmological Mass Function (Press and Schechter, 1974) and describes the number

of dark matter haloes within a mass range at a given redshift. Not only is the cosmological mass function set by the amplitude of the initial density perturbations, but also by the matter density of the universe Ω_m (and to a lesser extent Ω_Λ). A smaller value for Ω_m, for example, corresponds to a slower growth in structure and fewer bound systems at larger mass.

1.4 Galaxy clusters as cosmological probes

Galaxy clusters consist not only of galaxies (§1.6), but also of a hot intracluster cluster medium (ICM) of ionized gas that emits X-rays (§1.5), and a dark matter component. They comprise of ∼5%, ∼15% and ∼80% of the total inferred cluster mass respectively. The dark matter component of a cluster cannot be be detected directly but can be inferred from other cluster properties. As a consequence, galaxy clusters are typically detected via the starlight in their galaxies (Gladders and Yee, 2004; Miller et al., 2005; Koester et al., 2007b) or the X-ray emission from the ICM (Romer et al., 2001; Pacaud et al., 2007). Less typically, but increasingly popular clusters are detected via gravitational lensing (Dahle et al., 2003), or via the signature of the Sunyaev-Zel'dovich (SZ) effect (Vanderlinde et al., 2010).

Galaxy clusters have a range of masses, typically 10^{14}-10^{15}M$_\odot$ and can contain 1000s of galaxies. Objects with smaller masses typically 10^{13}-10^{14}M$_\odot$ are known as *Galaxy Groups*. Generally the distinction between a galaxy cluster and galaxy group is based on its temperature. The cut is somewhat arbitrary, however, systems with X-ray temperatures >2keV are generally classed as clusters.

Galaxy clusters are the largest gravitationally bound objects in the universe. As such, galaxy clusters are extremely useful for measuring the cosmological distribution of mass, as they lie at the extreme tail of the Cosmological Mass Function (§1.3). Hence, they are sensitive to Ω_m and the amplitude of the initial perturbations on galaxy cluster scales ($\sim 8h^{-1}$Mpc), described by a parameter known as σ_8 (σ_8=0.809±0.024, WMAP7 (Jarosik et al., 2010)). Cosmological simulations predict the mass function of dark matter haloes, including on cluster scales (Jenkins et al., 2001). Therefore by comparing the observed Cluster Mass Function and its evolution to those predicted from simulations, one should be able to determine the correct values for Ω_m and σ_8. This technique of measuring cosmological parameters is often referred to as 'cluster number counts' and this is the term we use herein.

Due to their large size it can be assumed that clusters provide a typical representation of

the baryonic matter content of the universe. The baryon fraction of a cluster is dominated by their X-ray gas. If we assume that this gas is coincident with the cluster dark matter halo, and that the gas fraction, f_{gas}, within a halo is the same for all clusters with given mass, then any changes in the measured gas fraction between clusters of a given mass is assumed to be due to changes in distance (Sasaki, 1996; Pen, 1997). Therefore, clusters can be used in a similar manner to standard candles. By measuring f_{gas} as a function of redshift, we have an alternative (to the cluster number counts) method to measure cosmological parameters (Allen et al., 2002; Mantz et al., 2009).

Both of these methods (f_{gas} and cluster number counts) require a determination of cluster mass, which is often represented by the virial mass of the cluster. As one cannot directly measure the mass of galaxy clusters, it must be inferred by other observables related to their halo mass. Proxies for mass include: the number of cluster galaxies (Rozo et al., 2009); the total optical light (Reyes et al., 2008), the velocity dispersion of cluster galaxies (Girardi et al., 1998), X-ray luminosity of the ICM (Rykoff et al., 2008), X-ray temperature of the ICM (Reiprich and Böhringer, 2002), SZ decrement (McInnes et al., 2009), and weak lensing profiles (Zhang et al., 2010). However, in order to use cluster observables as a proxy for mass one must first understand the observable to mass scaling relation and its possible evolution (§1.5.2, §1.6.3). Furthermore, in order to use the cluster number counts as a cosmological probe, one must also understand how the process of selecting a sample of clusters, *i.e.* the cluster *selection function*, affects the resulting values of the inferred cosmological parameters (Pacaud et al., 2007; Sahlén et al., 2009).

Paramater constraints derived using galaxy cluster number counts and/or f_{gas} provide independent and complementary constraints to other cosmological probes such as Type Ia supernovae (SNIa), CMB anisotropies, baryon acoustic oscillations (BAO) (Allen et al., 2002; Knop et al., 2003). Alternatively, joint constraints using clusters and other methods simultaneously, can be used to provide even tighter constraints.

For example, using X-ray selected clusters: Mantz et al. (2009) used 238 clusters detected by the ROSAT All-Sky Survey (RASS) to perform a joint fit combining f_{gas}, CMB, SNIa and BAO, and obtained Ω_m=0.23 $\pm$0.04, σ_8=0.82$\pm$0.05, and w=-1.01 $\pm$0.20, whilst simultaneously fitting on their L_X-M_X, T_X-M_X relations. Vikhlinin et al. (2009b) used Chandra observations of 86 clusters detected in ROSAT, to perform a fit using cluster number counts with CMB, SNIa and BAO parameter constraints. Thus providing values of Ω_m=0.255 $\pm$0.043 and $w = w_0$=-1.14$\pm$0.21. Pacaud et al. (2007) use the number counts of 29 clusters, with $z \leq 1.05$, detected by XMM-Newton to provide constraints on

Ω_m, σ_8 and w. It is worth noting that owing to the increased sensitivity of XMM-Newton, approximately half of the Pacaud et al. (2007) clusters were in fact galaxy groups with temperatures less than 2keV.

On the other hand, optically selected clusters have also been used to provide cosmological constraints. For example, using the number counts of 956 clusters (with z<0.95) the Red-Sequence Cluster Survey (RCS), Gladders et al. (2007) provide the constraints Ω_m=$0.31^{+0.11}_{-0.10}$, σ_8=$0.67^{+0.18}_{-0.13}$. Using clusters with redshift z<0.3 from the maxBCG catalog, Rozo et al. (2010) provide the constraints Ω_m=0.265 ±0.016, σ_8=0.807 ±0.020. These examples show the power of galaxy clusters as cosmological probes and their ability to constrain cosmological parameters using both their optical and X-ray properties.

1.5 X-ray properties of galaxy clusters

Galaxy clusters have a large gas component, the intracluster cluster medium (ICM), comprising of 15% of the total cluster mass. The ICM has a temperature of T≈10^7K and therefore exists as a hot ionized plasma. The dominant mechanism by which the ICM emits radiation is via Bremstrahlung radiation (or braking radiation). In this process a free electron is slowed during an encounter with a positive ion in the intracluster medium (ICM) and emits a photon, which is detected as X-ray emmission. Thus, the surface brightness or luminosity of the gas is proportional to its density as $n_e \mathrm{x} n_p \simeq n_e^2$. The emissivity of Bremstrahlung radiation can be quoted as:

$$\epsilon \propto g(\nu, T) T^{\frac{1}{2}} n_e^2 e^{\frac{-h\nu}{kT}} \tag{1.11}$$

where the Gaunt factor $g(\nu, T) \sim 1 + log(kT/h\nu)$.

Therefore, as the ICM is present throughout a cluster (albeit, concentrated towards the center of the gravitational potential well), the Bremstrahlung radiation emanating from a galaxy cluster is detected as extended X-ray emission. This extended emission provides an extremely useful and reliable tool for cluster detection. Furthermore, as this emission is bright, it can be detected over a range of redshifts. Moreover, because galaxy clusters are the dominant, extragalactic source of extended X-ray emission, and because the presence of an ICM is indicative of a gravitationally bound system, and because the emission is more concentrated toward the centre of the cluster; detecting clusters using the signature of X-ray extent is more reliable than detecting clusters from their optical light (Collins et al., 1995).

1.5.1 X-ray Scaling relations

The X-ray luminosity of a cluster is given by Equation 1.12.

$$L = \int n_e^2 \Lambda(T) dV \tag{1.12}$$

where $\Lambda(T)$ is the cooling function of the gas, which is $\propto T^{\frac{1}{2}}$ in the case of Bremsstrahlung emission.

If we assume that the thermodynamics of the ICM are controlled by gravitational processes alone, then we can assume that large clusters are simply the scaled up versions of small clusters and groups, *i.e.* self-similar (Kaiser, 1986). Thus, by using self-similar cluster scaling relations as determined for the ICM (shown below) we can infer the cluster mass from the cluster observables L_X and T_X:

$$T_X \propto M^{\frac{2}{3}} \tag{1.13}$$

and

$$L_X \propto M^{\frac{4}{3}} \propto T^2 \tag{1.14}$$

We also note that entropy (s) is a useful measure of the thermodynamical state of the system. The entropy of a system is always conserved and scales as $s = kT/n^{2/3}$ (Voit et al., 2005). Therefore, assuming self-similarity the entropy of the ICM scales with temperature as:

$$S \propto T_X \tag{1.15}$$

Based on these scaling relations, we would predict that the X-ray luminosity with T_X^2. However it is important to note that these relations rely on a simplistic model, based only on gravitational processes (see §1.5.2). This is known as the luminosity-temperature ($L_X - T_X$) relation. Therefore, the mass of a galaxy cluster can be estimated from its luminosity (Rykoff et al., 2008; Stanek et al., 2006), as well as its temperature (Reiprich and Böhringer, 2002; Zhang et al., 2007). The intracluster gas temperature is tightly correlated to the virial mass. The X-ray luminosity of the gas is a much less robust indicator of mass as it depends on the density profile which is hard to model; however, it is much easier to measure. Typically, one uses the $L_X - T_X$ relation to bootstrap from L_X to mass. Moreover, knowing the $L_X - T_X$ relation is required when deriving cosmological parameters from clusters (Mantz et al., 2009; Sahlén et al., 2009). Therefore, the determination of an accurate $L_X - T_X$ relation is one of the prime goals for XCS (§2.7).

1.5.2 Departures from self-similarity & feedback

Empirical studies have shown that cluster scaling relations do exist, however they have shown them to be inconsistent with a self-similar model (Markevitch, 1998; Arnaud and Evrard, 1999; Pratt et al., 2009). This implies that physical processes other than gravitation are present within the ICM. Evidence for a steeper $L_X - T_X$ relation of $L_X \propto T_X^3$ has been shown by several studies. Furthermore this relation appears to steepen further ($L_X \propto T_X^4$) at the low mass end thus suggesting a seperate $L_X - T_X$ relation for clusters and groups (Helsdon and Ponman, 2000). This implies a mechanism is suppressing the X-ray brightness and therefore gas density in low mass systems. Thus providing further evidence for similarity breaking.

As entropy is a measure of the thermodynamical state of the ICM it is often used to study departures from self-similarity. An adiabatic system always tends towards its lowest entropy state. This implies that the entropy of the gas must scale with cluster radius otherwise the gas would be convectively unstable and buoyant. However, the X-ray observations of Ponman et al. (2003) show the entropy in their clusters scale as $s \propto T^{1/3}$, rather than the self similar scaling relation of $s \propto T$. Once again, this implies some mechanism has raised the entropy in low mass systems toward the cluster core.

Radiative processes offer a possible explanation for an increased entropy in the cluster core. The intracluster gas is most dense in the centre of clusters. As the rate of radiative cooling is proportional to the square density of the gas, the cooling rate should be most efficient in the centre of clusters. Thus as the gas cools in the center of the cluster, additional gas moves in towards the core and therefore conserves entropy in the system. This would induce a 'cooling flow', thus increasing the core density further, in turn increasing the cooling rate. However, the observational evidence does not support this mechanism. Despite having a cooling time less than the Hubble time, high resolution X-ray spectroscopy shows the gas in cluster cores only appear to cool by up to a factor of 3 (Peterson and Fabian, 2006). This lack of a runaway cool core is known as the 'cooling flow problem'. Furthermore, this mechanism would require 50% of the gas in a cluster to cool into stars and observational evidence shows there are not enough stars to support this hypothesis. For example, Balogh et al. (2001) shows that only 10% of the cluster mass is in the form of stars. Hence, this implies non-radiative processes are occurring within the gas. Additionally, clusters in high resolution simulations suffer from a phenomenon known as 'overcooling' when only radiative processes are considered. These simulations predict a higher percentage than 10% (Muanwong et al., 2006) implying a too efficient cooling

mechanism within the simulation. Thus adding further support to non-radiative processes within clusters. We note that despite the lack of evidence for cooling flows, many clusters are cooler in the centre. These tend to be the most relaxed systems in the population and are often referred to as 'cool core clusters'.

Non-radiative feedback processes are believed to come from the galaxies in clusters. The two main types of feedback mechanisms proposed are starburst winds (Fabbiano et al., 2004) and AGN (Sijacki et al., 2007). As a result, these feedback processes are expected to be more common at high redshift due to the higher star formation rate and increased luminosity of AGN at high redshift. An additional pre-heating (Bialek et al., 2001) of gas may be required before its entry into the cluster. A suggested mechanism for this may be provided via supernovae injecting energy into the gas of a galaxy at high redshift (z>4).

The effect of feedback would be less prominent in rich clusters as heating of ICM caused by the injected energy is small compared to the virial temperature of the gas, unlike poorer clusters and groups. This enables rich clusters to exhibit a scaling relation closer to an approximate self-similar scaling relation, whereas poorer clusters and groups show large deviations from this trend.

In light of these potential feedback processes and the deviation of clusters from self similarity; large samples of clusters are needed spanning a range of masses and redshifts in order to pin down the $L_X - T_X$ relation to allow cosmological parameters to be derived. It is hoped that large scale $L_X - T_X$ studies, such as that planned by XCS, will shed light on the non-gravitational physics at play in clusters (Short et al., 2010).

1.6 Optical properties of galaxy clusters

Galaxy clusters are believed to form via hierarchical structure formation and exist at the intersections of filaments in the cosmic web. Thus the number of galaxies contained within them have been built up through a series of dark matter halo mergers, each containing galaxies. In addition, the largest cluster galaxies are thought to be built up through the accretion of stellar matter through galaxy mergers. As these processes are driven by gravity, the largest cluster galaxies are generally located towards the cluster core, which is coincident with the deepest part of the cluster halo potential well.

The dominant population of galaxies in a cluster are early-type galaxies *i.e.* Elliptical (E) or Lenticular (S0) galaxies. Elliptical galaxies are generally gas poor, with old stellar populations and show little sign of recent star formation. Therefore elliptical galaxies are believed to evolve passively. As a consequence their galaxy spectrum is made up of an

old cool population of stars with stellar spectra dominated by ionized metal lines. This accumulation of metal lines gives rise to a prominent drop at 4000Å in elliptical galaxy spectra which increases in strength with decreasing redshift. This drop is referred to as the *4000Å break*. As the 4000Å break is a strong, universal feature for elliptical galaxies, it is often used to infer redshift estimates for elliptical galaxies. Lenticular galaxies are similar to elliptical galaxies in that they have a dominant galactic buldge and similar stellar populations, however they also have a small, often faint, disk component. Galaxy clusters do contain late-type galaxies, *i.e.* spiral galaxies, however, these are typically located towards the outskirts of a cluster.

The probability distribution of galaxies over absolute magnitude is known as a *luminosity function* (LF). Luminosity functions are characterised by a Schechter function (Schechter, 1976) parameterised by their characteristic luminosity, known as L_*, and the slope of the distribution. Luminosity functions reveal information about the global population of galaxies within a cluster and thus by studying changes in the shape of a LF with redshift and environment, one can infer possible evolution in the galaxy population as a whole (Gilbank et al., 2008).

The center of galaxy clusters often host *Luminous Red Galaxies* (LRGs) (Wake et al., 2008). These are effectively giant elliptical galaxies that are intrinsically luminous ($L{>}3L_*$ see below) and red. Whilst ∼80% of LRGs are found to be consistent with an old, passively evolving stellar population; a small number of LRGs show spectral emmision lines indicative of a young stellar population, as well as a small number showing increasing evidence for recently quenched star formation with redshift (Roseboom et al., 2006). By definition, each cluster has a *Brightest Cluster Galaxy* (BCG). Occasionally, clusters may host a BCG with a large extended envelope of diffuse gas. These galaxies are referred to as cD galaxies and are believed to have formed through galaxy mergers. Indeed, some cD galaxies even show signs of multiple nuclei (Hoessel and Schneider, 1985). BCG's can often be used to infer the dynamical state of a cluster with knowledge of the X-ray gas. If a BCG is offset from the peak in X-ray gas this is usually indicative of a recent cluster merger. On the other hand, if a BCG is coincident with the X-ray peak, it may be indicative of a virialised system. Furthermore, 25% of BCGs have strong emission lines and are up to 1 magnitude bluer in colour compared to the typical colour of pasively evolving elliptical galaxies in a cluster, thus implying ongoing star formation (Bildfell et al., 2008). These blue BCGs reside in clusters that lie above the $L_X - T_X$ relation (§1.5.1) implying the presence of a cooling flow fueling star formation in the BCG.

Due to the filamentary nature of structure in the universe and the presence of clusters within them, a chance line-of-sight projection of galaxies can give rise to a false cluster detections and/or a false association of galaxies within that cluster (Collins et al., 1995). As such, the optical detection of clusters have historically suffered from projection effects. Thus numerous techniques have been utilised by various optical surveys in an attempt to alleviate this issue (see Gal (2006) for a review). Each of these techniques use prior assumptions on the general nature of galaxies in clusters as search criteria upon which to detect galaxy clusters. The relatively recent red sequence technique, utilises the tight relation of early-type galaxies in colour-magnitude space (§1.6.1), to make projection effects more of a benign problem (Gladders and Yee, 2000b).

1.6.1 The Cluster Red Sequence Relation

Dressler (1980) demonstrated that galaxy clusters exhibit a morphology-density relation (MDR), whereby, elliptical and lenticular galaxies are more frequently located in the cores of clusters, as opposed to their spiral galaxy counterparts which are located more towards their edge. It is these early-type galaxies that form the high mass end of the cluster luminosity function. In addition, these luminous early-type galaxies have statistically redder colours than the late-type galaxies within clusters (Visvanathan and Sandage, 1977). Observations of nearby clusters have shown these red, elliptical and lenticular galaxies form a tight sequence in colour and magnitude space with extremely small scatter (Sandage and Visvanathan, 1978; Bower et al., 1992; Stanford et al., 1998; López-Cruz et al., 2004). Ellis et al. (1997) found the scatter on the (U-V) red-sequence relation to be less than 0.05 in magnitude. As a result, this colour-magnitude relation (CMR) has been designated the *E/SO ridgeline* or the cluster *red sequence*.

The red sequence has proven to be extremely homogeneous within a cluster and between clusters at the same redshift. Bower et al. (1992) showed its tight relation extends 8 magnitudes down the cluster luminosity function for both the optically rich Coma cluster and relatively poor Virgo cluster at z=0.1. Moreover, the red sequence appears to be a ubiquitous property of clusters over a range of redshifts. Studies of the red sequence has shown it to extend to redshifts of z>1 (Mei et al., 2006). The cluster red sequence may be even be in place during the formation of a cluster, as suggested by the presence of a red sequence present around the radio galaxies of proto-clusters at z∼3 (Kodama et al., 2007). Furthermore, no evolution in scatter or slope of cluster colour magnitude relation has been found to z∼1 (Mei et al., 2009). This remarkable homogeneity suggests the stel-

lar populations of elliptical galaxies on the cluster red sequence formed from the same constituent gas. Furthermore, the existence of a red sequence to high redshift implies that cluster elliptical galaxies contain a passively evolving population of stars (Stanford et al., 1998; de Propris et al., 1999), even at early epochs.

The bright end of the cluster CMR can be fit with a linear relation parameterised by its slope and zeropoint. The slope of the present-day CMR can be interpreted as an age-metallicity or mass-metallicity relation. The more metals a galaxy contains, the redder it appears. Either luminous ellipticals are redder because their stellar populations are older, or because their stars are generally more metal rich. This age-metallicity degeneracy was effectively broken by Kodama and Arimoto (1997) who showed the colour-magnitude relation is most consistent with a mass-metallicity relation. If the colour-magnitude relation was an age sequence, their slopes would change rapidly with redshift as the fainter galaxies reach their formation epoch. This effect would be most pronounced for galaxies within 4 Gyrs of formation. However, if the slope is a metallicity relation from an old, passively evolving population of elliptical galaxies, formed at high redshift, then the slope would remain constant over a large redshift range. By comparing observed CMRs to model CM tracks predicted using simulated galaxies with various ages and metallicities, Kodama and Arimoto (1997) showed their slopes remained constant beyond z=0.3, in accordance with a mass-metallicity relation.

The scatter on the red sequence however, is likely an age effect. Using a sample of clusters between z=0.31 and z=1.27, Kodama et al. (1998), measured a maximum age difference of 1 Gyr for elliptical galaxies on the red sequence. Thus implying a coeval population of stars. Therefore, as the scatter on the red sequence is small, its dispersion provides constraints on the formation epoch of elliptical cluster galaxies and is estimated to be within z_f>2-4 (Kodama et al., 1998).

The theories behind the origin of the mass-metallicity relation depend on the nature of structure formation in the universe (De Lucia and Blaizot, 2007). In a *monolithic collapse* scenario; due to their larger potential well, massive elliptical galaxies are more likely to retain metals produced by supernovae during their initial starburst, in turn prolonging their starburst episode. However, these metals are more likely to be lost in smaller, fainter elliptical galaxies as the supernova winds causes sufficient heating of the ISM to lose the supernovae ejecta through the production of inter-galactic winds. In the hierarchical structure formation scenario, the mass-metallicity relation is still maintained if larger elliptical galaxies are formed through a larger number of mergers of metal rich spiral

galaxies.

The universality of the cluster red sequence, with its homogeneous and tight relation present in all clusters up to high redshift, implies that the majority of cluster elliptical galaxies are coeval, formed from the same constituent stellar population, at a minimum formation epoch of z_f=2.0. Furthermore, because cluster elliptical galaxies formed at high redshift and have evolved passively since, with little or no subsequent star formation, the zeropoint of the red sequence contains information about the bulk property of their stars (Kodama et al., 1998). As their young blue stars die, the overall stellar population becomes redder causing the CMR to move to increasingly redder colours in colour-magnitude space with decreasing redshift. This property of the red sequence, along with its uniformity and small scatter, allows it to be used as a precise redshift estimator (Sandage and Visvanathan, 1978), as well as a tool for the detection of galaxy clusters (Gladders and Yee, 2000b). Indeed, the red sequence has enabled the detection of galaxy clusters to redshifts z>1 (Wilson et al., 2009; Demarco et al., 2010).

1.6.2 Galaxy Evolution on the Red Sequence

Galaxy clusters provide samples of galaxies in similar environments over a range of epochs. This makes them very useful laboratories to test theories regarding galaxy evolution. However, their extreme environment presents a biased view of galaxy evolution towards the high mass tail of galaxies in the densest environments. Galaxy clusters exhibit a bi-modality in their galaxy populations (Baldry et al., 2006; Loh et al., 2008); a dominant population of passive galaxies that form a tight red sequence (§1.6.1), and a population of star forming galaxies referred to as the *blue cloud*. The probability of a galaxy belonging to red sequence or blue cloud depends on its stellar mass and its environment (Baldry et al., 2006). However, it is important to note, that this bi-modality is also seen within the field galaxy population and that the red sequence relation observed in clusters is also apparent for field galaxies (Bell et al., 2004). Thus, for a given mass, a galaxy will have the same metalicity whether it is located in a cluster or in the field. However, it is galaxy clusters that contain the largest galaxies in the universe.

The bright end of the red sequence relation (L>L_*) shows little sign of evolution to z≥1. Loh and Strauss (2006) showed the large magnitude gap ($\triangle_{12}$=0.8mags) between BCGs and the second brightest galaxy showed no evolution with redshift to z=0.4. Stott et al. (2008) also found similar results to z=1, with no correlation between BCG dominance and X-ray luminosity. Furthermore, by studying a sample of 5 BCGs in clusters be-

tween $1<z<1.4$, Collins et al. (2009) showed their stellar populations to be consistent with passive evolution with a formation time of $z_f = 3 - 2$. Moreover, $\sim$80% their stellar mass appeared to be in place by z=1.4, in disagreement with recent semi-analytic models (De Lucia and Blaizot, 2007), thus challenging theories of hierarchical structure formation for BCGs.

Although the cluster red sequence is observed to be in place at high redshift, the number of galaxies located on the red sequence appears to have doubled since z=1 (Gilbank et al., 2008). A deficit of faint red sequence galaxies is apparent between clusters at z=0.8 and z=0.4 (De Lucia et al., 2004, 2006). Stott et al. (2007) observe a similar trend between z=0.5 and z=0.1, along with a change in the slope of the red sequence which they attribute to this faint galaxy build-up (Stott et al., 2009). Gilbank and Balogh (2008) show that the red sequence dwarf to giant ratio (DGR) decreases with redshift for galaxies both in the field and in clusters. This observation is consistent with the cosmic *downsizing* scenario, whereby star formation progresses to lower mass systems with decreasing redshift (Cowie et al., 1996). However, the DGR is larger for clusters at all redshifts, suggesting that star formation for these faint galaxies ceased earlier. The deficit of faint red sequence galaxies at high redshift however, still remains under heated debate (Andreon (2007), Andreon (2006)). Additionally, Holden et al. (2004) and Mei et al. (2009) find no evolution in the red sequence slope to $z\sim1$, contrary to (Stott et al., 2009).

Interestingly, it is the population of lenticular galaxies on the red sequence that appears to increase. Conversely the populations of spiral galaxies decreases, whilst the population of elliptical galaxies remains unchanged (Dressler et al., 1997; Poggianti et al., 2009). Thus, the consensus view is that two populations form the present day red sequence relation; a primordial population in place during the formation of cluster; and a younger population of early-type galaxies gained through the accretion and transformation of spiral galaxies to ellipticals, which subsequently fall onto the observed red sequence relation (Poggianti et al., 2005). Poggianti et al. (2005) argue that downsizing alone cannot explain the build-up of faint galaxies, suggesting star formation must be quenched.

Consequently, studies of galaxy evolution in clusters have focused on processes that could quench star-formation and thus transform galaxies from the blue cloud onto the red sequence. However many factors could be at play within a cluster, *i.e.* their presence in a dense environment, interactions with the hot ICM, the mass of the cluster and the redshift of the galaxy, and as such, disentangling their effects remains a hard task. Suggested mechanisms include mergers, galaxy harassment, gas stripping and strangulation.

Of these, strangulation is the preferred mechanism affecting dwarf red sequence galaxies (Gilbank and Balogh, 2008). In this scenario, the loosely bound gas in a galaxy halo is stripped as it merges with the larger cluster halo, thus starving the galaxy of further star formation.

Linking transformation mechanisms to global cluster properties as a proxy for mass may provide further insight. However, studies have found no dependence on the faint build-up of cluster galaxies with the global cluster environment as given by X-ray luminosity, BCG dominance, velocity dispersion or cluster-centric distance (Wake et al., 2005; Stott et al., 2009; Pimbblet et al., 2002). Similarly, no dependence on galaxy number density has been found (Hogg et al., 2004). However, Poggianti et al. (2005) suggest a minimum mass exists ($M \sim 1-2\times10^{14}M_{\odot}$, *i.e.* systems with velocity dispersions on the order of 500-600 kms^{-1}) above which all star formation is quenched instantaneously. Below this mass, they find an anti-correlation between [OII] emission and velocity dispersion, indicating a truncation of star formation with mass in low mass cluster/group systems.

In summary, the red sequence seems to be a ubiquitous feature of all clusters (however, see Donahue et al. (2002) for an alternative view). Its origin and evolution is as yet poorly understood, however, this lack of knowledge does not prevent one using it to find clusters, measure redshifts, or measure a physically meaning 'richness'.

1.6.3 Cluster Optical scaling relations

Cluster galaxies can be used to infer cluster masses. Assuming a gravitationally bound system in virial equilibrium, the line of sight velocity dispersion of galaxies can be used to estimate the virial mass of a cluster (Girardi et al., 1998; Lopes et al., 2009). In addition, a direct measurement of cluster mass can be obtained through the distortion in the shape of background galaxies due to the gravitational lense of the cluster's mass -known as *weak lensing* (Sheldon et al., 2009; Zhang et al., 2010). Both of these methods are expensive in terms of telescope time. In addition, modelling the dark matter profile within a cluster is a difficult problem to solve, dogged by numerous systematics. Furthermore, if one assumes the cluster light traces the mass of the dark matter halo, one can use the number of galaxies or the summed optical light of the galaxies in a cluster to infer cluster mass (Rozo et al., 2010). In this manner, relatively inexpensive photometric surveys have recently given rise to the measurement of cosmological parameters (§1.4) by using calibrated optical to halo mass and optical to X-ray scaling relations (see below).

The CNOC1 Cluster Redshift Survey use the galaxy cluster center correlation ampli-

tude, *Bgc*, as their richness parameter (Yee and Ellingson, 2003) hereafter YE03. *Bgc* is the richness (not including the BCG) scaled by the cluster luminosity function and spatial distribution function (Yee et al., 1999). Assuming photometry accurate to within 0.2 magnitudes and knowledge of the luminosity function accurate to within 20%, YE03 count galaxies to a k and evolution corrected M_r of -20.0, out to a radius of $0.5h_{50}^{-1}$ Mpc. By using a small radius, they argue that variations in field galaxy contamination are kept to a minimum (important for high redshift systems where the background number density is high). Thus, YE03 measure optical richness scaling relations against X-ray luminosity, X-ray temperature and velocity dispersion (see Hicks et al. (2008, 2006) for similar results on CNOC1 and RCS clusters respectively).

On the other hand, the MaxBCG survey (Koester et al., 2007b), use the parameter N_{200} to estimate optical richness. N_{200}, as defined by MaxBCG, is the number of cluster galaxies within $\pm 2\sigma$ of the cluster red sequence colour, to a limiting magnitude of $0.4L_*$, out to the virial radius (R_{200}) of the cluster. Where R_{200} is the radius that encompasses 200 times that of the critical density ρ_{crit}, an approximation to the virial mass. In order to determine N_{200}, MaxBCG use the empirical scaling relation of Hansen et al. (2005) to convert between N_{gal} and N_{200} *i.e.* convert the number of red sequence galaxies within $3h^{-1}$Mpc to within R_{200}. In this manner, the number of red sequence galaxies is scaled to within R_{200}.

The MaxBCG catalogue comprises 13,823 clusters detected within SDSS, with a richness of $N_{200}>10$. Using this richness estimate, optical richness scaling relations were determined for MaxBCG clusters against velocity dispersion (Becker et al., 2007), X-ray luminosity (Rykoff et al., 2008), and halo-mass derived from weak lensing measurements (Johnston et al., 2007). In order to obtain an $N_{200} - L_X$ relation, Rykoff et al. (2008) stack X-ray emission from the ROSAT All-Sky Survey (RASS) for all MaxBCG clusters, to measure a mean X-ray luminosity as a function of optical richness and redshift.

A universal definition of richness has not been adopted in the literature, however attempts have been made in the literature to determine the 'best' optical richness estimate for cluster mass. One drawback of using optical richness to infer cluster mass is that this quantity is generally measured within an aperture based on knowledge of the cluster mass. Thus, Rozo et al. (2008) used MaxBCG clusters derived an 'improved' method for measuring optical richness without a priori knowledge of the cluster size. Using an iterative approach they aim to reduce the scatter in their chosen optical richness to X-ray luminosity relation to determine the optimum radius within which a cluster richness should

be measured. Furthermore, Reyes et al. (2008) investigated the optical mass estimates N_{200}, the total optical luminosity of N_{200} galaxies (L_{200}), the luminosity of the BCG (L_{bcg}), L_{bcg}+L_{200}, and L_{bcg}+N_{200}. By comparing these estimates to cluster mass estimates derived from weak lensing, they determine the most accurate optical mass tracer is a combination of the luminosity of the BCG and N200 (L_{bcg}+N_{200}). However, it is also important to note that some clusters do not lie on these scaling relations. Several studies have found a significant population of X-ray underluminous clusters as expected for a mass derived from velocity dispersions (Popesso et al., 2007; Gilbank et al., 2004; Donahue et al., 2001)

1.7 Discussion

The near future sees the advent of upcoming large optical imaging surveys. with associated science collaborations tasked with measuring cosmological parameters from optical data alone. Surveys such as the Dark Energy Survey (DES)[4] (whose operation phase is estimated to begin in 2011) plan to measure Ω_m and Ω_Λ using cluster masses derived from optical data. These collaborations need pre-existing scaling relations with which to calibrate their data. In light of this fact there is a growing need for a reliable optical proxy for cluster halo mass.

Several attempts to measure cluster optical to X-ray scaling relations have been presented in the literature. The most notable of which are those performed by MaxBCG, RCS and CNOC1 (§1.6.3). Similar to NXS, these surveys use large optical data sets from which they utilise the cluster red sequence (§1.6.1) to detect galaxy clusters and measure optical richness (*i.e* the number of cluster galaxies). Cluster halo mass for these surveys were estimated by using X-ray data, galaxy velocity dispersions, or weak lensing, which are then used to bootstrap their optical richness scaling relations. When using X-ray properties to infer cluster mass, X-ray data was either obtained by cross correlating large samples with publicly available data, or by targetting a small subset of their optical sample for X-ray follow-up. As a consequence, these surveys typically suffer from inhomogeneity and selection effects. Therefore there is a need for a fresh approach, as outlined in this thesis.

[4]https://www.darkenergysurvey.org/

Chapter 2

The XCS

The XMM Cluster Survey (XCS) Romer et al. (2001) is a serendipitous X-ray cluster survey exploiting public data from the XMM-Newton satellite. The survey is performed by an international collaboration consisting of 19 members (see Table 2.1). This chapter reviews the current status of the XMM-Cluster Survey and its preliminary results, placing emphasis on the aspects relevant to this thesis.

In Section 2.1 we overview the XCS. The generation of XCS reduced X-ray imaging data from the XMM public archive, and the algorithm utilised to extract XCS cluster candidates from within these data are discussed in Sections 2.2, 2.3 and 2.4. As a result, three internal data releases have been generated by XCS, described in Section 2.5, which shall be used to achieve the XCS goals outlined in Section 2.7. However, a clean cluster sample with additional redshift information is required to achieve these goals. Thus, in Section 2.8 we describe the redshift follow-up effort of XCS, along with an XCS effort to produce a confirmed cluster sample (§2.9).

2.1 XCS Overview

The XMM-Newton (X-ray Multi-Mirror Mission - Newton) satellite is an ESA mission and was launched on December 10th 1999. The satellite houses three European Photon Imaging Cameras (Epic): two cameras with MOS (Metal Oxide Semi-conductor) CCD arrays which receive approximately 50% of the incident flux each, and one camera with a pn CCD array located at the focus of the instrument which receives all of the incident flux. One or more cameras can be used in concert giving rise to numerous observing modes. XMM-Newton was designed to place greater importance on increased sensitivity, rather than spatial resolution. As a result, XMM-Newton enables the detection of X-ray sources

Table 2.1. Members of the XCS collaboration

Member	Institution	Country
Chris Collins	Liverpool John Moores University	UK
Michael Davidson	Royal Obsrvatory Edinburgh	UK
Matt Hilton	University of KwaZula-Natal SAAO	South Africa
Mark Hosmer	University of Sussex	UK
Ben Hoyle	Universitat de Barcelona	Spain
Scott Kay	University of Manchester	UK
Andrew Liddle	University of Sussex	UK
Ed Lloyd-Davies	University of Sussex	UK
Robert Mann	Royal Observatory Edinburgh	UK
Nicola Mehrtens	University of Sussex	UK
Chris Miller	University of Michigan	USA
Robert Nichol	University of Portsmouth	UK
Kathy Romer (PI)	University of Sussex	UK
Kivanc Sabirli	University of Sussex	UK
Martin Sahlén	Stockholm University	Sweden
Adam Stanford	Lawrence Livermore National Laboratory	USA
Pedro Viana	Universidade do Porto	Portugal
Mike West	European Southern Observatory	Chile

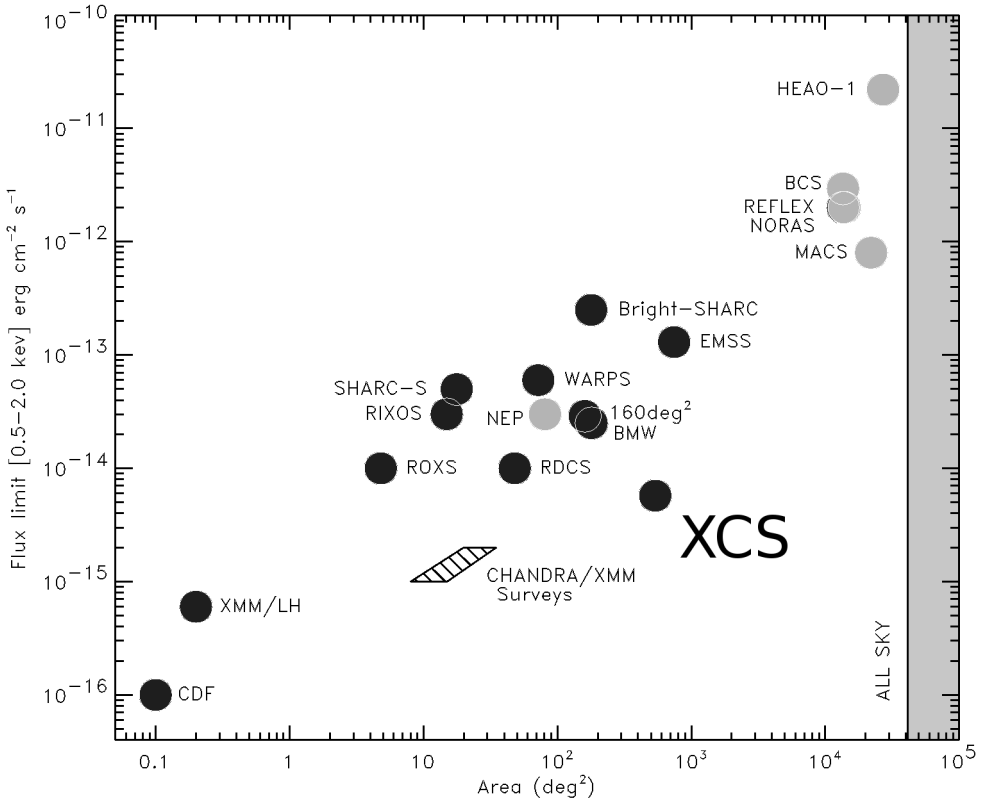

Figure 2.1 A comparison of survey area and limiting flux between XCS and pre-2002 serendipitous and pointed X-ray cluster surveys (given by dark and light circles respectively. The location of XCS is estimated based on a completed survey. [Figure credit: Davidson (2005), adapted from Rosati et al. (2002).]

to a limiting X-ray flux $f(0.5\text{-}2\text{keV}) \sim 10^{-17} \mathrm{erg\,cm^{-1}\,s^{-1}}$ (Alexander et al., 2003), making it the most sensitive X-ray telescope to date.

The XCS employs a cluster detection algorithm which is run on each observation file generated by the XMM-Newton satellite. This algorithm is called XAPA, standing for the XCS Automated Pipeline Algorithm, and its workings are briefly described in section §2.3. The result of XAPA is a homogeneously selected sample of galaxy cluster candidates. These cluster candidates are then optically followed-up to provide confirmed cluster identifications and redshift estimates. This confirmed sample will then allow the XCS to achieve the science goals stated in section §2.7. The XCS aims to achieve a completed survey area of $500\,\mathrm{deg}^2$. This large area, together with its typical flux limit of $f(0.5\text{-}2\text{keV}) \sim 1.5 \times 10^{-14} \mathrm{erg\,cm^{-1}\,s^{-1}}$ (Romer et al., 2001), and a typical exposure time of 10ks, makes the XCS a competitive project compared to existing X-ray cluster surveys (see Figure 2.1).

Data from XMM will be at the forefront of X-ray astronomy for at least another decade. The next generation of X-ray satellites, such as the International X-ray Observatory (IXO) (Vikhlinin et al., 2009a), are still in the planning stage and will not be launched until at least 2020. Whereas, eRosita (Predehl et al., 2010), an interim mission with worse sensitivity and spatial resolution than XMM will be launched in 2012. Thus, science results obtained by the XCS will remain at the leading edge of X-ray cluster astronomy for at least the next 10 years.

2.2 XCS image creation

For each observed location, XMM generates a series of data files, collectively known as ObsIDs hereafter, including event lists. Event lists contain information on the time, location and energy of each individual photon detected by the three cameras on XMM. Using the location and energy information in these lists, XCS images are created with corresponding exposure maps. In addition, a mask is created for each obsID. These image masks ensure regions unsuitable for cluster detection, *e.g.*, bleed trails and other artifacts due to bright sources, or extended objects *e.g.* Supernovae and low redshift galaxies are not included in the XCS science area (see Hosmer (2009) for more detail). These unsuitable regions are located by eye and masked out by hand using an interactive `IDL` tool. The resulting image masks are then taken into account by XAPA (§2.3). Thus, only sources obtained from within 'good' regions in the image mask make it into the extended source list.

2.3 XAPA

X-ray sources are detected within XCS images using the XCS Automatic Pipeline Algorithm (XAPA). XAPA is described in detail in Davidson (2005). However, we briefly outline the main points herein.

XAPA utilises the wavelet detection algorithm `WTRANSFORM` which is part of the package `WAVEDETECT`, written by Peter Freeman. Essentially, wavelets of differing sizes based on a Mexican-hat profile are used to detect sources within XCS images. Source detection occurs in two runs using two sets of wavelet scales; the first run (XapaRun1) uses small wavelets to locate point-like sources; the second run XapaRun2 uses larger wavelets to detect more extended sources, these extended sources typically contain XapaRun1 sources. If these XapaRun2 sources are larger than the XMM point spread function (PSF) at the location of the source, then these sources are classified as extended. This extended source list is

then filtered, using the flags listed below, to create a list of identified cluster candidates.

- **PSF sized flag**: The XCS uses a PSF model provided by the XMM community. However, modelling the PSF of XMM is complicated and this model is known to contain flaws. Therefore, in order to reduce the number of point-sources mis-classified as extended; sources detected with extent comparable to the PSF are removed from the XCS cluster candidate list.

- **Point-source contaminated flag**: If the flux of an extended source is dominated by an internal point-source/sources identified in XapaRun1, then this extended source is removed from the XCS cluster candidate list. This flag should also reduce the appearance of point-source blends in the extended source list.

As a result, a clean homogeneous cluster candidate sample is produced. This cluster candidate list is then subjected to the criteria discussed in §2.4 to create a final statistical sample of XCS cluster candidates (known as StatSam) ready for scientific analysis. Figure 2.2 shows an example of an XCS ObsID and it's corresponding image mask. Highlighted in green are sources that have been classified as extended, those marked by red circles have been classified as point sources. Sources highlighted in pink have obtained a PSF size flag. Thus only the sources highlighted in green have made it into the StatSam list.

Once sources have been detected by XAPA, their energy fluxes are estimated using energy conversion factors (ECF's). These ECF's assume an input spectral model and , in the case of XCS, are determined twice (one for the typical AGN spectrum and once for a typical cluster spectrum). More accurate fluxes and luminosities are calculated for confirmed clusters, once redshift information is obtained. For those clusters detected with sufficient counts, an X-ray temperature can be calculated (see Appendix A).

2.3.1 XAPA-2

In 2009, an alteration was made to the XCS image creation and exposure map pipelines (§2.2). To completely automate the XMM image reduction process, the image and exposure map generation pipelines were re-written by Ed Lloyd Davies (Lloyd-Davies et. al., in prep). These changes were desirable as they increase the efficiency and objectivity of the XCS source detection process. The XAPA pipeline described in section §2.3 is then run on these reduced XCS images to provide source lists. We refer to this new combined pipeline as XAPA-2, which was then applied to all public XMM data to provide the third internal data release, or XCSDR3. By comparison, the XCS source lists XCSDR1 and

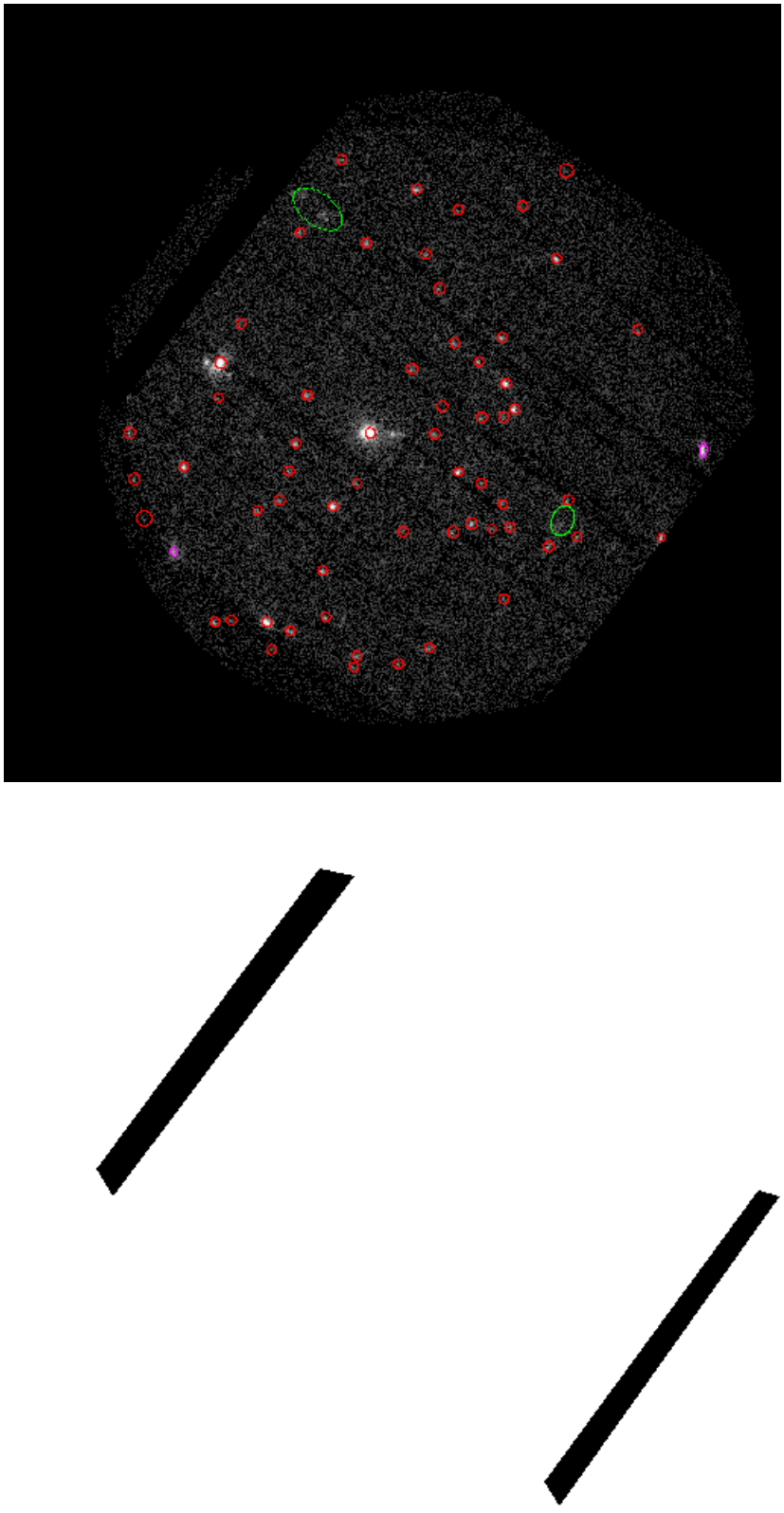

Figure 2.2 X-ray sources detected in the XCS processed XMM ObsID number 0202130101 (above) and corresponding image Mask (below). Extended sources (cluster candidates) are highlighted in green, point sources are highlighted in red, and psf sized sources are highlighted in pink. Masked regions of the ObsID are shaded in black.

Table 2.2 The number of XCS cluster candidates and corresponding area covered for each XCS internal data release. Listed are: the number of XCS ObsIDs processed; their total non-ovelapping area; the corresponding area in StatSam (§2.4); and number of XCS cluster candidates.

Data release	XCS ObsID	Total area	StatSam area	StatSam candidates
XCSDR1	1847	234.98	131.35	1411
XCSDR2	2395	297.27	160.2	1874
XCSDR3	4214	522.3	229.73	4092

XCSDR2(§2.5), created prior to 2009 were the product of XAPA-1. The total, non overlapping area in the corresponding data releases are given in Table 2.2. We note that the area in DR1+DR2 is contained within the area of DR3, although not all XCSDR1 and XCSDR2 cluster candidates were re-found in XCSDR3, as explained in Section 2.5.

XAPA-2 has the added capability of measuring X-ray temperatures (T_X) and X-ray Luminosities (L_X) (Appendix §A) for XCS clusters with redshift estimates (§2.8). Additionally, XAPA-2 measures X-ray redshifts (z_X) for XCS cluster candidates detected with a sufficient number of X-ray soft counts from their X-ray spectrum (Appendix §A). A small number of these cluster candidates with high X-ray redshift estimates (z_X>0.8) have been optically followed-up (§2.8 & §3.3.2), to test the veracity of their redshift estimates.

In the near future, as part of a planned XCSDR4, XCS will incorporate an XCS determined model of the XMM point spread function (Dubois et. al., in prep). This empirical PSF model utilises numerous high signal to noise XCSDR3 point sources detected over XCS image maps and should provide a more accurate model than the models currently available from the XMM support centre.

2.4 The XCS Statistical Sample

XAPA has been run on all publicly available data from the XMM archive (at the time of writing it had been run on > 4,000 ObsIDs). However, in order to meet the goals set by XCS, only fields/area meeting certain requirements are used to create an XCS Statistical Sample (StatSam) of galaxy cluster candidates.

For example, complications arise when measuring X-ray fluxes or assigning source identifications for X-ray sources detected in the Galactic plane. Therefore a cut is employed, excluding XCS pointings from StatSam with galactic latitude $|b|$<20 deg. Pointings close

to the Megallanic Clouds are also excluded for the same reason. XCS pointings which contain a cluster as the main XMM target are also excluded. This is because clusters tend to cluster (due to the nature of large scale structure), therefore the probability of detecting another cluster within a targetted XMM cluster pointing is greatly increased over random. Hence, cluster candidates detected within XMM targetted cluster pointings are not considered to be truly serendipitous detections[1]

Online databases, such as NASA/IPAC Extragalactic Database (NED)[2], SIMBAD[3] and BAX[4], contain large numbers of astrophysical sources with positions and object classifications. Therefore, the XCS makes use of these useful resources in order to further clean the XCS source list. XCS extended sources within a $2'$ matching radius of an object identified in an online database that is attributed to large extended X-ray phenomena such as supernova remnants, HII clouds, planetary nebulae *etc.* are removed from the StatSam.

As a consequence of these cuts, and the application of image masks created for each XCS ObsID (§2.2), the total non overlapping statistical sample area available to the XCS is greatly reduced from the total XMM image area processed by XAPA (shown in Table 2.2).

2.5 The XCS Internal Data Releases: XCSDR1, XCSDR2 and XCSDR3

The XCS has produced 3 internal data releases of statistical cluster candidate samples: XCSDR1 released in 2005; XCSDR2 released in 2006, and XCSDR3 released in 2009. Figure 2.3 shows their distribution across the sky. For the creation of XCSDR3, XAPA-2 was run on all XCS ObsIDs previously processed by DR1 and DR2, in addition to all ObsIDs observed by XMM after 2006. XCSDR3 yielded a 70% increase in area over XCSDR2. The cumulative non-overlapping area and number of distinct cluster candidates for each data release are stated in Table 2.2.

XCSDR1 (XCSDR2) was generated by Micheal Davidson (Mark Hosmer), using image files, exposure maps and ECFs created by Kivanc Sabirli. XCSDR3 was created by Mark

[1]For completeness, we note that the re-introduction of XMM targetted cluster pointings into the statistical survey area is currently being considered in order to increase the StatSam area. Only cluster candidates located a sufficient physical distance from a target cluster would be included.

[2]http://nedwww.ipac.caltech.edu/

[3]http://simbad.u-strasbg.fr/simbad/

[4]http://bax.ast.obs-mip.fr/

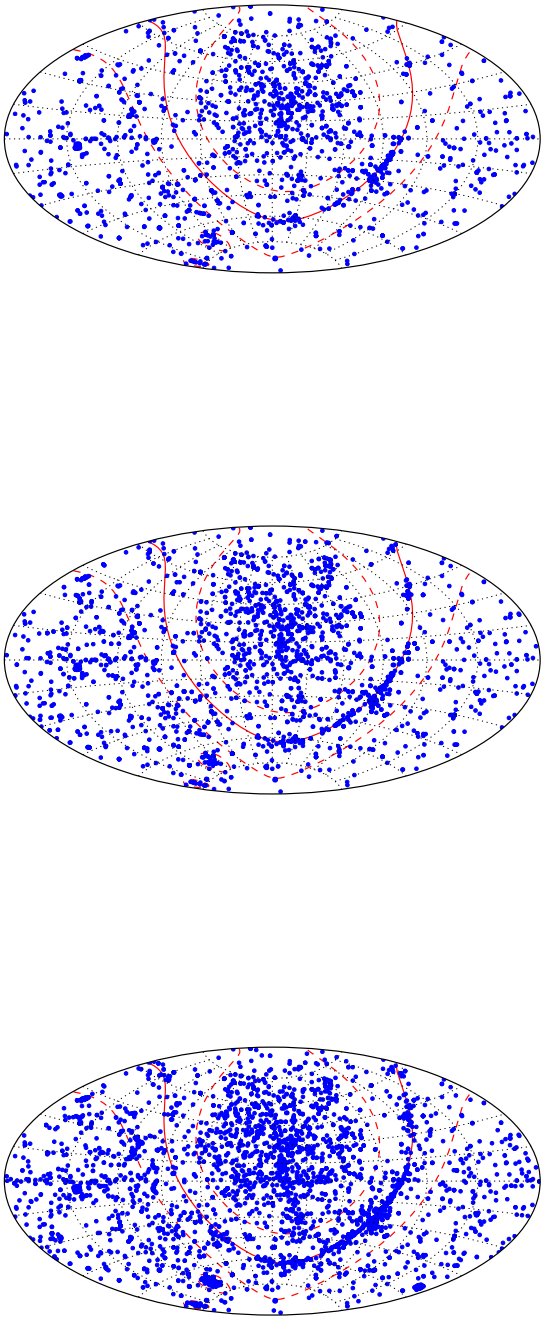

Figure 2.3 The survey coverage of the XCS across the sky. Points represent individual XCSObsIDs taken from the combined StatSam samples of XCSDR1 (top), XCSDR2 (middle) and XCSDR3 (bottom). XCSObsIDs are plotted by their central coordinates in Right Ascension (along the x-axis) and Declination (along the y-axis). The red solid and dashed lines respresent the galactic plane and the 20 degree galactic latitude cuts used to create the tatistical sample. [Figure credit: Ed Lloyd-Davies]

Hosmer, using exposure maps and ECFs generated by Ed Lloyd-Davies. Image masks for XCSDR1, XCSDR2 and XCSDR3 were generated by Micheal Davidson, Mark Hosmer and Mark Hosmer respectively.

As mentioned in Section 2.3.1, a switch-over occurred in 2009 between implementation of XAPA-1 and XAPA-2. Due to the alterations made to the XAPA pipeline between XCSDR2 and XCSDR3 we naturally expect the source lists of reprocessed area to differ slightly. However, after XCSDR3 was first produced in 2009, it was realised that XAPA-2 contained a problem in its treatment of solar flare-correction. Solar flares shower the XMM cameras with particles resulting in greatly enhanced X-ray background measurements compared to normal levels. Time intervals during which a solar flare is occurring should not be included when creating an X-ray image map from a prolonged XMM exposure. An automated flare-correction algorithm designed for XAPA-2, which removes time intervals associated with solar-flares, resulted in abnormally high background counts within some ($\sim$15%) of the reduced XMM images. Thus the original version of XAPA-2 resulted in a large number spurious sources, characterised by abnormally high ellipticity and large angular extent, and often located in chip gaps or at the edges of an XCS ObsID (see Figure 2.4). In addition, some genuine clusters, confirmed in XCSDR1 and XCSDR2 follow-up (§2.8) were missed.

A corrected version of XAPA-2 is currently being finalised and initial results have shown that most of the XCSDR1 and XCSDR2 candidates that had been missing in XCSDR3 are recovered (see Figure 2.4). Moreover, the problem of spurious sources mentioned above have been removed. Unfortunately the timing for the production of a corrected XCSDR3-v2 catalog is too late to be included in this thesis, therefore we use the initial (uncorrected) version, XCSDR3 herein. Because XCSDR3 is known to miss genuine XCSDR1 and XCSDR2 clusters, we also include these data releases in this thesis. This approach of mixing XCSDR3 with XCSDR1 and XCSDR2 should not pose a problem with regard to our results and discussion in subsequent chapters. For example, spurious candidates (*e.g.* on chip gaps) in XCSDR3 will be removed from our sample via XCS ClusterZoo (§2.9). Moreover, the addition (to XCSDR3) of extra clusters from XCSDR1 and XCSDR2 does not significantly impare our ability to define fair optical to X-ray scaling relations (§7.7 & §7.8).

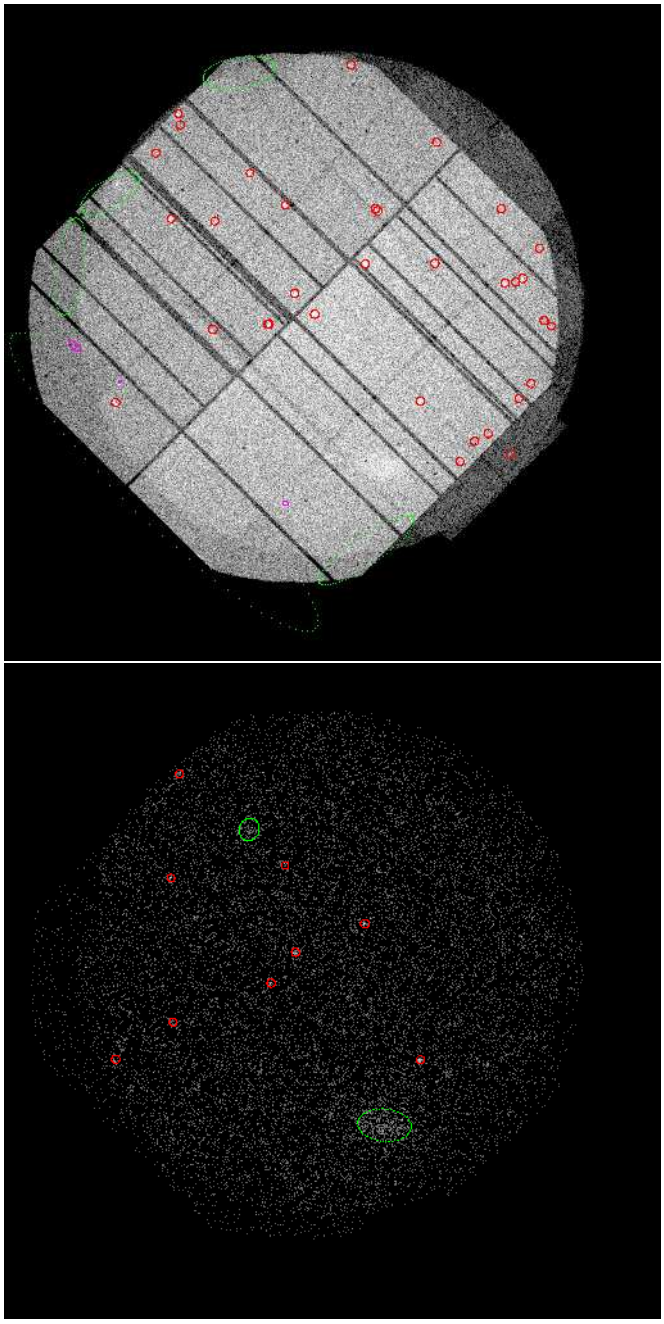

Figure 2.4 The XCS ObsID 0032140101 as processed by XAPA-2 (top) and XAPA-2v2 (bottom). The top figure clearly show a bright X-ray background compared to the bottom figure. In addition, the large, highly elliptical sources, detected as cluster candidates are removed in the reprocessed figure. [Figure credit: Mark Hosmer.]

2.6 XCS Selection Function

One advantage of an XCS defined cluster sample, over for example the heterogeneous cluster sample of Maughan (2007), will be the ability to determine accurate selection functions. The determination of cosmological parameters from cluster number count evolution (§1.4) requires knowledge of how the cluster selection process impacts the obtained science results. Therefore, in order to understand how the clusters detected by XCS represent the true underlying cluster population, a series of XCS selection function models are calculated. These selection function models test the XAPA recovery rate of fake simulated clusters placed within real XMM image maps, spanning a set range of cluster redshifts, luminosities and spatial density profiles. The results can then be folded into any cluster sample used to infer science results. The XCS selection functions require large processing times and are still being refined by the collaboration. An initial set has been processed and explained in detail in Section 2.2 of Sahlén et al. (2009).

2.7 The XCS Science Goals

The XCS has three main science goals which are listed below:

Cosmological Parameters The primary goal of the XCS is to measure the cluster mass function, thereby providing observational constraints on the cosmological parameters Ω_m and σ_8, using the cluster number counts technique (§1.3). For this measurement, a sample of optically confirmed XCS clusters detected with sufficient counts to allow a T_X measurement will be used. For simplicity in the selection function, it is planned to use a single count threshold e.g. 500 counts (referred to as the XCS500 sample hereafter). With at least 500 counts one can measure a temperature accurate to within 20% from the cluster X-ray spectrum (Sahlén et al., 2009). Cosmological predictions have estimated that for a full XCS500 sample, *i.e.* from a final survey area of 500deg^2, Ω_m can be measured to within ± 0.03 and σ_8 to within ± 0.05 (Sahlén et al., 2009). Sahlén et al. (2009) conclude that, the measurement of these cosmological parameters is heavily dependent on the cluster $L_X - T_X$ relation (see X-ray Scaling Relations below). The Sahlén et al. (2009) predictions were based on the forecasted redshift and flux distributions of clusters detected by the XCS (using the XCS selection function (§2.6) and assuming a flat universe Ω_Λ=0), measured by a Monte-Carlo Markov chain analysis.

X-ray Scaling Relations The XCS aims to measure self-consistent X-ray scaling relations, including the cluster X-ray luminosity to X-ray temperature ($L_X - T_X$) relation. To measure the $L_X - T_X$ relation, the XCS will use a sample of optically confirmed clusters, detected with at least 300 soft counts (known as the XCS300 sample), with redshift and temperature measurements. Furthermore, the cosmological parameters (mentioned above) shall be fitted in conjunction with the XCS $L_X - T_X$ scaling relation. This is desirable as X-ray temperature is being used as proxy for mass, and a joint fit provides consistency between XCS measured parameters. Using an inaccurate $L_X - T_X$ relation can cause large systematic offsets in the measured values of Ω_m and σ_8. Based on the cosmological predictions of Sahlén et al. (2009) we can expect to measure the slope and normalisation of the $L_X - T_X$ relation to within 13% and 6% respectively. We note that at the time of writing more than 500 XCS clusters with T_X values were available, compared to the next largest sample of 115 (Maughan, 2007).

Galaxy Evolution The high sensitivity of XMM allows the XCS to detect clusters to z>1 (Stanford et al., 2006). Hence, the XCS cluster sample will naturally contain many high redshift clusters with which to perform galaxy evolution studies within the high density environments of clusters to z>1 (Hilton et al., 2007, 2009; Collins et al., 2009). However, the detection of high redshift clusters depends on the exposure time and background levels of each XMM observation. In addition, their detection also depends on their location within the XMM image map due to the existence of vignetting and the XMM point spread function (PSF). This is because high redshift sources appear more point like due to their reduced angular diameter distance with redshift and reduced flux. Therefore, XCS has decided not to include very high redshift clusters in its cosmology analysis, due to the related uncertainty in the selection function.

2.8 Redshift follow-up to XCS

In order to meet the goals set by the XCS collaboration (§2.7), cluster candidates must be confirmed as clusters and be supported with measured redshifts. Redshift estimates are required, not only to measure both the cluster mass function and scaling relations, but also to measure X-ray temperatures, T_X, and X-ray luminosities, L_X: T_X and redshift are degenerate in X-ray spectral fits. With over 4,000 candidates in total (Table 2.2), emphasis was placed on the optical follow-up of cluster candidates detected with sufficient counts to allow an XCS T_X measurement, in particular those with more than 500 soft

counts (XCS500). In addition, small programs *e.g.* at Keck, targetted high ($z \geq 1$) redshift cluster candidates.

The XCS collaboration use publicly available optical data and redshift estimates whenever possible. The sources of publicly obtained redshifts are discussed below in sections §2.8.1 and §2.8.3. However, due to the distribution of XCS cluster candidates across the sky and their broad redshift range, additional dedicated XCS follow-up has had to be performed. The largest XCS follow-up programme to date has been the NOAO-XCS Survey (NXS, see chapter 3). In addition to the NXS, other smaller optical campaigns have been carried out at NTT, WHT, Keck and Gemini (§2.8.2).

2.8.1 Literature redshifts

The main resources used by XCS to find published cluster redshifts are astronomical journals and NED. Cluster redshifts listed in astronomical journals are cross-matched to XCS cluster candidate positions on an adhoc basis as they appear on astro-ph[5], *e.g.* XMMXCS J100750.5+125822.7 at z=1.082 (Schwope et al., 2010). However, this is not a fool-proof system and due to the large number of cluster candidates in the XCS StatSam, an automated approach was adopted to locate as many XCS cluster redshifts as possible in the literature. The NED check pipeline was originally written by Micheal Davidson and overhauled by Ed Lloyd-Davies in 2009.

The NED check algorithm locates published cluster redshifts (spectroscopic only) in NED, within a matching radius, which is defined iteratively from the X-ray properties of each XCS cluster candidate. This radius is the angular extent on the sky, estimated by using the number of detected source counts and assuming the cluster is at a particular (iterated) redshift, with an estimated (iterated) temperature from an assumed $L_X - T_X$ relation. In addition to cluster redshifts, the pipeline also retrieves redshifts (spectroscopic and photometric) for individual galaxies. Where available, the cluster candidate is either assigned the published cluster redshift, or assigned a mean spectroscopic redshift measured from a designated group of galaxies lying within z =0.05 of each other. This NED check pipeline is run upon every candidate in XCS StatSam.

[5]http://arxiv.org/archive/astro-ph

2.8.2 Spectroscopic follow-up

High redshift candidates

The XCS goal of studying galaxy evolution requires the follow-up of suspected high redshift (particularly at $z \geq 1$) clusters contained in the StatSam candidate list. High redshift candidates ($z \geq 0.7$) have been identified in public (*e.g.* §2.9) and proprietary (§3) optical/IR imaging, and by using XCS X-ray redshifts (Appendix A.3). These high redshift candidates have been observed at 8-m telescopes such as Keck[6], GEMINI[7], and Subaru[8]. High redshift candidates ($z > 0.7$) identified in NXS optical imaging have been targetted for spectroscopy at Keck and Gemini. Target selection was performed by Nicola Mehrtens and Matt Hilton and followed-up at Keck by Adam Stanford and Matt Hilton.

For example, this has allowed XCS to detect the highest redshift, X-ray selected cluster *XMMXCS J2215-1738* known to date, which was optically confirmed at Keck in 2006 to be at $z = 1.45$ (Stanford et al., 2006; Hilton et al., 2007, 2009). In addition, high redshift candidates have been identified by cross matching XCS candidates sources identified with a PSF flag (§2.3) with UKIDDS UDS IR imaging data. Sources were then eyeballed and cluster candidates follow-up at Subaru by John Stott.

NTT and WHT spectroscopic redshifts

The XCS have acquired telescope time by providing spectroscopic targets to the SDSS-II Supernova Survey (Dilday et al. (2010); SDSS-SN hereafter) to fill RA gaps in their observing campaigns. In this manner, long slit spectroscopy of XCS clusters was performed at NTT and WHT by members of the SDSS-SN team. When choosing targets, priority was placed on XCS clusters with photometric redshift estimates greater than $z \sim 0.4$ due to the lack of spectroscopic redshifts in that redshift range. This was motivated by the need to calibrate XCS and SDSS photometric redshifts estimated by the XCSRedSeq algorithm (§5.5). However clusters with a range of photometric estimates were included to compensate for a differing weather conditions and RA availability. At NTT, the positions of BCGs within XCS clusters, and occasionally a second potential cluster galaxy, were located by eye from the NXS/SDSS imaging to determine the location and orientation of the slit. Cluster targets and BCG positions were selected by Nicola Mehrtens and observed by Mat Smith (an XCS associate member) and Kathy Romer. Their spectroscopic redshifts

[6] http://www.keckobservatory.org/

[7] http://www.gemini.edu/

[8] http://www.naoj.org/

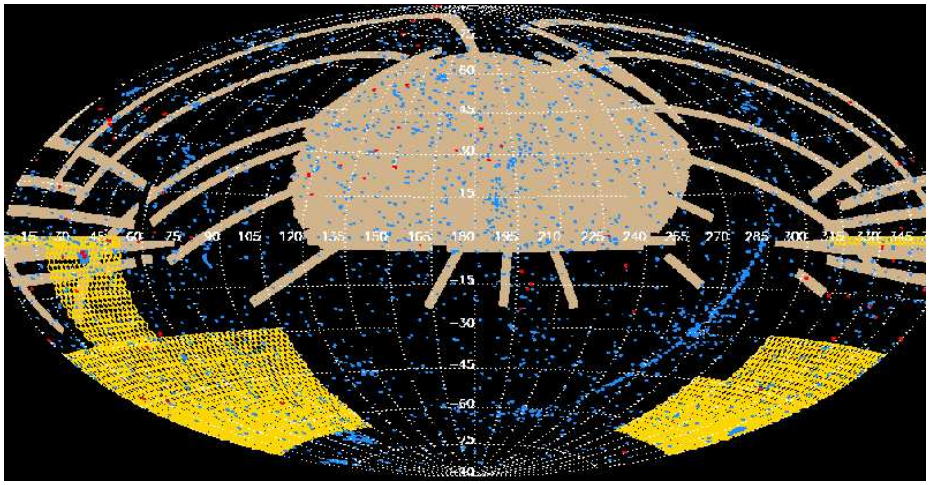

Figure 2.5 The XCS survey area (blue) and overlapping survey areas of NXS (§3.7, red), SDSS (§6.6, tan) and DES (yellow). [Figure credit: Chris Miller.]

were measured by Matt Hilton and Mat Smith. In the same manner, 2 additional NXS clusters were targetted for long slit spectroscopy at WHT. Targets were selected by Nicola Mehrtens, observed and reduced by Alistair Edge.

In addition to SDSS-SN runs, XCS was awarded time at NTT to follow up a sample of 5 NXS clusters at $z\sim0.5$ with >300 soft counts. These cluster were chosen to confirm NXS redshift estimates, and provide velocity dispersions (with the aim of measuring the $\sigma_v - T_X$ scaling relation). Targets were selected by Nicola Mehrtens and observations and reduction were carried out by Matt Hilton.

2.8.3 SdssDR6 LRG Redshifts

The Sloan Digital Sky Survey (SDSS) provides publicly available optical data covering a quarter of the sky (see Chapter 6). Multi-colour photometric data in the five Sloan filters (u, g, r, i, z) and spectroscopic data for more than 900,000 galaxies are retrievable via an online database[9]. Thus, SDSS provides an excellent resource to obtain cluster redshift estimates for XCS. Figure 2.5 illustrates the overlap of XCS with SDSS.

Two methods are used by XCS to extract cluster redshifts from SDSS data. The first, designed by the author, uses a red sequence technique inspired by Gladders and Yee (2000b) and is described in detail in Chapters 5 & 6. The second method, was developed by Ben Hoyle (Hoyle, 2008) using Luminous Red Galaxies (LRGs, see §1.6) taken from SdssDR6[10]

[9]http://casjobs.sdss.org/CasJobs/

[10]The sixth public SDSS data release.

In Hoyle's method, LRGs are identified within SDSS data using the colour-cuts devised by Eisenstein et al. (2001). Eisenstein et al. (2001) argue that LRG colour cuts can provide reliable photometric redshifts out to a redshift of $z = 0.55$. LRGs are identified within 175 Kpc of each XCS cluster candidate and their photometric, or if available, spectroscopic redshifts in the SDSS database are allocated to the XCS cluster candidate. If multiple LRGs are found within this region a mean redshift is obtained. If multiple groups of LRGs are found within 175 kpc, then the redshift of the lower redshift LRG group is assigned to the cluster candidate. In some instances, an XCS candidate may be a genuine cluster but if no LRGs are found within the matching radius, then a redshift cannot be assigned. This is the case when the cluster redshift is beyond the survey depth of SDSS. There are also occasions when a genuine cluster is at a redshift accessible by the SDSS but the LRG colour cuts and matching radius have failed to identify an LRG within the cluster. For example, XCSRedSeq(§4.3.1) acquired 41 additional redshift estimates for XCSDR1 candidates using SDSS data (all confirmed as clusters by ClusterZoo, §2.9), that had not been assigned an LRG redshift.

Hoyle's LRG algorithm was run on the XCSDR1 and XCSDR2 samples. In this manner, 62 XCSDR1 and 6 XCSDR2 spectroscopic redshifts respectively, were assigned to XCS cluster candidates between z=0.07 and z=0.3. The algorithm produced a further 120 XCSDR1 and 36 XCSDR2 photometric redshifts respectively between z=0.1 and z=0.7. We note that at the time of writing, Hoyle's LRG algorithm had not been applied to the XCSDR3 sample. We also note that, SDSS spectroscopic redshift information is only available to a redshift of $z\approx$0.3, therefore any LRG assigned redshifts beyond this are photometric redshifts.

2.9 XCS ClusterZoo

In 2007, an XCS online project took place, developed by Ben Hoyle, called XCS ClusterZoo, which attempted to classify 610 XSCDR1 StatSam cluster candidates falling within the survey regions of SdssDR6[11]. Subsequently, additional ClusterZoo's have taken place (§7.6.2), so we refer to this 2007 Zoo as XCS-SDSS ClsuterZoo I hereafter.

XCS-SDSS ClusterZoo I is based on SDSS Galaxy Zoo[12] (Lintott et al., 2008). XCS-SDSS ClusterZoo I used public SDSS colour-composite images, together with XCS images

[11] SdssDR6 was the latest SDSS data release at the time.

[12] In the SDSS project Galaxy Zoo, the morphologies of galaxies are classified by the public via the online website; www.galaxyzoo.org

created by Mark Hosmer. XCSDR1 cluster candidates were then classified by the XCS community following the classifications as stated on the XCS-SDSS ClusterZooI website:

- *Gold Cluster/Group*: Clear overdensity of galaxies. Extended X-ray source present and centered near the galaxy over-density.
- *Silver Cluster/Group*: Overdensity of galaxies present. Extended source present but not necessarily centered on the galaxies.
- *Bronze Cluster/Group*: Overdensity of galaxies present. Questionable X-ray extended source i.e., low signal, messy signal, highly elliptical signal, point sources, etc.
- *High-z Candidate*: No overdensity of galaxies present. Extended source present and of reasonable quality.
- *Not a Cluster/Group*: No overdensity of galaxies present. Questionable X-ray extended source i.e., low signal, messy signal, highly elliptical signal, point sources, etc.
- *Cannot Classify*: Missing/bad SDSS or x-ray data e.g., bright stars, masked region, at the edge of a field, UFO in the way, etc.
- *Unsure*: If you cannot use any of the above categories, use this one.

Each classification was assigned a number; *Gold Cluster* being the highest, *Not a Cluster* being the lowest. The average classification value for each cluster candidate was then adopted, taking the conservative approach of rounding down to the lower classification status. In this manner, 181 XCSDR1 cluster candidates were classified as either a Gold, Silver or Bronze cluster. Of the total sample containing 610 XCS candidates, 44% were classified as not being clusters (after taking into account potential *High redshift candidates* that were beyond the depths of the SDSS survey).

The XCS-SDSS ClusterZoo I classifications for the XCSDR1 candidates were then compared to the number of X-ray soft counts measured by XCS. This comparison is illustrated in Figure 2.6. Figure 2.6 demonstrates that in general, an XCSDR1 cluster candidate, detected with at least 300 soft counts, is likely to be a genuine cluster detection ($\leq$15% contamination). Below this threshold, the contamination rate of non-cluster sources in the XCS candidate list, greatly increased with decreasing counts. Therefore, using 300 soft counts as a cut-off, the XCS collaboration was able to ensure a clean candidate list for

optical follow-up (and to not waste telescope time). Coincidentally, clusters detected with at least 300 counts obtained reduced temperature errors in X-ray spectral fits compared to those clusters detected with fewer counts (see Figure 2.6). This enabled XCS to place a minimum count threshold above which to measure X-ray temperatures, reducing the pre-2007 count threshold of 500 counts (used in Sahlén et al. (2009)) to 300 counts.

2.10 Discussion

The XCS has produced an X-ray selected cluster catalog containing more than 4000 cluster candidates covering 230 $\deg^2$ on the sky. Importantly, this catalog is homogeneous with a well defined selection function. This selection function is vital, as shown by Pacaud et al. (2007) and Sahlén et al. (2009), if XCS, or any other X-ray cluster survey, is to measure reliable cosmological parameters via cluster number counts, or investigate cluster scaling relations.

Furthermore, additional XCS pipelines have been utilised to efficiently produce objective luminosity and temperature estimates for each confirmed cluster with a measured redshift. Using these pipelines, a sample of 513 XCS clusters with measured temperatures has been produced.

These clusters have enabled XCS to measure the $L_X - T_X$ relation. This preliminary $L_X - T_X$ relation is shown in Figure 2.7 (it is preliminary because it has yet to be corrected for the XCS selection function). It has been produced using a sample that is 5 times larger than the next biggest sample, (Maughan, 2007), which was a heterogeneous compilation of clusters, without a defined selection function, unlike XCS. The XCS cluster T_X sample covers a wide range in redshifts. This places XCS in a unique position to measure possible evolution of the $L_X - T_X$ relation. These field-leading results will remain at the forefront of cluster astronomy for the next 10 years.

It is interesting to note that the increased sensitivity of XMM, over previous X-ray satellites, has enabled XCS to catalog a large sample of galaxy groups. Indeed, Figure 2.8 shows that $\sim$40% of the clusters detected by XCS are in fact groups with temperatures less than 2keV. This finding is similar to that obtained by the XMMLSS survey (Pacaud et al., 2007), who also detect X-ray clusters with XMM, albeit over an area of 5 $\deg^2$. The detection of galaxy groups is interesting, as this will enable XCS to investigate possible departures from self-similar scaling relations (§1.5.2).

Furthermore, the sensitivity of XMM has enabled the XCS detection of high redshift (z>1) clusters. This has resulted in the highest spectroscopically confirmed, X-ray selected

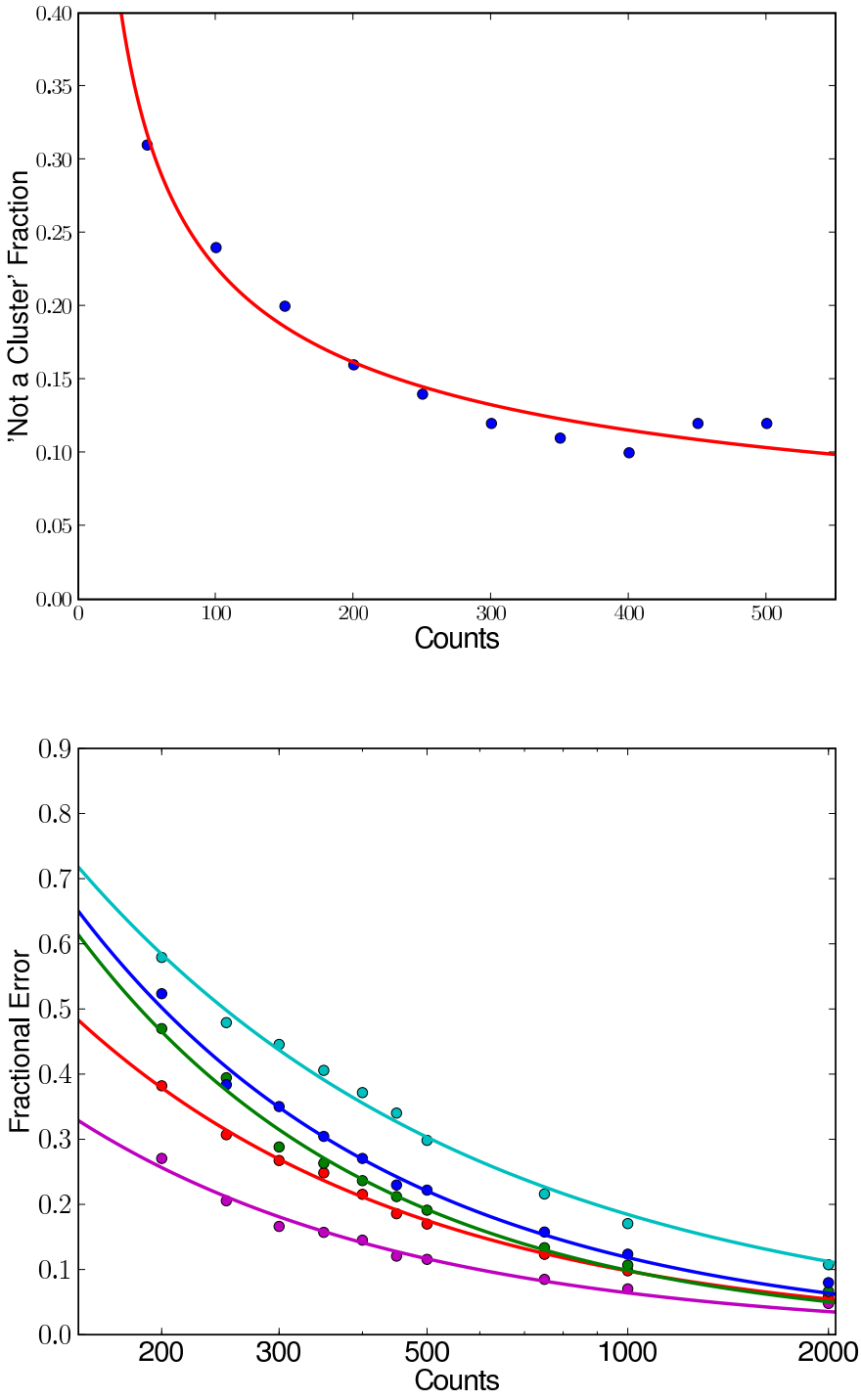

Figure 2.6 The results of XCS-SDSS ClusterZoo I (top) and the fractional error on measured temperature (bottom) for XCS candidates with respect to detected soft counts. Thus, providing justification of a minimum soft count threshold of 300 counts above which XCS temperatures are typically to be measured. [Figure credit: Ed Lloyd-Davies]

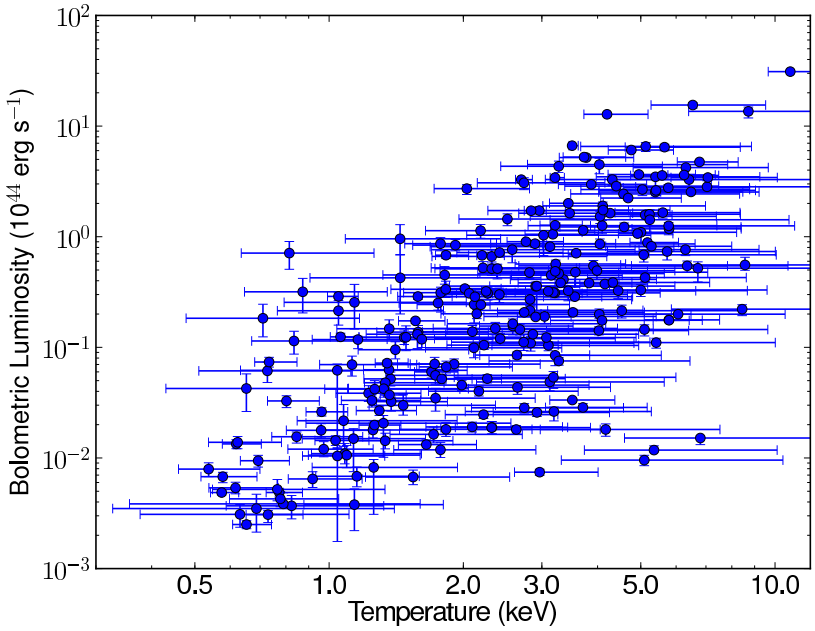

Figure 2.7 The preliminary $L_X - T_X$ relation as measured by XCS. X-ray luminosity and temperature are measured within a radius assumed to be R_{500}. [Figure credit: Ed Lloyd-Davies.]

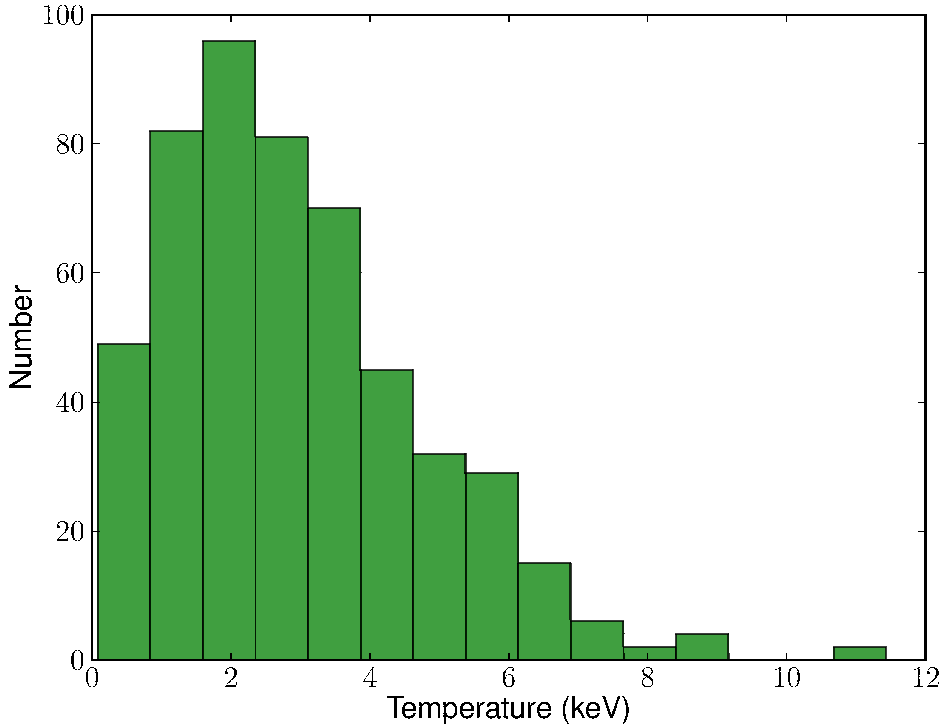

Figure 2.8 The distribution of XCS measured X-ray temperatures for the XCS cluster sample. [Figure credit: Ed Lloyd-Davies.]

cluster to date, XMMXCS J2215-1738 at z=1.45. In addition, these high redshift clusters have been investigated for galaxy evolution studies to probe the potential evolution of BCGs (Collins et al., 2009). Relatively small numbers of high redshift clusters are known, so, it is important to find more examples to support galaxy evolution studies (§1.6.2).

Monte-Carlo simulations of a forecasted XCS cluster catalogue (*i.e.* covering a completed survey area of 500 deg^2), have predicted that XCS will measure cosmological parameters Ω_m and σ_8 to within $\pm$0.03 and $\pm$0.05 respectively (Sahlén et al., 2009). These constraints are tighter than the current best estimates, produced by Vikhlinin et al. (2009b) and Mantz et al. (2009) using X-ray selected cluster number counts. However, XCS cannot compete with the cosmological parameter estimates expected from large upcoming optical cluster surveys, such as the DES which will cover $\sim$12,000 deg^2. DES will provide larger cluster samples to higher redshifts compared to XCS, thus producing more accurate constraints. However, XCS can provide much needed optical to X-ray scaling relations which DES can use to calibrate their data (§7.9).

However, in order for XCS to realise any of its goals, many more cluster candidates need to be confirmed and supported with measured redshifts. A number of redshifts have been acquired from the literature and public optical imaging (in particular from SDSS), however due to the vast number of candidates, their large redshift range, and their distribution over the sky, additional optical follow-up is required. The timescales required to obtain spectroscopic follow-up of the entire XCS cluster candidate sample are impractical given the fact that XCS has no guaranteed telescope access. So, an imaging survey, designed to measure photometric redshift estimates was deemed to be the most efficient and reasonable route with which to confirm clusters and measure cluster redshifts. The redshift distribution of the combined XCS redshift follow-up effort is presented in Figure 2.9

In the next three chapters we describe the NOAO-XCS Survey (NXS), the photometric optical follow-up campaign to XCS. We go on to describe in Chapter 6, how additional (to the LRG sample, §2.8.3) redshifts have been extracted from the SDSS. These new redshifts have been combined with X-ray data to derive optical to X-ray scaling relations presented in Chapter 7.

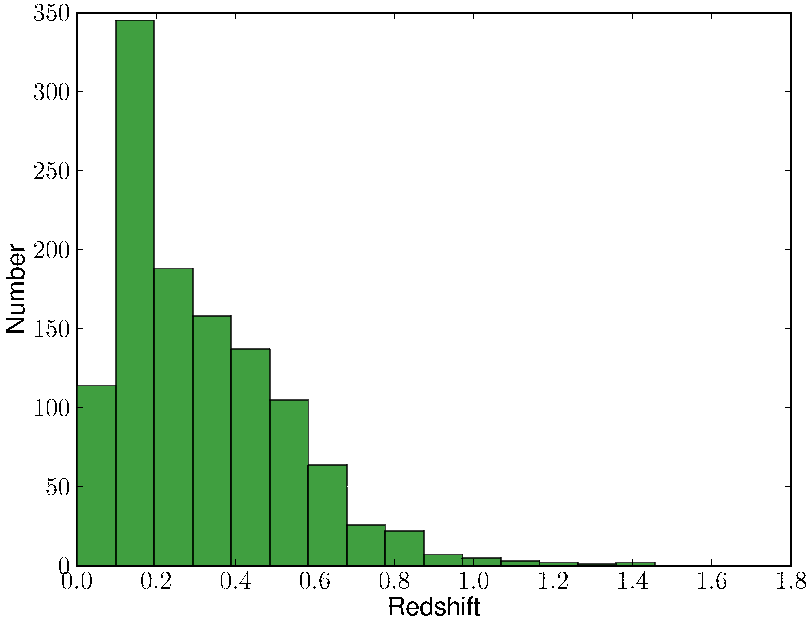

Figure 2.9 The redshift distribution of XCS clusters. [Figure credit: Ed Lloyd-Davies.]

Chapter 3

The NXS: Observations & Data Reduction Procedures

3.1 Introduction

In order for the XCS to fulfill its science goals (§2.7), each cluster candidate must be confirmed and assigned an accurate redshift (§2.8). This is particularly true of the cluster candidates detected with enough counts to measure an X-ray temperature as T_X and z are degenerate in spectral fits (§1.5).

When an optical follow-up survey for XCS was being devised in 2005, the XCS candidate list (XCSDR1) contained a total of 1766 cluster candidates. Only 142 of the XCSDR1 candidates had corresponding matches in the literature with redshifts to $0.1 \leq z \leq 1.0$. To optically confirm and determine a redshift for the remaining cluster candidates promised to be a huge undertaking, particularly owing to the clusters spanning such a large redshift range and being distributed across the sky. Fortunately, a large area of the XCS overlaps with pre-existing optical surveys such as SDSS (§2.8.3). SDSS covers 11,663 deg^2 of the sky to a depth of r=22.2. By using publicly available optical data from the SDSS (Abazajian et al., 2009), one can gain reliable cluster redshift estimates up to $z \sim 0.5$ by using colour magnitude relations (see §6.4.1), as well as using LRGs (§1.6) located near XCS candidate centroids (§2.8.3). However, as there is not complete overlap between XCS and SDSS, and because XCS can detect clusters out to redshifts well beyond $z \sim 0.5$ (Stanford et al., 2006), it was still important to secure additional optical follow-up for XCSDR1.

To spectroscopically confirm every XCSDR1 candidate was thought to be unfeasible given the timeline and science goals of XCS. Therefore the approach chosen in 2005 was to

conduct a targetted, deep (r=24), photometric survey for a sub-sample of XCSDR1 candidates. These photometric redshifts would be obtained using a modified version of the Gladders and Yee red sequence technique (Gladders and Yee (2000b), hereafter GY00). The candidate subsample would contain a complete list of XCSDR1 XCS500 clusters, *i.e.* those for which a T_X, and hence mass, could be measured. Any high redshift candidates ($z_{photo}\geq$0.7) highlighted by the photometry would be targetted for spectroscopic confirmation with Gemini and Keck, thus providing cluster samples for galaxy evolution studies to high redshift (z>1, §2.8.2). With these goals in mind, we proposed the NOAO-XCS Survey (NXS, PI Chris Miller) in April 2005. This chapter describes the NXS survey; its strategy, observations, and data reduction. The calibration and production of object catalogs from the NXS are described in Chapter 4.5.

3.2 NXS Design

The proposal was successful; thirty-eight nights of wide-field MOSAIC CCD imaging were awarded at the NOAO 4m telescopes at Kitt Peak National Observatory (KPNO, Arizona), and Cerro Tololo Inter-American Observatorio (CTIO, Chile) divided over the period November 2005 to April 2008 in 6 observing campaigns. In addition to this time, two extra nights were made available to the XCS collaboration in March 2008 (which we refer to in the following as Run6). XCS has cluster candidates all over the sky (§2.5), thus observing campaigns were alternated between the northern and southern winters to maximise the number of clusters observed. Slightly more time (by 3 nights) was allocated to the southern hemisphere due to larger optical archival coverage in the north. KPNO is situated at a latitude of +31.9 and CTIO at latitiude of -30.0. Therefore targets would typically be chosen between declinations of $+10 \leq \delta \leq +80$ and $-80 \leq \delta \leq +10$ respectively.

The XCSDR1 StatSam survey area covers regions down to a Galactic lattitude of b $\pm$15 deg (§2.4), however due to complications in reducing and performing photometry on, crowded fields, we decided to limit NXS imaging to b $\pm$20 deg. Some Statsam ObsIDs were further deselected for optical follow-up because, upon inspection of public optical imaging data (*i.e.* from the SDSS, the DSS[1] and the INT-WFS[2]), they were found to lie in regions of dense source crowding and/or contain very bright stars. Bright stars are a problem as they saturate the CCD and cause inaccurate magnitude and colour

[1]The Digitized Sky Survey (DSS): digital version of scanned photographic plate images obtained by the Palomar and UK Shmidt telescopes.

[2]The Isaac Newton Telescope Wide Field Survey (McMahon et al. (2001))

measurements for neighbouring objects.

Both the KPNO and CTIO 4m telescopes are equipped with identical wide-field mosaic CCD cameras. The KPNO MOSAIC I and CTIO MOSAIC II cameras consist of an 4x2 array of 2048x4096 pixel CCDs. These CCDs are separated by gaps of 35 pixels between columns and 50 pixels between rows. MOSAIC I is read out by 8 amplifiers (one per chip), whereas MOSAIC II is read out by 16 amplifiers (two per chip). These amplifiers are controlled by 4 ARCON CCD controllers. The similarity of the two MOSAIC instruments allows NXS to produce homogenous datasets across the sky. Each pixel is $0.26''$x$0.26''$ wide corresponding to a total imaging area of $36'$x$36'$ or $0.38\,\mathrm{deg}^2$. Hence, each NOAO field can encompass one XCS ObsID. Since each ObsID generally contains multiple extended sources (see Figure 3.1), we chose to centre the MOSAIC on the center of the XCS ObsID field of view rather than on a specific XCS candidate. This ensures an efficient follow-up and generated extra (to XCS500) z>0.7 high redshift candidates.

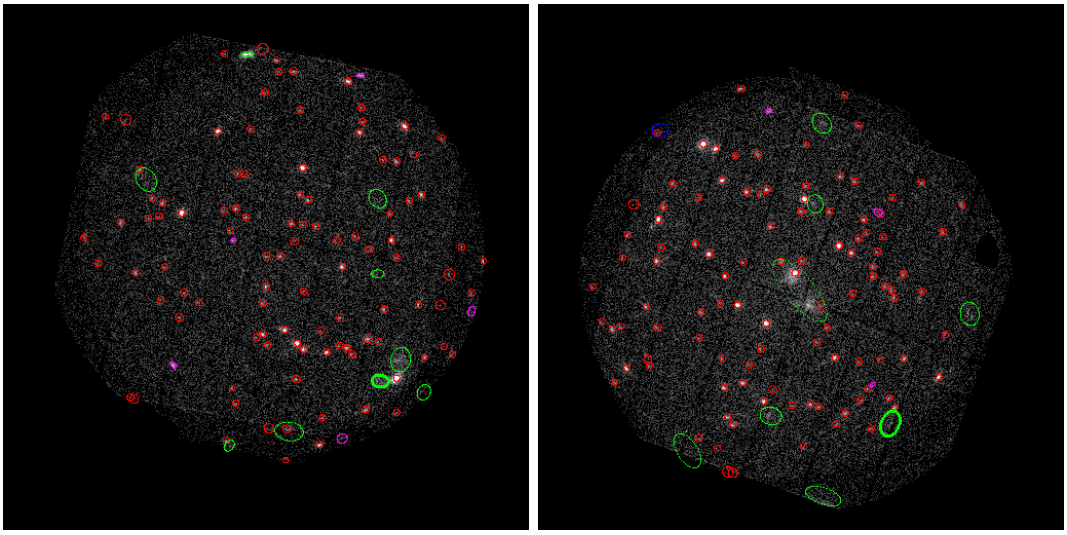

Figure 3.1 The XCS ObsIDs XCS0041170101 and XCS0100440101. Extended X-ray sources classified as potential cluster candidates, are highlighted by green ellipses; whereas X-ray sources classified as point sources are highlighted by red circles.

To effectively detect a cluster red sequence relation (§1.6.1), filter sets are typically chosen to sample either side of the rest frame 4000Å break of red sequence galaxies (GY00). At the time the NXS proposal was submitted, it was predicted that the majority of clusters detected by XCS would have redshifts between $z = 0.4$ and $z = 1.2$. Therefore, the SDSS r-band (centered at ∼6000Å) and z-band (centered at ∼9500Å) filters were chosen (see Figure 3.2). At these redshifts, the r-band filter samples the continuum of an elliptical galaxy spectrum blue-ward of the 4000Å break. At redshift $z = 0.5$ the break moves into

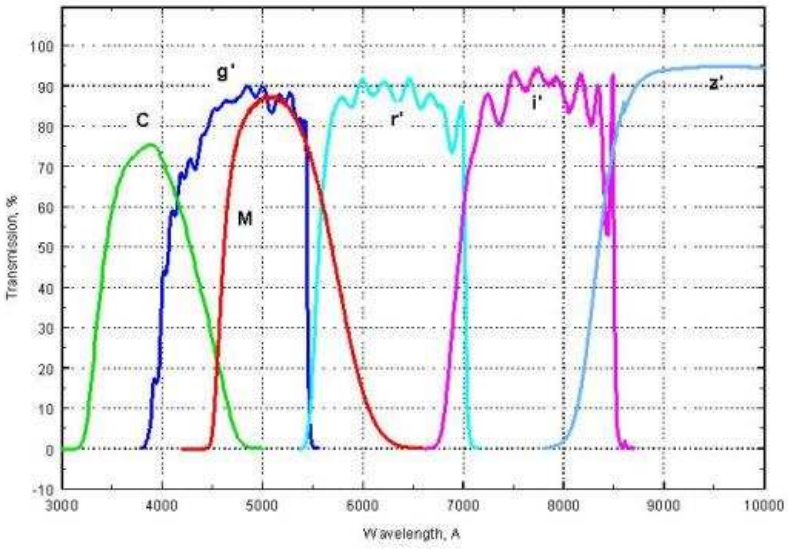

Figure 3.2 The Broad-band SDSS and Washington Filters as used by the NOAO MOSAIC cameras. [Figure credit: http://www.noao.edu.html]

the z-band filter, thus providing the biggest colour differences for galaxies around this redshift and therefore the widest separation between colour magnitude relations. Beyond redshift $z \sim 0.7$, the migration of the 4000Å break with increasing redshift results in diminishing colour differences observed between the filter sets. By a redshift of $z \approx 1.2$ no observable colour difference is seen and the colour magnitude relations are degenerate. Consequently, for a given cluster, the most accurate redshift estimates would be obtained around a redshift of $z \approx 0.5$ with redshift estimates becoming increasingly uncertain above a redshift of $z \approx 0.7$.

GY00 argue that most of the cluster light comes from galaxies greater than $0.5L_*$. This equates to an apparent magnitude of r=24.1 at a redshift of $z \approx 1$. Therefore survey depths of r=24.7 and z=22.2 were necessary to detect a redshift $z\sim1$, $0.5L_*$ galaxy at 10σ. This depth thus enables the detection of lower luminous cluster galaxies at lower redshifts.

Longer exposure times are required in the z-band to compensate for the reduced sensitivity of CCDs (see Figure 3.3) and increased sky noise. Therefore, assuming good observing conditions, combined integration times of 1200s and 1500s in the r and z bands respectively would be carried out in a dithered sequence of exposures (typically 2 or 3). This should enable the detection of redshift $z \sim 1$ clusters whilst controlling the background sky levels. Multiple exposures also allows for the removal of cosmic rays, satellite trails and chip gaps.

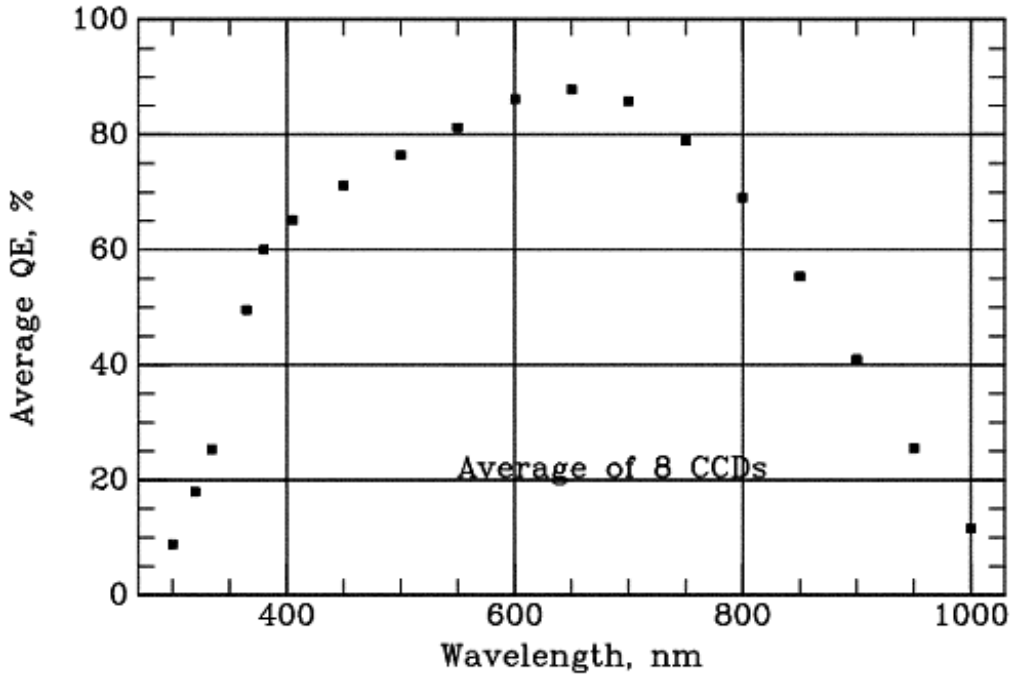

Figure 3.3 The Average quantum efficiency for the 8 CCDs in MOSAIC I. [Figure credit: http://www.noao.edu.html]

As seen in Figure 3.3, an alternative would have been to observe in the SDSS i-band filter, as opposed to the z-band, due to the increased sensitivity of the MOSAIC CCDs in this wavelength range. However, as the spectrum of an elliptical galaxy varies much less in the z-band than the i-band with redshift, the subsequent k-corrections[3] needed to accurately compare elliptical galaxies at different redshifts are much smaller in the z-band than the i-band. Therefore it was deemed preferable to observe in the z-band as this band would introduce less uncertainty in the measured rest frame magnitudes.

With increasing cluster redshift, the number of cluster galaxies detected in the r-band decreases due to the r-band sampling more of the lower level continuum below the 4000Å break (this is compounded by the $(1+z)^4$ redshift dimming). Thus high redshift galaxies may be detected in the z-band, but fail to be detected in the r-band. Therefore the limiting factor in detecting high redshift clusters is ultimately determined by the r-band exposure time.

Using integration times of 1200s (r-band) and 1500s (z-band) it was expected that the observation of an NXS-field would take ≈1hr to complete, allowing for typical observational overhead (*e.g.* slewing into position, standard star observations, *etc.*). Therefore, assuming a typical winter night lasts ∼9hrs between evening and morning twilight, we expected to

[3]A correction made to compensate for the shifting of a galaxy's rest frame spectrum into different observing bands with redshift

image ∼330 XCS fields (containing ∼500 cluster candidates) over the course of the 38 nights awarded to NXS.

3.3 NXS Execution

For the NXS survey, we observe XCS ObsIDs mostly from the XCSDR1 StatSam, and occasionally from XCSDR2, rather than individual XCS cluster candidates. Because many of the 1847 (548) ObsIDs in XCSDR1 (DR2) overlap on the sky, the full StatSam list was converted into a *Master ObsID list* for the purposes of NXS planning (§3.3.1). The ranking of the ObsIDs within this list is explained in §3.3.2. The primary ranking criterion was the existence of an XCS500 candidate within the given ObsID, but secondary criteria, such as location on the sky, were also used. Note that, in the following, we use the term *NXS-field* to describe an XCS ObsID in the Master ObsID list and *NXS-target* to describe an XCS cluster candidate within an NXS-Field.

3.3.1 NXS Master ObsID List

As XCS is a serendipitous survey using all publicly available observations in the XMM archive, many ObsIDs are repeat observations of the same patch of sky or contain overlapping regions. Therefore a cluster candidate may fall in more than one XCS ObsID. To avoid re-observations by NXS of the same location, *i.e.* waste telescope time, overlapping XCS ObsIDs were identified and assigned individual *Master ObsIDs*. NXS fields were then selected from the Master ObsID list, not from the StatSam ObsID list.

To produce the Master ObsID list, XCS ObsIDs were ordered by RA and any fields with centers separated by less than 0.15 deg (a quarter the width of an NXS image) were identified as a duplicate ObsID. The duplicate ObsID at the lowest RA in a set of duplicate ObsIDs was then assigned as the Master ObsID for each set of duplicate ObsIDs. This introduced an element of ambiguity for a small number of Master ObsIDs where, for example, a set of 3 duplicate ObsIDs may exist in which the center of the 3rd duplicate ObsID is more than 0.15 deg from the 1st duplicate ObsID but less than 0.15 deg from the 2nd. In this case the 2nd XCS ObsID would be identified as a duplicate of the 1st, but the 3rd XCS ObsID would be identified as a duplicate of the 2nd. Thus, the 2nd duplicate ObsID would also become a Master obsID, thus introducing potential overlap in the NXS observations. Despite this potential overlap, these fields were kept in the NXS Master ObsID list for completeness. With the addition of XCSDR2 (§2.5) the number of target XCS ObsIDs increased. These additional XCS ObsIDs where tested for duplicate ObsIDs

with existing Master ObsIDs from XCSDR1 and the remainder subjected to the process above.

3.3.2 NXS target selection

As the survey progressed, target selection evolved with each subsequent run due to factors such as: the diminishing number of targets; RA overlap between campaigns; and RA overlap with the Galactic plane. Target selection priorities are listed below. Lower priority was generally placed on fields with existing optical coverage from SDSS as redshift estimates could be provided using archival data (§6, §2.8.3). In the following; XCS500, XCS300 and XCS100 refer to cluster candidates detected with more than 500, 300 and 100 soft counts respectively; XCShiZloCT and XCSloCT refer to cluster candidates detected with less than 100 but are suspected to be at high redshift (*i.e.* $z \geq 0.7$) and low redshift (*i.e.* $z < 0.7$) respectively; XCS z_X refers to cluster candidates with a redshift estimated from X-ray spectral fits (Appendix A.3).

- Priority 1: XCSDR1 XCS500 (Runs 1-5); XCSDR1 XCS300 (Runs 6-7).
- Priority 2: XCSDR1 XCS100.
- Priority 3: XCSDR1 XCShiZloCT.
- Priority 4: XCSDR2 XCS500 (Runs 1-5); XCSDR2 XCS300 (Runs 6-7).
- Priority 5: XCSDR1 XCSloCT.
- Priority 6: XCSDR1 XCS calibration redshifts.
- Priority 7: XMM targetted cluster fields.
- Priority 8: XCS $z_X > 0.8$.

It is important to also note that the XCS XAPA (§2.3) was tuned for completeness rather than purity. As a result, the NXS target list naturally contained a number of spurious candidates. This became evident after the first observing campaign at KPNO in November 2005. It was subsequently decided that careful inspection of the targets was required to remove the most obvious offenders, so as to not waste telescope time. Therefore, each candidate would be eyeballed using available optical data (*i.e.* DSS, SDSS, INT) to rule out the possibility of the extended X-ray source being due to a large star or nearby galaxy.

XCSDR1 XCS500 (Runs 1-5); XCSDR1 XCS300 (Runs 6-7) The main goal of NXS was to complete the redshift follow-up of the DR1XCS500 sample so the XCS collaboration could measure cosmological parameters (Sahlén et al., 2009). Therefore highest priority was given to XCS ObsIDs containing XCS500 clusters. As the survey progressed the XCS collaboration determined that an X-ray temperature could be measured from a cluster candidates detected with 300 soft counts[4]. Therefore the cut at 500 soft counts was subsequently changed to 300 soft counts, so as to include the DR1XCS300 sample.

XCSDR1 XCS100 Prioritisation of the remaining XCSDR1 cluster candidates was based on X-ray counts, because with increasing counts one can extract more physical quantities out of the data. As a reliable X-ray luminosity can be measured from ≥ 100 soft counts[4] the cut off for this priority group was made at 100 soft counts.

XCSDR1 XCShiZloCT Although a reliable X-ray temperature or X-ray luminosity could not be extracted from sources with less than 100 detected soft counts, some such candidates were still followed up, if they had the potential to be high redshift (z>0.5) clusters. These cluster candidates with extended X-ray emission and no obvious optical counterpart in SDSS, despite falling in the SDSS footprint. As their host ObsIDs often contained lower redshift clusters with SDSS LRG spectroscopic redshifts, these NXS-fields would also aid in the calibration of the NXS photometric cluster redshifts.

XCSDR2 XCS500; XCSDR2 XCS300 By the third NXS campaign, the XCSDR2 cluster catalog had been created. As the goal of NXS was to observe the complete sample of XCSDR1 XCS500 cluster candidates (§3.1), XCSDR2 cluster candidates were only used to fill in RA gaps in the XCSDR1 target list. Priority was placed on XCSDR2 candidates with sufficient soft counts to measure a temperature, although candidates with with lower counts were occasionally observed to fill in XCSDR1 RA gaps.

XCSDR1 calibration redshifts A small number of fields containing clusters with published redshifts, or spectroscopic redshifts assigned by associated LRGs in SDSS (see §2.8.3), were deemed useful to aid in the calibration of NXS photometric redshifts. This was particularly true if the spectroscopic redshift was greater than z=0.4, due to the lack of spectroscopically confirmed XCS clusters with literature redshifts beyond z=0.4 (see §2.8.1).

[4]Depending on other factors such as T_X, background levels, *etc.*

XMM targetted cluster fields. As clusters tend to cluster, XMM fields with a cluster target were removed from the XCS STATSAM, as clusters found within these fields were deemed not to be truly serendipitous (§2.4). To test the legitimacy of this assumption, a small number of ObsIDs centered on known clusters were targetted by NXS, especially to fill in RA gaps.

DR1XCS z_X>0.8 Towards the end of the NXS survey a method had been devised by Ed Lloyd-Davies to assign X-ray redshifts to XCS clusters (See Appendix A.3). Targets identified as having redshifts of z_X>0.8 were flagged as interesting targets for NXS follow-up in order to test the efficacy of the X-ray redshift method and to provide pre-imaging for spectroscopic follow-up.

3.3.3 NXS observing procedure

A standard observing procedure was adopted for NXS and used for all campaigns at both telescopes. During each night, science frames of NXS-fields and calibration frames were obtained. Calibration frames were generally taken during twilight. These included a minimum of ten bias frames, followed by ten dome flat frames in the r- and z-band filters. Bias frames are zero second exposures that measure and correct for instrumental noise which is added to each exposure during read out. Dome flat images are short exposure frames taken of a flat uniformly illuminated surface. These are used to measure and correct for artifacts caused by the pixel-to-pixel variations in sensitivity across the detector. The pixel-to-pixel sensitivity varies due to: quantum efficiency variations across the MOSAIC camera; vignetting; dust on the optics, *etc.* Dome flat exposure times were chosen to obtain count levels (ADU) approximately between 8000<ADU<1200 counts across all chips. This provided adequate illumination across the CCD whilst not saturating the chips, thus ensuring a linear response across the MOSAIC camera. Often, sky flat images are taken to further calibrate imaging data. They account for the colour differences between the night sky and the dome lamps and are particularly necessary if trying to measure magnitudes for low signal-to-noise galaxies. The median sky level in the sky flat effectively acts as a uniformly illuminated surface of the sky. In order to make sky flat corrections, we created a sky flat image for each run, night, or part there of (see §3.5). This sky flat image was compiled from an amalgamation of background skies taken from science frames obtained during the respective period.

Whilst combined integration times remained the same throughout the survey, the number of exposures taken in each band varied to compensate for bad weather and high levels of

moon illumination. During the first NXS observing campaign, RUN1, the typical observing sequence for an NXS-field was 2x600s r-band and 2x750s z-band exposures. Thereafter, the typical observing sequence became 2x600s r-band and 3x500s z-band exposures. This was preferred, despite extra read out overhead, to reduce background sky levels. For a given NXS-field, each exposure in the r- or z-band was typically offset by $30''$ in RA and Dec to eliminate the mosaic chip gaps in the final stacked image. Most observations were taken at less than 1.6 airmass to keep seeing below $1.5''$. Each set of exposures required for an NXS-field were generally made on the same night. However, in certain circumstances, it was necessary to split exposures across different nights in a run, and occasionally, even across runs, especially if extra calibration frames were needed. This was particularly true if certain exposures were originally taken under non-photometric conditions.

Throughout the observing campaigns at CTIO, we employed a program written by The SuperMACHO Microlensing Survey[5] team which analysed the MOSAIC images in real time estimating sky levels, seeing and photometric zeropoints. This was used to help monitor our exposure times and target selection. Use of this program required all target and dither positions to be inputted via a script.

We note that, unlike KPNO, CTIO offers the opportunity for remote observing at the NOAO compound in La Serena. NXS took advantage of this facility for approximately half of the first two CTIO observing campaigns (RUN2, §3.4.2 and RUN4, §3.4.4).

Photometric Calibration A combination of Landolt standard stars (Landolt, 1992) and Southern Standard Fields (Smith et al., 2002) measured in the SDSS photometric system were observed to calibrate the photometry of the NXS data. Standard stars were observed periodically during the photometric parts of each night. In addition, as SDSS provides photometric calibration accurate to within 3% (Abazajian et al., 2004), calibration of NXS-fields in the SDSS footprint can obtained without reference to standard stars. In this manner, SDSS-0340(§4.2.5) was specifically targetted to assisted in photometric calibration. During the second observing campaign, RUN2, repeat 600s r-band and 500s z-band observations of XCS fields XCS0109520601 and XCS0100240801 were taken each night to act as consistency checks thereafter. These two fields were chosen because their declinations lay close to the equator enabling them to be observed from both hemispheres, thus providing consistency checks between telescopes on subsequent runs. Furthermore, to calibrate non-photometric data, short calibration re-observations were taken of NXS

[5]A survey attempting to detect dark matter candidates in the Large Magellanic Cloud (LMC) and nearby galaxies via gravitational lensing (Becker et al., 2004).

fields initially taken under non-photometric NXS fields on subsequent photometric nights and/or runs.

Target Of Opportunity NOAO exercises a Target Of Opportunity program in which time is granted to science groups allowing the immediate observations of unpredictable phenomena (e.g. Gamma-Ray Bursts) during scheduled observing runs. If a Target Of Opportunity arose during an NXS observing run, all NXS observations would be suspended until the requested observations of the target were taken. Target Of Opportunities observations occurred twice during the NXS survey, as mentioned in §3.4.3 and §3.4.4.

3.4 The NXS Observing Runs

A description of each NXS observing run is given below. A summarized observing log for RUN1 is presented in 3.4.1, with the remaining summarized observing logs provided in Appendix B.1 to B.5. The column descriptions for the summary observing logs is given in Table 3.1.

3.4.1 Run1: KPNO November 2005

Observers present: Adam Stanford, Matt Hilton, Nicola Mehrtens.

The first NXS observing run (RUN1) was six nights long and took place at KPNO between the 23rd and 29th of November 2005. Targets were provided by Micheal Davidson following a ranking system based on the source counts of each cluster candidate to maintain the integrity of the XCS selection function (see §2.7).

Typically, two consecutive r- and z-band exposures were taken on each night with the exception of the 27th where cloud conditions made it favorable to observe the z-band only, with their matching r-band frames taken on the 28th. Also 3 z-band exposures were taken on 27th to compensate for poor seeing. To calibrate the data, a set of SDSS-Landolt standard stars (Smith et al., 2002) were taken on clear nights. Additionally short 30s exposures of sky centered on the coordinates (03^h40^m, $00°00^m$), and overlapping with SDSS, were taken on the 28th and 29th. This field, designated SDSS-0340 hereafter, contained numerous stars between $14 < r < 17$.

Thirty-five NXS fields were observed during RUN1, 25 of which under photometric conditions. A total of 135 XCSDR1 and 3 XCSDR2[6] cluster candidates were thus followed

[6]XCSDR2 candidates observed during RUN1 were not specifically targetted but were discovered in XCSDR1 ObsIDs after the production of XCSDR2.

Table 3.1. Column descriptions of the summarised observing logs for Run1-Run6

Column name	Description
XCS ObsID	The identifier of the XCS ObsID observed by NXS.
R.A. (J2000)	RA of the target XCS ObsID given in J2000 coordinates.
Dec. (J2000)	Dec of the target XCS ObsID given in J2000 coordinates.
r-band	The number of r-band exposures taken of the XCS ObsID.
z-band	The number of z-band exposures taken of the XCS ObsID.
XCS Release	The XCS internal data release from which the XCS ObsID was selected.
XCSDR1 (XCS500)	The number of XCSDR1 cluster candidate contained within the XCSObsID. The corresponding number of that which are XCSDR1 XCS500 cluster candidates is given in brackets.
XCSDR2 (XCS500)	As above, but for DR2. For the majority of NXS observations the number of XCSDR2 XCS500 is zero, however we include this column for all NXS observing runs for consistency.
Observing Flag	An NXS observing flag representing photometric conditions. An observing flag of 1 and 2 correspond to data taken under non-photometric and photometric conditions respectively.

up (100 XCSDR1 in photometric conditions). A summary of RUN1 is shown in Table 3.2.

3.4.2 Run2: CTIO July 2006

Observers present: Chris Miller, Nicola Mehrtens, Mark Hosmer.

The second NXS run (RUN2) was six nights long and took place at CTIO between the 25th and 30th of July 2006. During the 25th-27th observations were performed at the telescope, however the remainder of the run was performed remotely at the NOAO compound in La Serena. Targets for this run were selected by Chris Miller following the priorities mentioned in §3.3.2. We note that RUN2 was the first run whereby XCS candidates were eyeballed as part of the target selection (§3.3.2).

A total of 32 NXS-fields were observed during RUN2, 29 of which under photometric conditions. A total of 85 XCSDR1 cluster candidates where thus followed up (80 XCSDR1 under photometric conditions). A summary of RUN2 is shown in Appendix B.1.

3.4.3 Run3: KPNO January 2007

Observers present: Adam Stanford, Nicola Mehrtens.

The third NXS run (RUN3) was six nights long and took place at KPNO between the 13th and 18th of January 2007. Target selection was performed by Nicola Mehrtens following the priorities listed in §3.3.2. The target selection strategy altered slightly for this run due to it's partial RA overlap with RUN1 and the Milky Way causing a lack of XCSDR1 targets with more than 100 soft counts. Therefore targets were mainly selected with priorities 3-7.

Short calibration images of non-photometric exposures from RUN1 were taken on the 14th and photometric parts of the 16th. Standard stars were not observed due to the large SDSS overlap. In addition, 5 astrometric fields were taken on behalf of The SuperMACHO Microlensing Survey (Becker et al., 2004) to assist the SuperMACHO team in achieving 1% photometry (Stubbs and Tonry, 2006). Three SuperMACHO astronometric calibration fields were observed on the 13th. Another two SuperMACHO photometric calibration fields were observed on the 14th and during the photometric parts of the 16th.

Unfortunately RUN3 suffered from a number of instrumental problems. ARCON failure, experienced throughout the run, made it impossible to take a sequence of exposures, this was particularly problematic when taking biases and domeflats. As a result, no bias frames were taken on the 13th. Throughout the run the ARCON would often hang, requiring a reboot several times a night. Additionally, the ARCON occasionally failed to read out all

chips during read-out causing them to drop out of the final image, these then had to be retaken. No observations were taken on the 15th despite photometric conditions due to a mirror support failure rendering the telescope useless. In addition, approximately 1 hour was lost on the 17th due to a target of opportunity.

A total of 21 NXS-fields were observed during Run3, 8 of which under photometric conditions. Thus 44 XCSDR1 cluster candidates were followed up (17 XCSDR1 cluster candidates under photometric conditions). In addition, two fields observed during Run1 under non-photometric conditions where targetted for photometric calibration containing 8 XCSDR1 cluster candidates. A summary of Run3 is shown in Table B.2.

3.4.4 Run4: CTIO July 2007

Observers present: Chris Miller, Nicola Mehrtens.

The fourth run (Run4) took place at CTIO between the 16th and 22nd of June 2007. Observations were performed at CTIO between the 16th and 19th and remotely from the NOAO compound in La Serena between the 20th and 22nd (the 22nd by Chris Miller only). Target selection was performed by Nicola Mehrtens according to the priorities outlined in §3.3.2.

Only the 19th was photometric with good seeing, so standard star fields were taken to calibrate the data. Despite clear conditions, no standard stars were imaged on the 22nd or at the end of the 21st due to the poor seeing conditions. Repeat observations of non-photometric data from the 16th and 17th were taken during the better observing conditions of the 20th and 21st. The 20th-22nd suffered from increasingly high levels of Moon illumination. To combat this, the number of observations were doubled in each filter and integration times halved to 300s and 250s for the beginning of the 21st and 22nd until the Moon had set and sky counts had reached a more manageable level. In these instances the pointings were dithered every other exposure as opposed to every exposure. In addition, approximately 1 hour was lost on the 21st due to a target of opportunity.

A total of 39 NXS-fields were observed during Run4, 13 under photometric conditions. Thus 56 XCSDR1 and 39 XCSDR2 cluster candidates were followed up (28 XCSDR1 and 10 XCSDR2 in photometric conditions). A log of Run4 is shown in Table B.3.

3.4.5 Run5: KPNO September 2007

Observers present: Adam Stanford, Nicola Mehrtens, Ben Hoyle.

The fifth run (Run5) took place at KPNO between the 11th and 16th of September

2007. Target selection was performed by Nicola Mehrtens and followed the priorities outlined in §3.3.2. No technical difficulties were experienced during RUN5. However, thunderstorms, high winds and 90-100% humidity forced the dome to close for most of the 14th and all of the 15th and 16th. All observations were taken without any Moon illumination.

A total of 28 NXS-fields were observed during RUN5, 13 of which were photometric, containing 23 XCSDR1 cluster candidates (14 under photometric conditions) and 30 XCSDR2 cluster candidates (13 under photometric conditions). A summary of RUN5 is shown in B.4.

3.4.6 Run6: CTIO March 2008

Observers present: Chris Miller.

The sixth run (RUN6) took place at CTIO on the 4th and 5th of March. NXS targets were observed to fill in RA gaps during a REXCESS[7] optical follow-up campaign. NXS target selection was performed by Nicola Mehrtens. In addition to XCSDR1 XCS500 candidates, targets were selected to provide extra short calibration images or re-observations of non-photometric data from previous runs. Photometric calibration was obtained using NXS-fields overlapping with SDSS. All images were observed under photometric conditions with sub-arcsecond seeing.

A total of 6 NXS-fields were observed during this run (2 of which were re-observations of poor non-photometric fields from RUN4). Thus, 17 XCSDR1 cluster candidates were followed up. In addition, calibration images were taken for 3 XCS ObsIDs observed during RUN4, containing 10 XCSDR1 cluster candidates. A summary of NXS fields observed during RUN6 is shown in Table B.5.

3.4.7 Run7: CTIO April 2008

Observers present: Nicola Mehrtens, Leon Baruah.

The seventh run (RUN7) was performed at CTIO between the 24th and 30th of April. Target selection was performed by Nicola Mehrtens following the priorities outlined in §3.3.2. This observing run suffered from a combination of ARCON failure, heavy clouds and high levels of Moon illumination. Observations were taken when possible, however the data were subsequently deemed unfit for science. The ARCON failure caused a 5% noise level fluctuations in all frames (see Figure 3.4). Moveover, this noise was variable

[7]The Representative XMM-Newton Cluster Structure Survey (Boehringer et al., 2007).

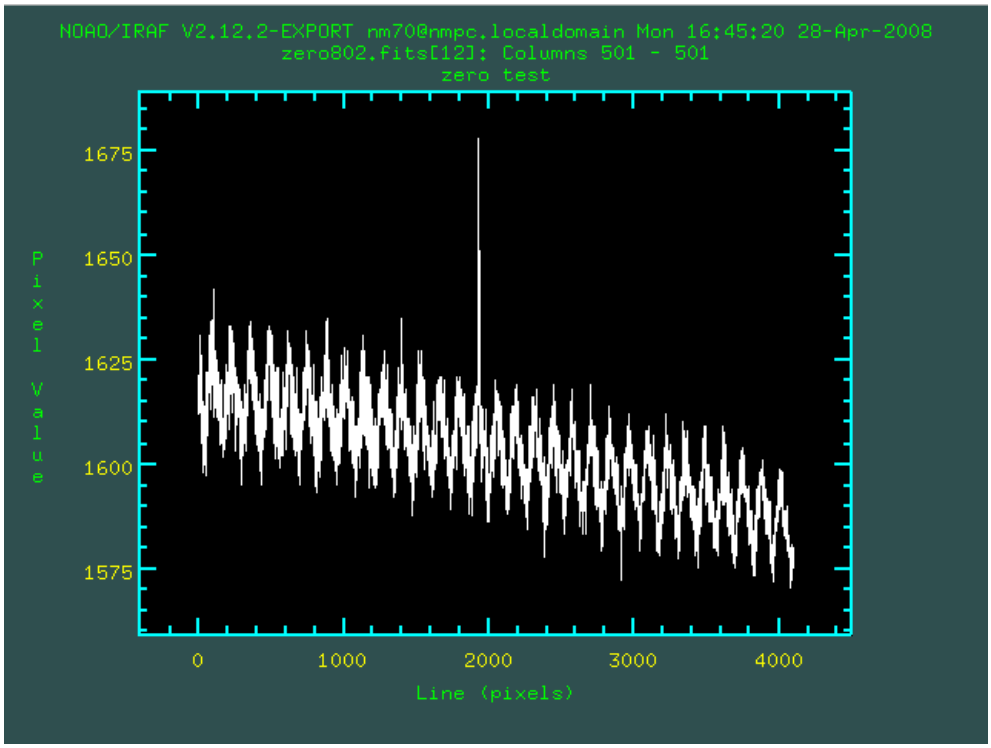

Figure 3.4 Illustration of the noise fluctuations present in an NXS bias calibration frame resulting from the de-synchronisation of the ARCON controllers during RUN7.

making it impossible to remove. For completeness, we state that the instrumental failure was due to a problem with the synchronization between the four ARCON controllers. In order to ensure a more stable performance of the ARCON, thus allowing observations to take place, the ARCON controllers were operated unsynchronised. It was this act that caused the noise fluctuations in each frame.

A total of 16 XCS fields were observed during this run, containing 54 XCS cluster candidates. However, due to these instrument problems, none of the images taken during RUN7 were reduced. Consequently, no observing logs are provided in this thesis.

Table 3.2. Summary of NXS-fields observed during Run1

XCS ObsID	R.A (J2000)	Dec.(J2000)	r-band	z-band	XCSRelease	DR1 (XCS500)	DR2 (XCS500)	comments
0101441501	04:24:17.8	+14:44:24.1	x2	x3	DR1	4(0)	0 (0)	1
0083000101	07:35:15.2	+43:45:53.3	x2	x2	DR1	8(1)	0 (0)	1
0202140301	23:22:13.3	+19:43:26.8	x2	x2	DR1	5(2)	0 (0)	2
0101040101	00:06:26.1	+20:11:40.7	x2	x2	DR1	2(0)	0 (0)	2
0109661101	01:45:32.6	-04:35:42.0	x2	x2	DR1	4(1)	0 (0)	2
0149780101	01:57:45.3	+37:47:07.4	x2	x2	DR1	4(1)	0 (0)	2
0112550201	02:43:35.4	+37:19:19.2	x2	x2	DR1	5(1)	0 (0)	2
0041170101	03:02:43.5	+00:06:29.9	x2	x2	DR1	9(1)	0 (0)	2
0029340101	06:41:43.3	+82:14:31.4	x2	x2	DR1	4(1)	0 (0)	2
0123100101	07:44:15.7	+74:32:16.9	x2	x2	DR1	5(0)	0 (0)	2
0143653901	08:36:11.8	+55:40:30.7	x2	x2	DR1	2(1)	0 (0)	2
0149010201	09:20:39.9	+37:09:36.0	x1	x1	DR1	8(2)	0 (0)	2
0001930101	00:26:12.7	+10:40:24.3	x2	x3	DR1	2(0)	0 (0)	1
0109270401	00:46:31.0	+42:17:31.9	x2	x2	DR1	2(1)	0 (0)	1
0025541601	01:24:40.8	+03:46:30.7	x2	x3	DR1	4(0)	0 (0)	1
0111490401	02:48:50.1	+31:05:57.1	x2	x2	DR1	3(0)	0 (0)	1

Table 3.2 (cont'd)

XCS ObsID	R.A (J2000)	Dec.(J2000)	r-band	z-band	XCSRelease	DR1 (XCS500)	DR2 (XCS500)	comments
0094780101	03:47:12.8	+24:23:44.8	x2	x2	DR1	3(2)	0 (0)	1
0152840101	04:33:06.1	+05:22:23.5	x2	x2	DR1	3(0)	0 (0)	1
0143430101	07:19:06.0	+65:59:13.0	x2	x3	DR1	2(0)	0 (0)	1
0112520601	08:19:34.8	+70:40:41.8	x2	x3	DR1	3(0)	3 (1)	1
0151581101	00:33:44.5	+39:30:42.9	x3	x3	DR1	2(0)	0 (0)	2
0112551501	01:48:51.2	+05:55:19.9	x3	x3	DR1	2(0)	0 (0)	2
0141400301	04:19:41.9	+14:32:18.0	x0	x3	DR1	2(0)	0 (0)	2
0010620101	05:15:45.0	+01:03:14.6	x0	x2	DR1	3(0)	0 (0)	2
0144230101	06:52:32.0	+74:24:30.3	x0	x3	DR1	1(0)	0 (0)	2
0138951401	08:07:45.0	+38:58:39.1	x0	x3	DR1	1(0)	0 (0)	2
0149170501	09:18:50.6	+21:15:38.1	x0	x4	DR1	1(0)	0 (0)	2
0093190301	23:51:16.5	+20:06:42.2	x2	x2	DR1	3(1)	0 (0)	2
0100640101	00:43:36.0	+85:19:00.8	x2	x2	DR1	4(1)	0 (0)	2
0141400301	04:19:41.9	+14:32:18.0	x2	x0	DR1	2(0)	0 (0)	2
0142610101	03:06:46.1	+00:00:01.8	x2	x2	DR1	3(2)	0 (0)	2
0010620101	05:15:45.0	+01:03:14.6	x2	x0	DR1	3(0)	0 (0)	2

Table 3.2 (cont'd)

XCS ObsID	R.A (J2000)	Dec.(J2000)	r-band	z-band	XCSRelease	DR1 (XCS500)	DR2 (XCS500)	comments
0144230101	06:52:32.0	+74:24:30.3	x2	x0	DR1	1(0)	0 (0)	2
0138951401	08:07:45.0	+38:58:39.1	x2	x0	DR1	1(0)	0 (0)	2
0092800201	08:31:46.4	+52:43:41.4	x2	x2	DR1	8(2)	0 (0)	2
0149010201	09:20:39.9	+37:09:36.0	x2	x0	DR1	8(2)	0 (0)	2
0149170501	09:18:50.6	+21:15:38.1	x2	x0	DR1	1(0)	0 (0)	2
0152150101	04:19:42.7	+02:23:21.0	x2	x2	DR1	2(0)	0 (0)	2
0094400101	05:16:17.0	+79:41:34.8	x3	x2	DR1	3(0)	0 (0)	2
0150800101	08:06:20.5	+15:29:08.8	x2	x2	DR1	4(1)	0 (0)	2
0112520101	09:34:02.1	+55:12:35.3	x2	x2	DR1	5(0)	0 (0)	2

3.5 NOAO MOSAIC I and MOSAIC II Reduction

Reduction of the NXS images was largely carried out following version 7.02 of Buell Jannuzi's reduction notes[8] for the NOAO Deep Wide Field Survey (NDWFS; Brown et al. (2003). These reduction procedures utilise the `MSCRED` package (Valdes, 1998) written for the `IRAF`[9] environment (Tody, 1993). `MSCRED` is specifically written to reduce data taken by the NOAO MOSAIC I and MOSAIC II cameras and aims to treat data reduction for the mosaic camera as a single CCD. `IRAF` Version 2.12 and `MSCRED` version 4.7 were used to reduce the data from each run. Figure 3.5 shows a MOSAIC I image map with the corresponding IRAF nomenclature for each CCD within the image.

Cross Talk and Overscan During the reduction process all images were initially corrected for cross talk and had their overscan regions trimmed. Cross talk results from an Arcon controlling each pair of mosaic CCDs leaking current from one CCD to the other, creating a false image in the latter CCD. These 'echos' are bright enough to warrant their removal, particularly in the cases of saturated stars. We have used the NOAO determined cross talk corrections specific to each MOSAIC camera. Overscan regions are the result of CCD rows and columns along the edge of each MOSAIC camera that are not exposed to light. These overscan regions (or dark regions) in each MOSAIC image may then act as a dark frame and be directly subtracted from each MOSAIC image.

Calibration Frames Nightly bias frames were created and applied to the science and dome flat images taken each night. As the MOSAIC cameras have negligible dark current (an accumulation of charge in the CCDs) its correction was deemed unnecessary. A nightly Master dome flat was created for each night by combining the 10 dome flat exposures taken per filter. Master dome flats were then applied to the science images taken each night (see Sky Flats below).

Bad Pixel Masks Bad pixel masks were then created for each science image. The NOAO determined bad pixel regions for the MOSAIC I camera were used as the basis for a bad pixel mask. However, an updated bad pixel mask supplied by the SUPERMACHO group was used to identify bad regions in the MOSAIC II camera. These bad pixel masks

[8] http://www.noao.edu/noao/noaodeep/ReductionOpt/frames.html

[9] IRAF is distributed by the National Optical Astronomy Observatories, which are operated by the Association of Universities for Research in Astronomy, Inc., under cooperative agreement with the National Science Foundation.

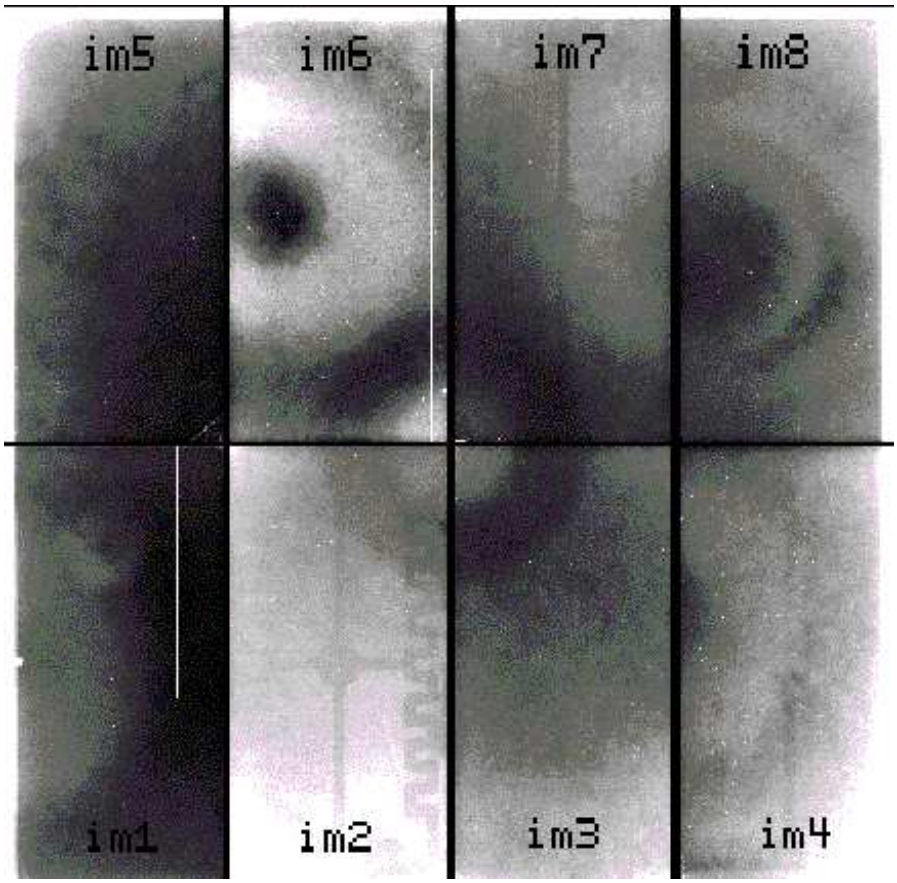

Figure 3.5 *A Flat-field (R band) map of the CCDs in the MOSAIC I camera with their 'extensions' (im1, im2, im3, etc.) as used in the IRAF nomenclature.* [Figure credit and caption: http://www.noao.edu.html]

were then updated for saturated stars and bleed trails in each object image using the NOAO pre-determined saturation levels for the MOSAIC I and II chips respectively.

Interference Fringing Both MOSAIC I and II cameras suffer from interference fringing in their i and z-band filters because the width of the redder chips becomes comparable to the wavelength of the incident radiation. This causes a wave-like interference pattern in the resulting images. Therefore the z-band images need to be corrected for this fringing effect. It can be removed with the `MSCRED` task `MSCFRINGE` when skyflattening the object images (see **Sky Flats** below).

Pupil Ghost The MOSAIC I camera at KPNO has the added problem of a prevalent pupil ghost occuring in its z-band images resulting from an internal reflection off the instrument's corrector (see Figure 3.6). Therefore the MOSAIC I z-band images also need to be corrected for this effect using the `MSCRED` tasks `MSCPUPIL` when skyflattening the object images (see **Sky Flats** below).

Sky Flats To correct for the difference between the dome lamps and the night sky, r and z-band sky flats need to be applied to science images taken in the appropriate filter. It is recommended by NDWFS that sky flats should be generated using 20-30 images taken in similar conditions. Objects (*e.g.* stars, galaxies) need to be removed from the images before they are combined to make a sky flat. Therefore, object removal was performed using the `MSCRED` task `objmasks`. NDWFS suggest setting the `objmasks` parameter `hsig` (which specifies what significance a source must have above the background before it is detected as an object) to 3. This value was adopted for the NXS r-band images, however we had to change this value for the z-band images to `hsig`=9 and `hsig`=5 for the MOSAIC I and MOSAIC II data respectively in order to remove the z-band pupil ghost and interference fringing. Using a smaller significance value resulted in certain fringe and pupil ghost regions repeatedly being detected as objects and being masked out, thus creating holes in the subsequent images. This problem was particularly prevalent in images taken in bad weather. A higher significance value was necessary for MOSAIC I data in order to remove the added pupil ghost image. Whereas for MOSAIC II, detecting objects at greater than 5σ caused no noticeable improvement in the residual fringing.

Ideally, one would create a sky flat for each night. However, a lack of frames with adequate sky coverage sometimes forced us to combine images from consecutive nights. Short calibration frames were not combined to make a sky flat. Care was taken to exclude

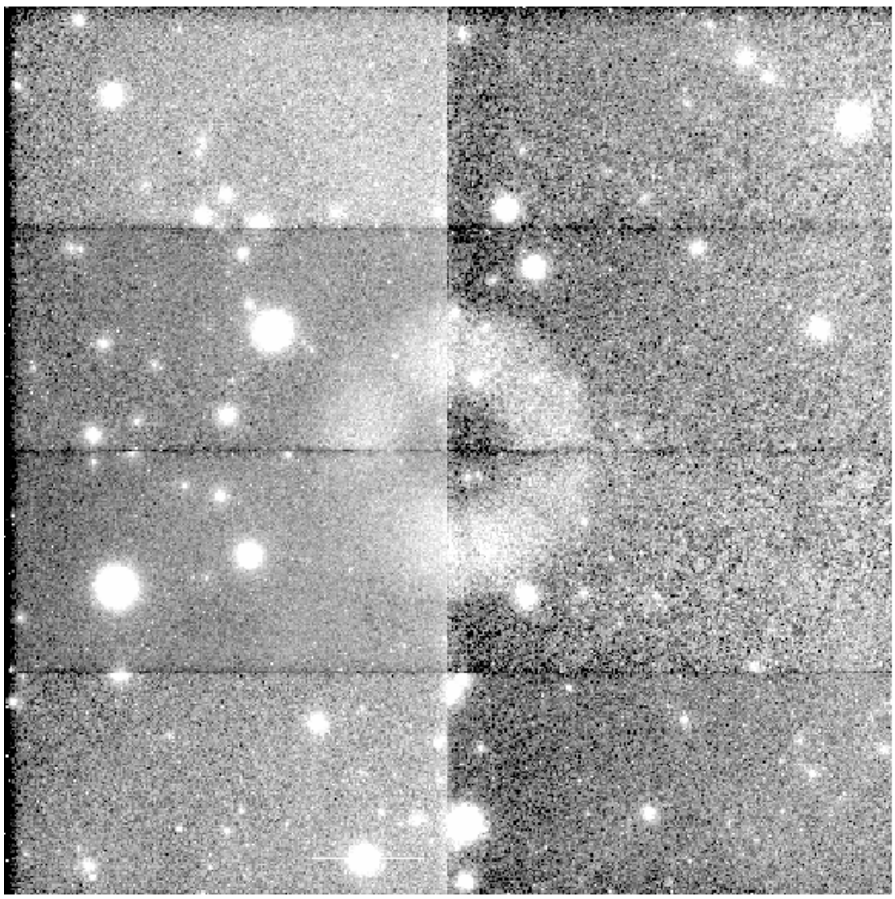

Figure 3.6 A bias and dome flat corrected z-band image of the NXS-field NXS0041170101, demonstrating the prevalent pupil ghost in the centre of the NXS-field as well as the prominent fringing apparent across the entire image.

images used to create a sky flat image that were not representative of the average sky, *e.g.* those containing nearby bright objects, galaxies or nebulae.

World Coordinate System (WCS) A more accurate world coordinate system (to that within the fits header) was then applied to each image (see §3.5.1).

Cosmic Rays Cosmic rays are energetic particles. These are detected by the MOSAIC camera and result in 'hot' pixels. A 10 minute exposure results in hundreds of cosmic rays. Cosmic rays were added to the bad pixel masks using the task `CRAVERAGE` in the `IRAF CRUTIL` package and interpolated over using the task `FIXPIX` run on each image chip. These interpolated pixels are not used in the final stacked image. Upon visual inspection `CRAVERAGE` removed almost all cosmic rays and as the XCS redshift algorithm (§5.5) is largely insensitive to cosmic rays (as their small extent will exclude them from NXS galaxy catalogues §4.3) it wasn't necessary to remove the remaining offenders by hand for the

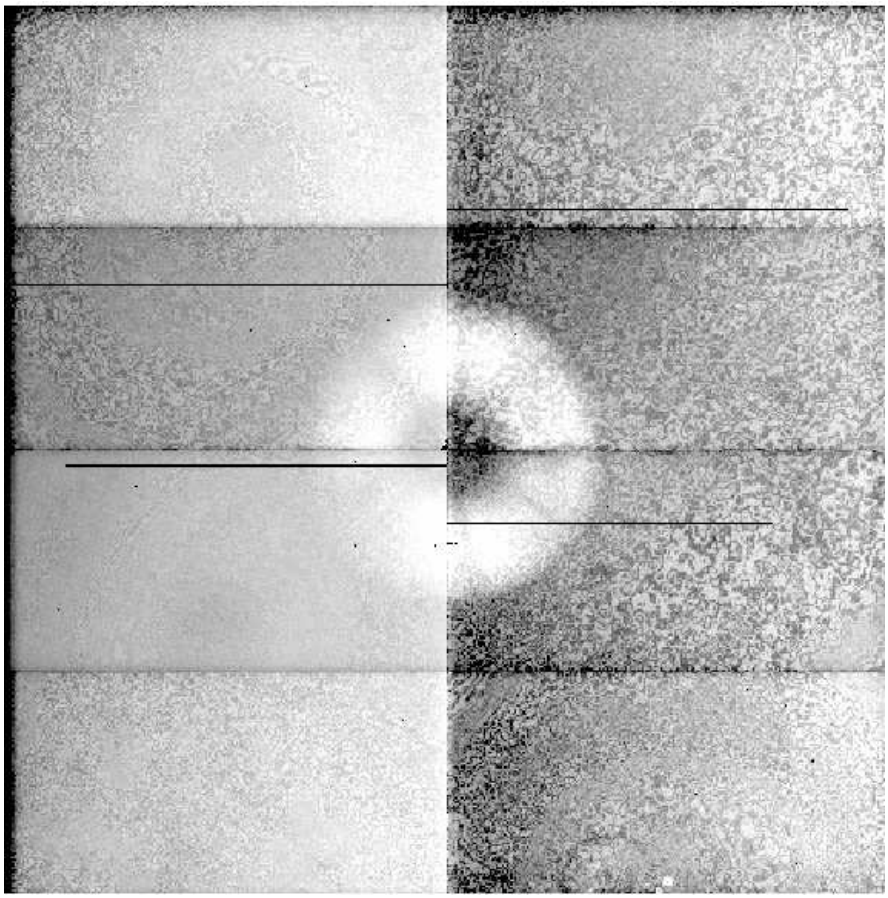

Figure 3.7 Example of a z-band sky flat image used to calibrate data taken during RUN1. The image shows the detection of the pupil ghost and fringing artifacts. As a consequence, application of the sky flat on an NXS-field should remove these artifacts within them.

purposes of the survey.

Tangent-plane Projection Tangent-plane projected images were then created with the task `MSCIMAGE` which translates the positions of stars in the focal plane of the telescope to their celestial coordinates. Each image in a pointing was projected to chip 1 (Figure 3.5) of the first image taken in a sequence.

Sky Gradient The large scale sky gradient (caused by light pollution) was removed, and relative scalings matched between images in each pointing with the tasks `MSCSKYSUB` and `MSCIMATCH` respectively. For most pointings the relative scaling was close to 1, however this was not the case for a few fields taken in bad weather where varying cloud cover significantly altered sky levels. In these explicable cases the relative scaling was accepted.

Satellite trails Images containing satellite trails had their positions identified by eye and removed using the script `sat-b-gon.pl`[10] written by Matthew Hunt. `Sat-b-gon.pl` allows the user to vary the width of the satellite trail mask to adequately remove the trail from each image. If a satellite trail had been added to a bad pixel mask, `FIXPIX` was re-run and the resultant image inspected for any obvious defects.

Stacked images Final stacked images and exposure maps were then created using the `MSCSTACK` task and selecting the option `goodvalues`, rejecting cosmic rays and an `average` of the frames.

3.5.1 World Coordinate System (WCS)

A WCS is fitted to each image using the automated task `MSCCMATCH`. The task matches USNO-A2.0 stars (Monet and et al., 1998) to those in the image to derive an improved WCS over that existing in the header. USNO-A2.0 is a catalog of standard stars with calibrated positions extracted from photographic plates taken by the Palomar Observatory Sky Survey (POSS-I). Only stars with magnitudes between $9 \leq R \leq 17.5$ were used for astrometric correction, so to exclude both saturated stars and stars so faint that they'd be matched with noise in the image. The `MSCCMATCH` parameters were set similar to those suggested by NDWFS using 150 positions within a search radius of $90''$ to obtain a typical rms fit good to within $0.3''$. In a few cases it was necessary to match up the reference star positions to their corresponding stars in the image manually using the task `MSCZERO`

[10] http://www.ifa.hawaii.edu/ rgal/science/lfcred/sat-b-gon

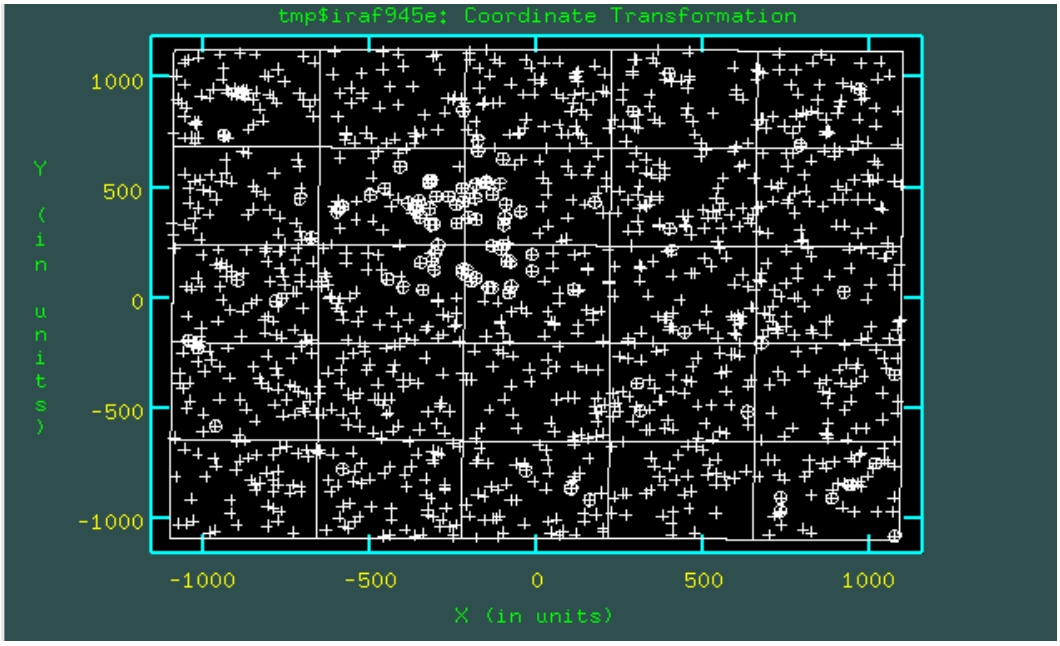

Figure 3.8 Illustration of the position of stars used to astrometrically calibrate an NXS-field. Stars marked by crosses demonstrate an acceptable fit (generally less than 0.03″), stars marked by circles do not. The figure highlights a locus of stars with poor astrometric fits corresponding to chip 6 of the MOSAIC field.

where the task had failed to recognise a pattern. In these cases a pattern was easy to spot. Occasionally during read out at the telescope the WCS information gets lost from the header. In these cases it is necessary to manually input the coordinates and reset the WCS with `SETWCS` and re-run the `MSCCMATCH` task. Also, there were a couple of instances where the NOAO server failed to return coordinates of USNO-A2 stars, these then had to be downloaded from the USNO-A2 catalog on VIZIER[11] for input into `MSCCMATCH`.

Unfortunately, for approximately 40% of the MOSAIC II images, the `MSCCMATCH` task could not fit a WCS for the entire CCD. Figures 3.9 and 3.8 show an example of a poorly fit WCS. A subset of stars, mostly corresponding to CCD chip 6, had an inaccurate WCS fit, betrayed by their outlying residuals from the main trend (seen in Figure 3.9). In these cases it was necessary to split the CCD MOSAIC into it's constituent chips (using the `MSCRED` task `MSCSPLIT`) and fit the WCS for each CCD chip individually. The task `MSCCMATCH` was repeated, tuning the required paramters until a fit was achieved. These individually WCS fitted CCD chips were once again joined (using the `MSCRED` task `MSCJOIN`) to form a MOSAIC CCD and the task `MSCCMATCH` was re-run on the newly WCS fitted MOSAIC image.

Figures 3.11 and 3.10 show the consequences of an ill-fitted WCS in final stacked

[11] http://vizier.u-strasbg.fr/cgi-bin/VizieR

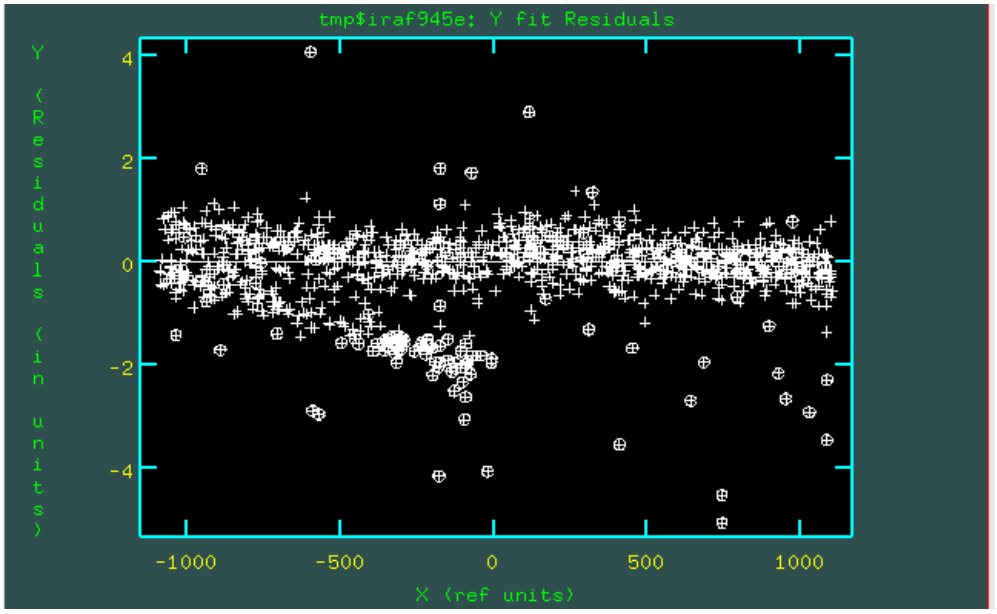

Figure 3.9 Illustration of the residuals in the fit of stars used to astrometrically calibrate an NXS-field. The image shows a clear deviation from the main trend for a subset of stars in the image where the adopted WCS has failed.

colour-composite images. Offsets in the r-band and z-band positions are clearly shown by the 'halos' around each object in Figure 3.10. These cases will produce erroneous colour measurements if colours are measured using the same aperture size and positions in each band. Figure 3.11 shows the presence of an inaccurate fit between chips leading to the distorted image at the top right hand corner of the image giving rise to a complete offset between the galaxies detected in both bands resulting in duplicate galaxy detections.

3.5.2 Reduction processes specific to each observing campaign.

Run1: KPNO November 2005

Technical Difficulties None Experienced.

Sky Flat Two skyflats were created in each band. The first using 39 r and 44 z-band images from the first three nights and the second using 30 r and 38 z-band images from the last three nights. These sky flats were then applied to the corresponding night's science images.

Run2: CTIO reduction

Technical Difficulties All images taken on the 27th had a number of doughnut shaped artifacts over their images caused by dust. Using the dome flats images taken the 27th

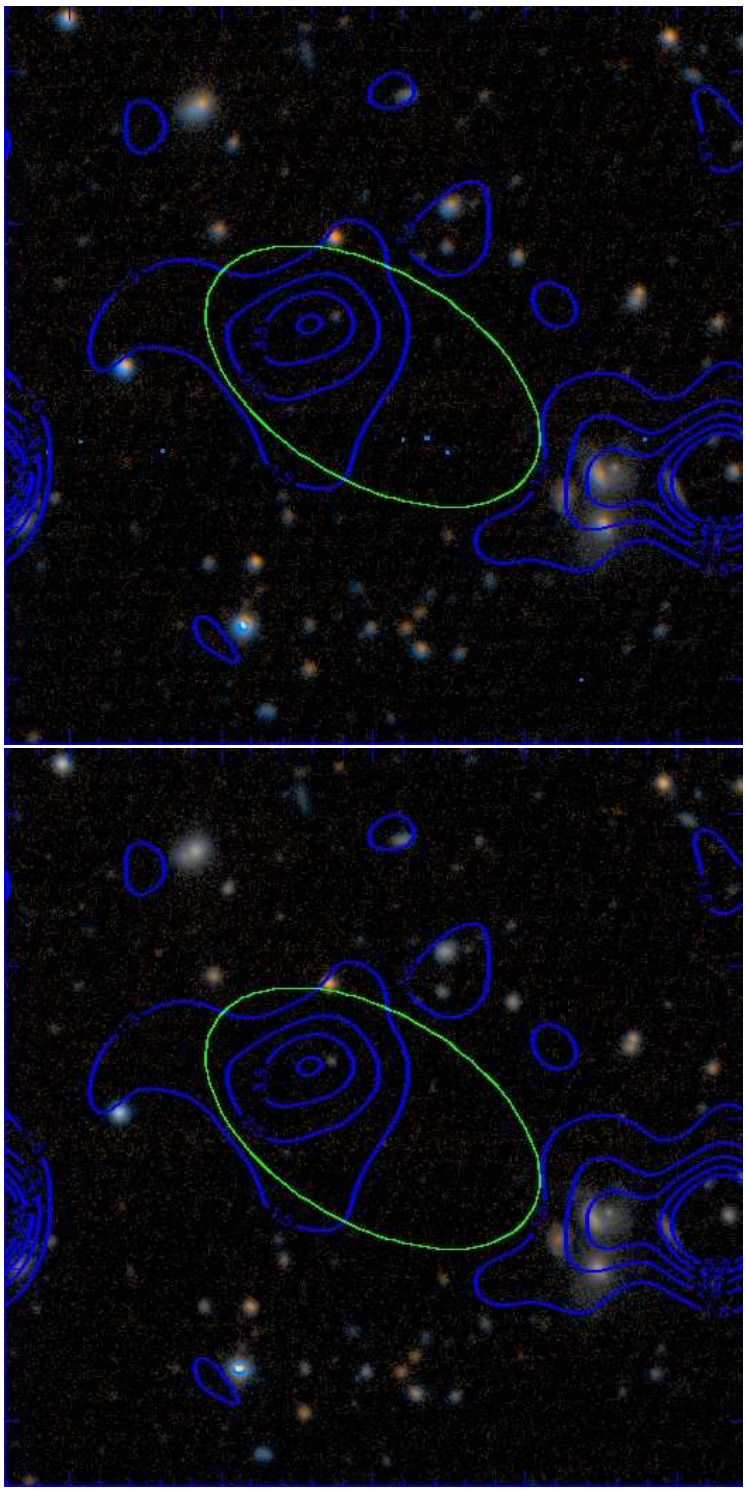

Figure 3.10 Colour-composite images of the XCS candidate XMMXCS J022258.8-041609.5 contained within the NXS-field 0109520601. The top figure shows evidence of an inaccurate WCS fit made apparent by the displacement in colour caused by r-band and z-band positional offsets. The bottom figure shows the corresponding image resulting from the WCS corrected field.

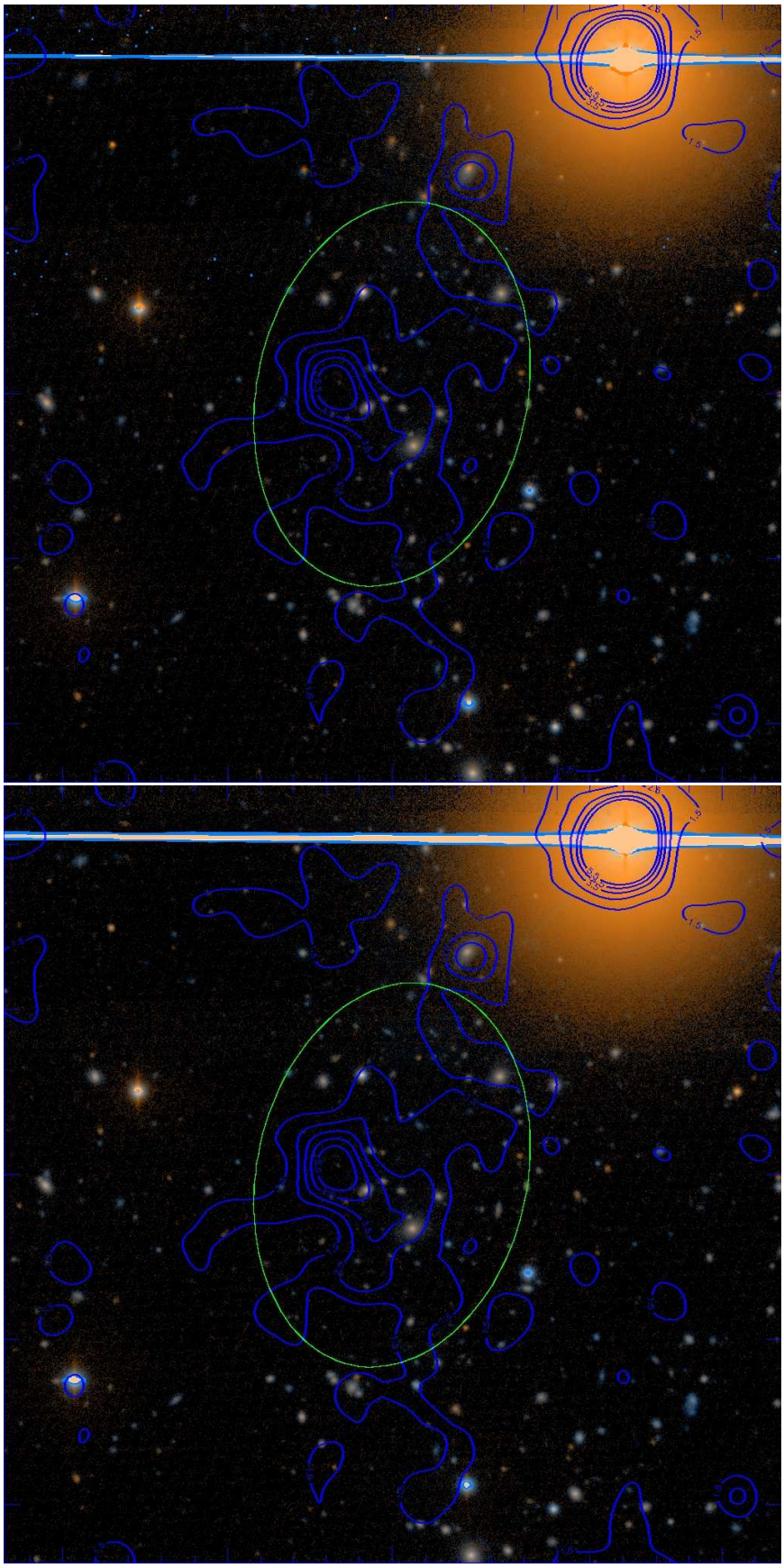

Figure 3.11 Caption as for Figure 3.10 but illustrating an inaccurate WCS fit located across a MOSAIC chip gap made apparent by the colour displacement for stars located at the top right hand corner of the image.

introduced additional dust doughnuts in the object images taken that night. Dome flat images taken on subsequent nights were free from these artifacts. Therefore Master dome-flat frames created from the 28th were applied to the object images taken on the 27th. Even after this step, 3 dust doughnuts remained in each object image taken on the 27th.

Sky Flat Despite only having 16 r and 24 z images taken on the 27th, a night specific sky flat was created in each filter and used solely on the object images taken on the 27th, to remove the dust doughnuts mentioned above. This resulted in an increased sky noise compared to the other nights of the run. For the remainder of the run it was necessary to combine images taken on consecutive nights to make a sky flat image. An r-band Master skyflat was created combining 34 images from the 28th-30th after discarding 14 images deemed unsuitable. With the increased number of z-band exposures, it was possible to create a Master sky flat solely for the 28th using 28 images. A third z-band sky flat was then made using 30 z-band exposures from and applied to the images taken on the 29th and 30th.

Run3: KPNO January 2007

Technical Difficulties Technical difficulties at the telescope resulted in the occasional chip with very low counts in a number of bias and dome flat images. Several bias frames also had conspicuous streaks across chip 5. No bias frames were taken on the 13th. Only 3 frames were taken at the end of the 14th, all of which exhibited these streaks. Although no object frames were imaged on the 15th, instrument calibration frames were taken. Twenty-four bias frames were taken this night, the first half of which exhibited streaks and the occasional missing chip. Therefore only the second half in the sequence of bias frames were combined to create a Master bias frame which was then applied to the images from the 13th and 14th. It was later found that the dome flat images taken on the 14th had greatly varying count levels, this was most likely due to ambient light still present in the dome. Therefore master dome flats from the 13th were applied to the object frames taken on the 17th. Nightly bias frames (free from artifacts) and domeflats were then applied to the images taken on the 16th-18th.

Sky Flat Due to the small number of images taken over the course of this observing run, 25 r-band and 38 z-band object frames from the 13th, 14th and 16th were combined to create master sky flats in each filter. We disregarded object images taken on the 17th and 18th when generating a sky flat as they were taken through heavy cloud cover and had

higher sky levels compared to the object images taken on previous nights. Additionally, there were only 3 object frames taken on both the 17th and 18th, not enough to create a specific skyflat and their poor quality later resulted in them not being used for the survey.

Run4: CTIO June 2007

Technical Difficulties None experienced.

Sky Flat Complications for this run arose from the large variations in sky levels caused by observing the Moon in bright time at 0.72-0.50 illumination, as well as the large variation in cloud cover. This forced us to create two sky flats in the z-band; a lower level sky flat and a higher level sky flat. These sky flats were created by combining all images deemed to be suitable taken from every night of the run based on their sky counts and photometric conditions. A lower level sky flat was generated using images with sky levels between 6000 and 10500 counts. Whereas, a high level skyflat using images with sky levels between 10500 and 15000. Splitting the count ranges further yielded too few images to combine into a master skyflat image. This resulted in 53 and 49 images being combined to create the low and high level sky flats respectively, however it should be noted that many of these fields were repeat observations of the same position (taken to reduce background levels). Similarly, a single r-band skyflat was created using 54 images taken over the run with sky counts ranging between 2700 and 6700 adu. These skyflats were then applied to the appropriate images.

Run5: KPNO September 2007

Technical Difficulties None experienced.

Sky Flat Due to the lack of images taken throughout the run, all target frames taken during the first 4 nights were combined to create a single master skyflat in each band.

Run6: CTIO March 2008

Technical Difficulties Only 6 NXS target fields were taken during RUN6 and these images were used to create a sky flat image. However after removing the large scale sky-gradient it became apparent that the small number of images used to create a master skyflat had left 'holes' in each image *i.e.* regions containing less counts due to inadequate sky coverage (see Figure 3.12). To help rectify this, initially the master sky flat created from the CTIO July 06 run (RUN2) were applied to the pre-skyflattened target frames. A

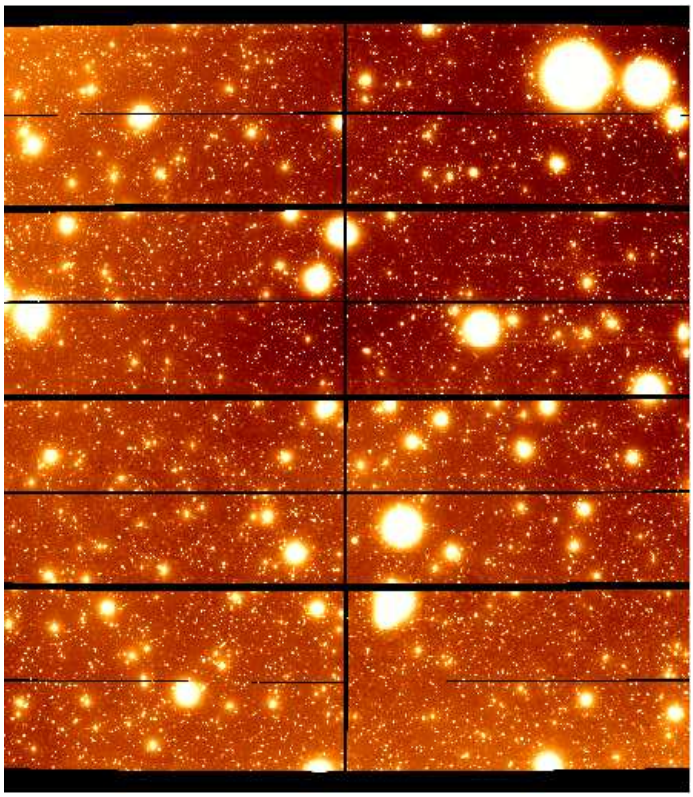

Figure 3.12 Example of an reduced NXS image taken during RUN6 illustrating the non-uniformity of the background sky level across the NXS-field

sky flat from RUN2 was chosen due to its similar observing conditions to RUN6, whereas RUN4 suffered from high levels of Moon illumination causing large variations in sky levels. Unfortunately the RUN2 master sky flat introduced an artifact that was specific to the object images taken during RUN2.

To address this problem we took at different approach and used data reduced by Frank Valdes using an automated pipeline based on `MSCRED`. In order to effectively sky flatten the RUN6 images, Frank Valdes created Master sky flat images in the r and z-band using every object frame ever taken by CTIO MOSAIC II camera. This automated pipeline produced sky flattened and WCS corrected images, which were reduced to the pre-tangent plane projected stage with all defects masked out. Upon receiving the resulting images, we projected and removed their sky gradients to reveal no apparent 'holes' or large scale gradients within them.

Sky Flat Master sky flat image created by automated pipeline written by Frank Valdes using every object frame taken by CTIO MOSAIC II camera (see above).

3.6 NXS survey summary

As of March 2008 the NXS survey had completed 38 nights of wide-field MOSAIC CCD imaging using the NOAO 4m telescopes at KPNO, Arizona; and CTIO, Chile. A total of 154 NXS-fields were observed. Of these 154 fields, 90 were observed under photometric conditions. A further 11 NXS-fields observed under non-photometric conditions were subsequently calibrated using SDSS coverage or short calibration frames.

The 154 NXS-fields contained 381 XCSDR1 and 80 XCSDR2 cluster candidates of which 267 XCSDR1 and 32 XCSDR2 were observed in photometric conditions. A further 34 XCSDR1 cluster candidates observed under non-photometric conditions were later photometrically calibrated. In July 2009, the XCS collaboration created XCSDR3 (§2.5) using XAPA-2 (§2.3.1). Contained within the 154 NXS-fields observed by the NXS survey were 381 XCSDR3 candidates, 214 of which were previously detected in XCSDR1 and XCSDR2. A summary of the NXS survey is shown in Table 3.3. Thus, the total number of XCS candidates observed by NXS was 628.

3.7 Discussion

In this chapter, we have presented the methodology and outcome of the NXS.

Comparison to Pre-Survey Predictions

The total number of NXS-fields observed (154) is less than the expected 330 fields proposed for the survey. This discrepancy is due to loosing ≈50% of survey time to instrument failure and bad weather forcing dome closures. Despite this loss in telescope time, the goal of observing ≈500 cluster candidates was met due to there generally being more cluster candidates per observed NXS field than estimated in the proposal (∼4 c.f. ∼2). This was in part due to preferentially selecting targets with a greater number of candidates per field and in part due to influx of area and cluster candidates with the addition XCSDR2.

Impact of Eyeballing Targets

In the attempt to not waste telescope time and observe spurious XCS cluster candidates, XCS targets were eyeballed and target selection became a subjective process. As a consequence, the integrity of the XCS selection function has not been maintained. However, the XCS selection function only applies to XCS500 clusters and follow-up of XCSDR1 XCS500 is ∼80% complete. Additional targets can be observed individually, either through des-

Table 3.3 The total number of NXS-fields and XCS candidates observed during Runs 1-6. These total numbers are broken down into those observed under "photometric" and "Non-photometric" condidtions, as well as those observed under "Non-photometric" conditions that were subsequently calibrated "NonPhot-Calibrated". The subset of observed NXS-fields, corresponding to their XCS internal data release (XCSDR1 and XCSDR2), are also presented. In addition, the subset of observed XCS candidates within each data release (XCSDR1, XCSDR2 and XCSDR3), is also presented, as is their break down in terms of soft counts.

	Total	Photometric	Non-photometric	NonPhot-Calibrated
Number of NXS-fields observed				
Total	**154**	**90**	**64**	**11**
XCSDR1	124	79	45	11
XCSDR2	30	11	19	0
Number of XCSDR1 cluster candidates observed				
Total	**381**	**267**	**114**	**34**
XCS500	50	42	8	3
XCS300	88	73	15	7
XCS100	253	182	71	22
Number of XCSDR2 cluster candidates observed				
Total	**80**	**32**	**48**	**0**
XCS500	16	4	12	0
XCS300	24	8	16	0
XCS100	61	24	37	0
Number of XCSDR3 cluster candidates observed				
Total	**381**	**255**	**126**	**34**
XCS500	68	47	21	3
XCS300	119	84	35	5
XCS100	258	179	79	17

ignated follow-up or acquiring second hand follow-up *e.g.* as in the case of Run6. This will then create a complete XCS500 sample for the XCS measurement of cosmological parameters with a known selection function.

Non-Optimum RA Cover

The timing and overlap of NXS runs in the Winter months had resulted in a significant RA gap in XCS follow-up between 10hrs<RA <15hrs in the Northern hemisphere, and 2hrs<RA <5hrs in the South, which included XCS high priority targets. In hindsight, the XCS follow-up performed by NXS would have been more effective if times between NXS runs were separated further, compensating for overlap with the Galactic plane and overlapping further with the Summer months in the respective hemispheres despite the shorter observing nights. In addition, SDSS enabled extensive follow-up of XCS candidates. The coverage and resulting redshift estimates from SDSS should have been taken into account when designing the observing times of NXS runs to make the most use of its increased Depth.

Planned Work

With the RA gap in mind, and because 50% of the allocated survey time was lost to bad weather and instrument failure, XCS proposed for additional observing time. Preference was placed on the sky obsevable during the Summer months, due to the existance of unobserved high priority targets remaining within their RA range. The proposal was successful and an additional 10 nights were awarded and carried out in April 2009. This data will be reduced and included in the analysis presented in Chapter 5. We refer to this NXS observing run as Run8, however, we do not discuss the results of Run8 in this thesis.

Data Reduction

With regard to the NXS data reduction method, an alternative would have been to use the NOAO automated reduction pipeline. Utilising a pipeline would have produced uniformly reduced NXS images at a much more efficient rate. An automated pipeline would have created reduced NXS images with a more accurate and uniformly produced WCS, as well as a more uniform sky level in each image. Indeed, initial reductions were performed in concert by Frank Valdes for the NXS data taken in Run1. However, these automated reductions were deemed to be poorer than those produced by NXS. Therefore, utilisation

of the NOAO pipeline may have been preferable only upon the creation of a Master sky flat obtained for both KPNO and CTIO. However, a Master sky flat only became available for CTIO images after Run7 and thus was too late for the timescale of this thesis and time constraints of XCS. One possible drawback of the NOAO Master sky flat, is the assumed presence of specific artifacts particular to a given night that may not get removed by a general sky flat image, rather than one tailored to the night/run. However, in these cases the regions around remaining artifacts could be simply be avoided by NXS due to their possible influence on cluster detections.

Survey Successes

As of Run7, NXS had imaged a total of 154 fields. Of these, 111 could be photometrically calibrated using existing data taken by the survey. These 154 fields contained 381 XCSDR1 and 80 XCSDR2 cluster candidates, of which, 267 XCSDR1 and 32 XCSDR2 were observed under photometric conditions, and a further 34 were subsequently calibrated using short calibration frames. It was subsequently found, that the production of XCSDR3 generated an additional 167 XCSDR3 cluster candidates falling within the survey area of NXS.

Chapter 4

The NXS: Photometric Calibration & Object Catalogues

As of March 2008, 38 nights of wide-field MOSAIC imaging had been carried out by the NXS (§3). This was the first major optical follow-up campaign to XCS (§2.10). As a result, 154 NXS-fields were observed and reduced, covering 628 NXS-targets. This chapter describes the detection of objects within these fields (§4.1), their photometric calibration (§4.2) and the creation of NXS galaxy catalogs (§4.3).

4.1 NXS Object Detection

Object detection on NXS-fields was performed using `SExtractor` (Bertin and Arnouts, 1996), which has been used by multiple surveys due to its highly configurable nature and efficiency in producing automated and reliable object catalogs on large image sets. For each NXS run `SExtractor` was configured in a consistent way. Objects were detected in dual-image mode whereby object positions and apertures are determined in the z-band and then applied to the r-band to measure magnitudes and colours in both filters simultaneously. This ensures a matched object catalog between bands and accurate colour measurements. To use `SExtractor` in dual-mode it is essential that both images are aligned to within 1 pixel. Although the r-band data was imaged to greater depth, thus containing a greater number of fainter objects, source detection was preferable in the z-band as these would contain stronger detections of intrinsically redder objects and objects at higher redshifts.

Weight map generation We employ external weight maps for each image to mark the relative contribution of flux from each pixel. Weight maps are computed by combining an

NXS exposure map (§3.5) with a bright mask (*i.e.* a map containing the regions covered by bright sources created in an initial run through of `SExtractor`. Bright objects were found by detecting a minimum of 3000 connected pixels at 1σ above the background. Sources were deblended using a minimum contrast threshold of 0.01 with the recommended default value of 32 sub-thresholds. We chose to apply a Gaussian filter to smooth each image prior to bright source detection using a 3σ filter threshold and assuming a global background. For smoothing we used a 5x5 convolution kernel of 4 pixels at FWHM.

Source detection Sources were detected, utilising NXS weight maps, in a second run of `SExtractor`. In order to detect sources in 'dual mode', science images and weight maps were aligned to better than 1 pixel accuracy using the `IRAF` tasks `GEOMAP` and `GEOTRAN`. The `SExtractor` parameter file was set to match that used to create the weight map images, with the exception that a detection limit of >3 connected pixels (rather than 3000) at 1σ above the background was used to detect sources, and that we used using a minimum contrast threshold of 0.001 to deblend sources (rather than 0.01). In addition, we chose the `SExtractor` option to clean the output catalog for spurious sources close to bright objects setting the cleaning efficiency to the default value 1.0.

Several types of instrumental magnitudes were measured for each detected object simultaneously: four separate aperture magnitudes; MAGAUTO; and MAGISO. Aperture magnitudes measure the flux within a fixed circular radius. We used four circular apertures set to 4, 8, 12 and 38 pixels in diameter to measure four separate aperture magnitudes. MAGAUTO measures KRON type magnitude (Kron, 1980) within an elliptical aperture estimated for each galaxy. Whereas, MAGISO measures the light above a certain threshold.

On examining the MAGAUTO apertures chosen by SExtractor around detected objects, it was clear that `SExtractor` had detected all objects in the z-band images that could be identified by eye. However, as expected, it had failed to detect numerous faint objects apparent only in the r-band images. Before final object catalogs were created, several tests were made altering the following `SExtractor` input parameters: the number of connected pixels; the detection threshold; use of filtering; background mesh size. The values stated above produced the optimum results. In addition, for greater computing efficiency, each MOSAIC image was split into 6 image sections (containing a 50 pixel overlap) prior to source detection. The outputted catalogs for each section were then combined and duplicate objects removed to create a master catalog. The 'raw' instrumental magnitudes of objects contained within these catalogues then had to be calibrated to magnitudes within a standard photometric system (§4.2) before any scientific analysis could take place.

4.2 MOSAIC I and MOSAIC II photometric calibration

The measured flux of a particular object varies depending on the instrument. In addition, the amount of light received by a detector is diminished as it travels through the atmosphere. The greater the atmospheric mass (airmass) through which the light travels, the greater the extinction. As an object may be observed through a range of airmass we must compensate for this effect. In addition, although a filter set is built to replicate the performance of a standard photometric system, *e.g.* Johnson-Cousins or SDSS, small differences between the instrumental and standard magnitudes may exist. Moreover, these may be filter dependent. Therefore, when measuring colours for a given object it is often necessary to correct for the instrument to standard offset by introducing a colour term. In theory a colour term and zeropoint should not vary for an instrument during an observing run unless the instrument undergoes technical changes (e.g. an upgrade).

In summary, in order to accurately compare galaxy magnitudes within a catalog, instrumental magnitudes need to be converted into magnitudes in the desired standard photometric system, using a relation given by equation 4.1.

$$M_c = M_i + Z + \kappa X + C(a - b) \tag{4.1}$$

Where:

M_c= magnitude in the standard photometric system.

M_i= magnitude measured by the instrument.

Z= The instrumental zeropoint, *i.e.* difference between a magnitude measured by the instrument and the magnitude in the target standard photometric system.

X= The airmass *i.e.* the path length travelled by the light through the atmosphere ($X = sec(z)$ where z is the angle subtending the object and the zenith, *i.e.* the shortest distance through the atmosphere).

κ= The amount of atmospheric extinction undergone by the light measured in each filter. In the following, κ is set to the NOAO standard values.

$C(a-b)$= The colour term; the difference between the magnitude in a filter measured by the instrument (a) and the target photometric system (b). In the following, the colour term is assumed to be zero.

4.2.1 NXS use of SExtractor for calibration

When calibrating an NXS-field using multiple stars with known magnitudes distributed across the MOSAIC CCD, objects in that field were detected using `SExtractor` as parametised in §4.1. Instrumental magnitudes were measured in an aperture with a fixed radius of 19 pixels ($\approx 5''$). This magnitude was chosen after testing a range of smaller and larger aperture sizes. It was found that instrumental magnitudes (of point sources) converged at radius of 19 pixels, whereas larger radii introduced an increased risk of overlapping apertures. Standard star catalog positions and calibrated magnitudes were then cross matched using a matching radius of $1''$.

4.2.2 NXS use of the `IRAF` task `FITPARAMS`

The photometric zeropoint of a MOSAIC image was fitted using the `IRAF` task `FITPARAMS`. Instrumental magnitudes with corresponding standard magnitude and airmass values, were collated into a single input file for the task `FITPARAMS`. If more than one image was used to derive a zeropoint for a single night, the measurements for all images were collated into a single input file. When fitting a zeropoint for MOSAIC I, we applied the NOAO determined extinction corrections of 0.119 and 0.030 in the r and z band filters respectively. Whereas for MOSAIC II, we used the NOAO determined extinction corrections of 0.11 and 0.053 in the r and z band filters respectively. These extinction values were supplied by the `IRAF` task `ONEDSPEC`. For the NXS survey we fit a single zeropoint across the MOSAIC image and neglect to fit for a colour term, as justified in §4.2.3.

4.2.3 Photometric consistency across the MOSAIC camera

The MOSAIC camera is an array of CCDs. Due to the differing quantum efficiencies of each MOSAIC chip (seen in Figure 4.1), it would be best to derive zeropoints, airmass and colour terms for each CCD. But this would require the same standard star to be observed separately in each CCD over a range of airmasses, over the course of each photometric night. Long readout times (150s) for the MOSAIC cameras, and the scarcity of photometric conditions, made this task unfeasible. Therefore, during Run1, we chose to test the differing response across the MOSAIC CCD by observing a region of SDSS (designated SDSS-0340). This field contained many non-crowded 14th magnitude stars covering the entire MOSAIC camera, thus avoiding substantial loss of telescope time. We then used this field to assess the effect of differing responses for each chip on their zeropoint values.

Thirty second exposures of SDSS-0340 in each filter were observed on night 6 and night

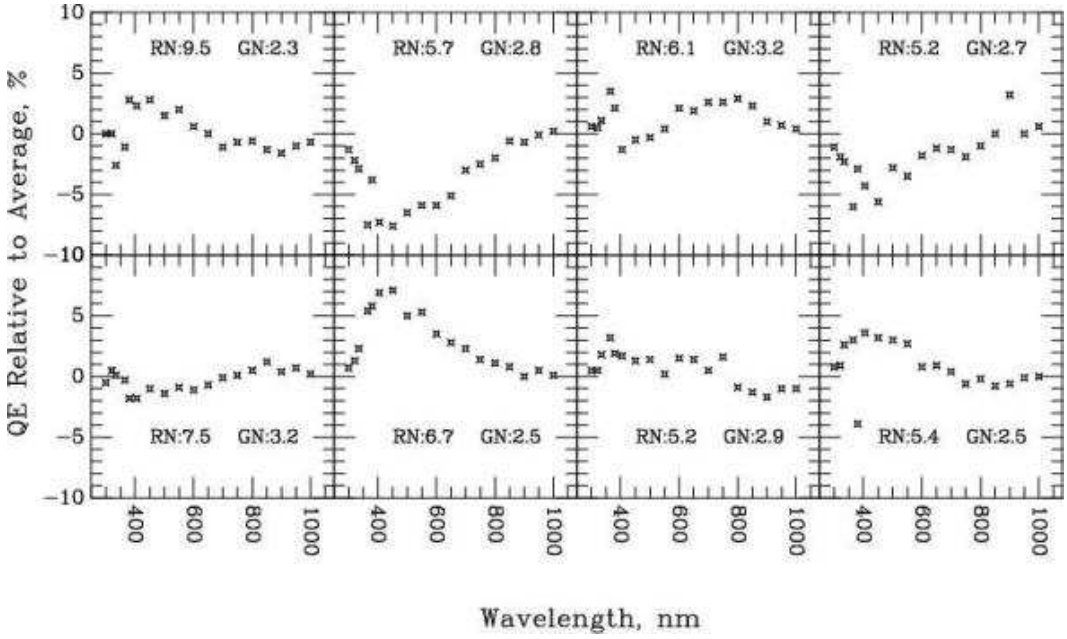

Figure 4.1 *The QE differences relative to the average for the 8 CCDs in Mosaic I. Also shown are the readnoise (RN) and gain (GN) values for each CCD.* [Figure and caption credit: http://www.noao.edu.html]

7 of Run1. Each NXS image of SDSS-0340 was then broken up into its constituent chips and instrumental catalogues measured by SExtractor (§4.2.1). SDSS catalog positions and calibrated magnitudes were downloaded via the SDSS online database[1] for all stars within this region following the instructions[2] for extracting objects with clean photometry. Clean photometry ensures that all galaxies are the primary target, unsaturated, have not been deblended and have no interpolation problems. Zeropoints were then fitted using the `IRAF` task `FITPARAMS`. As the variation in zeropoints across the MOSAIC CCD is small, we choose to fit a single zeropoint for the entire MOSAIC CCD. This greatly simplifies the photometric calibration required as NXS observations of a field are ditthered resulting in a significant number objects being detected by multiple chips.

4.2.4 Calibration using NXS fields with SDSS overlap

A large number of NXS-fields, particularly in the northern hemisphere, had coverage with SDSS. Due to the distributed coverage of SDSS-stars across the entire MOSAIC CCD, these fields (NXS-SDSS-fields hereafter), can be photometrically calibrated without reference to traditional standard stars.

For these fields, sources were detected and instrumental magnitudes were measured,

[1] http://cas.sdss.org/astrodr7/en/tools/search/sql.asp

[2] http://cas.sdss.org/astrodr7/en/help/docs/realquery.aspflags

by assuming a 'dummy' zeropoint and using `SExtractor` as parameterised in section §4.2.1. SDSS stars with calibrated magnitudes were then downloaded via the SDSS online database[1] for objects with clean photometry[2]. The positions of objects in the standard catalogue were cross matched with those in the instrumental catalog using a $1''$ matching radius.

The instrumental versus calibrated magnitude relation was then eyeballed for each NXS-SDSS-field to determine an appropriate magnitude range upon which to fit the data. Magnitude ranges were based upon using stars bright enough to have accurate measurements but faint enough not to be saturated, as evidenced by a consistent relation. The chosen magnitude ranges were generally $18<r<20$ and $17<z<19$ using stars with a photometric error less than 0.05. Zeropoints were then fitted using the `IRAF` task `FITPARAMS`.

4.2.5 Calibration using NXS targetted SDSS regions

A region of SDSS, designated SDSS-0340 §3.4.1, was specifically targetted for photometric calibration purposes, despite this region containing no NXS-targets. This NXS-SDSS-field was used to calibrate the last two nights of RUN1 and was subjected to the calibration procedure described in Section §4.2.4.

4.2.6 Calibration using Southern Standard Fields

Three Southern Standard Fields (Smith et al., 2002) were observed to calibrate the NXS data observed during RUN2; SA-140-A, TPhe-B, and DL135911. These fields, in particular DL135911, contain many standard stars covering the entire MOSAIC II camera and are therefore preferable to standard fields containing only one or two stars. Instrumental magnitudes were extracted from the NXS images using `SExtractor` as parameterised in section §4.2.1 and catalogue positions were cross matched with those in the images using a $1''$ matching radius. Their instrumental magnitudes were subsequently collated and used to derive a single zeropoint in each band for the night using the `IRAF` task `FITPARAMS` §4.2.2.

When fitting for a zeropoint, only stars between the magnitude range $12<r<17$ were included for the field DL135911, whereas, due to their smaller number, all standard stars in the fields SA140A and TPHE-B were used.

4.2.7 Calibration using NXS Standard star fields

As discussed in Section §3.3.3, the NXS fields (NXS0109520601 and NXS0100240801) were adopted as standard star fields to be used for both calibration and as a consistency check between runs and nights. Object catalogues for these NXS standard fields were created using `SExtractor`. Instrumental magnitudes where obtained by assuming a 'dummy' zeropoint. Whereas, standard magnitudes for the same NXS standard field were obtained by assuming a zeropoint derived from other standard stars observed that night.

Only objects with calibrated magnitudes between $18<r<20$ and $17<r<19$ with a photometric error less than 0.05 were used to derive a single zeropoint for the night. These magnitude ranges were chosen as they provided a consistent relation between calibrated and instrumental magnitudes, hence they were neither saturated or too faint to have inaccurate measurements. NXS standard star fields were used to assist photometric calibration for Runs 1 to 5.

4.2.8 Calibration using Landolt standard stars

On occasion, observations of Landolt standard stars were taken to calibrate the instrumental magnitudes of an entire, or partially photometric, night. These fields typically contain only a small number of stars with limited coverage over the MOSAIC CCD. However, these stars are brighter than the typical stars used in NXS and SDSS calibration fields, therefore these stars were faster to measure. They can also be found over all RA's whereas the other calibrators were not. Due to the small number of standard stars detected within an NXS-field, we chose to perform standard star photometry on individual standard stars using the Starlink Graphical Astronomy and Image Analysis Tool `GAIA`[3] rather than `SExtractor`. In the `GAIA` aperture photometry tool, we set the parameters as follows: initial frame zeropoint=`0`; measurement errors=`sky variance`; sky estimator=`mode`; photons per data unit=2.75 (the MOSAIC gain value); and exposure time as given by the image header. Stars were photometered with fixed apertures of 19 pixels ($\approx 5''$) in radius. The local sky was measured using a 5 pixel wide annulus ring centered on each star, starting at a radius of 21 pixels. Any stars that had their photometered annulii falling on chip gaps were not used when measuring a zeropoint. Zeropoints were then fitted using the `IRAF` task `FITPARAMS`.

[3] http://astro.dur.ac.uk/ pdraper/gaia/gaia.html

4.2.9 Photometric calibration results for KPNO and CTIO

The calibration fields used for each NXS run is outlined in Table 4.1. Observations of these calibration fields are described in Chapter 3.7 and logged in Appendix B. The derived zeropoints (Z_r,Z_z) for each NXS run are given in Tables 4.2 and 4.3.

Table 4.1. NXS-fields used to calibrate the data for each NXS run

Date	Conditions	Calibration image	Consistency check image	Comments
		RUN1		
23/11/2005	Non-photometric	-	-	-
24/11/2005	Photometric	NXS-SDSS 0041170101	NXS-SDSS 0143653901	-
25/11/2005	Non-photometric	-	-	-
26/11/2005	Non-photometric	-	-	-
27/11/2005	Photometric	Landolt stars (Smith et al. 2002)	-	-
28/11/2005	Photometric	SDSS-0340	-	-
29/11/2005	Photometric	SDSS-0340	-	-
		RUN2		
24/07/2006	Dome closed	-	-	-
25/07/2006	Dome closed	-	-	-
26/07/2006	Dome closed	-	-	-

Table 4.1 (cont'd)

Date	Conditions	Calibration image	Consistency check image	Comments
27/07/2006	Photometric	NXS 0109520601	-	-
28/07/2006	Photometric	SA-140-A; TPhe-B; DL135911	-	NXS 0109520601 calibrated
29/07/2006	Photometric	DL135911; NXS 0109520601	-	NXS 0100240801 calibrated
30/07/2006	Non-photometric	-	-	-
		Run3		
13/01/2007	Non-photometric	-	-	-
14/01/2007	Photometric	NXS-SDSS 0110070401	NXS-SDSS 0200730101	-
-	-	NXS-SDSS 0041170201	-	
15/01/2007	Dome closed	-	-	-
16/01/2007	Part photometric	NXS 0109520601	-	First 4 hrs calibrated
-	-	-	-	by NXS 0109520601.
-	-	-	-	NXS-SDSS 002554030; 0203361801;
-	-	-	-	0102040201; 0104860501;
-	-	-	-	0056020901 calibrated seperately

Table 4.1 (cont'd)

Date	Conditions	Calibration image	Consistency check image	Comments
13/01/2007	Non-photometric	-	-	-
13/01/2007	Non-photometric	-	-	-
		Run4		
16/06/2007	Non-photometric	-	-	NXS-SDSS 0148520101
-	-	-	-	repeated on the 20th.
17/06/2007	Non-photometric	-	-	NXS-SDSS 0021540101 & 0203170301
-	-	-	-	calibrated seperately.
18/06/2007	Non-photometric	-	-	-
19/06/2007	Non-photometric	-	-	-
20/06/2007	Photometric	NXS-SDSS 0148520101	NXS 0100240801	-
18/06/2007	Partially photometric	-	-	Poor seeing.
18/06/2007	Photometric	-	-	Poor seeing.
		Run5		

Table 4.1 (cont'd)

Date	Conditions	Calibration image	Consistency check image	Comments
11/09/2007	Photometric (apart from 1st field)	NXS 0203050601	NXS 0109520101	-
12/09/2007	Partially photometric	NXS 0109520601	-	First half of night calibrated
13/09/2007	Partially photometric	SA-96-737 (Smith et al 2002)	-	last field calibrated
14/09/2007	Non-photometric	-	-	NXS-SDSS 0203390101
-	-	-	-	calibrated seperately
15/09/2007	Dome closed	-	-	-
16/09/2007	Dome closed	-	-	-
		Run6		
04/03/2008	Photometric	NXS-SDSS 0148740101	-	-
05/03/2008	Photometric	NXS-SDSS 0093640301	NXS-SDSS 0070940101	-

4.3 NXS object catalog generation

NXS object catalogs were created using `SExtractor` as parameterised in Section 4.1. As justified in Section 4.2.3, we applied a global zeropoint, appropriate to each NXS-field, to the entire image, irrespective of the differing response of each individual mosaic chip. Furthermore, we used the `SExtractor` MAGAUTO as an estimate of a galaxy's total magnitude. However, we use the `SExtractor` isophotal aperture MAGISO for colour estimations. MAGISO takes into account the radial profile of the galaxy and is therefore less sensitive to colour gradients within galaxies.

Furthermore, we apply a correction to the measured object magnitudes for Galactic dust extinction based on the dust maps by Schlegel et al. (1998). This correction removes the additional reddening of extragalactic light caused by Galactic dust particles absorbing and scattering light to longer (redder) wavelengths. By using dust maps one can calculate 'dereddened' magnitudes. Corrections were made on all objects in each image section using its central coordinates.

4.3.1 Star-Galaxy Separation

We apply our own star-galaxy separation on each field using the method of Metcalfe et al. (1991) based on the locus of the objects in half-light radius versus magnitude diagrams. This method exploits the fact that stars have a smaller radius than galaxies at a given magnitude. This results in a line or 'stellar locus' where the stars are clearly separated from the galaxies at magnitudes $r\sim$21-22. Beyond this magnitude the stars are too faint to be distinguished from galaxies. The concentration value occupied by the stellar locus depends on the seeing value of each image. Therefore a star-galaxy separation must be determined for each individual NXS field. We apply our cuts in the r-band as these images generally had better seeing. We compute the concentration using magnitudes measured in fixed circular apertures of 4 and 12 pixels in diameter. These magnitudes are measured simultaneously along side those of MAGAUTO and MAGISO.

Figure 4.2 shows concentration versus magnitude for the field NXS0101040101 and its corresponding star-galaxy cuts. The stellar locus is mainly bounded by lines 1, 2 and 4. Objects below the line marked 'line 1' have a concentration smaller than that of the point spread function of the MOSAIC instrument and are classed as spurious objects. Objects above 'line 2' are extended and therefore classed as galaxies. Objects with a magnitude brighter than 'line 3' are assumed to bright nearby stars. This 'line 3' cut may remove bright galaxies in low redshift clusters from our galaxy catalog. However, for these low

Table 4.2 NXS zeropoints (Z) and the calibration fields from which they were derived for observing nights at KPNO

Date (KPNO)	Z_r	Z_z	Photometric standard field
24/11/2005	26.523 ± 0.001	25.286 ± 0.003	NXS 0041170101
27/11/2005	26.473 ± 0.004	25.286 ± 0.007	Smith et al. (2002)
28/11/2005	26.544 ± 0.001	25.326 ± 0.003	SDSS 0340
29/11/2005	26.527 ± 0.001	25.337 ± 0.003	SDSS 0340
14/01/2007	26.541 ± 0.001	25.373 ± 0.002	NXS 0110070401 & NXS 0041170201
16/01/2007	26.5173 ± 0.0008	25.276 ± 0.002	NXS 0109520601
16/01/2007	26.561 ± 0.001	25.379 ± 0.002	NXS 0025540301
16/01/2007	26.551 ± 0.002	25.386 ± 0.003	NXS 0203361801
16/01/2007	26.544 ± 0.002	25.382 ± 0.002	NXS 0102040201
16/01/2007	26.517 ± 0.004	25.384 ± 0.004	NXS 0104860501
16/01/2007	26.545 ± 0.002	25.374 ± 0.004	NXS 0056020901
11/09/2007	26.438 ± 0.001	25.155 ± 0.003	NXS 0203050601
12/09/2007	26.503 ± 0.001	25.139 ± 0.002	NXS 0109520601
13/09/2007	26.395 ± 0.000	25.133 ± 0.004	Smith et al (2002)
14/09/2007	26.366 ± 0.007	25.130 ± 0.003	NXS 0203390101

Table 4.3 NXS zeropoints (Z) and the calibration fields from which they were derived for observing nights at CTIO

Date (KPNO)	Z_r	Z_z	Photometric standard field
27/07/2006	26.717 ± 0.005	25.538 ± 0.001	NXS 0109520601
28/07/2006	26.712 ± 0.002	25.519 ± 0.004	Smith et al. (2002)
29/07/2006	26.686 ± 0.003	25.503 ± 0.005	Smith et al. (2002)
17/06/2007	26.690 ± 0.001	25.219 ± 0.003	NXS 0021540101
20/06/2007	26.662 ± 0.001	25.486 ± 0.003	Smith et al. (2002)
04/03/2008	26.634 ± 0.004	25.413 ± 0.003	NXS 0148740101
05/03/2008	26.711 ± 0.003	25.464 ± 0.002	NXS 0070940101 & NXS 0093640301

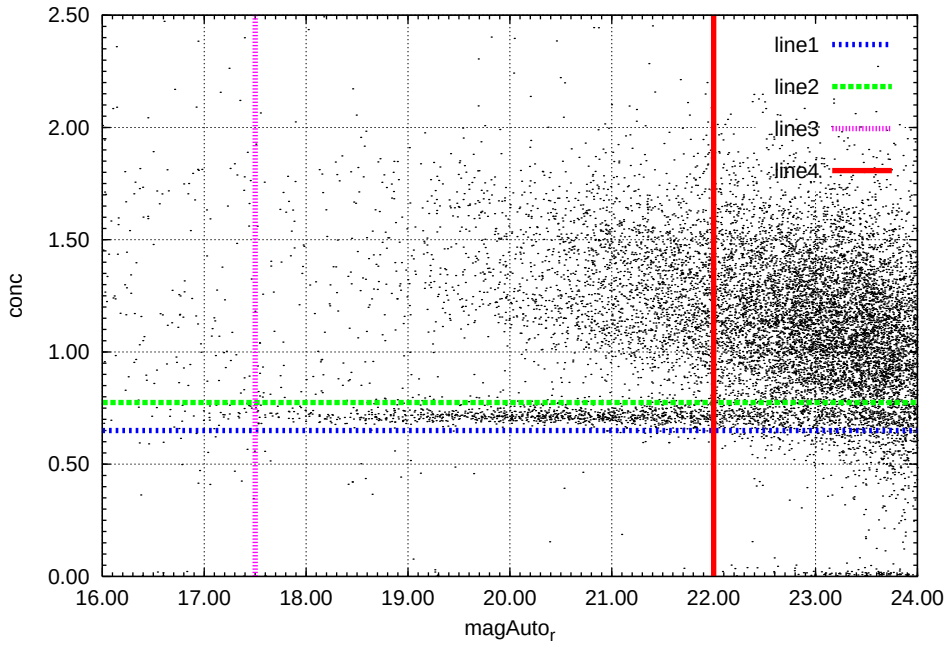

Figure 4.2 Star-galaxy separation plot for NXS0101040101, with seeing 0.96″ taken during RUN1. The figure shows the separation between the stellar locus and the galaxy population, as made evident by the horizontal relation bounded by lines 1 and 2. Galaxies lie mostly right of line 3 and above line 2. Thus objects located between lines 1 and 2 and left of line 3 are classified as stars. In addition, all objects brighter than line 3 are classified as stars. All objects located below line 1 are classified as spurious detections.

redshift clusters there should remain enough classified galaxies along the red sequence to measure a red sequence relation. 'Line 4' marks where the star-galaxy separation becomes less defined and objects fainter than this magnitudes are uniformly classed as galaxies. All remaining objects are classed as stars. These classifications are then used to remove stars and spurious objects from the object catalogs and create galaxy catalogs for each NXS image.

As the seeing of the image increases, the stellar locus becomes less defined. Figure 4.3 shows additional examples of concentration verses magnitude plots for NXS fields with a range of seeing values. The bottom right hand example shows the concentration versus magnitude plots for the field NXS0093190301, in this case a star-galaxy separation could not be determined and as such a galaxy catalog could not be created for this image.

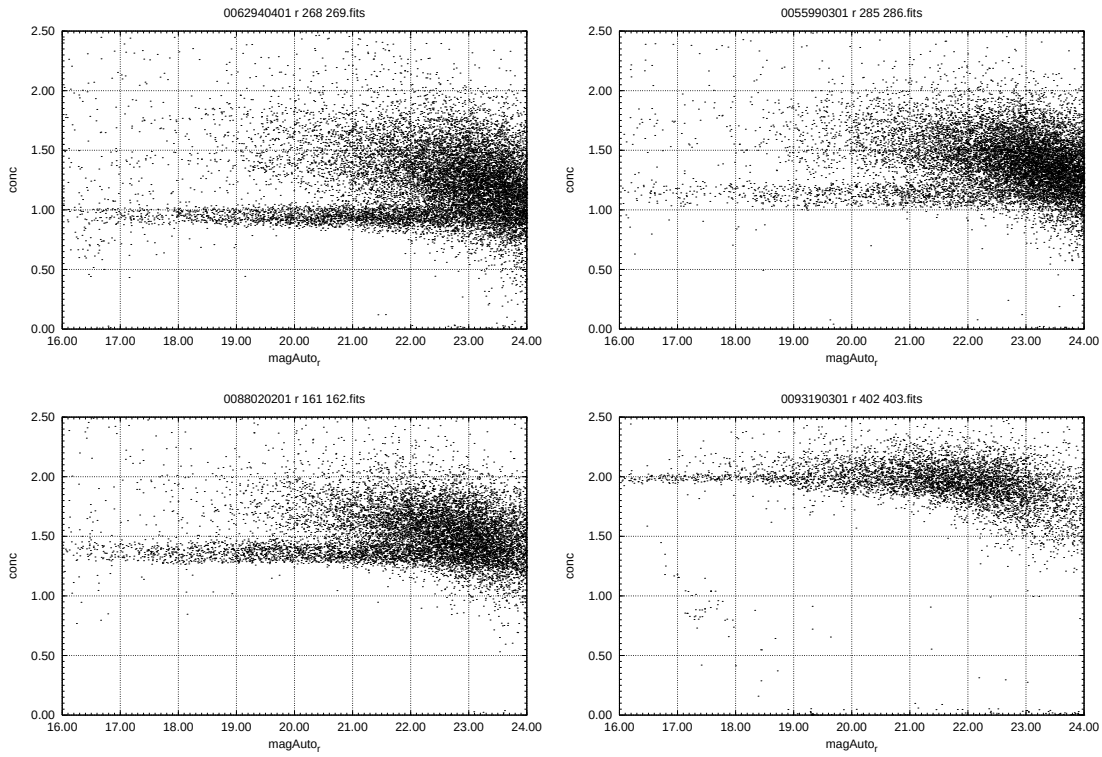

Figure 4.3 Star-galaxy separation plots for the NXS-fields NXS0062940401, NXS0055990301, NXS0088020201, NXS0093190301 with seeing values of 1.21″, 1.34″, 1.63″ and 2.65″ respectively. The concentration versus magnitude for all objects within the r-band image of each NXS-field are plotted. The figure shows the increased concentration and decreased definition of the stellar locus, as marked by the horizontal relation, taken under increased seeing conditions.

.

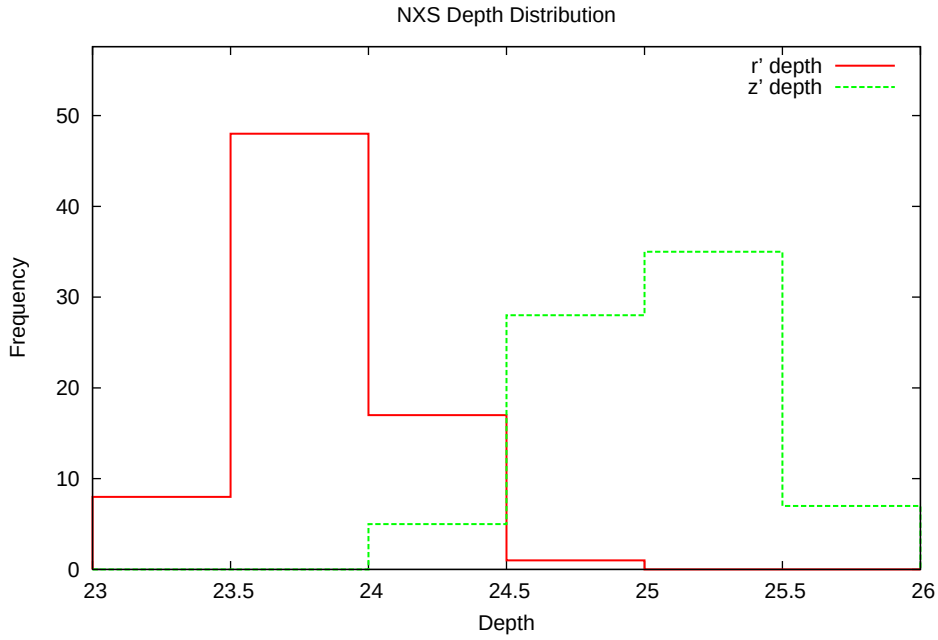

Figure 4.4 Distribution of the 5–σ point source detection limit of NXS-fields taken under photometric conditions.

4.4 NXS seeing and depth values

NXS Seeing and depth distributions for fields taken under photometric conditions are shown in Figures 4.4 and 4.5. Seeing and depth measurements on photometric data were made for each NXS stacked image using the object catalogs produced by `SExtractor` (see below).

The seeing of an image can be obtained by multiplying the measured FWHM of a point source (in pixels, as measured by `SExtractor`) by the pixel size (in arcseconds). Objects with calibrated magnitudes $18.5<r<20.0$ and $17.5<z<19.0$ were used to calculate the typical FWHM of a point source for each NXS image. This value was taken to be the bi-weight mean of the FWHM values falling within the top 25% of the smallest FHWM values. This FWHM value was then multiplied by the typical pixel size to provide a seeing estimate for each NXS field. The mean seing values for the NXS survey across all runs are $1.39''$ and $1.23''$ in the r-band and z-band respectively.

For NXS we use the 5σ point source detection as the limiting magnitude for each image. A signal-to-noise of 5 corresponds to a fixed magnitude error of 0.198 (Gwyn, 2008). Therefore, to measure the 5σ point source limit we find the faintest object in an image with an associated error less than 0.198 mags. The mean depth values for the NXS survey across all runs are r=25.00 and z=23.79.

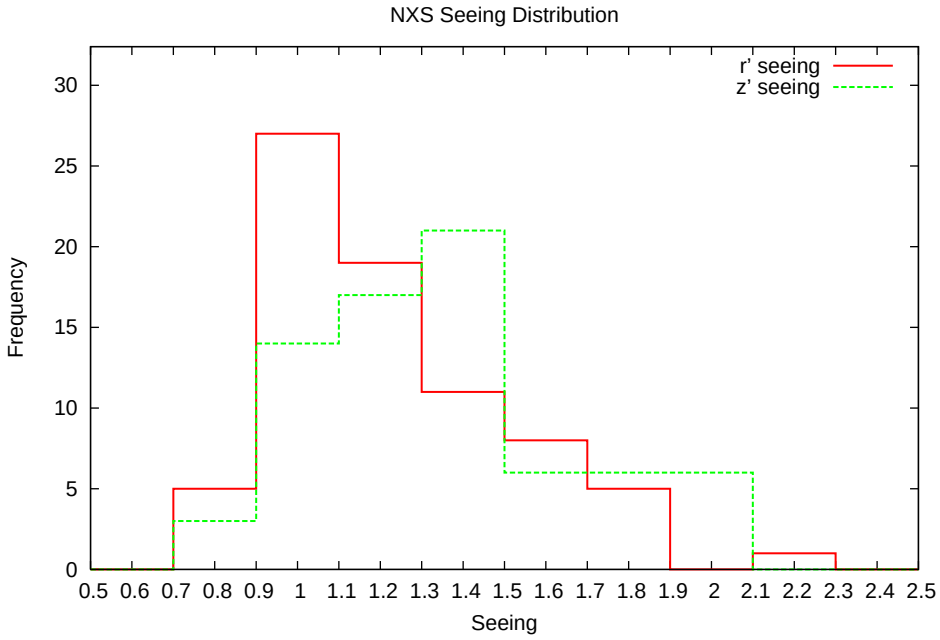

Figure 4.5 Seeing distribution, in arcseconds, of NXS-fields taken under photometric conditions.

4.5 Discussion

In this chapter, we have presented the photometric calibration of the NXS survey and production of NXS galaxy catalogues.

This has been achieved via the use of SDSS overlap fields, Landolt standard stars and NXS standard frames. In this manner, 90 NXS-fields deemed to be taken under photometric conditions were calibrated. An additional 11 fields where subsequently calibrated using short calibration frames taken on subsequent photometric nights/runs. Galaxy catalogs were produced for all NXS-fields by performing a star-galaxy separation similar to that described by Metcalfe et al. (1991). These galaxy catalogues have been used to derive photometric redshifts for NXS clusters as described in Chapter5.

For those fields taken under photometric conditions, the mean seeing and depth values (as given by the 5-σ detection limit) were 1.39$''$ and r=25.00 in the r-band, and 1.23$''$ and z=23.79 in the z-band.

Chapter 5

The NXS: Redshift Algorithms and Results

The purpose of the NXS is to confirm cluster detections and measure photometric redshifts for XCS cluster candidates. To do this, we have modified the red sequence method developed by optical cluster surveys, *e.g.* RCS & MaxBCG, to detect clusters and assign redshifts. The cluster red sequence relation has been observed to be ubiquitous and homogeneous within clusters over a wide range of redshifts and masses, meaning we can apply our technique to the wide variety of systems detected by XCS. Moreover, as red sequence galaxies inhabit the bright end of the cluster luminosity function, we can measure redshifts out to large distances.

In this chapter we describe the technique developed to determine red sequence redshifts from NXS observations. In Section 5.1, we review the methods used by the RCS and MaxBCG (methods we have built on herein). In Section 5.2, we describe how cluster and field samples are derived from NXS galaxy catalogues (§ 4.3). In Sections 5.3, 5.4 and 5.5, we outline three approaches that were developed to determine redshifts for NXS clusters. The third approach, known as XCSRedSeq, performs the best and in Section 5.6, we present the results of its application to 473 XCS cluster candidates with NXS photometry.

5.1 A Review of Red Sequence Cluster Finders

Several recent, ongoing and planned cluster surveys rely upon the red sequence relation to detect galaxy clusters within large optical data sets. The main premise of these surveys is the assumption that all clusters are made up of a centrally concentrated clump of homogeneous, old, passively evolving elliptical galaxies. These galaxies, having formed

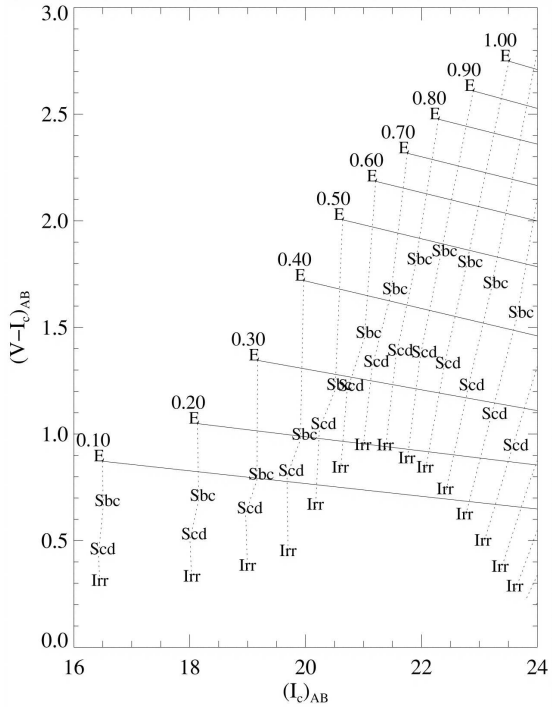

Figure 5.1 The model tracks in colour for synthetic elliptical and spiral galaxy spectra at a given redshift and magnitude, based on the Bruzual and Charlot population synthesis models. [Figure credit: Gladders and Yee (2000b)]

their stars at a similar time from the same constituent gas, should have similar metallicities and stellar ages and thus exhibit a tight relation in colour-magnitude space -the cluster red sequence relation (see §1.6.1).

The red sequence technique is effective at detecting clusters because elliptical galaxies are the reddest galaxies at a given redshift, and all lower redshifts (as demonstrated by the model galaxy tracks in Figure 5.1). Therefore, by detecting clusters via their red sequence galaxies, all foreground field contamination should be removed, as these galaxies are bluer than the red sequence relation. Furthermore, by targetting/adding increased weight to the brightest galaxies in a red sequence relation, contamination from background field galaxies should be minimised. This is because even if there are blue field galaxies at higher redshifts falling onto the red sequence relation by chance, they'll be at fainter magnitudes and won't be weighted as highly.

We review below the methodology of two optical cluster surveys. The NXS red sequence redshift finder is a hybrid of these two methods.

The RCS Method

To detect galaxy clusters, the Red-sequence Cluster Survey (RCS; Gladders and Yee (2004); Yee et al. (2007)) search for overdensities in colour and surface density using the algorithm of Gladders and Yee (2000b) (GY00, hereafter). They construct a theoretical map of red sequence colour relations with redshift (shown in Figure 5.2) based on the measured slope of the Coma cluster. This low redshift relation is then evolved with redshift using the Bruzual and Charlot population synthesis models (Bruzual and Charlot (2003); BC03, hereafter). A set of colour slices is then defined between red sequence relations. The width of each colour slice is determined by the the intrinsic width of the red sequence and the photometric scatter of the data. These slices are then overlapped as to not undersample clusters lying on the borders between slices.

Each colour slice is then populated with galaxies from the survey data. The subset of galaxies belonging to each slice is selected based on the probability that the galaxy's colour belongs to that slice (determined by intergrating the assumed Gaussian colour error distribution). In addition, each galaxy is weighted by its magnitude. This is because the faint end of each colour slice suffers from an increased amount of (background) field contamination compared to bright end whose (foreground) field contamination is greatly reduced by the red sequence colour cuts. A spatial filter (based on an NFW profile) is then applied to the subset of galaxies within each colour slice to create a density map. The density maps from each colour slice are then stacked together to create a volume. Galaxy clusters are then identified as peaks within this volume, with a redshift assigned by the location of the peak along the colour axis. In this manner, the RCS detected $\sim$1000 clusters, over 90 $\deg^2$ to a redshift of $z\sim1$.

In NXS, we have used the GY00 technique of constructing of a theoretic map of red sequence colour relations with redshift. This map is then used to determine the redshift of a cluster via the colour of its red sequence relation.

The MaxBCG Method

The MaxBCG algorithm (Koester et al., 2007b) differs from RCS in that it constructs a likelihood model (Equation 5.1) for a galaxy cluster with which to filter the data. The matched filter is a two-part likelihood model, comprising of a BCG likelihood model, L_{BCG}, and an E/S0-ridgeline (red sequence) likelihood, L_R, which they adopt from the Palomar Distant Cluster Survey (PDCS; Postman et al. (1996)). For each galaxy in SDSS, MaxBCG evaluate the likelihood of that galaxy being a BCG, surrounded by red sequence

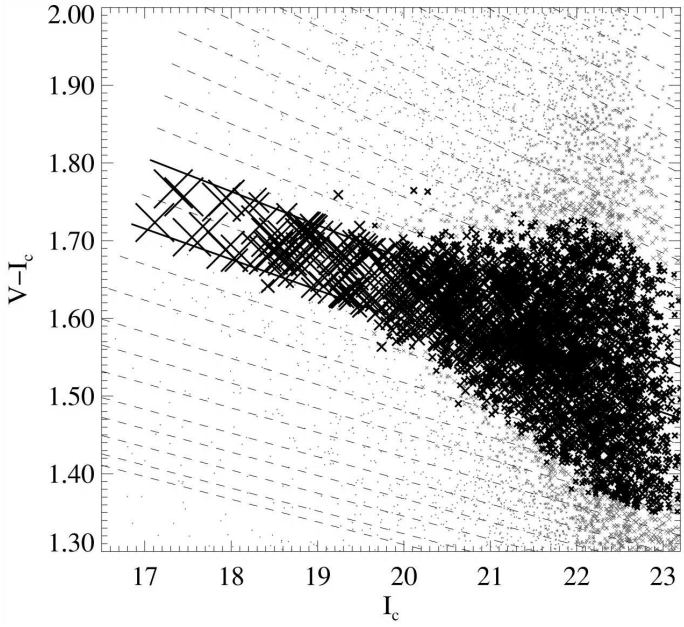

Figure 5.2 Figure illustrating the theoretrical map of red sequence relations and the determined population of galaxies drawn from RCS data belonging to a particular slice weighted by their colour error.

galaxies within a radius of $3h^{-1}$Mpc (as calculated from the redshift of the assumed BCG).

$$L_{tot}^{max}(z) = L_R(z_{max})L_{BCG}(z_{max}), \tag{5.1}$$

where L_{tot} is the total likelihood, L_R is the E/S0 ridgeline likelihood model (Equation 5.2), and L_{BCG} the BCG likelihood model, all of which are evaluated as a function of redshift, z. The redshift at which total likelihood model (L_{tot}^{max}) is maximized, given by z_{max}, determines the most likely redshift (z) of the cluster.

MaxBCG constructs the E/SO ridgeline likelihood as follows (Equation 5.2) which is maximised on red sequence colour, c, and richness, Λ_N,

$$L_R \sim \frac{1}{\sigma} exp \frac{[b(c) + \Lambda_N M(r,c) - D(r,c)]^2}{\sigma^2}, \tag{5.2}$$

here $b(c)$ is the background distribution, $M(r,c)$ the assumed red-sequence cluster model, Λ_N a measure of the cluster richness, $D(r,c)$ is the total number of galaxies within their aperture ($3h^{-1}$Mpc), and σ is the uncertainty in the colour of the E-S0 ridgeline width.

The set of galaxies for which Equation 5.1 is maximised then defines a cluster detection. As a consequence, a measure of the cluster redshift (z_{max}) and number of red sequence galaxies (Λ_N) within $3h^{-1}$Mpc, is obtained. In this manner, MaxBCG detected 13,823 clusters between $0.1<z<0.3$, covering 7500 deg^2 (Koester et al., 2007a).

In NXS (algorithm 3 only), we have made use of constructing an E/S0 ridgeline likelihood to determine the most likely red sequence colour and richness of NXS clusters. However, one particular drawback of the MaxBCG method is that the ridgeline likelihood, L_R shown in Equation 5.2, only holds if the assumption of the Gaussian nature of galaxy number counts within their aperture is correct (Postman et al., 1996). MaxBCG argue that despite sampling from a Poissonian distribution (as the background dominates within an aperture), a Gaussian approximation can be made, as their number counts are large enough to be considered as a Poisson distribution with a high mean. In NXS we have mitigated this problem by using the CASH statistic (§5.5) to maximise the ridgeline likelihood. We also note that as the NXS has imaging data in 2 bands, we are unable to use colour cuts to select LRGs and therefore do not construct an L_{BCG} likelihood.

5.2 The NXS Red Sequence Method

It is important to note that the NXS is not a cluster finder; it is a redshift follow-up program. Therefore, as positional information has already been provided by the XCS, the NXS method of measuring redshifts using the red sequence technique is more simplified than those used by the RCS and MaxBCG. As a consequence, we adopt two main assumptions: first, that clusters are composed of a core population of passively evolving elliptical galaxies that form a tight red sequence relation; and second, that these galaxies are coincident with a hot X-ray emitting intracluster medium. We therefore construct a redshift algorithm that seeks out overdensities of galaxies near the cluster X-ray centroid, with similar colours above that of the background field distribution. In the subsections below we describe three important elements of the NXS redshift algorithm: *i*) the generation of cluster and *ii*) field galaxy samples and *iii* an empricial red sequence model. The subsequent sections explain how these elements are combined to derive photometric redshift estimates.

5.2.1 NXS Cluster Galaxy Sample

Cluster and field (§5.2.2) galaxy samples were created from galaxy catalogs stored in a `MySQL` [2] database obtained from each NXS-field (§4.3). These galaxy catalogues contain positional information, r and z band dereddened magnitudes and r-z band colours.

To measure a cluster redshift we wish to utilize the elliptical galaxies located in the cluster core that populate the red sequence. This cluster core is also coincident with the

[2] `MySQL` is a commonly used open source relational database management system.

hot X-ray emitting cluster gas detected by XCS. Thus, for each XCS cluster candidate in turn, galaxies are extracted from NXS galaxy catalogues within a search radius of twice the X-ray source extent (as measured by the XCS source detection pipeline XAPA described in Section §2.3) from the central RA and Dec of the cluster candidate. This results in a galaxy sample comprising of both potential cluster galaxies and background/foreground field galaxies.

5.2.2 NXS Field Galaxy Sample

There are two approaches one can take when defining a field sample. Either a universal field sample can be created from regions known to contain no clusters, which is then used to test the cluster signal of each cluster candidate. Or, a local field sample can be used containing galaxies close to each cluster candidate beyond a radius assumed to be attributed to the cluster. Both have their advantages and disadvantages. A universal field sample may increase the chances of filaments local to the cluster candidate being detected as a cluster signal. Whereas, using a local field sample may suppress a real cluster signal by making the red sequence less identifiable and/or providing artificially low richness estimates. For NXS we choose to employ a local field sample created from each NXS image rather than from the entire survey. This was preferable as the seeing and depth conditions of each NXS field varied. Hence, using a field and cluster galaxy from the image allows a more accurate comparison of their colour distributions. Furthermore, by using a field sample local to each candidate we should hopefully minimise the detections of local large scale structure as false cluster detections.

In order to produce a field galaxy sample for each NXS-field, all galaxies within that field were retrieved from the NXS galaxy catalogue database (§4.3). An initial field area is then calculated from the minimum and maximum RA and Dec of galaxies within that field (assuming a common flat sensitivity across each image). The area associated with each XCS cluster candidate, within the field, is then masked out using a fixed masking radius of 0.15 deg. A fixed radius is used as we have no prior knowledge of the clusters' redshifts and temperatures and hence angular extent on the sky. A radius of 0.15 deg is sufficient at all reasonable redshifts detected by XCS, as it corresponds to the typical virial radius ($\sim$1.5Mpc) of a T_X=4keV, z=0.15 cluster. As shown in Figure 2.8, most clusters detected by XCS are below T_X=4keV. The remainder of the image is assumed to be separate from the cluster candidates and constitutes the background distribution. All galaxies falling within the masked regions are then removed from the retrieved field galaxy

sample, thus forming the final field galaxy sample. A final field area is then calculated by comparing the percentage of the field area masked out to the initial field area. This field sample, unique to each NXS image, is then applied to the cluster candidates within that NXS image.

5.2.3 The empirical red sequence model

The redshift algorithm derives photometric redshifts for the cluster candidates within each NXS-field, by comparing an observed cluster red sequence relation to an *empirical red sequence model* (Figure 5.3). In this manner, one NXS-field is analysed at a time, measuring photometric redshifts for each XCS cluster candidate within that field in turn.

An empirical red sequence model was derived using synthetic spectra created by BC03. The model is calibrated against an observed cluster red sequence relation at low redshift. Previous studies have shown that the cluster red-sequence is a mass-metallicity relation populated by elliptical galaxies that form at high redshift ($2<z_f<3$), go through a single short burst (1Gyr) of star formation and then evolve passively to the present day (see §1.6.1). Therefore, as input to the BC03 code, we choose a single burst, Salpeter IMF (Salpeter, 1955) model with a formation redshift of z_f=2.5. Using this model we evolve the synthetic spectra for two elliptical galaxies with different metallicities, one with a low metallicity of Z=0.004 and the other with a solar metallicity of Z=0.02. This outputs a list theoretical dereddened magnitudes and colours with redshift for each synthetic spectrum from the formation redshift of z=2.5 to z=0.05. We choose to output the theoretical magnitudes as though they are observed through the Sloan r- and z-band filters (the filters used by the NXS survey).

For our observed low redshift red sequence relation we use a composite red sequence relation of 73 clusters at redshift $z\sim$0.1 (Hilton, 2006) detected by the C4 survey (Miller et al., 2005). The theoretical colours of both synthetic spectra are then calibrated against this relation. From this, an empirical red sequence slope and zeropoint is derived at redshift z=0.1 which is then evolved with redshift using the output of the BC03 code. This provides a list of red sequence slopes and zeropoints with redshift (see Figure 5.3). This model is stored as an array of redshift, slope and zeropoints and called upon by each of the redshift algorithms described below.

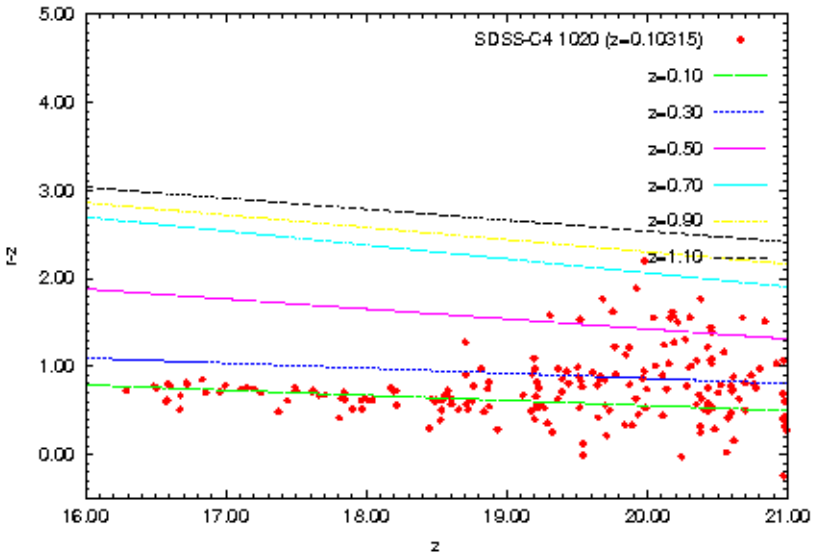

Figure 5.3 The NXS theoretical red sequence model based on an average z=0.10 red sequence relation of 74 C4 galaxy clusters (shown in red) that is evolved using a Bruzual and Charlot galaxy evolution model (see §5.2.3). [Figure credit: Matt Hilton.]

5.3 Algorithm 1: The Hilton Algorithm

The first attempt by NXS at assigning redshifts to XCS clusters was performed using a redshift algorithm written by Matt Hilton (hereafter the Hilton algorithm). This algorithm measures cluster photometric redshifts using a method similar to that used by GY00 (§5.1) and uses a statistical background subtraction similar to Pimbblet et al. (2002). A detailed explanation can be found in Hilton's thesis, however the main procedures are reviewed in this section.

Similar to GY00, a redshift estimate is made for each individual galaxy within an NXS image using the assumption that each galaxy is a red sequence galaxy, lying on its own colour-magnitude relation. Using the observed r-z band colour and z-band dereddened magnitude for that galaxy, we infer a red sequence colour-magnitude relation and zeropoint using the empirical red sequence model (§5.2.3). This zeropoint is then compared to the zeropoints of the two nearest empirical red sequence model relations and a linear interpolation between them determines the estimated redshift of the 'red sequence' galaxy.

Using the field (§5.2.2) and cluster (§5.2.1) galaxy samples obtained for each XCS cluster candidate, the probability of each galaxy being a cluster galaxy or a field galaxy is then evaluated using a statistical background subtraction similar to Pimbblet et al. (2002).

The potential cluster population is compared to a field galaxy population scaled to the cluster area (Equation 5.3).

$$P_{field} = \frac{N_{field}}{N_{cluster+field}} \frac{A_{cluster+field}}{A_{field}}, \tag{5.3}$$

where P_{field} is the probability of a given galaxy being a field galaxy; N_{field} is the number of galaxies in the field sample; $N_{cluster+field}$ is the number of galaxies in cluster candidate sample; A_{field} is the total area of the field sample; and $A_{cluster+field}$ is the assumed area of the cluster candidate (in this case taken to be twice the X-ray extent detected by XAPA; §2.3).

The cluster candidate galaxies and field galaxies are binned into Δz=0.05 red sequence strips on the colour magnitude diagram (based on the empirical red sequence model). Each galaxy in a bin is then weighted by its colour error, as more luminous galaxies are more likely to be cluster galaxies (see §1.6) which are in turn detected at brighter magnitudes and thus with smaller colour errors. A random number generator assigns a number between 0 and 1 to each bin and if the probability of a galaxy being a field galaxy in that bin is greater than this number then it is picked as a cluster galaxy. Furthermore, in this background subtraction method, the number of galaxies in the cluster and field distribution is binned and re-binned in such a way that the probability of finding a field galaxy in a field-and-cluster galaxy distribution is always positive. See Figure A1 of Pimbblet et al. (2002) for an illustration of this method. In this manner, 100 statistical subtractions of the field galaxy population is performed to select a sample of cluster galaxies.

If more than 5 cluster galaxies are chosen, a robust bi-weight fit[3] is performed on the chosen galaxy redshifts to determine a trial redshift for the cluster. If more than 5 of the 100 background subtractions yields a redshift estimate, then the mean redshift of those trials is chosen as the initial redshift estimate of the cluster and the standard deviation assigned as its error. This initial redshift is then used to calculate a new physical search radius of 500 kpc at the cluster redshift and the above procedure is repeated. Five iterations are then performed on the cluster area and the trial redshift with the highest significance is chosen as the final redshift of the cluster.

Furthermore, a quality flag is then assigned to each cluster detection. A real cluster detection would be assigned if there are three times the number of cluster+field galaxies compared to the field galaxy number within $\pm 3\sigma$ of the cluster redshift.

[3]A robust bi-weight fit assigns smaller weights to outliers (Beers et al., 1990)

5.3.1 Performance of Algorithm 1

As each NXS field generally contains multiple clusters, a small number of fields contain clusters with published redshifts in addition to the XCS candidates targetted for follow-up imaging. To assist the photometric calibration of NXS photometric redshifts, spectroscopic redshifts were also measured for a subsection of NXS clusters (§2.8.2). Thus, comparing photometric redshifts to measured spectroscopic redshifts we can estimate typical errors on the NXS photometric redshifts.

The Hilton algorithm was applied (by Matt Hilton) to data taken during the first NXS observing run performed at KPNO in 2005 (Run1, §3.4.1). Of the 91 XCS cluster candidates observed by the NXS in photometric conditions in Run1 (§3.4.1), 14 were assigned photometric redshifts and confirmed as clusters (using the quality flag mentioned in Section 5.3). The algorithm was also applied (by Matt Hilton) to public SDSS data for 672 XCS clusters candidates lying within the survey regions of SdssDR5[1]. Of the 672 cluster candidates, 126 were thus assigned photometric redshift estimates with a 'confirmed cluster' quality flag.

Figure 5.4 shows a comparison of cluster photometric redshifts obtained by the Hilton algorithm to spectroscopic LRG redshifts (§2.8.3) for XCS clusters using SdssDR5 data[2]. The comparison shows the algorithm to be generally successful in reproducing the spectroscopic redshift of XCS clusters, thus validating the method of using red-sequence galaxies to measure cluster redshifts. However, as can be seen in Figure 5.4, the performance of the code shows a systematic bias, against high redshift clusters (z>0.4), towards lower redshift. In addition to this, there was also a failure to detect low richness clusters (suggested by the detection of 14 out of 91 NXS targets). This is a particular problem for XCS as the sensitivity of XMM-Newton has allowed XCS to detect a large number of low mass clusters and groups (§2.10).

5.4 Redshift Algorithm 2: A Modified Hilton Algorithm

In an effort to improve the performance of the Hilton algorithm, a modified version of the Hilton algorithm was devised by the author. Alterations were made with the aim of improving the detection of optically poor systems and also, redshift measurements for z>0.4 clusters. These alterations are listed below:

[1] SdssDR5 is the fifth SDSS public data release and was the latest SDSS data release at the time.

[2] Due to the small number of NXS clusters with both photometric and spectroscopic redshifts, a comparison was not made using the NXS sample

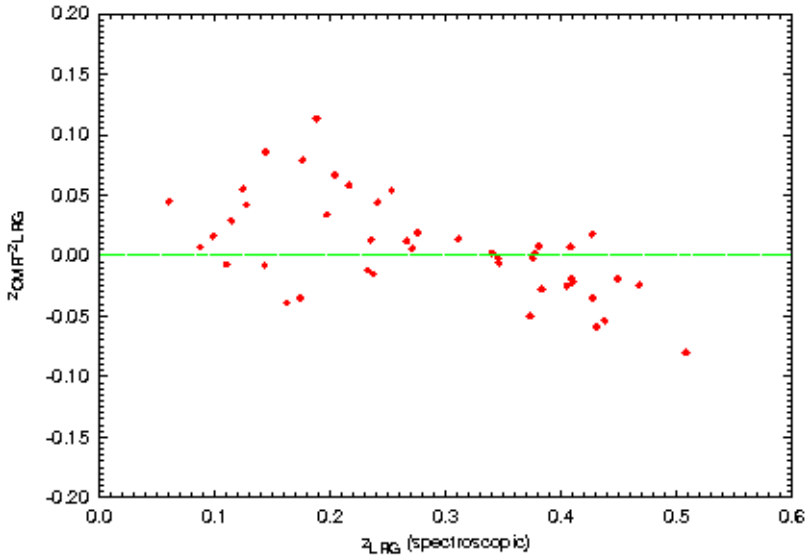

Figure 5.4 *Comparison between red sequence photometric redshifts and spectroscopic LRG redshifts as a function of z. Only clusters with contrast C>3σ above the background, as determined by the photometric redshift code, are considered.* [Figure and Caption credit: Matt Hilton]

Assignment of galaxy photo-z's In the Hilton algorithm, a photometric red sequence redshift was assigned to each galaxy by comparing the theoretical zeropoints (*i.e.* where the slope crosses the $r-z$ axis at z=0.0) of the model red sequence relations either side of the zeropoint of the assumed red sequence relation for the galaxy. However, the model red sequence lines have non-parallel slopes. Red sequence relation lines cross over at high redshift, thus the two closest red sequence relation zeropoints may not be either side the zeropoint of the assumed galaxy red sequence relation. Therefore, in the modified algorithm, when assigning a red sequence redshift for a galaxy, we assign a redshift by comparing the colours of the model red sequence relations at the magnitude of the galaxy (*i.e.* we do not extrapolate to zero).

Bin width The Hilton algorithm had a slight technical problem when performing the statistical background subtraction. In the case of an unphysical probability (*i.e.* where the probability of finding a field galaxy in a cluster+field galaxy distribution is less than 1, thus implying no galaxies (cluster or field) are located within a particular redshift bin), redshift bins were widened to include adjacent bins and increase the number of constituent galaxies, however it did not keep track of the overall normalisation. Rather

than renormalising all bins, as shown in Figure A1 of Pimbblet et al. (2002), all other bins were kept the same. Thus adjacent redshift bins were counted twice allowing more cluster galaxies to be selected than physically available. Therefore in the modified algorithm, we altered the code to renormalise all redshift bins in the instance of an unphysical probability. However, on occasion this resulted in a renormalised bin being created that spanned the entire redshift range covered by the empirical red sequence model. Therefore a cap was set (Δz=0.2) on the maximum width of a bin.

Restriction on minimum cluster galaxies Additionally, in the Hilton algorithm, only trials with more than 5 background subtracted cluster galaxies were considered. However a Monte-Carlo simulation should consider all realisations to provide an accurate assessment of the data. Therefore, in the modified algorithm, the minimum requirement was reduced to two galaxies. If fewer than 5 galaxies were chosen then a simple median redshift of these galaxies was chosen as the redshift of the cluster, rather than a bi-weight fit. If fewer than two galaxies were chosen, a warning was printed out by the code.

5.4.1 Performance of Algorithm 2

The modified algorithm was run on 101 XCS cluster candidates observed by NXS in photometric conditions from Run1-3[3] (§3.4). Although the modified algorithm was designed to improve the performance of the Hilton algorithm, when comparing cluster photometric to spectroscopic redshifts, systematic biases still remained. High redshift clusters were still biased toward lower redshifts. In addition, a significant number of low richness clusters (obvious to the eye) failed to be detected. The most probable cause of this is using a statistical background subtraction method combined with a bi-weight fit. Both high redshift and low mass clusters suffer from the same problem, in that they will present themselves as a small number of galaxies within the field distribution. Clusters observed in poor weather conditions will also suffer from a decreased number of detected galaxies due to the higher detection limit. When performing the statistical background subtraction, the bin sizes increase until there is a physical probability of a galaxy being a cluster galaxy. However when there is a weak cluster signal, the rebinning process allows an increasing number of field galaxies to be chosen as cluster galaxies. This is a particular problem around z=0.4 where the field distribution peaks (see, for example, the green line on Figure 5.5). As a consequence, when performing the bi-weight fit, all z>0.4 redshift clusters

[3]It was not tested on SDSS data

(unless sufficiently rich) have their photometric redshifts systematically underestimated by the algorithm.

In addition, when performing the statistical background subtraction, each galaxy was weighted by its colour error. This was done in order to increase the chances of selecting the more luminous and therefore more likely cluster galaxies in each redshift bin. Each redshift bin thus contained the sum of weights which were then used as a probability in the background subtraction. However, although this process increases the chances of detecting more luminous galaxies, it biases bins towards the high magnitude low redshift galaxies. Rather than using the colour errors to assign weights, it would be more useful to turn the colour errors into a probability of each galaxy belonging to a particular redshift slice as in GY00. This would also utilise the fact that galaxies are measured with a colour range rather than a fixed colour. Given the failure of a statistical background subtraction method to detect low cluster signals (§5.3.1 & §5.4.1), we decided to change the method by which NXS measures redshifts (see below).

5.5 Algorithm 3: XCSRedSeq

In our third algorithm, we decided not to select probable cluster galaxies using a statistical background subtraction as in Pimbblet et al. (2002). Instead, we choose to fit a cluster model to the observed overdensity, in colour space, above the background field distribution, similar to MaxBCG (§5.1). The colour at which the overdensity peaks thus corresponds to the inferred red sequence colour of the cluster and therefore the redshift of the cluster. Therefore, for each galaxy within our cluster sample we evaluate the likelihood of it belonging to a cluster at a given redshift and richness.

As the NXS observed in two bands, providing only one colour measurement, colour-colour cuts cannot be used to detect LRGs as used by MaxBCG. However, a ridgeline likelihood can still be measured. Similar to MaxBCG (§5.1) we derive a cluster red sequence model and then determine the likelihood that our model fits the actual data.

However, unlike MaxBCG, we choose not to make the assumption that our number counts approximates to a Gaussian distribution. We do not assume this, as 40% of the clusters detected by XCS are low mass clusters and groups (see Figure 2.8). In many cases the statistical background subtraction method (§5.3 & §5.4) failed for such systems due to the small number of cluster galaxies available above the background distribution. Therefore, as the number of detected cluster galaxies can often be small, we choose to maximise the ridgeline likelihood using the CASH statistic (Cash (1979), see Equation

5.4).

$$C = -2L = 2(E - \Sigma lnI), \tag{5.4}$$

where L is the loglikelihood, E is the observed distribution of the sampled data and I is the probability of each sampled data point matching the predicted distribution of a particular model (which is summed over all sampled galaxies).

The CASH statistic is used when counts are sampled from a Poissonian distribution. It works in the low-count regime where the more commonly used Chi-Squared statistic fails. It can be used regardless of the number of counts in each bin. However, the CASH statistic approximates to a chi-squared if there are more than 5 counts per bin. Therefore, it is widely used in X-ray astronomy where the number of detected X-ray source counts is often small above the background distribution.

Using the Cash statistic to maximise our ridgeline likelihood on redshift and richness, Equation 5.4 becomes:

$$-2L = 2(D(z) - \Sigma(ln(b(z) + \Lambda_N M(z)))), \tag{5.5}$$

or:

$$L = \Sigma(ln(b(z) + \Lambda_N M(z))) - D(z), \tag{5.6}$$

where L is the loglikelihood; $b(z)$ is the number density of the background distribution for each sampled galaxy; Λ_N is the cluster richness; $M(z)$ is the probability density of the red sequence cluster model (Equation 5.7) for each sampled galaxy; Σ refers to the summation, over all sampled galaxies, of the log of the combined number densities predicted from the background and cluster model distributions for each sampled galaxy; and $D(z)$ and is the total number of cluster galaxies sampled.

In Equation 5.6, Λ_N is a measure of cluster richness and corresponds to the total number of cluster galaxies, N_{gal}, above the background distribution (with no magnitude limit applied). Our background distribution, $b(z)$, is a simple histogram in colour space derived from all field galaxies within each NXS image, scaled to the assumed area of the cluster candidate (taken to be twice the X-ray extent detected by XAPA; §2.3). The data is represented by $D(z)$ and is the total number of (red-sequence) galaxies within our circular aperture (*i.e.* a radius of twice the X-ray extent defined by XAPA).

We use the same red sequence cluster model as MaxBCG which we take to be a simple Gaussian distribution in redshift given by Equation 5.7.

$$M(z) = \frac{1}{\sqrt{2\pi}\sigma} exp \frac{(x_{r-z} - \bar{x}(z)_{r-z})^2}{2\sigma^2}, \tag{5.7}$$

where: σ is the Gaussian width of the cluster model red sequence (Equation 5.8); x_{r-z} is the colour of a sampled galaxy; and $\bar{x}(z)_{r-z}$ is the colour of the red sequence at the cluster redshift being tested.

The width of the cluster red sequence model, σ, is given by the intrinsic width of the red sequence and the measurement error on each potential cluster galaxy being tested. The intrinsic width of the Red Sequence is assumed to be 0.05 magnitudes in colour (López-Cruz et al., 2004) and constant with redshift.

$$\sigma = \sqrt{\sigma^2_{r-z} + (\sigma^r_{r-z})^2}, \tag{5.8}$$

where σ^2_{r-z} is the measured uncertainty of a galaxy colour as estimated by SExtractor (§sec:NXS object catalog generation) and σ^r_{r-z} is the intrinsic width of the red sequence.

We assume Gaussian colour errors on each galaxy. Thus all galaxies within twice the X-ray extent can be viewed as a set of overlapping Gaussians in redshift space, whose width is given by their colour error. Therefore, each galaxy is weighted by its colour error, as those with smaller errors are more strongly peaked and contribute more strongly to the cluster overdensity at their colour. In addition, unlike the Hilton Algorithm (§5.3), this takes into account the fact that galaxies are measured with a colour range rather than a fixed colour.

We maximise our likelihood in colour space across a grid of redshift $0.1 \leq z \leq 1.2$ and richness $0 \leq \Lambda_N \leq 50$ in discrete redshift steps of $z=0.01$ and richness steps of $\Lambda_N=1$ respectively. For each cluster model being tested we convert its redshift to a red sequence colour using the same empirical red-sequence model described in §5.2.3. The colour of each potential cluster galaxy is then compared to this cluster red sequence colour at the magnitude of the galaxy. The background value for each galaxy being tested is given by the total number of galaxies between its colour error limits in the background distribution. The red sequence colour at which the likelihood is maximised is then converted back into a redshift using our empirical red-sequence model. The model cluster redshift and richness at which the likelihood is maximised are the assumed properties of the cluster candidate. In this way our method is a hybrid of MaxBCG and RCS, as we have used the MaxBCG of determining the most likely red sequence colour and richness of NXS clusters, and because we have used an empirical red sequence model similar to RCS to convert this likely red sequence colour into a redshift estimate.

In addition, for each cluster, all galaxies falling within $\pm 3\sigma$ of the chosen cluster red sequence colour are assumed to be red sequence galaxies. If no overdensity is detected, the likelihood isn't maximised and yields a redshift of z=0.1 with a richness of 0 galaxies. However, it is important to note that the cluster richness measured here is not a representation of the true cluster richness. This is because it is measured from within the X-ray extent defined by XAPA. This extent depends on exposure time rather than an a property intrinsic to the cluster (see §7.3 for a more physical determination of N_{gal}).

5.5.1 XCSRedSeq Errors

Although we have used the Cash Statistic to maximise our likelihood equation, we have used the Chi-Statistic to estimate the statistical error on each likelihood fit. These errors are solely used as an indication. The typical NXS photometric redshift has been determined via a comparison with measured spectroscopic redshifts (§5.6.1). In all cases we assign our cluster candidates the properties of the strongest likelihood peak. However there are occasions where the second most likely peak is the real representation of the data. We consider these cases to be catastrophic failures. Catastrophic failures are taken into account either when comparing estimated photometric redshifts to measured spectroscopic redshifts (§5.6.1) or through the use of NXS ClusterZoo, as these cases are easy to identify by eye (§7.6.1).

5.5.2 XCSRedSeq Flags

Edge Flag As NXS is not a contiguous survey, problems arise when attempting to identify cluster candidates on the edges of NXS fields. In these cases the candidate cluster extent may fall off the edge of the field, thus providing less accurate redshift estimates and inaccurate richness estimates. In this instance an 'edge flag' is assigned to the cluster.

***r*-band drop out Flag** Furthermore, only if a galaxy is detected in both bands, thus producing a colour estimate, can it be used by the redshift algorithm. At high redshift, faint cluster galaxies may be detected in the z band but fail to be detected in the r-band. In order to help identify possible high redshift candidates for future spectroscopic follow-up, a flag was assigned to each cluster stating the number of r-band drop outs (*i.e.* the number of galaxies solely detected in the z-band). This flag is then used to assist in the identification of high redshift clusters.

NXS Cluster flag It is important to note that a cluster detection does not necessarily signify that a real galaxy cluster exists within the data. In order to objectively quantify whether a real cluster exists we use two measures; the cluster richness as given by Λ_N, and a Kolmogorov-Smirnov (KS) test to determine whether the cluster distribution is significantly different from the background distribution. The results of NXS ClusterZoo (§7.6.1) on the entire NXS cluster sample will in future be used to define a richness and KS probability cut. These cuts will then be implemented on the NXS cluster results to create a statistical sample.

5.5.3 XCSRedSeq plots

A number of plots are generated by XCSRedSeq when measuring the redshift and richness of each cluster. Examples of such plots are shown in Figures 5.5 to 5.8 for the cluster XMMXCS J022457.8-034851.1, detected in NXS with a XCSRedSeq measured redshift of z=0.60 (literature redshift z=0.61) and N_{gal}=50. For example, a histrogram distribution in XCSRedSeq-colour redshift is generated, presenting the number density of cluster galaxies selected from within twice the X-ray extent defined by XAPA, compared to the scaled field distribution (Figure 5.5) . A colour-magnitude diagram is generated, displaying the inferred red sequence relation measured by XCSRedSeq (Figure 5.6). In addition, two Figures are generated displaying the outputs of likelihood fit: a likelihood grid (Figure 5.7); and a contour plot of the likelihood grid (Figure 5.8). Examples of other XCS clusters and their corresponding XCSRedSeq plots are presented throughout the thesis.

5.6 NXS XCSRedSeq Results

The redshift algorithm was run on 473 cluster candidates contained within photometrically calibrated NXS data (§3.6). At the time of writing this thesis, NXS ClusterZoo had not been performed on the entire NXS cluster sample. Hence, for the purposses of this thesis we use a temporary richness cut of 5 galaxies to define a cluster detection. This richness cut produced an initial sample of 314 NXS cluster candidates with both redshift and richness estimates. However, we note that these clusters must be subjected to NXS ClusterZoo, and final richness and KS probability cuts implemented before a final sample can be published. The redshift and richness distributions of these 314 NXS cluster sample are shown in Figures 5.9 and 5.10 respectively. Some of these cluster redshifts were previously known to XCS, however 257 are new.

Figures 5.11 to 5.14 shows examples of 8 NXS clusters detected at various redshifts

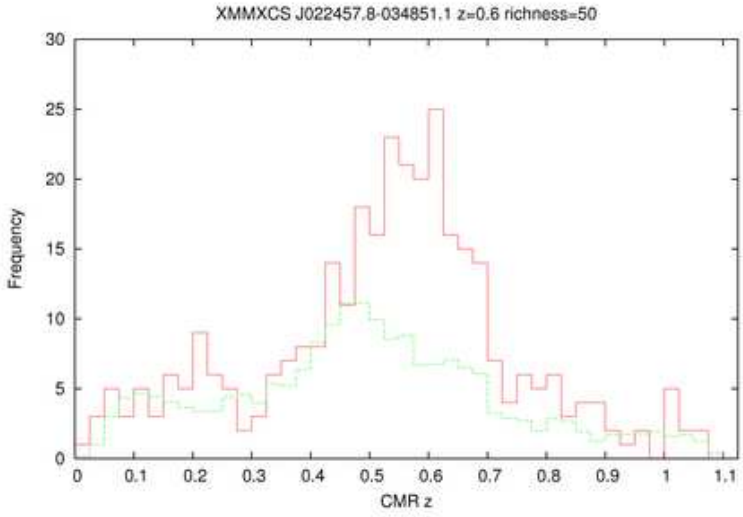

Figure 5.5 Redshift distribution (determined by the XCSRedSeq red sequence colour) of all galaxies within twice the X-ray extent of the XCS cluster candidate (in red) compared to the normalised field distribution (in green). Each galaxy is assumed to lie on a red sequence relation.

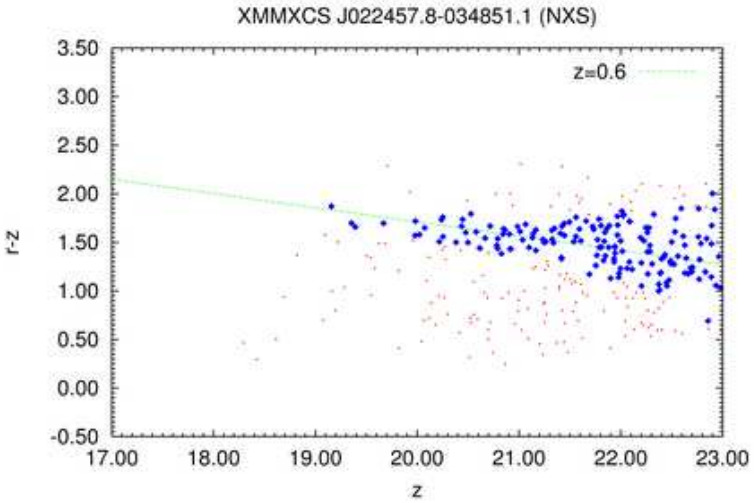

Figure 5.6 Colour-magnitude diagram displaying the inferred red sequence relation (in green) measured by XCSRedSeq. All galaxies within twice the XAPA X-ray extent are displayed. All galaxies within $\pm 2\sigma$ of the chosen red sequence colour are highlighted in blue.

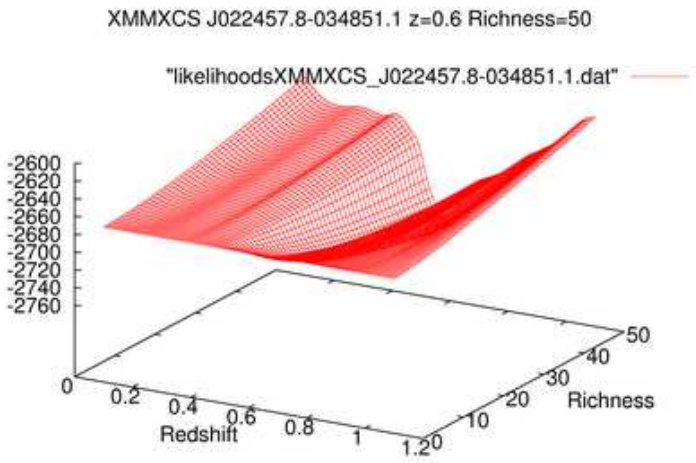

Figure 5.7 Grid of likelihood values calculated for each combination of redshift and richness for of all galaxies within twice the X-ray extent of the XCS cluster candidate.

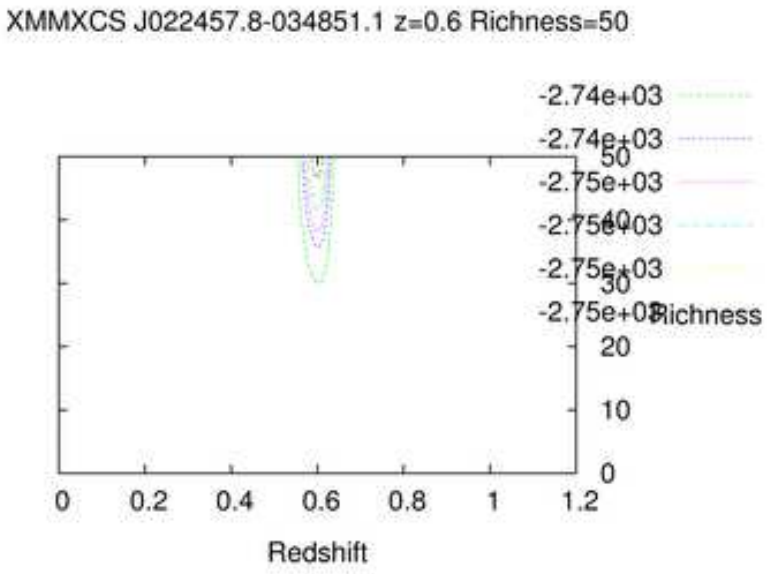

Figure 5.8 Contour plot derived from the values of the likelihood grid (Figure 5.7) for all galaxies within twice the X-ray extent of the XCS cluster candidate. Contours are 1σ, 90%, 2σ, 99%, 3σ, 99.999% errrors. (Errors assume a gaussian distribution and are only an indication of the actual errors).

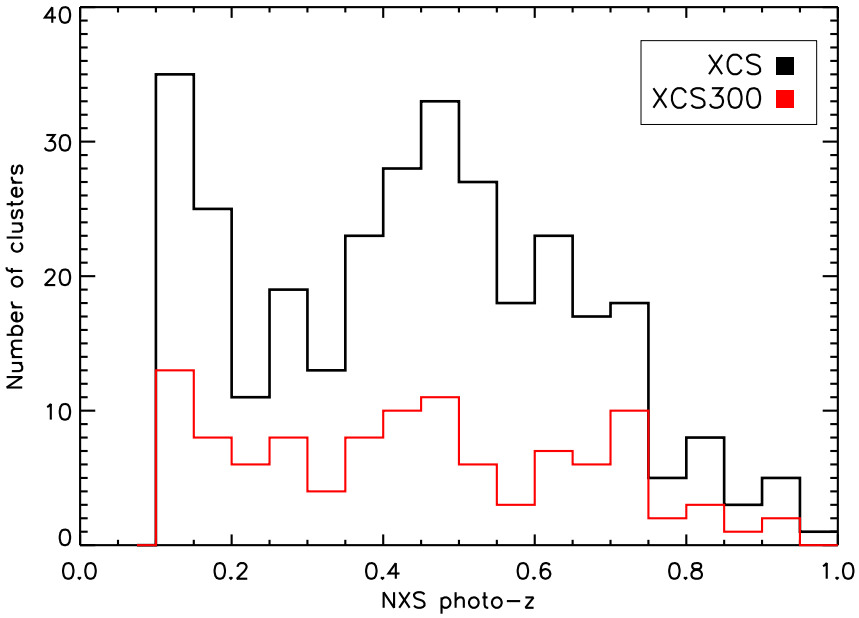

Figure 5.9 The redshift distribution of NXS clusters observed in photometrically calibrated data. The number of XCS candidates detected by XAPA with all and with greater than 300 soft counts are given by the black and red lines respectively.

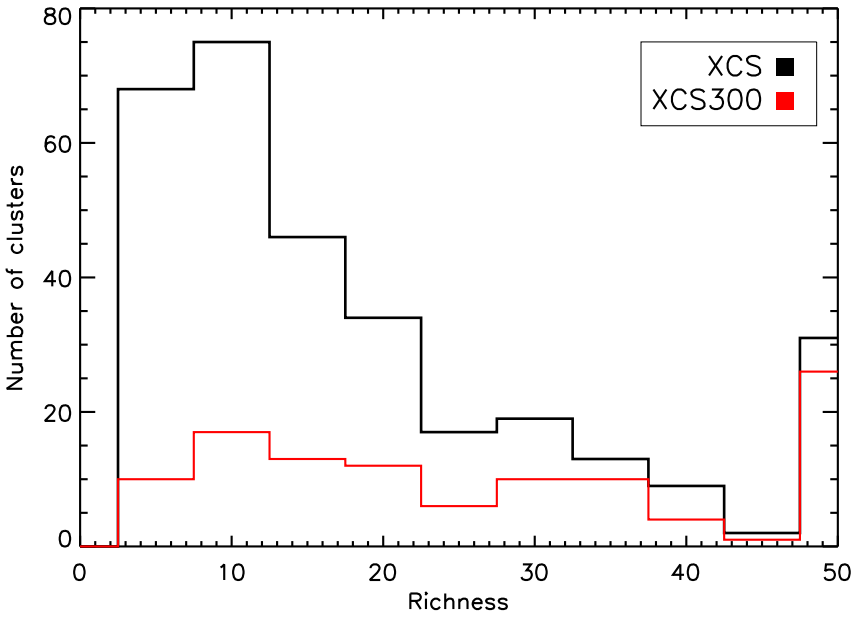

Figure 5.10 The richness distribution of NXS clusters observed in photometrically calibrated data. The number of XCS candidates detected by XAPA with all and with greater than 300 soft counts are given by the black and red lines respectively.

between $0.1<z<0.7$.

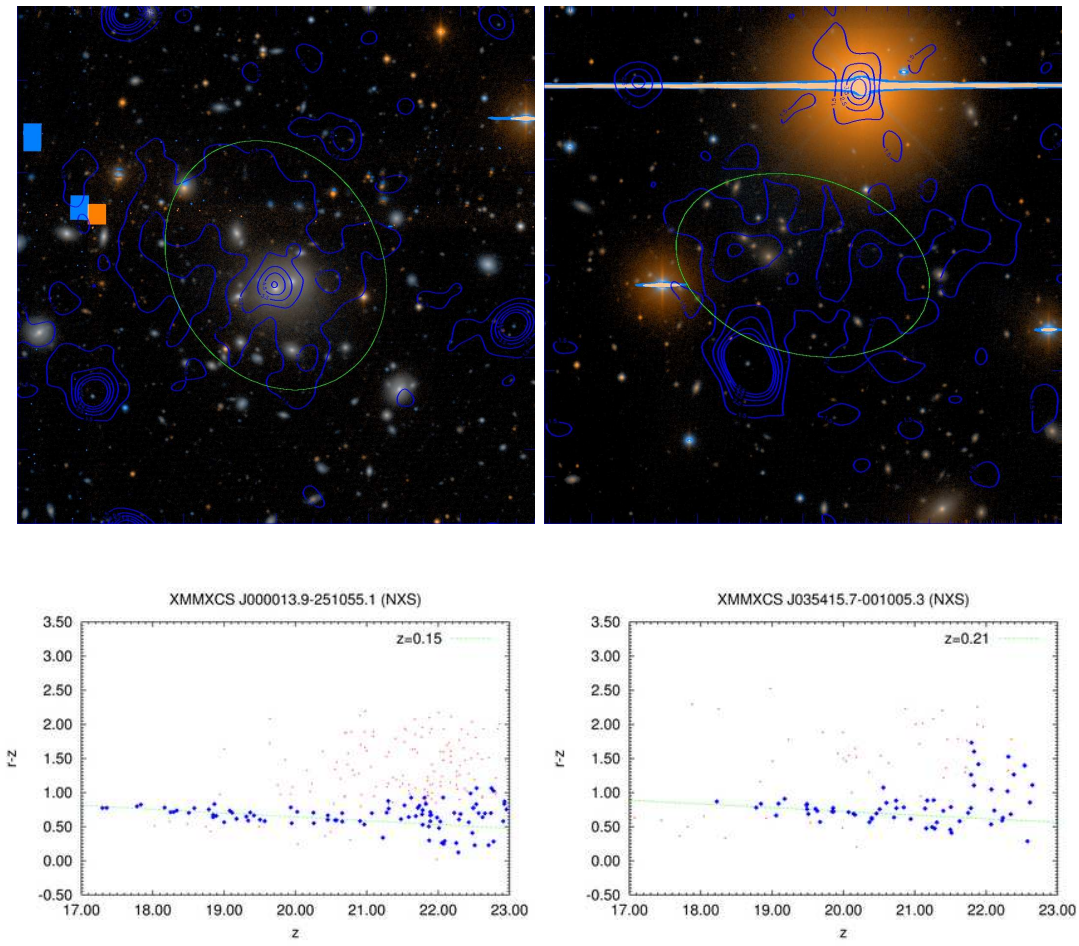

Figure 5.11 NXS colour-composite images and XCSRedSeq red sequence relations for XMMXCS J000014.0-251057.3 and XMMXCS J035415.7-001005.3 detected in NXS to be at redshifts $z = 0.15$ and $z = 0.21$ (XCS spectroscopic redshift z=0.21).

An additional (to the 473 mentioned above) 136 NXS clusters were observed in non-photometric conditions with data that could not be calibrated to gain a photometric zeropoint. Despite this, the redshift algorithm was run on this data with 'dummy' zeropoints to deduce the existence of possible clusters. These clusters could then be calibrated at a later date or targetted for spectroscopic follow-up. After implementing the temporary richness cut of 5 galaxies, this process yielded a further 85 clusters with richness and 'dummy' redshift estimates. Although these redshifts are meaningless, the detection of a red sequence relation signifies the presence of cluster. The measured richnesses can be used to prioritise targets for additional follow-up. Figure 5.15 shows the richness distribution of non-photometric clusters detected in NXS.

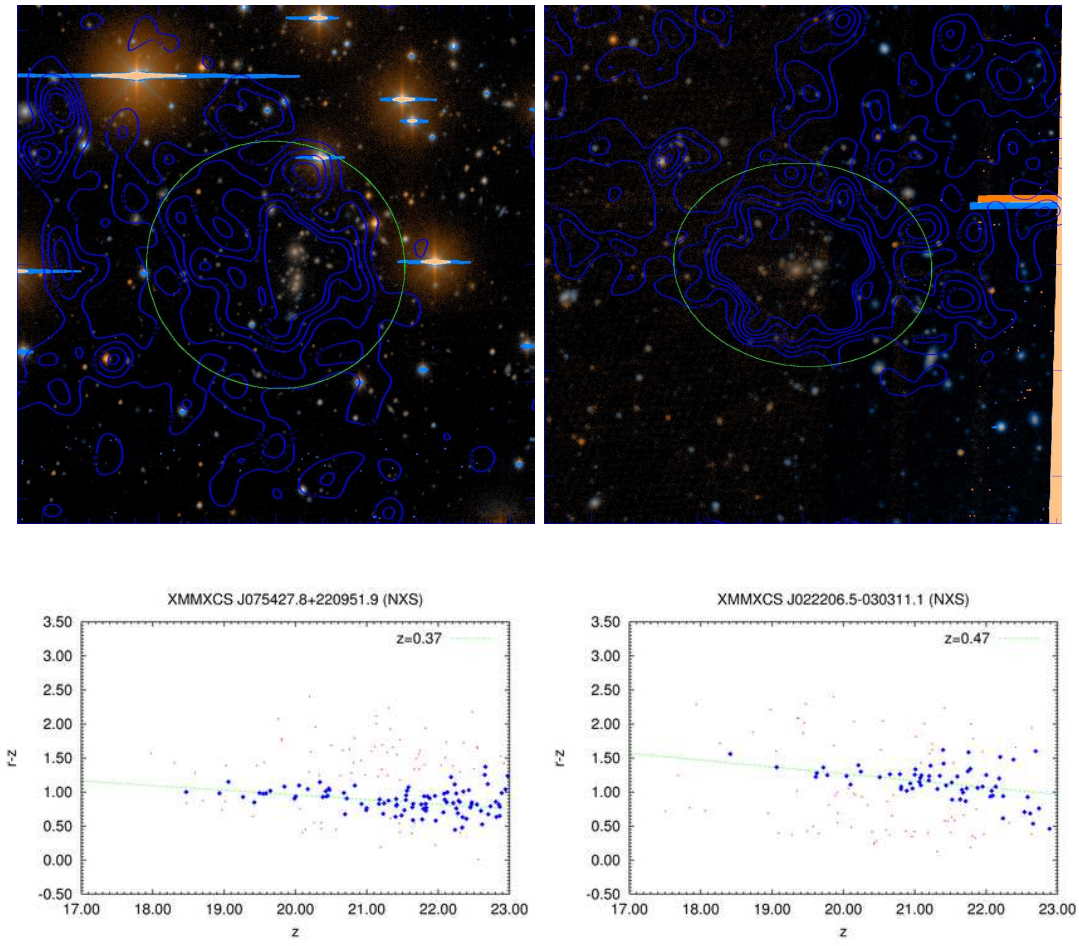

Figure 5.12 NXS colour composite images and XCSRedSeq red sequence relations for XMMXCS J075427.8+220951.9 and XMMXCS J022206.5-030311.1 detected in NXS to be at redshifts $z = 0.37$ and z=0.47 (literature redshift z=0.49) and respectively.

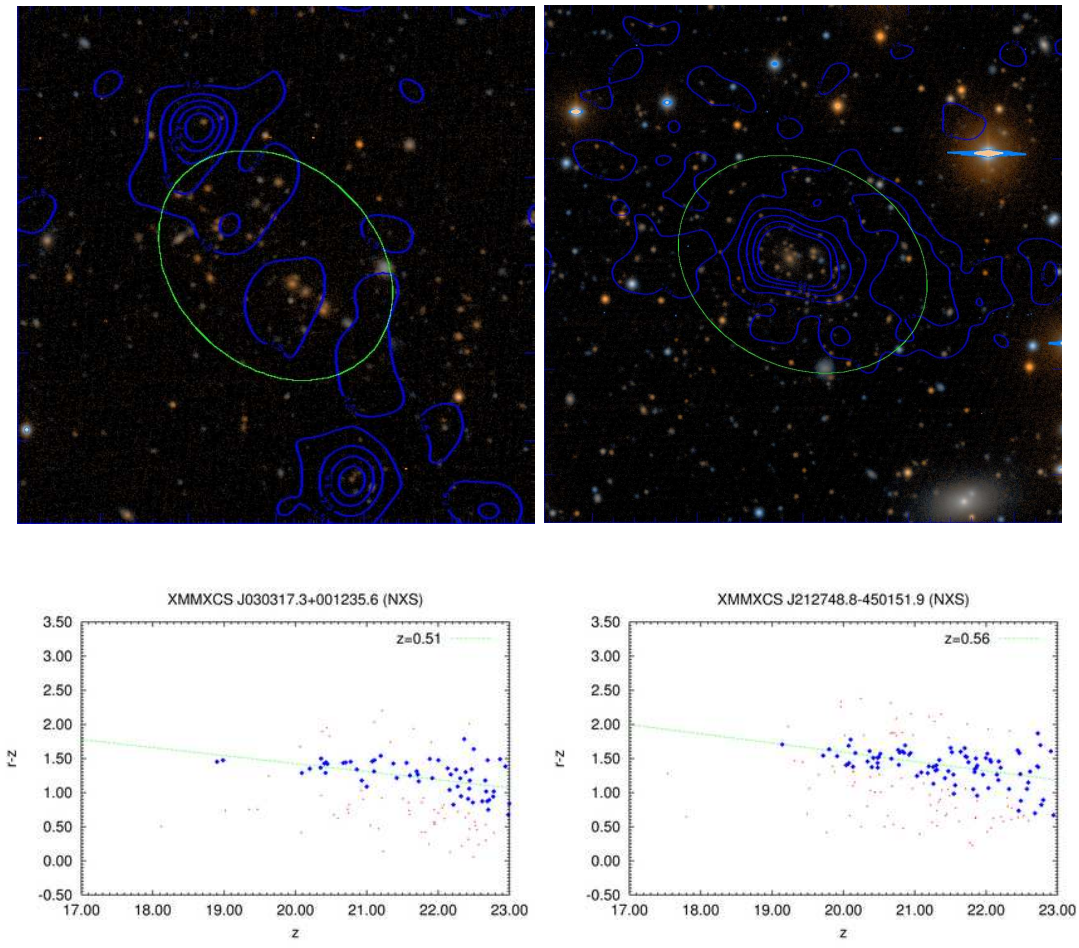

Figure 5.13 NXS colour composite images and XCSRedSeq red sequence relations for XMMXCS J030317.3+001235.6, XMMXCS J212748.8-450151.9 detected in NXS to be at redshifts $z = 0.51$ (XCS spectroscopic redshift z=0.59) and $z = 0.56$ respectively.

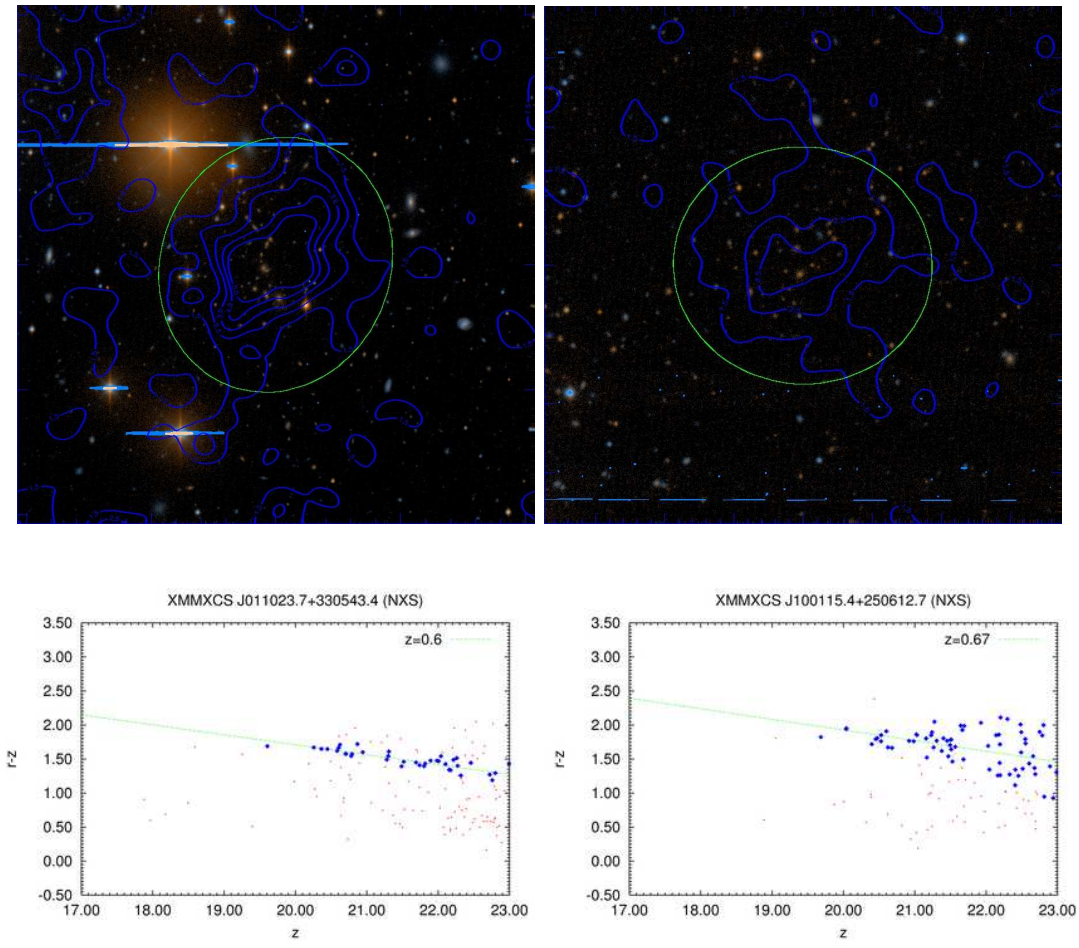

Figure 5.14 NXS colour composite images and XCSRedSeq red sequence relations for XMMXCS J011023.7+330543.4 and XMMXCS J100115.4+250612.7 detected in NXS to be at redshifts $z = 0.60$ and $z = 0.67$ respectively.

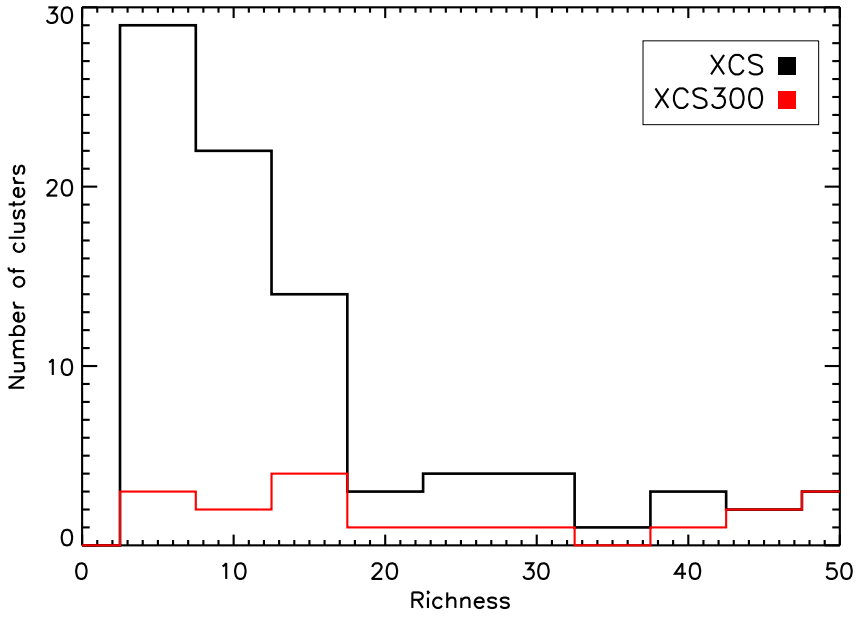

Figure 5.15 The richness distribution of NXS clusters in non-photometrically calibrated data. The number of XCS candidates detected by XAPA with all and with greater than 300 soft counts are given by the black and red lines respectively.

5.6.1 Validation XCSRedSeq

The performance of XCSRedSeq was tested using a subsample of 42 (out of 314) NXS clusters with spectroscopic redshifts (§2.8.1, §2.8.2 & §2.8.3). A comparison between the XCSRedSeq measured photometric redshift and corresponding spectroscopic redshift for these clusters is shown in Figure 5.16. The Figure shows a correlation between estimated XCSRedSeq photometric redshifts and measured spectroscopic redshifts for NXS clusters, thus demonstrating the ability of XCSRedSeq to measure accurate cluster photometric redshifts. However, as can be seen in the Figure, there is an apparent failure of XCSRedSeq to measure accurate redshifts for both low redshift (z<0.1) and high redshift (z>1.0) clusters. Low redshift clusters are overestimated, whereas high redshift clusters are underestimated to lower redshifts. The cause of catastrophic failures at redshifts z<0.1, may be due to using bands optimised to provide more accurate redshifts at z=0.4, as well as using a relatively small background field sample.

High redshift systems are largely beyond the survey depths of NXS. As such, the majority of galaxies contained with them are undetectable within one or both of the r- and z-band images obtained from NXS. As a consequence, a cluster galaxy sample has been entirely selected from, or is swamped by, a population of field galaxies. In these cases,

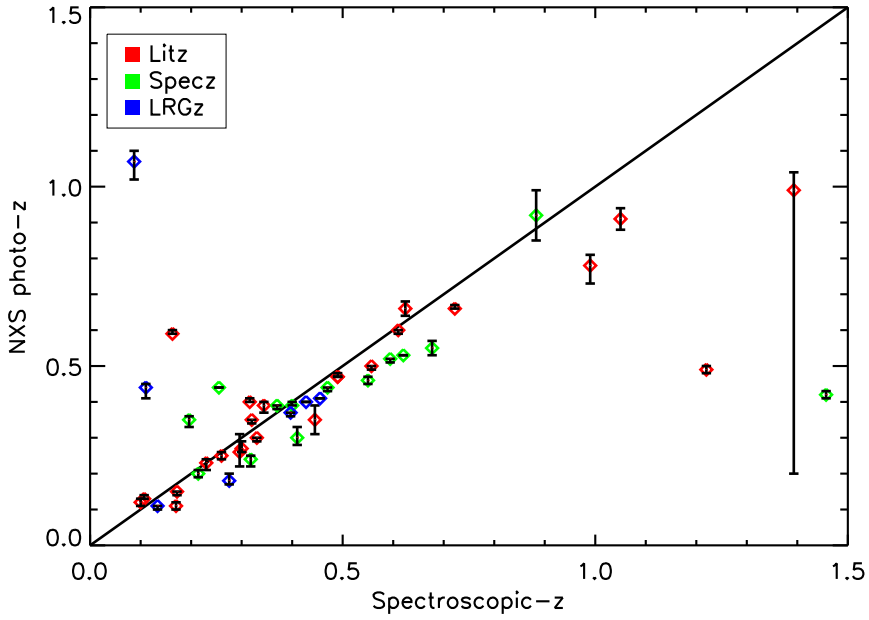

Figure 5.16 Comparison of the NXS XCSRedSeq redshifts with published/XCS spectroscopic redshifts

catastrophic failures are identifiable by eye, made evident by the lack of identifiable cluster galaxies within the location of the X-ray extent. According to this limited sample of NXS clusters used in the comparison plot, we expect a catastrophic failure rate of ∼15%.

When utilising the entire redshift range probed by XCS ($0.05<z<1.5$), the photometric error of XCSRedSeq is estimated to be $\Delta z=0.16$[4]. However, as both the low redshift and high redshift cluster catastrophic failures are easy to identify by eye, we assume that these cases will be filtered out by the use of NXS ClusterZoo. Hence, when limiting this sample to those NXS clusters with spectroscopic redshifts between $0.15<z<1.0$, the estimated error on XCSRedSeq photometric redshifts is reduced to $\Delta z=0.07$[4]. Therfore, post NXS ClusterZoo we expect to produce a sample of NXS clusters with measured redshifts between ($0.15<z<1$) to within $\Delta z=0.07$.

5.7 Discussion

In this chapter we have discussed the development of XCSRedSeq, the adopted method of assigning photometric redshifts to XCS clusters, using the red sequence technique.

[4]Based on a 3σ clipped mean

Performance of XCSRedSeq

The XCSRedSeq algorithm was applied to data taken by the NXS under photometric conditions to provide 257 new redshift estimates for XCS cluster candidates between $0.1 \leq z \leq 1$. The subsample of NXS clusters with additional spectroscopic redshift information has suggested that XCSRedSeq provides redshift estimates good to within an estimated $\Delta z = 0.07$. This suggests that XCSRedSeq performs reasonably well for the requirements of XCS, and that the NXS data reduction and photometric calibration is adequate. Furthermore, XCSRedSeq has enabled the detection of high redshift (≥ 0.7) clusters. For example, the NXS cluster XMMXCS J012400.0+035110.8, measured to be at $z=0.92$ (with an XCS spectroscopic redshift of $z_{spec}=0.884$), and XMMXCS J022404.2-041327.9, measured to be at $z=0.91$ (with a literature redshift of $z_{lit}=1.05$). However, we also note that the typical NXS photometric error is larger than that estimated for the RCS ($\Delta z = 0.05$). In addition, this redshift error is increased at $z \leq 0.1$ and $z \geq 1$ (beyond the depth accessible to the NXS). Furthermore, we expect a catastrophic failure rate of $\sim$15%, although it is hoped that these cases will be flagged through the use of NXS ClusterZoo.

Although the XCSRedSeq method of using a maximum likelihood to fit a cluster model to the data should help reduce the systematics produced by a statistical background subtraction, the problems of detecting high redshift systems, encountered by the statistical background subtraction (§5.4.1), still remain. In this way NXS has not performed to expectations, especially with regard to clusters at $z \geq 1$. For example, XCSRedSeq has failed to measure an accurate redshift for XMMXCS J083025.5+524128.2, assigned an XCSRedSeq redshift of $z=0.7$ (with a literature redshift of $z_{lit}=0.99$). For high redshift clusters, the detection of small numbers of galaxies at the bright end of the luminosity function, is compounded by increasing colour errors, and decreasing distance between red sequence relations. Together these factors suppress the overall cluster signal above that of the background field distribution. These factors still remain despite the choice of filter sets enhancing a high redshift overdensity compared to the field distribution. Therefore, as a general rule, clusters measured with NXS photometric redshifts of $z > 0.7$ cannot be considered to have secure redshifts. However, the value of such systems (§1.6.2) means that they are worthy of spectroscopic follow-up (§2.8.2), and the availability of an NXS photometric redshift estimates enhances the success of submitted proposals and observations.

Potential improvements to XCSRedSeq

We could have placed additional constraints on our cluster model when measuring cluster photometric redshifts in order to further suppress background fluctuations that could falsely be attributed to a cluster detection. For example, to further reduce projection effects, RCS also include assumptions about a cluster luminosity function. They argue that high luminosity galaxies are more likely to be cluster galaxies than field galaxies. Therefore they impose a luminosity function at each redshift slice and weight each galaxy by its magnitude. This reduces the chances of a field galaxy wrongly being assigned to a cluster. We choose not to assume a cluster luminosity function as the presence of an extended X-ray emission coincident with a red-sequence relation was deemed sufficient to assume a cluster detection. However, this step could be added to improve the performance of XCSRedSeq.

Additionally, optical cluster finders such as RCS and MaxBCG impose a spatial filter when detecting clusters. They assume a NFW cluster profile with which they smooth their galaxy maps. However, since XCS had already provided positional information in the form of X-ray centroid, this step was deemed unnecessary. A spatial filter would add weight to the central galaxies located near the X-ray centroid, but as these galaxies are generally brighter, with smaller associated photometric magnitude errors, these galaxies should already be favored by our likelihood fit. However, the X-ray extent is a relatively unphysical representation of the cluster size and an iterative approach based on an $L_X - T_X$ relation, similar to that adopted for the literature redshift search, might be appropriate.

In terms of the data used, we could have excluded galaxies with colour errors larger than the intrinsic width of the red sequence. However our measurement errors are such that this would potentially have suppressed most of the signal at high redshift and limit our detections to only the most richest clusters at high redshift. We intend to examine this further to discover if a colour error limit is justified.

Planned Work

A number of analyses need to be carried out to finalise the work of the NXS, before the results of NXS XCSRedSeq redshifts can be published. For example, it is important to note that the redshifts produced by XCSRedSeq are based on an empirical red sequence model. This model is based on a specific set of strong underlying assumptions inputted into the BC03 code. But as it is based on assumptions, rather than intrinsic evidence, it is possible to tweak this model by calibrating model red sequence relations to the observed

red sequence colours of spectroscopically confirmed NXS clusters. Indeed, this would be particularly desirable to enhance the accuracy of photometric redshifts for clusters detected at high redshifts, due to the suggested systematic bias towards lower redshifts beyond z=0.5 (Figure 5.16). Thus, we plan to calibrate the empirical red sequence model using the red sequence relations of spectroscopically confirmed clusters. It is hoped that XCS will acquire more spectroscopic redshifts of NXS clusters to aid this process, particularly at $z \geq 0.5$.

Importantly, each NXS detected cluster must be subjected to NXS ClusterZoo. Although this process is largely subjective, it can be used to determine assumed thresholds of XCSRedSeq obtained values, upon which a statistical sample can be created. In addition, this step is required if the production of the NXS cluster sample is to mimic that used to estimate a typical photometric redshift error.

The NXS, imaged 131 cluster candidates in non-photometric conditions. This non-photometric sample includes genuine clusters. As such, XCS plans to eyeball the optical imaging of non-photometric clusters to determine the presence of a genuine cluster, along with information on detected red sequence relations to determine identified clusters within the list. These clusters, particularly those with more than 300 soft counts, or high redshift candidates will be targetted for follow-up, via additional imaging or spectroscopy.

Furthermore, the results of XCSRedSeq and optical imaging have highlighted a number of promising high redshift clusters ($z \geq 0.7$) within the NXS photometric data. It is hoped that these high redshift candidates will be targetted for spectroscopy at Keck or Gemini. This clusters will then aid high redshift galaxy evolution studies.

Comment on NXS Strategy

The NXS solely used 2 band survey data, under the assumption that accurate redshifts could be measured using one colour via the detection of the red sequence, as advocated by GY00. By adding a 3rd band to the NXS survey, colour-cuts could have been implemented to improve the accuracy of the redshift estimates. In this manner, colour cuts could have been used to identify potential LRGs within NXS clusters, similar to MaxBCG. Or, the presence of a red sequence relation could have been required in two colours would greatly minimise the background fluctuations further. Alternatively, two colours could have been used, whereby the red sequence of NXS clusters are detected in the bands most widely separated at its measured redshift, thus providing more accurate redshift estimates. However, using more than 2 bands would have reduced the total number of NXS-fields, and

thus XCS clusters, targetted for optical follow-up. Due to vast number of XCS candidates, priority was placed on number rather than accuracy. In addition, exposure times could have been increased in the z-band filter, thereby increasing the z-band depth to produce more accurate colour measurements for high redshift clusters. As a consequence these high redshift galaxies would span a smaller range in red sequence colour, limiting their use in the E/S0 likelihood fit to smaller redshift ranges, thereby improving the accuracy of the inferred cluster redshift.

An increased depth in the z-band NXS-fields would have produced more accurate colour measurements for high redshift clusters. In addition, increased depth in the r-band could have been obtained for cluster candidates with 'r-band drop outs'. However, high redshift systems (z>0.6) are rarely detected by XCS (Figure 2.9). As such, the survey times and depths acquired by NXS are adequate for the redshift range probed and purposes of XCS.

Chapter 6

The XCS: SDSS Red Sequence Redshifts

With high quality, multi-colour data covering a quarter of the sky, SDSS provides an excellent resource to verify and measure photometric and spectroscopic redshifts for a large number of XCS cluster candidates. The XCS footprint within SDSSDR7 is shown in Figure 2.5. In this chapter we describe how the XCSREDSEQ algorithm (§5.5) has been applied to SDSS data in regions that overlap with XCS.

In Section 6.1 we review SDSS. Sections 6.2 and 6.3 we describe the method applied to standard SDSS data (SDSSDR7), and STRIPE82 data respectively. The resulting redshifts obtained from SDSSDR7 and STRIPE82 are presented in Sections 6.4 and 6.5 and are discussed in Section 6.6.

6.1 SDSS Overview

The Sloan Digital Sky Survey (SDSS) has been in operation since 2000. It uses a dedicated 2.5m telescope at Apache Point Observatory, New Mexico, containing two instruments. The first instrument is a wide field imager made up of 30 2048x2048 CCDs with a pixel scale of $0.396''$ covering 1.5 deg on the sky. The imager operates in drift scan mode obtaining near simultaneous images in the Sloan r, i, u, g, z bands respectively. The second instrument is a pair of spectrographs able to measure 600 spectra in a single observation. A set of automated pipelines then reduce and calibrate the data.

Using these instruments, SDSS began The Sloan Legacy Survey in 2000. The Sloan Legacy Survey aimed to image and take spectroscopy for a quarter of the sky. The 8,400 deg^2 contiguous survey has produced imaging and spectra for 930,000 galaxies in

the northern Galactic cap to high latitude. In 2005, SDSS began two additional projects; The Sloan Extension for Galactic Understanding (SEGUE, Yanny et al. (2009)); and The Sloan Supernova Survey (Dilday et al., 2010). SEGUE aimed to take imaging and spectra at low galactic latitude to study the kinematics and evolution of stars within the Milky Way. The Sloan Supernova Survey operated during the autumn months, taking multiple observations of a 270 $\deg^2$ patch of sky designated Stripe82. These repeat observations enabled the detection of 500 spectroscopically confirmed Type Ia supernova and the measurement of their diminishing light curves to study the expansion of the universe. Stripe82 is a 120 deg long by 2.5 deg wide region that lies between -70 deg<RA<70 deg and -1.25 deg<Dec<1.25 deg in the Southern Galactic cap. A total of 122 observations of Stripe82 were obtained, covering the region between 20 to 40 times. When combined into a co-added image, the Stripe82 data reaches a depth $\sim$2 magnitudes fainter than the main SDSS survey.

Since 2000, SDSS has completed two phases of operation. SDSS-I operating between 2000 and 2005, and SDSS-II operating between 2005-2008. As of July 2008, SDSS began its third phase SDSS-III expected to end in 2014. So far SDSS have produced seven public data releases. The seventh data release (SdssDR7), made public in 2008, marks the final data release of SDSS-II. SdssDR7 covers a total imaging area of 11,663 $\deg^2$ containing five band photometry for 357 million objects, and contains spectra for 1.6 million objects covering an area of 9,380 $\deg^2$. The area covered by SdssDR7 and Stripe82 is shown in Figure 6.1.

The SdssDR7 imaging data, photometric and spectroscopic catalogs (including redshift information), are available for download via a public website[2]. All imaging data is taken under photometric conditions and has a median seeing value of $1.4''$ in the r -band (Hogg et al. (2001)). The mean 95% completeness limits (for point sources) of the imaging data have been measured to be 22.0, 22.2, 22.2, 21.3, 20.5 in the u, g, r, i, z bands respectively (Abazajian et al., 2004). All data is photometrically calibrated to within 3%, with astrometry good to within $0.1''$. Included in SdssDR7 is a public release of the Stripe82. SDSS Stripe82 imaging data and photometric catalogs are available via public download from a dedicated SDSS Stripe82 website[3].

[2]http://cas.sdss.org/astrodr7/en/

[3]http://cas.sdss.org/stripe82/en/

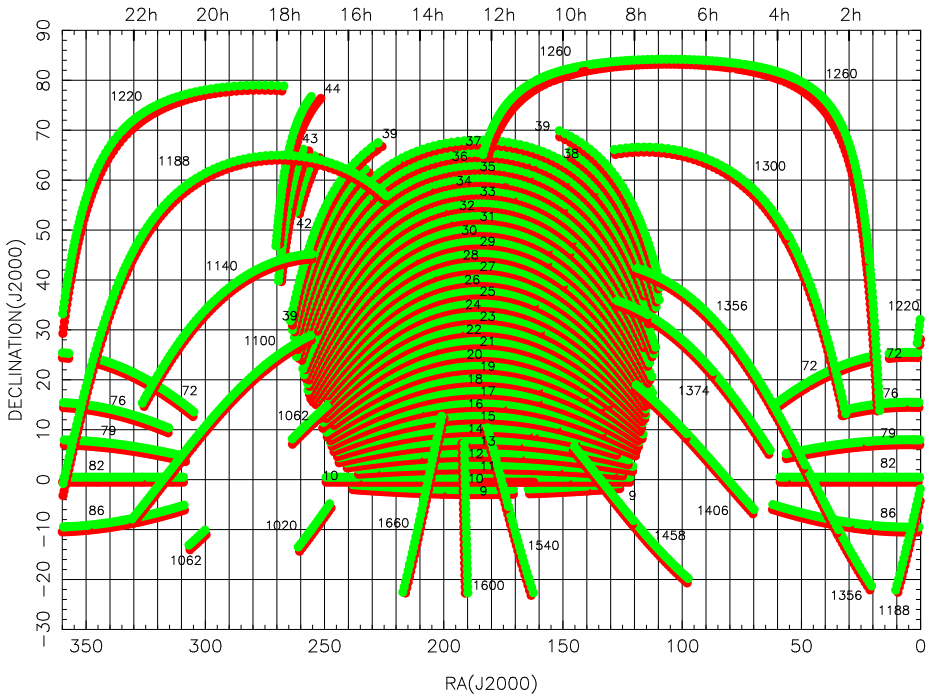

Figure 6.1 The SDSSDR7 Sloan Survey footprint in Equatorial coordinates with respect to its individual stripes. Each 2.5 deg stripe is made up of two strips. A single strip is observed in one continuous scan (or RUN). The red and green strips represent the first and second scans combined to create a stripe. Each stripe is allocated a number by SDSS and is labeled beside its corresponding stripe in the above figure. [Figure credit: www.sdss.org[1]]

6.2 Applying XCSRedSeq to SdssDR7 Data

We chose to confirm XCS cluster candidates in SDSS and measure their photometric redshifts via their red sequence relation. To do this we ran an adapted version of the NXS redshift algorithm (XCSRedSeq, described in §5.5) on all XCS cluster candidates within the survey regions of SdssDR7 to produce additional redshift and richness estimates.

SDSS provides publicly available calibrated, extinction corrected, r and z-band photometric catalogs, along with star-galaxy classifications for each detected object. Therefore we were able to retain the same SDSS r and z-band filter sets used by XCSRedSeq as well as the same empirical red-sequence model used to obtain photometric redshifts (described in §5.2.3). This enabled a consistent method of assigning redshifts between the two imaging surveys. However, unlike NXS, SDSS is a contiguous and homogeneous survey and we altered the redshift algorithm to exploit these attributes accordingly. First, the redshift of each cluster candidate falling within SDSS did not have to be measured on a image-by-image basis, thus removing cases of cluster candidates being truncated by the edge of an XCS/SDSS ObsID (see §5.5.2). Second, a field sample did not have to be derived from each individual image, as was the case for NXS (§5.2.2). Therefore we simplified the process and created a single external field sample (§6.2.2). This allowed us to create a much larger field sample covering a greater area, providing a more accurate representation of the true universal field distribution. As was done for NXS, all galaxies within twice the X-ray extent (as measured by XAPA §2.3) are allocated a red sequence colour according to the empirical red sequence model. This cluster distribution in colour is then compared to the background field distribution to determine a red sequence redshift and richness estimate for each cluster via a maximum likelihood fit (Equation 5.6).

6.2.1 Extracting SdssDR7 data for clusters

Using the publicly available SdssDR7 database, XCS cluster candidates in XCSDR3 detected with more than 300 counts (XCS300) and all XCS candidates for XCSDR1 were uploaded to the CasJobs website[4] to find matches to SDSS objects within 1.5 arcminutes of the XCS candidate coordinates to determine the presence of SDSS coverage. This task revealed a total of 731 XCSDR3 XCS300 and 278 XCSDR1 cluster candidates (overlaps between XCSDR1 and XCSDR3 are excluded from the XCSDR1 total) within the survey regions of SdssDR7. We note that the XCSDR2 sample was not included in this analysis.

We use the SDSS Galaxy Table from which to extract galaxies from the SDSS

[4] http://cas.sdss.org/astrodr7/en/

database. The GALAXY TABLE is a *view* of the PHOTOOBJ TABLE, which contains all primary objects targeted by SDSS and subsequently classified as galaxies. We chose to use the SDSS measurement 'MODELMAG'[5] to provide magnitudes and colours for each galaxy. We also apply the Galactic extinction values for each galaxy supplied in the SDSS database produced by using the Schlegel dust maps (Schlegel et al., 1998).

We specify that all galaxies must contain clean photometry flags in both the r and z-bands following the instructions given in the example provided by SDSS survey[6] (§4.2.3). In this manner, deredenned (§4.3) model r-band and z-band magnitudes were downloaded from the SDSS database and placed into a MYSQL database for all galaxies falling within twice the X-ray extent of each XCS cluster candidate.

6.2.2 Creation of SdssDR7 field sample

For an external field sample we need an average representation of a cluster free region of sky. To construct a field sample we chose random patches of the sky covered by SDSS in which both XCS cluster candidates and known clusters are masked out. To do this, we first determined which XCS ObsIDs in XCSDR3 had coverage in SDSSDR7. We did this by using the nearest neighbours search on the `CasJobs` website, to find SDSS objects within $5'$ of the ObsID center. For this, we used the XCS ObsIDs in XCSDR3, rather than XCSDR1 or XCSDR2, as this list contained the greatest number of XCS ObsIDs from which to choose a field sample. This process revealed a total of 441 XCSDR3 fields with at least partial coverage in SDSSDR7. An SDSSDR7 image was then downloaded for each XCS ObsID and eyeballed to *i*) ensure SDSS coverage was present across the entire XCS ObsID, and *ii*) to remove fields containing image defects and large objects bright enough to affect the photometry for the galaxies in the image. This process removed a further 51 fields. A random number generator then chose 50 fields from the remaining sample of 390 fields as the basis for a field sample. Deredenned, model r-band and z-band magnitudes were extracted from the SDSSDR7 GALAXY TABLE for all galaxies with clean photometry across each of the 50 fields, and placed into a local MYSQL database.

For each one of the randomly chosen 50 fields, all XCS cluster candidates therein were masked out. For this we use an estimated virial radius (§1.3) to predict the extent of each cluster across a field. Estimating a virial radius requires knowledge of the cluster

[5]The SDSS photometric pipeline measures galaxy magnitudes by fitting both an exponential galaxy profile model and a DeVaucouleurs galaxy profile model to the images of each galaxy. MODELMAG is the magnitude obtained from the better of these two fits.

[6]http://cas.sdss.org/astrodr7/en/help/docs/realquery.aspflags

temperature and the assumption that the cluster is in hydrostatic equilibrium. This produces an estimated proper size of the cluster which is then converted into an angular extent using the cluster redshift and angular diameter distance formula (§1.2).

As we do not know the XCS cluster redshift or temperature in advance, we assume a virial radius predicted for a cluster at a redshift of z=0.15 and a temperature of 4 keV. The greater the temperature, and lower the redshift, the larger the extent of the cluster viewed on the sky. As shown in Figure 2.8, the majority of clusters detected by XCS have a temperature below 4 keV (§2.8.1). By choosing a T=4 keV and z=0.15, we ensure the removal of any galaxies members of clusters over the redshift range covered by XCS. Any additional clusters or groups in the literature falling within each field were then identified with the NASA/IPAC Extragalactic Database (NED)[7] in the same manner as used to obtain literature redshifts (§2.8.1). The literature redshift was adopted for each cluster along with an assumed temperature of 4 keV to calculate a estimated virial radius for each cluster. This virial radius was then used to mask out any area associated with a cluster and remove potential cluster galaxies from the field sample. An example of an image mask is shown in Figure 6.2.

This process yielded a single combined field sample containing 41,950 galaxies covering a total area of 15.70 deg^2. This field sample was then called upon by XCSRedSeq and the total field area scaled to the area of each individual cluster candidate. The cluster photometric redshifts obtained from SdssDR7 data are presented in Section §6.4.

6.3 Applying XCSRedSeq to Stripe82 Data

As mentioned in §6.1, Stripe82 is a 270 deg^2 co-added stripe of SDSS reaching ∼2 magnitudes fainter than the main SdssDR7 survey.

Due to its increased depth, running the SDSS redshift algorithm on SDSS Stripe82 data enables the detection of higher redshift clusters than the standard SdssDR7 data release. It also allows XCS to probe further down the cluster luminosity function of lower redshift clusters. Stripe82 should therefore produce more reliable redshift estimates than SdssDR7 for the XCS cluster candidates that it covers. Figure 6.3 illustrates the increased depth of Stripe82 compared to SdssDR7 for XCS cluster candidates covering a range of redshifts. As seen in the Figure, many more galaxies are visible in the Stripe82 field including many more of the red galaxies one expects to see in high redshift clusters (particularly in the case of XMMXCS J020019.3+001932.3 shown in the last panel).

[7] http://nedwww.ipac.caltech.edu/

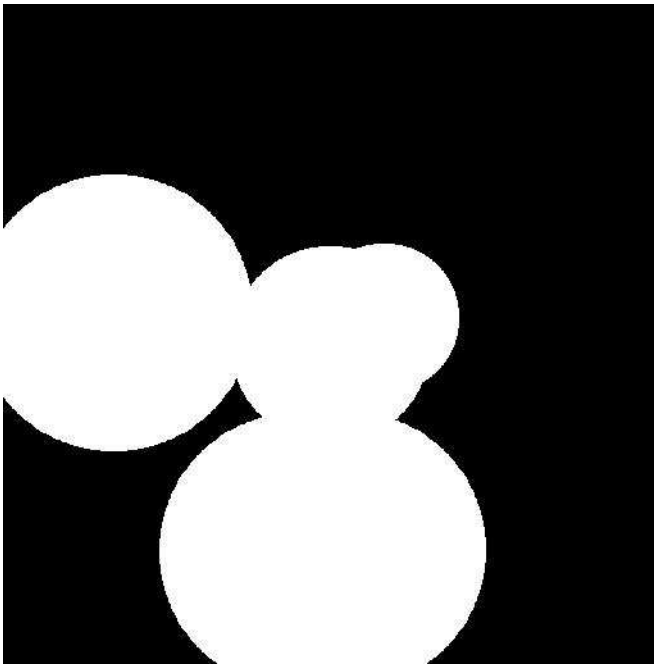

Figure 6.2 Image mask for XCSObsID XCS0504100601, one of the XCS pointings used to create a SDSSDR7 field sample. Masked areas (highlighted in white) represent the estimated coverage of cluster candidates on the sky in each pointing. In this example 1 white circle corresponds to an XCS cluster candidate (white circle on the far left) the remaining 3 correspond to clusters identified in the literature.

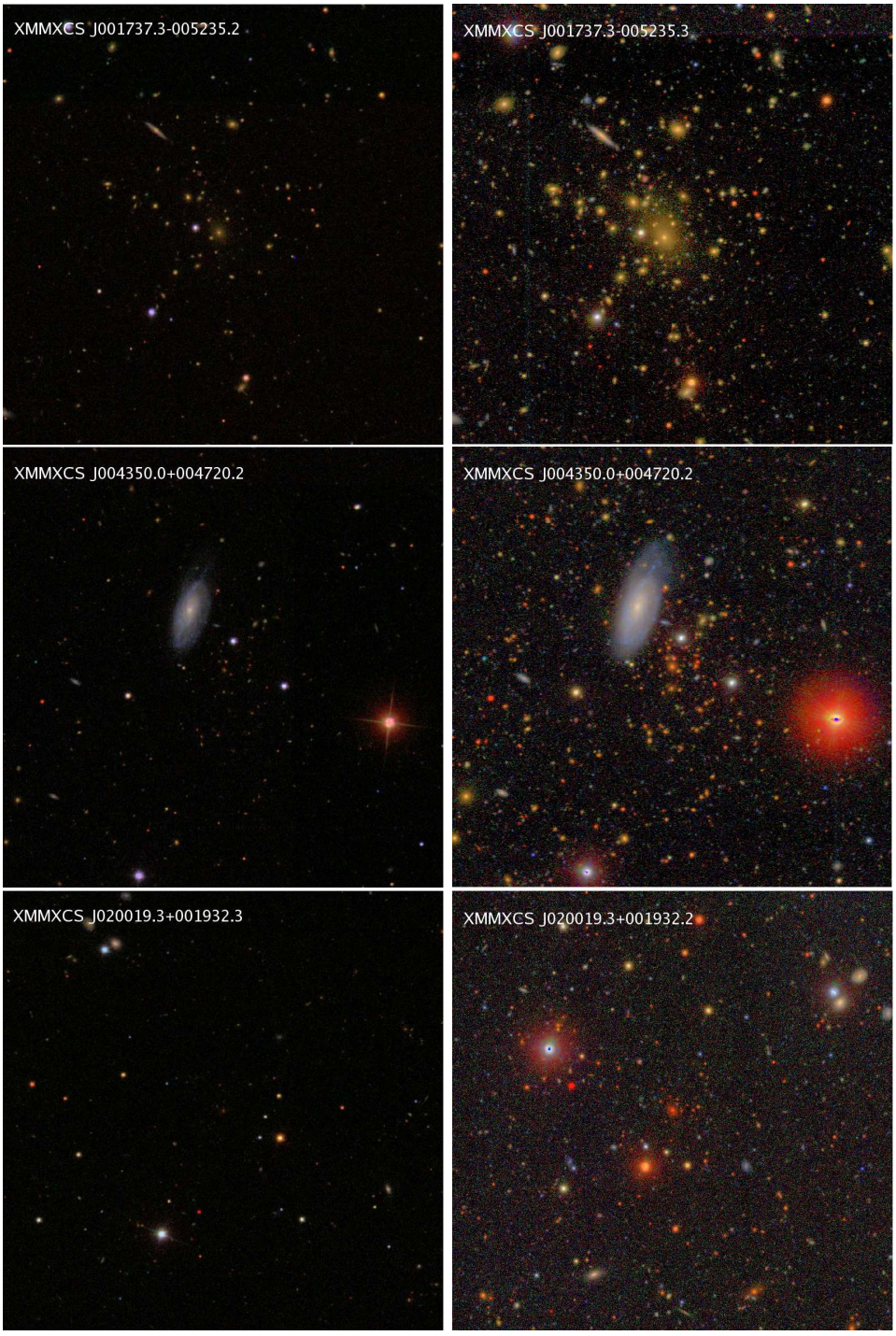

Figure 6.3 Side by side comparison of SDSSDR7 (left had side) and STRIPE82 (right hand side) imaging data for the three XCS cluster candidates XMMXCS J001737.3-005235.3 (z=0.21), XMMXCS J004350.0+004720.2 (z=0.46) and XMMXCS J020019.3+001932.3 (z=0.66). [Figure credit: Edd Edmondson, Portsmouth University, creation of STRIPE82 colour composite images.]

As an amalgamation of co-added SDSSDR7 data, the STRIPE82 database naturally contains photometric catalogs in the same SDSS filter sets. This enables us to use the SDSS redshift algorithm without any modifications.

A particular application of this work will be to the DES[8] because STRIPE82 reaches a comparable depth. The XCS-STRIPE82 sample will provide a calibration of optical to X-ray scaling relations at redshifts sampled to DES.

6.3.1 Extracting Stripe82 data for clusters

In an attempt to find potential high redshift clusters and maximise overlap with DES (Figure 2.5), we choose to apply no soft count restrictions and measure photometric cluster redshifts for all candidates in the internal XCS data releases (unlike when finding cluster redshifts in SDSSDR7).

Similar to the method applied to SDSSDR7 (§6.2.1), the positions of the XCS candidates for XCSDR1, XCSDR2 and XCSDR3 were uploaded to the `CasJob` website[9]. Using the `Neighbours` search function, all XCS candidates with SDSS STRIPE82 object matches within $1.5'$ of the central XCS coords were returned, thereby providing information on which XCS candidates had coverage within STRIPE82. This process returned 100 XCSDR3, 22 XCSDR1, 9 XCSDR2 cluster candidates (XCSDR1 & XCSDR2 overlaps with XCSDR3 have been removed) within the survey regions of SDSS STRIPE82.

For each XCS candidate, catalogues of galaxies within twice the X-ray extent (as defined by XAPA) from the central X-ray coordinates were extracted from the STRIPE82 database. Galaxies were extracted from the STRIPE82 GALAXY TABLE using standard `clean photometry` flags (§4.2.3) and specifying RUNS 106 and 206 containing the co-added data. Neglecting to specify these particular two co-added runs results in multiple object detections being returned from each individual STRIPE82 run prior to being co-added. These galaxy catalogs, containing dereddened r and z-band magnitudes and positional data, were then uploaded into a MYSQL database that was called upon by XCSREDSEQ.

6.3.2 Creation of Stripe82 field sample

When measuring redshift and richness values for XCS candidates in SDSS STRIPE82 we were able to exploit the fact that STRIPE82 is a contiguous and homogeneous survey. As such an external STRIPE82 field sample was utilised (similar to SDSSDR7) and redshifts and richness estimated analysed for each cluster in turn.

[8] https://www.darkenergysurvey.org/

[9] http://casjobs.sdss.org/CasJobs/

An external field sample specific to SDSS Stripe82 was constructed using the method described above for SdssDR7 (see §6.2.2). In short, 30 XCS ObsIDs were found to have at least partial coverage with SDSS Stripe82. Of these fields, 20 had complete coverage with Stripe82 that were deemed to be free from image defects, incomplete coverage, and large saturated stars that would erroneously affect the measured magnitudes of galaxies within a field. This clean sample of 20 XCS ObsIDs with Stripe82 overlap was then used as a field sample in which the estimated area covered by all published clusters and XCS candidates were masked out (using the method prescribed above). This resulted in a single combined Stripe82 field sample containing 228,034 galaxies, covering a total area of $5.40\,\mathrm{deg}^2$. This Stripe82 field sample (contained in a MySQL database) was then called upon whilst running the redshift algorithm on Stripe82 data which scales the total field area to the area of each cluster candidate. The cluster photometric redshifts obtained from Stripe82 data are presented in Section §6.5.

6.4 SdssDR7 XCSRedSeq redshift results

SDSS-XCSRedSeq was run on 731 XCSDR3 cluster candidates detected with more than 300 counts (XCS300) and 278 XCSDR1 cluster candidates (with no count restriction, overlaps between XCSDR1 and XCSDR3 have been removed). This produced redshift and richness estimates for 474 XCSDR3 XCS300 clusters and 222 XCSDR1 clusters respectively. All were detected with a minimum of five red sequence galaxies (see section 5.6 for this choice of threshold).

Figures 6.4 to 6.7 show examples of cluster candidates that have been detected with at least 5 red sequence galaxies at $z = 0.1$, $z = 0.24$, $z = 0.29$ and $z = 0.44$ respectively. Each Figure shows a false colour composite image of the cluster candidate, a second image highlighting the chosen red sequence galaxies, a histogram of galaxies within twice the X-ray extent compared to a field distribution (in XCSRedSeq red sequence colour, scaled to the area of the cluster candidate), a colour-magnitude relation showing the cluster red sequence relation, a maximum likelihood grid and a contour plot of the maximum likelihood (explained in §5.6).

Resulting redshift and richness histrograms of the XCS-SDSS sample for XCS300DR3 and XCSDR1 are shown in Figures 6.9 and 6.8.

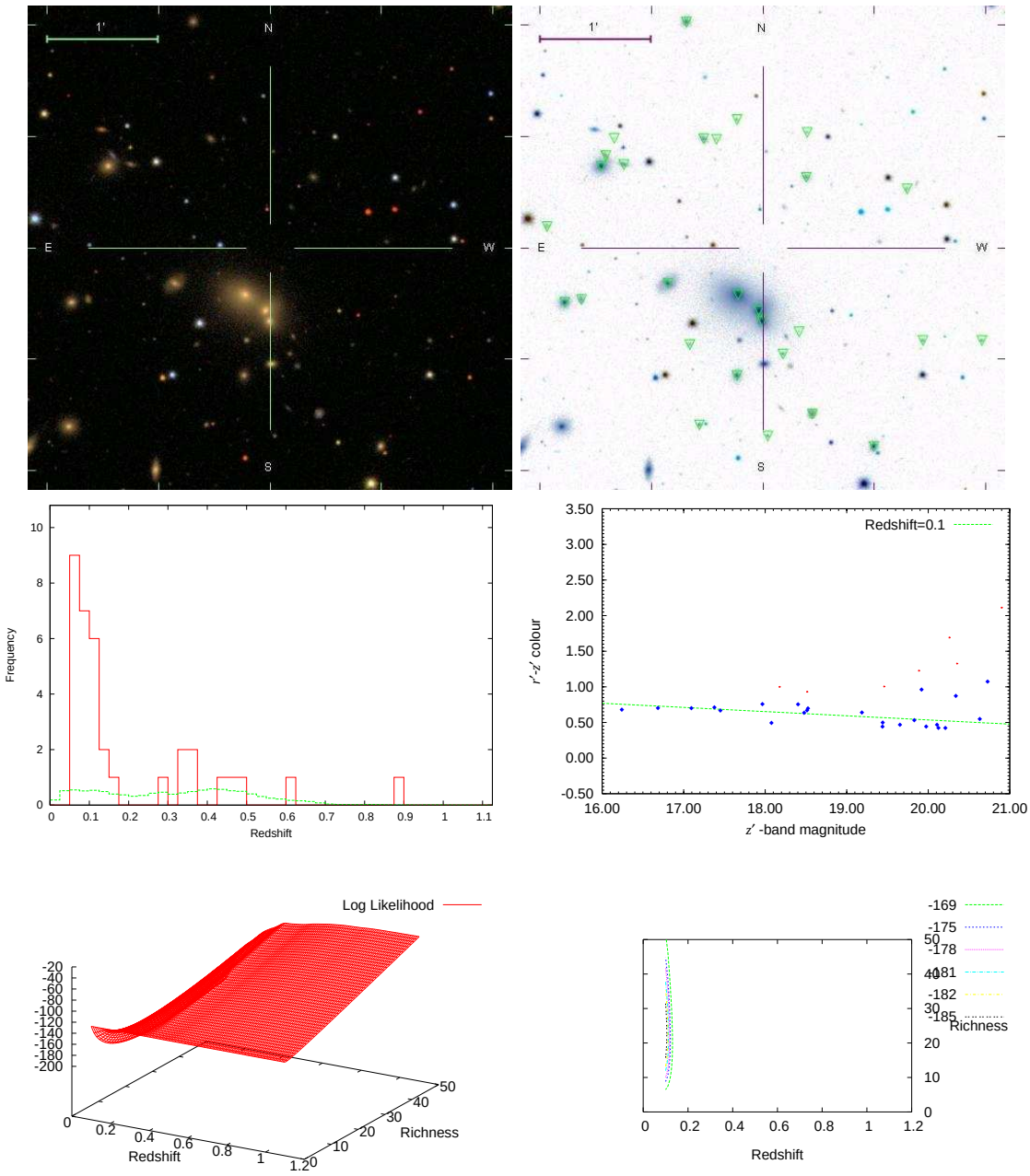

Figure 6.4 SDSSDR7 colour composite images and XCSREDSEQ results for XMMXCS J150824.8-001533.7 detected at $z = 0.1$ with 23 red sequence galaxies. SDSSDR7 colour composite image covering twice the X-ray extent of the cluster candidate measured by XCS (top left); the same, highlighting all galaxies within $\pm 2\sigma$ of the chosen red sequence colour (green triangles, top right); redshift distribution (middle left, see Figure 5.5 for caption); CMR diagram (middle right, see Figure 5.6 for caption); likelihood grid (bottom left, see Figure 5.7 for caption); and the likelihood contours (bottom right, see Figure 5.8 for caption).

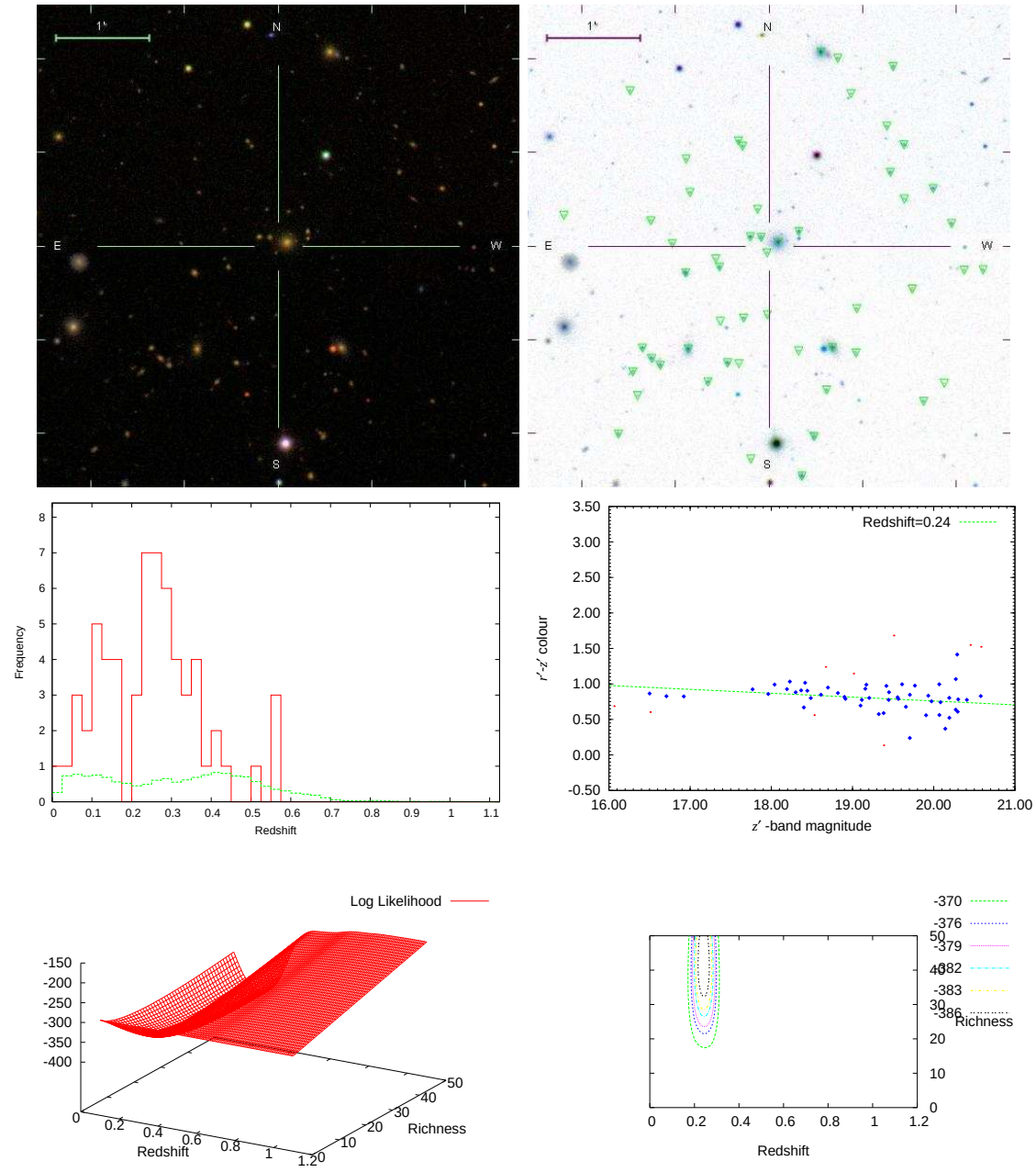

Figure 6.5 SDSSDR7 colour composite images and XCSREDSEQ results for XMMXCS J123144.3+413731.1 detected at $z = 0.24$ with 42 red sequence galaxies. See 6.4 for caption.

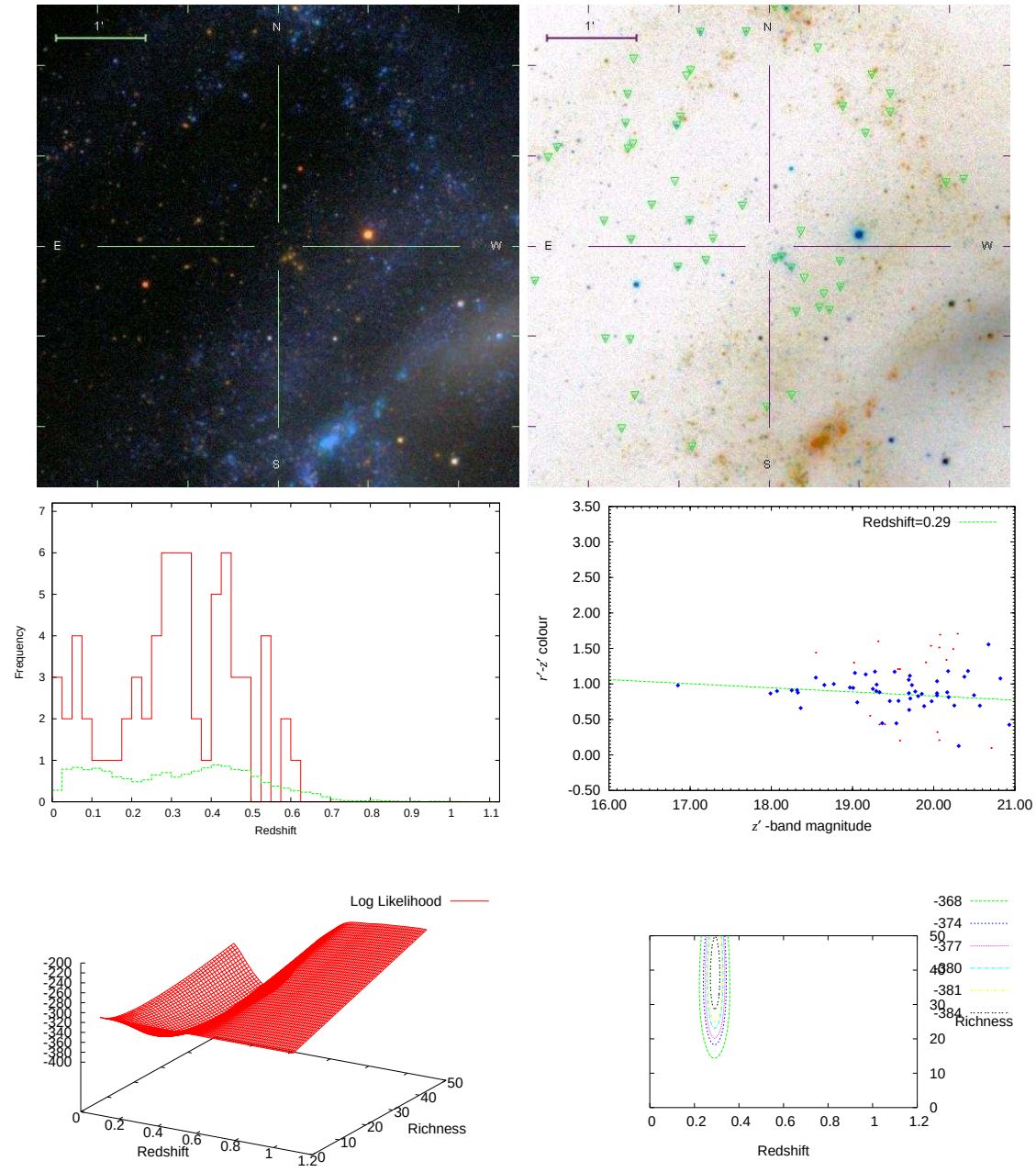

Figure 6.6 SDSSDR7 colour composite images and XCSREDSEQ results for XMMXCS J122600.5+333348.1 detected at $z = 0.29$ with 29 red sequence galaxies. See 6.4 for caption.

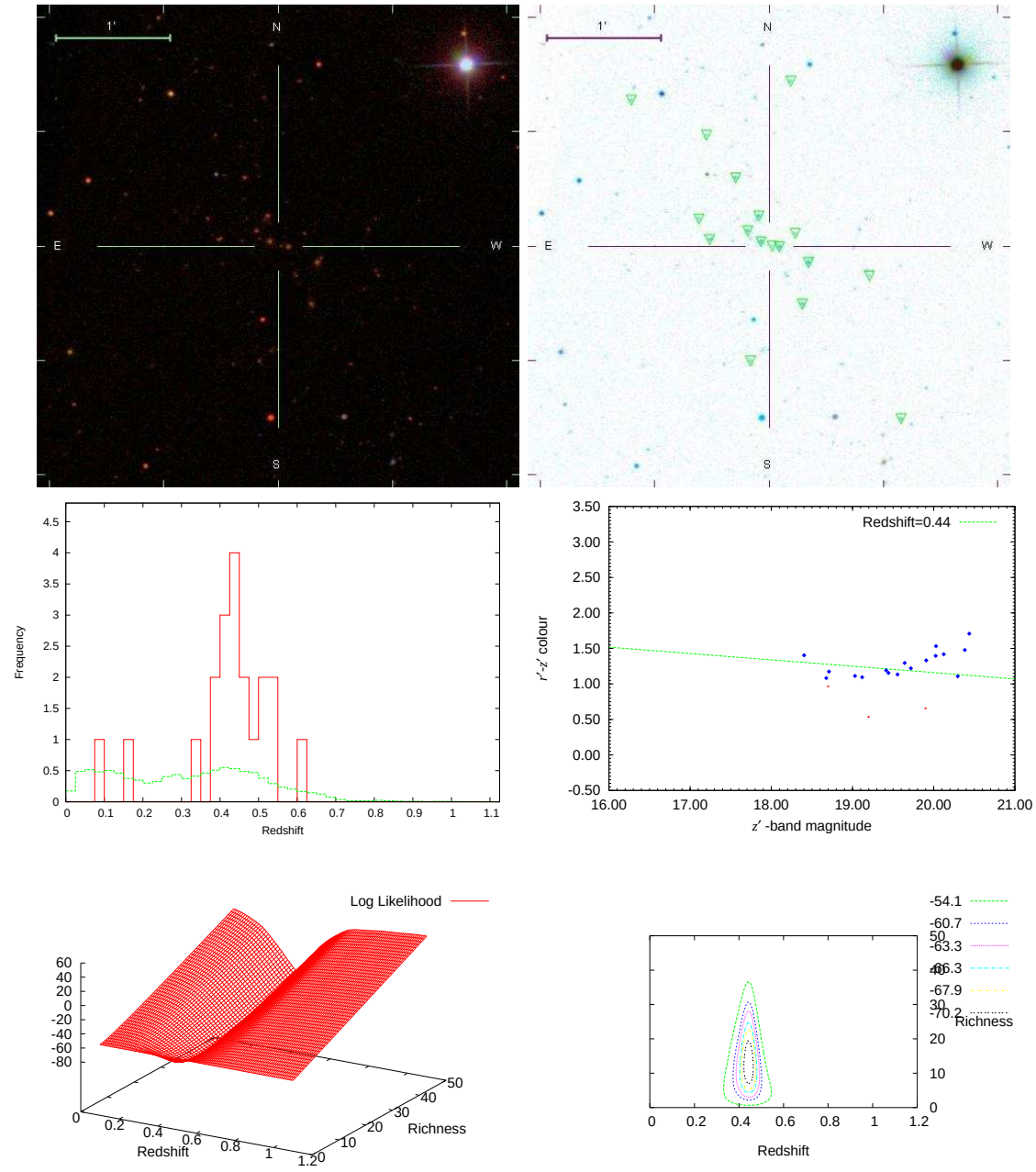

Figure 6.7 SDSSDR7 colour composite images and XCSREDSEQ results for XMMXCS J112259.3+465915.9 detected at $z = 0.44$ with 12 red sequence galaxies. See 6.4 for caption.

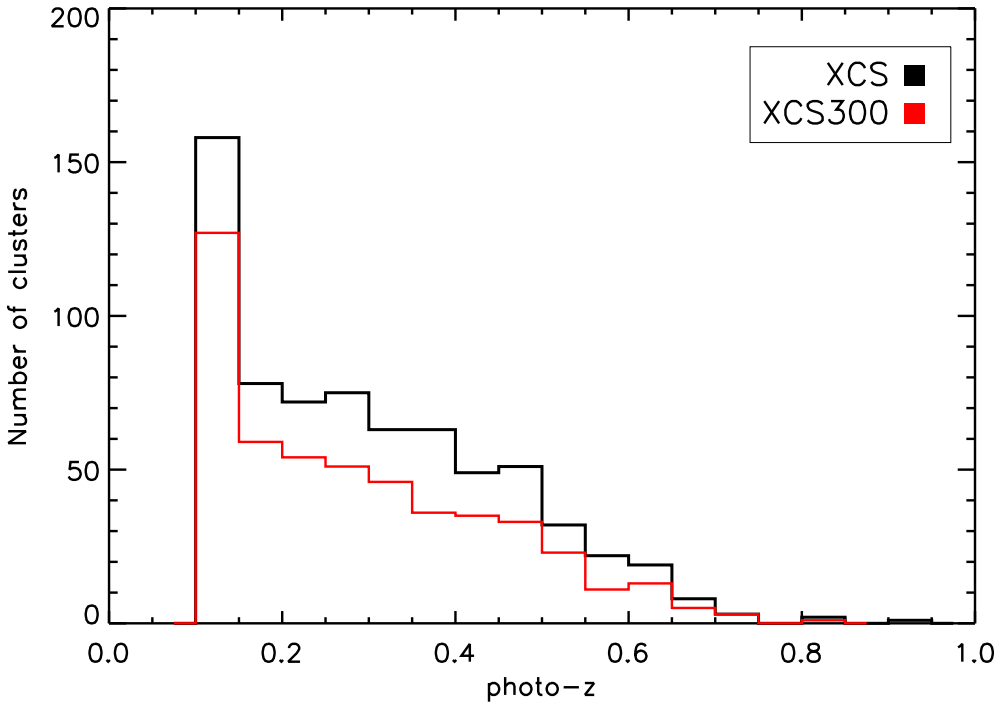

Figure 6.8 Distribution in XCSRedSeq redshift of the XCSDR3 and XCSDR1 samples (overlaps with XCSDR3 have been removed). The subset of clusters detected with more than 300 counts is shown in red. Clusters have been detected in SdssDR7 with a minimum of 5 red sequence galaxies.

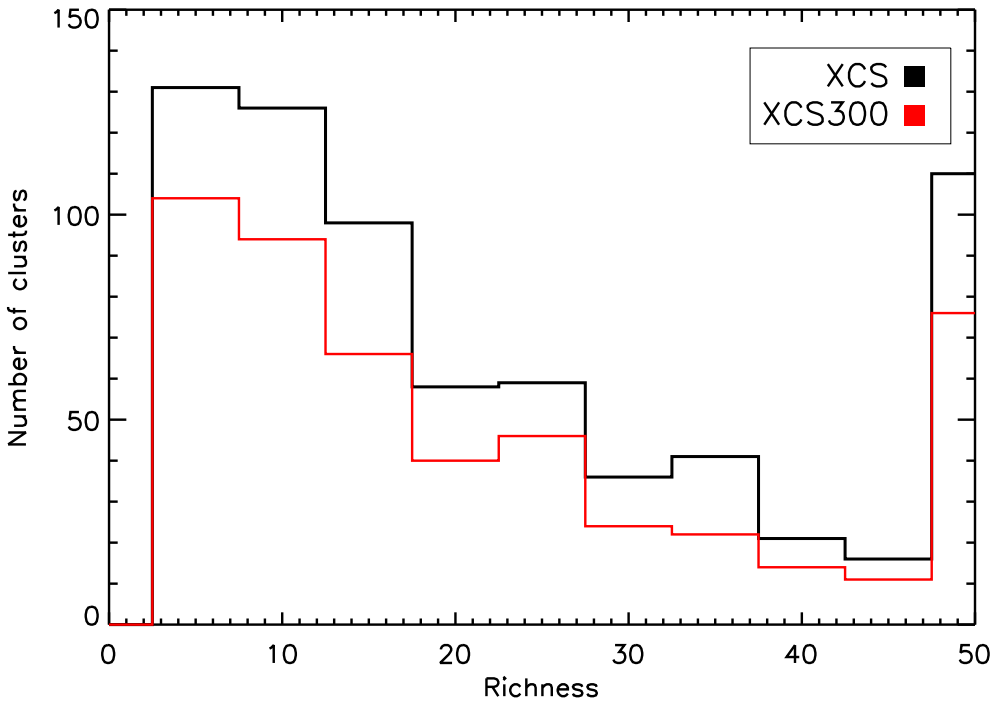

Figure 6.9 Distribution in XCSRedSeq richness of the XCSDR3 and XCSDR1 samples (overlaps with XCSDR3 have been removed). The subset of clusters detected with more than 300 counts is shown in red. Clusters have been detected in SdssDR7 with a minimum of 5 red sequence galaxies.

6.4.1 Validation of SdssDR7 XCSRedSeq redshifts

To deduce the efficacy of XCSRedSeq on SdssDR7, a comparison was made using 131 XCS clusters with spectroscopic redshifts from either the literature (§2.8.1); LRGs (§2.8.3); or XCS measured spectroscopic redshifts (§2.8.2). We note that LRG spectroscopic redshifts were only used if the respective candidate had been subjected to XCS-SDSS ClusterZoo I (§2.9) and subsequently been classed as either a *Bronze*, *Silver* or *Gold Cluster*, and the LRG is deemed to be within the core. Figure 6.10 shows a comparison of SDSS photometric redshift versus spectroscopic redshift. We have chosen to perform this test using DR1 clusters because XCS-SDSS ClusterZoo II on the DR3 sample (§7.6.2) was incomplete. Figure 6.10 shows a correlation between XCSRedSeq photometric redshift estimates and spectroscopic redshifts, thus showing the ability of XCSRedSeq to generate reasonably accurate redshifts in SDSS. Similar to the photometric to spectroscopic redshift comparison performed for NXS, catastrophic failures exist for clusters at low redshift ($z \leq 0.1$) and redshifts beyond the depth accessible to the survey ($z \geq 0.5$). It is assumed

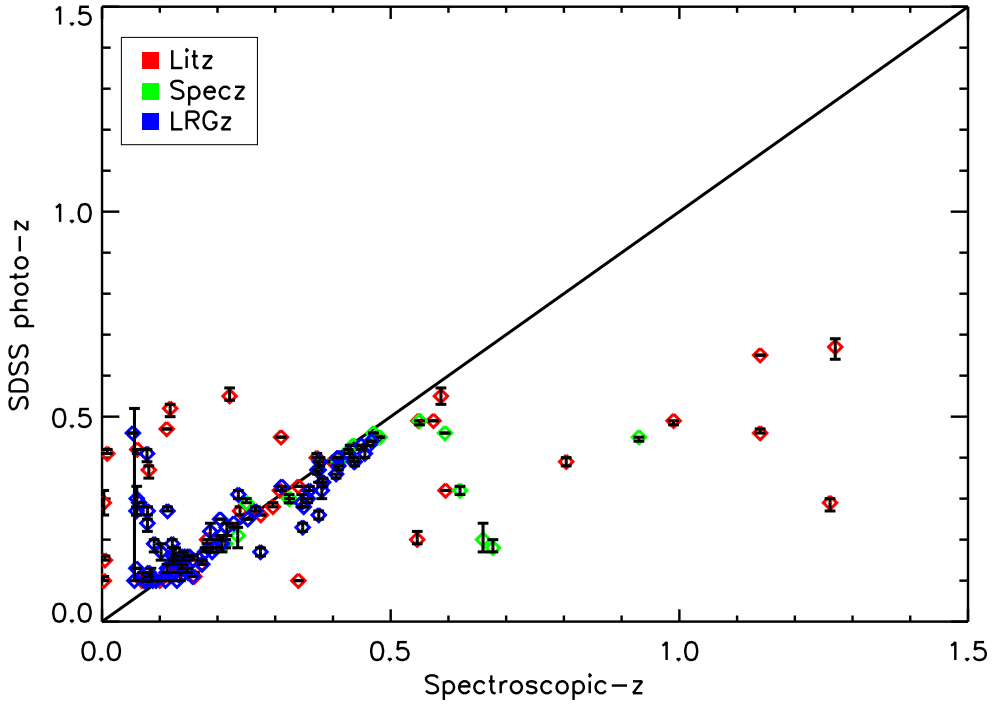

Figure 6.10 Comparison of XCSRedSeq photometric redshift and literature/XCS spectroscopic redshifts for the XCSDR1 sample plotted with respect to their spectroscopic redshift source. Spec-zs obtained from the literature, SdssDR5 LRG spec-zs and XCS dedicated spectroscopic follow-up are plotted in red, blue and green respectively.

that these catastrophic failures will be removed through the use of XCS-SDSS ClusterZoo II, as these cases are easy to identify by eye. Including the entire redshift range probed by XCS ($0 \leq z \leq 1.45$), the photometric redshift error is estimated to be $\Delta z = 0.13$. However, when excluding clusters at $z \leq 0.15$ and $z \geq 0.5$, this redshift error is reduced to $\Delta z = 0.04$. As XCS-SDSS ClusterZoo II will be performed on the entire SDSS sample, we adopt a typical photometric redshift error of $\Delta z = 0.04$ for the SdssDR7 sample.

Figure 6.11 shows a comparison between the assigned photometric redshift and spectroscopic redshift for XCSDR1 clusters with respect to their XCS-SDSS ClusterZoo I classifications.

As can be seen in the Figure, the performance of the redshift algorithm remains consistent for XCS clusters with *Gold* and *Silver* classifications. The redshift algorithm performs less well for *Bronze* clusters as exhibited by their increased scatter in Figure 6.11. The cause of this is most likely a combination of the small cluster signal with respect to the field for these poorer clusters as well as positional offsets between the central galaxy and the cluster center as determined by their questionable X-ray extent. By definition (§2.9),

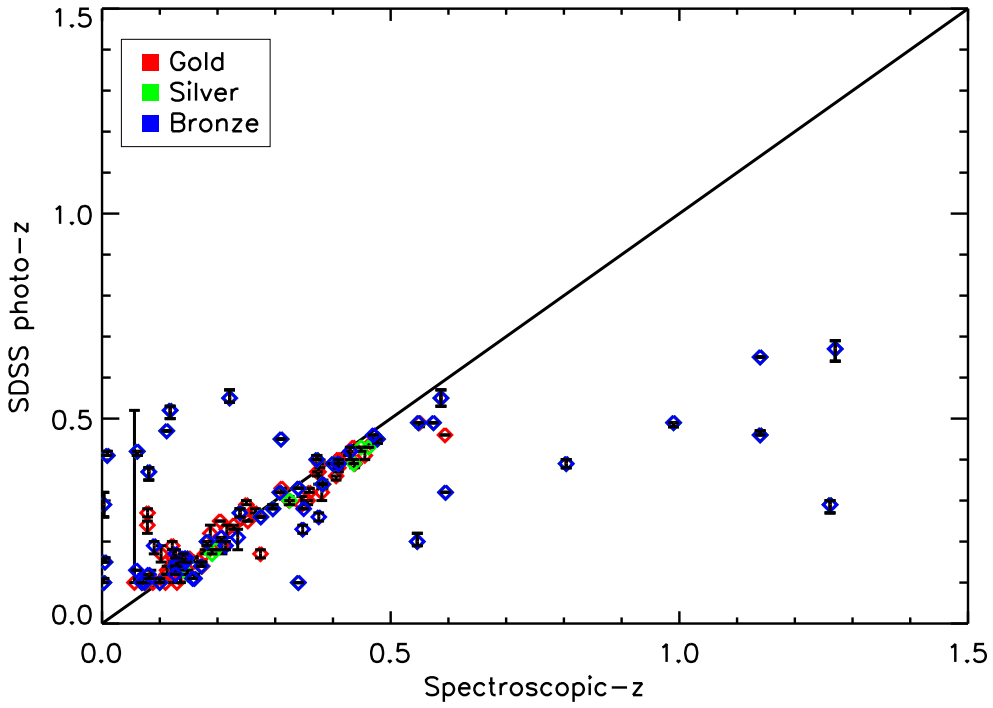

Figure 6.11 Comparison of XCSRedSeq photometric redshift and literature/XCS spectroscopic redshifts for the XCSDR1 sample plotted with respect to their XCS-SDSS Cluster-Zoo I Gold, Silver and Bronze classifications shown in red, green and blue respectively.

Bronze clusters have greater potential for positional offsets. If the X-ray extent was highly elliptical then potential cluster galaxies will be selected from a greater area thus weakening the cluster signal. However, as long as there is an overdensity of galaxies, and the XCS cluster position, as determined by the X-rays, is sufficiently good (i.e. a *Gold* or *Silver* classification), then XCSRedSeq performs adequately producing cluster redshifts to within Δz=0.04.

6.5 Stripe82 XCSRedSeq redshift results

SDSS-XCSRedSeq was run on 100 XCSDR3, 22 XCSDR1, and 9 XCSDR2 cluster candidates (XCSDR1 and XCSDR2 overlaps with XCSDR3 have been removed) using Stripe82 data. This produced redshift and richness estimates for 78 XCSDR3, 15 XCSDR1, and 7 XCSDR2 cluster candidates. All of these were detected with at least 5 red sequence galaxies.

Figures 6.12 and 6.13 show examples of SDSS Stripe82 images and corresponding red sequence relations for XCS cluster candidates detected at $z = 0.1$, $z = 0.2$ & $z = 0.36$ (Figure 6.12) and $z = 0.46$, $z = 0.54$ & $z = 0.66$ (Figure 6.13) respectively.

Figures 6.14 and 6.15 show similar examples for 4 XCS cluster candidates detected above a redshift of $z = 0.5$ where redshift results from SdssDR7 breaks down. With the exception of XMMXCS J030205.5-000001.8, none of these candidates were detected as clusters (i.e. a system containing a minimum of 5 red sequence galaxies) when solely using the relatively shallow standard SdssDR7 data alone. In the case of XMMXCS J030205.5-000001.8, a cluster was detected but at the erroneous redshift of $z = 0.31$. Beside each Stripe82 image are the colour magnitude diagrams of each cluster. Galaxies depicted in blue show galaxies with colours within $\pm 2\sigma$ of the chosen red sequence relation. As can be seen in these high redshift examples, the scatter on the red sequence relation increases towards fainter magnitudes. This is because magnitude errors on galaxies increase towards fainter magnitudes.

The resulting redshift and richness histograms for the XCS-SDSS Stripe82 sample are shown in Figures 6.16 and 6.17.

6.5.1 Validation of Stripe82 XCSRedSeq redshifts

To deduce the efficacy of XCSRedSeq on Stripe82, a comparison was made using eight XCS clusters with spectroscopic redshifts from the literature (§2.8.1) and XCS measured spectroscopic redshifts (§2.8.2). Figure 6.18 shows the comparison between the XCSRed-

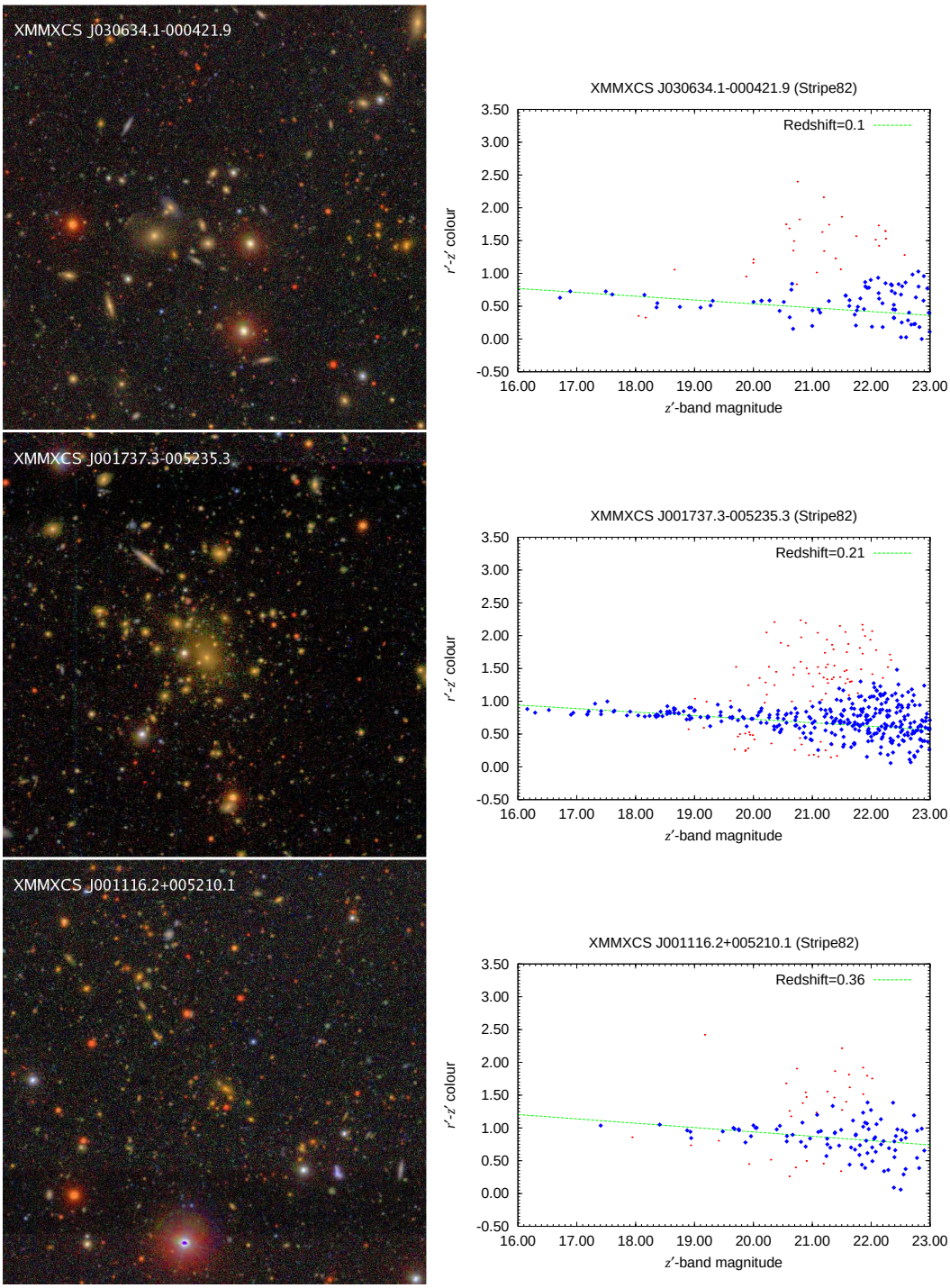

Figure 6.12 STRIPE82 colour composite images (6′by6′) and XCSREDSEQ red sequence relations for XMMXCS J030634.1-000421.9, XMMXCS J001737.3-005235.3 and XMMXCS J001116.2+005210.1 detected in STRIPE82 to be at redshifts $z = 0.1$, $z = 0.21$ and $z = 0.36$ respectively. CMR diagrams show all galaxies chosen as red sequence galaxies i.e. $\pm 2\sigma$ of the chosen red sequence colour (blue points) and field (red points) within twice the X-ray extent of the XCS cluster candidate (measured by XCS) and the best fit red sequence relation (green line). Each galaxy is assumed to be a red sequence galaxy. [Figure credit: Edd Edmondson, Portsmouth University, creation of STRIPE82 colour composite images.]

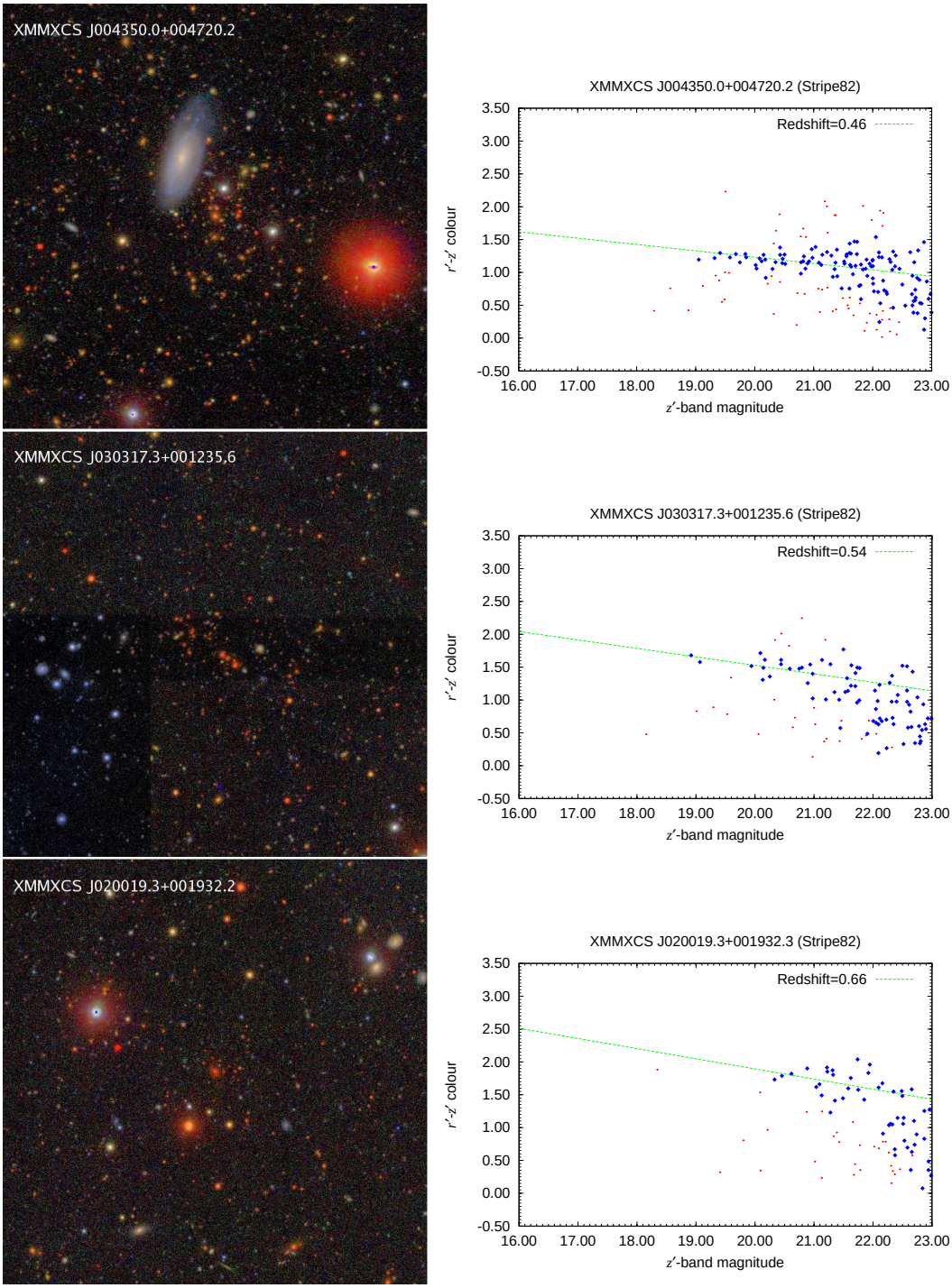

Figure 6.13 STRIPE82 colour composite images (6′by6′) and XCSREDSEQ red sequence relations for XMMXCS J004350.0+004720.2, XMMXCS J030317.3+001235.6 and XMMXCS J020019.3+001932.3 detected in STRIPE82 to be at redshifts $z = 0.46$, $z = 0.54$ and $z = 0.66$ respectively. See 6.12 for figure caption.

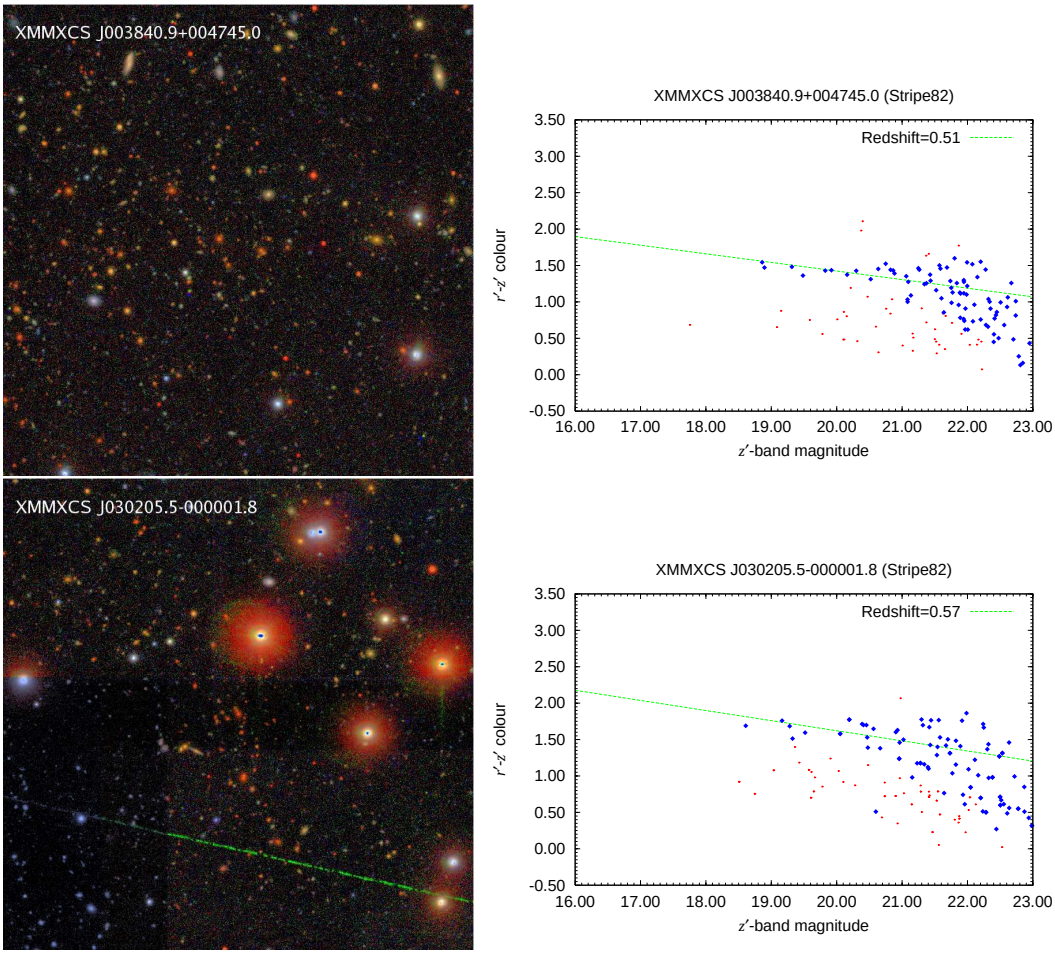

Figure 6.14 STRIPE82 colour composite images (6′by6′) and XCSREDSEQ red sequence relations for XMMXCS J003840.9+004745.0 and XMMXCS J030205.5-000001.8 detected in STRIPE82 to be at redshifts $z = 0.51$ and $z = 0.57$ respectively. See 6.12 for figure caption.

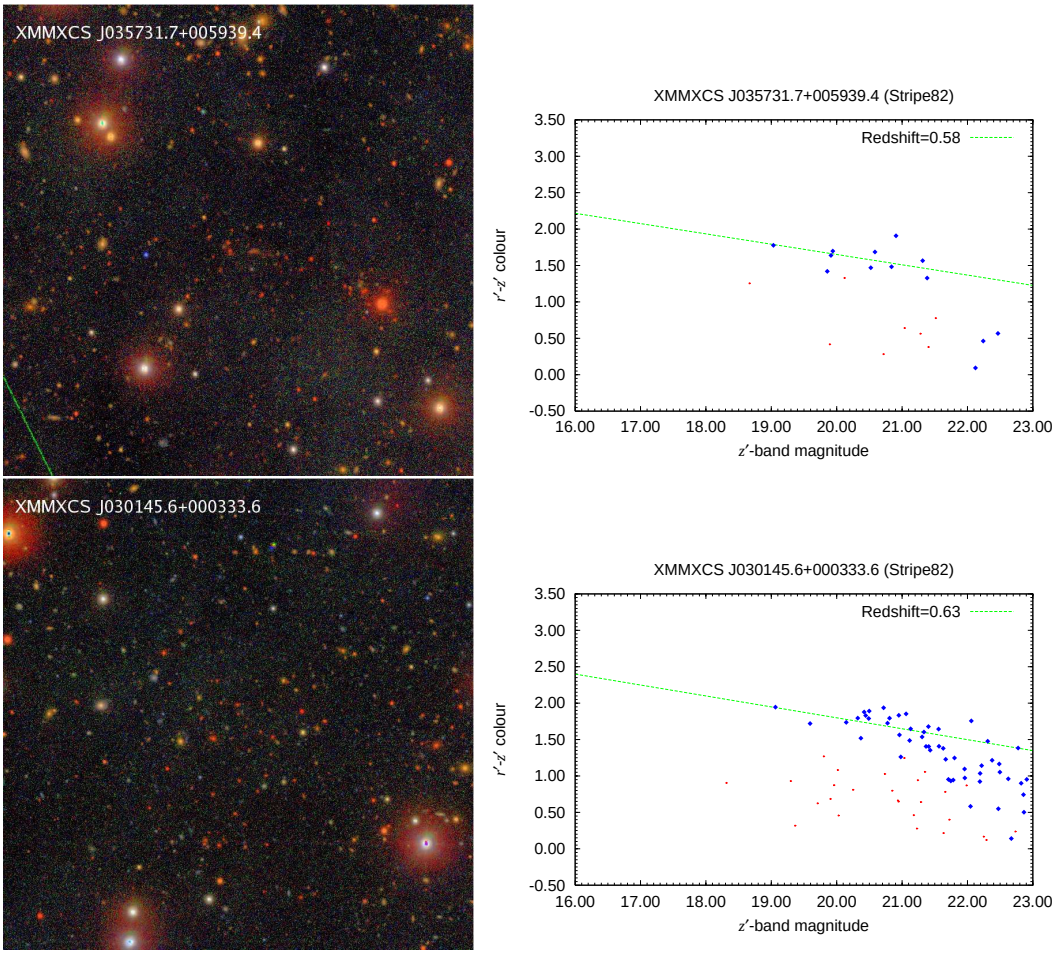

Figure 6.15 STRIPE82 colour composite images (6′by6′) and XCSREDSEQ red sequence relations for XMMXCS J035731.7+005939.4 and XMMXCS J030145.6+000333.6 detected in STRIPE82 to be at redshifts $z = 0.58$ and $z = 0.63$ respectively. See 6.12 for figure caption.

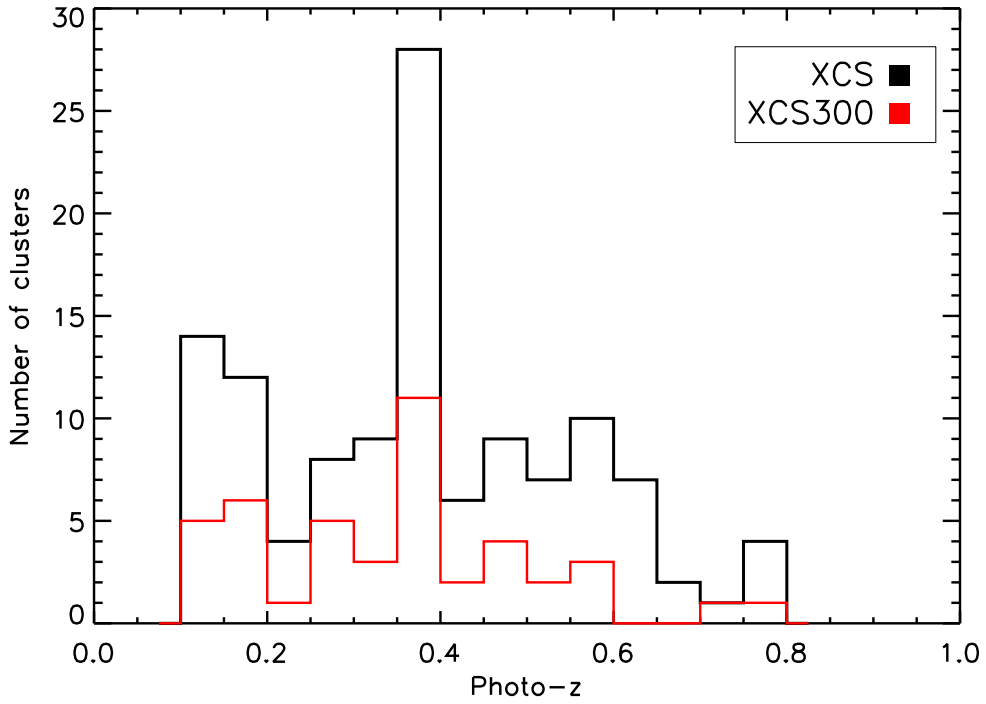

Figure 6.16 Distribution in XCSRedSeq redshift of the XCSDR3, XCSDR1 and XCSDR2 samples (overlaps with XCSDR3 have been removed). The subset of clusters detected with more than 300 counts is shown in red. Clusters have been detected in Stripe82 with a minimum of 5 red sequence galaxies.

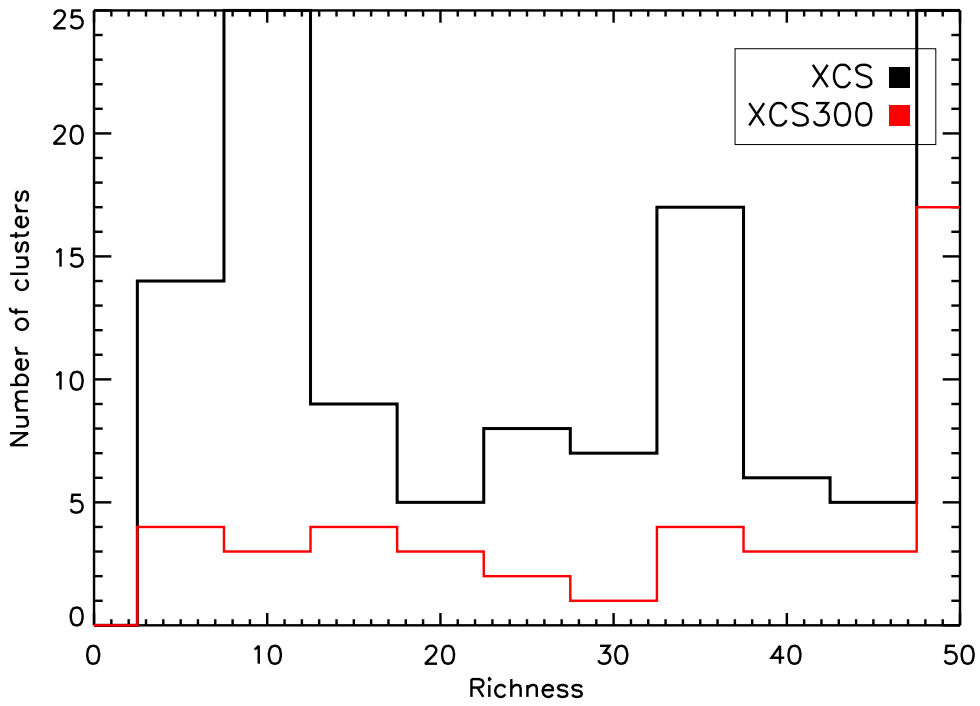

Figure 6.17 Distribution in XCSRedSeq richness of the XCSDR3, XCSDR1 and XCSDR2 samples (overlaps with XCSDR3 have been removed). The subset of clusters detected with more than 300 counts is shown in red. Clusters have been detected in Stripe82 with a minimum of 5 red sequence galaxies.

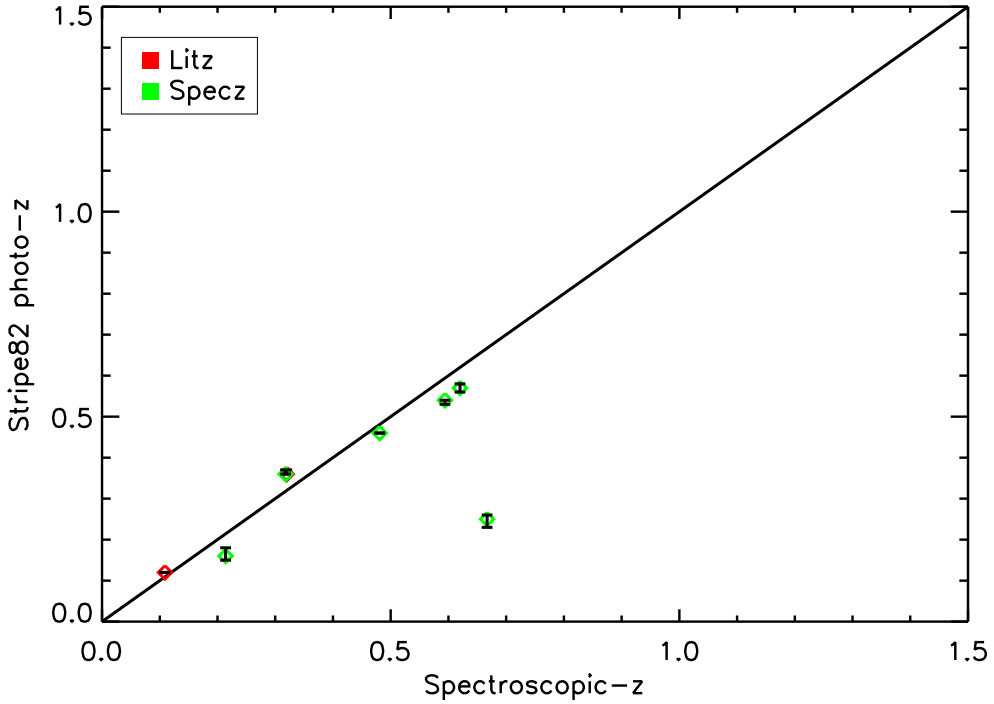

Figure 6.18 Comparison of XCSRedSeq photometric redshift and literature/XCS spectroscopic redshifts. Spectroscopic redshifts obtained from the literature and XCS dedicated spectroscopic follow-up are plotted in red and green respectively.

Seq photometric redshifts and spectroscopic redshifts for this sample. Although only a small number of clusters has been used, the Figure shows a correlation between estimated Stripe82 XCSRedSeq photometric redshifts and measured spectroscopic redshift. Thus showing the ability of XCSRedSeq to generate reasonably accurate photometric redshifts in Stripe82. Using this sample, the photometric redshift error is estimated to be Δz=0.15. However, as this sample is small, we assume that the significant outlier on the photometric redshift to spectroscopic relation is a rarely occuring catastrophic failure, biasing the error estimate[10]. Thus we choose to remove this cluster from our error estimate. This resulted in an estimated photometric error of Δz=0.04 on the redshifts generated from Stripe82, consistent with the error generated from SdssDR7.

[10]We note that this outlier subsequently failed to be classified as either a *Gold* or *Silver* cluster in a Cluster Zoo (see Section 2.9) performed on candidates imaged by the SDSS Stripe82 co-add.

6.6 Discussion

In this chapter, we have presented the application of XCSRedSeq to the SDSS data products SdssDR7 and Stripe82. This has resulted in 696 redshift estimates for XCS clusters between $0.1 \leq z \leq 0.5$ for those clusters falling within the survey regions of SdssDR7. A subsample of 100 clusters have also obtained photometric estimates using the deeper imaging of Stripe82, between z=$0.1 \leq z \leq 0.8$.

The photometric redshifts obtained by both samples are assumed to be accurate to within an estimated error of Δz=0.04. This redshift error is within the tolerance required for XCS to constrain cosmological parameters via cluster number counts. Hence, this has shown that XCSRedSeq has worked effectively to within the requirements of the XCS. However a larger sample of spectroscopic redshifts for Stripe82 is required to confirm this error estimate, as is the assumption that clusters beyond the survey depths of SDSSDR7 will be filtered out through the use of XCS-SDSS ClusterZoo II (§6.4.1 & §6.5.1).

In addition, XCSRedSeq has provided new redshift estimates for confirmed clusters that had not been assigned LRG redshifts via the Hoyle Algorithm (§2.8.3). Although, the Hoyle Algorithm is yet to be run on the XCSDR3 sample, it is interesting to compare it to the results generated by XCSRedSeq for the XCSDR1 sample. Generally, we find XCSRedSeq to measure more photometric redshifts than that measured by the Hoyle Algorithm. Forty-one ClusterZoo confirmed XCS clusters had received a redshift from XCSRedSeq and not from the Hoyle Algorithm had failed. However, the Hoyle Algorithm provides accurate spectroscopic redshifts where available, and where not, the estimated error on its photometric redshifts are estimated to be Δz=0.03. Thus, redshifts generated by the Hoyle algorithm are typically more accurate than those generated by XCSRedSeq. This again suggests, more colours should be utilised to make better use of LRGs (§5.7).

Thus, SDSS has provided an excellent resource for gaining redshift estimates for XCS cluster candidates. It is assumed that the improved cluster photometric redshift accuracy of SDSSDR7 and Stripe82 over that obtained by NXS, is due to the increased homogeneity and superior photometric calibration of the SDSS data compared to the NXS. In addition, the use of an external field sample for both SDSS data sets, has provided a consistent background subtraction for these clusters, rather than the varying field samples used for NXS. In addition, as SDSS is a contiguous survey, the issue of 'Edge-effects' does not have to be addressed. Thus in many ways, SDSS has provided a better resource than NXS for XCS, albeit, mostly to a lower depth. In order to make a fair comparison between the photometric redshift and richness estimates generated from SdssDR7, Stripe82 and

NXS, all clusters in the overlapping samples must be subjected to ClusterZoo and confirmed as clusters. Unfortunately, this procedure had not occurred within the timescale of this thesis.

Possible improvements to XCSRedSeq

The algorithm XCSRedSeq was tuned to the data products of the NXS. However, the r and z-bands utilised by XCSRedSeq have been chosen to provide maximum separation around z=0.5. This redshift is largely beyond that accessible to SDSS. It is assumed that by choosing, the g and r-band combination, and altering the empirical red sequence model accordingly, more accurate redshift estimates will be generated by XCSRedSeq.

Moreover, as a consequence of its desired application to NXS, XCSRedSeq only utilises 2 bands for the production of photometric redshifts. As SDSS provides survey imaging data in 5 bands, all of this data can be utilised by XCSRedSeq in a manner discussed in Section 5.7, this would be particularly true for the Stripe82 data set where cluster redshifts are detected over a larger redshift range.

Furthermore, due to its comparable depth, the Stripe82 external field sample could be used to test the effects of a consistent field sample on the cluster redshifts generated from NXS.

Planned work

Before publication of the Optical to X-ray scaling relations (see Chapter 7) can occur, some improvements to the work presented in this Chapter are planned. Upon the production of XCSDR3-v2, XCSRedSeq will be run on resulting cluster candidate sample, without any soft count restriction, to provide a larger sample of photometric estimates for XCS. In addition, this sample will be subjected to XCS-SDSS ClusterZoo II, to confirm clusters, and test the assumptions of the photometric error estimates.

These confirmed SDSS clusters, with XCSRedSeq photometric error estimates, will then be used by XCS to measure both cosmological parameters through the use of cluster number counts, as well as measure and test evolution of an XCS determined L_X–T_X relation. We note that the XCS clusters with XCSRedSeq generaterd redshift estimates from SDSS so far have been used to produce a preliminary L_X–T_X relation, shown in Section 2.10.

In parallel, a number of high redshift candidates have been identified in SdssDR7 and Stripe82 it is hoped that these clusters will be targetted for additional follow-up at 8m

telescopes, such as Keck, or Gemini.

Chapter 7

The XCS: Optical to X-ray Scaling Relations

In this chapter, we present preliminary results on XCS optical to X-ray scaling relations. We begin by describing the algorithm designed to measure optical richness for XCS clusters (§7.3). Its application to the NXS and SDSS data sets is then outlined in Sections 7.4 and 7.5 respectively. These samples were then cleaned of spurious cluster detections using the results of XCS ClusterZoo II (§7.6). The XCS-NXS, and XCS-SDSS optical scaling relations are presented in Sections 7.7 and 7.8 respectively.

7.1 The XCS Measure of Optical Richness

Chapter 5 describes the NXS method of confirming XCS cluster candidates and assigning cluster photometric redshifts using the XCSRedSeq algorithm (§5.5). As a bi-product, an estimate is produced of the number of red sequence galaxies (N_{gal}), at all magnitudes, within twice the cluster X-ray extent defined by XAPA (§2.3). This measured X-ray extent is largely determined by the exposure time of the respective XMM observation, which varies between XCS fields, rather than the physical size of the cluster. As such, this optical richness measurement is not a true representation of the cluster richness. Thus in order to measure optical to X-ray scaling relations, XCS must define a 'true' optical richness measure for each cluster.

A universal measure of optical richness has not been defined in the literature (§1.6.3). Hence, given the similarity between the NXS and MaxBCG methods of measuring cluster redshift and richnesses estimates, we choose to adopt the optical richness measure N_{200} as used by MaxBCG (Koester et al., 2007b). N_{200}, as defined by MaxBCG, is the number of

cluster galaxies within $\pm 2\sigma$ of the cluster red sequence colour, to a limiting magnitude of $0.4L_*$, out to the virial radius (R_{200}) of the cluster (§1.6.3).

7.2 Expected Scaling Relations

Using simple assumptions on the physics of clusters one can predict the expected scaling relation of N_{200}–T_X. If one assumes that clusters are self-similar (*i.e.* that only gravitationally forces determine the state of a cluster), so that larger clusters are simply scaled up versions of smaller clusters, and that these clusters are in virial equilibrium and an isothermal sphere of X-ray emitting gas; then cluster mass is related to the X-ray observable T_X by the relation (see Section 1.5.1):

$$T_X \propto M^{\frac{2}{3}} \tag{7.1}$$

Similarly, if one assumes that galaxies are biased traces of the dark matter in clusters, then the total mass contained within cluster galaxies should be proportional to the total mass of a cluster, and hence:

$$M_{gal} \propto M \tag{7.2}$$

Furthermore, if we assume that the total mass of these cluster galaxies are evenly distributed between all cluster galaxies and that they have a constant mass to light ratio so that all galaxies are detected above $0.4L_*$, then the number of cluster galaxies within the virial radius (as given by R_{200}) should be proportional to the total cluster galaxy mass.

$$M_{gal} \propto N_{200} \tag{7.3}$$

Indeed, Lin et al. (2004) have found this relation to scale as a power law with a slope close to unity. Therefore one can assume that the number of cluster galaxies out to the virial radius should scale with cluster temperature by the following relation:

$$T_X \propto N_{200}^{\frac{2}{3}} \tag{7.4}$$

or

$$N_{200} \propto T_X^{\frac{3}{2}} \tag{7.5}$$

7.3 Adapting XCSRedSeq to Measure N_{200}: XCSRedSeqN_{200}

The optical richness (N_{200}) of XCS clusters is measured using the algorithm XCSRedSeqN_{200}, an adapted version of the XCSRedSeq algorithm (§5.5). XCSRedSeqN_{200} employs the same E/S0 ridgeline likelihood (Equation 5.6; §5.5) as used by XCSRedSeq to measure richness estimates. In addition, the same empirical red sequence model (§5.2.3) is used to estimate the colour of the red sequence relation at a given cluster redshift.

Therefore, similar to XCSRedSeq, XCSRedSeqN_{200} uses the E/S0 ridgeline likelihood to locate overdensities in colour-space (attributed to the cluster red sequence), above the background field distribution and derive a cluster richness estimate. Thus, by fitting the cluster signal above the background distribution, a background field subtraction is performed on the acquired N_{200} values.

The key difference between XCSRedSeq and XCSRedSeqN_{200} are the cluster and field galaxy samples used in the likelihood fit. As mentioned in Section 7.1, we wish to measure the optical richness of clusters to within R_{200} (§7.1). Therefore, rather than selecting a sample of cluster galaxies from within twice the X-ray extent, galaxies are selected from within something more physical, *i.e.* an approximation to the virial radius (R_{200}). This radius is estimated using the cluster redshift, X-ray temperature and the model defined in Section 7.3.1 (consequently, only clusters with measured temperature and redshift estimates are used to obtain N_{200} values). Furthermore, as a consequence of the desired luminosity limit (§7.1), only galaxies brighter than $0.4L^*$ are included in the cluster and field galaxy samples. Thus, for each cluster being evaluted, the value of $0.4L^*$ is determined given the redshift of the cluster and the model defined in Section 7.3.2.

As with XCSRedSeq, the E/S0 ridgeline likelihood is evaluated for each galaxy. However, when maximising the E/S0 ridgeline likelihood, we fix the cluster redshift to that previously measured by XCSRedSeq, and maximise in richness steps of $_N$=1 galaxy, rather than across a grid of redshift and richness. The redshift is fixed, because in changing the aperture size from twice the XAPA X-ray extent, to the virial radius (R_{200}), we are changing the sample of selected cluster galaxies and field galaxies used in the E/S0 likelihood fit. This change in galaxy samples, would result in a different set of redshift values being measured by XCSRedSeqN_{200}, compared to those measured by XCSRedSeq, for a particular cluster. Furthermore, the virial radius of a given cluster is often larger than twice the XAPA X-ray extent. Using a larger aperture introduces an increased amount of field contamination that may swamp the cluster signal. By not fixing the redshift in the likelihood fit, this increased level of field contamination will result in erroneous redshift

measurements and thus, an inaccurate number of red sequence galaxies included in the richness estimate.

In the XCSRedSeqN$_{200}$ algorithm, the Gaussian width of the E/S0 ridgeline likelihood (Equation 5.8) is set to take into account the intrinsic width of the red sequence and include galaxies with colours within $\pm 2\sigma$ of the red sequence colour. Thus, by using XCSRedSeqN$_{200}$, optical richness estimates (N$_{200}$) are produced from the number of cluster galaxies within $\pm 2\sigma$ of the cluster red sequence colour, to a limiting magnitude of $0.4L_*$, out to the virial radius (R$_{200}$) of the cluster. In addition, a simultaneous estimate is produced of the number of field galaxies (N$_{field,200}$) falling within $\pm 2\sigma$ of the red sequence colour, brighter than $0.4L^*$, scaled to the virial radius of the cluster. The $0.4L_*$ and R$_{200}$ calculations are described in Sections 7.3.1 and 7.3.2 below.

7.3.1 Estimating R$_{200}$

For XCS, R$_{200}$ is estimated using the measured X-ray temperature of a cluster. By using the X-ray temperature together with knowledge of the cluster redshift, one can derive a virial mass and radius of a cluster (§1.4). A discrete set of theoretical cluster masses and virial radii (R$_{200}$) were provided by Martin Sahlen for a set of clusters covering a range of temperatures ($0 \leq T \leq 10$ keV, $\Delta T = 0.1$) and redshifts ($0 \leq z \leq 1.5$, $\Delta z = 0.01$). Figure 7.1 shows how the virial radius estimate (R$_{200}$) scales with temperature for systems at a selection of different redshifts (z=0.1,0.3,0.8,1.0). To convert temperature to mass, an $M_{200} - T_X$ relation was used, normalised to the local cluster population using HIFLUGS data (Sahlén et al., 2009). These masses were estimated assuming a fiducial cosmology with $\Omega_m = 0.3$ and Ω_λ=0.7, along with the assumption of an NFW halo profile with a concentration paramter=5. We note that scatter in the $M_{200} - T_X$ relation was not taken into account.

For XCS clusters with redshift estimates, X-ray temperatures were measured by Ed Lloyd-Davies for those clusters detected with a sufficient number of X-ray soft counts (Appendix A). These redshift and temperature measurements were then used to interpolate between the discrete redshift and temperature values in the above model and provide a theoretical virial mass ($h^{-1}10^{15}M_\odot$) and virial radius (R$_{200}$, h^{-1} Mpc) for each cluster. The proper size of each cluster is then converted into angular extent on the sky using the angular diameter distance formula (§1.2) and knowledge of the cluster redshift.

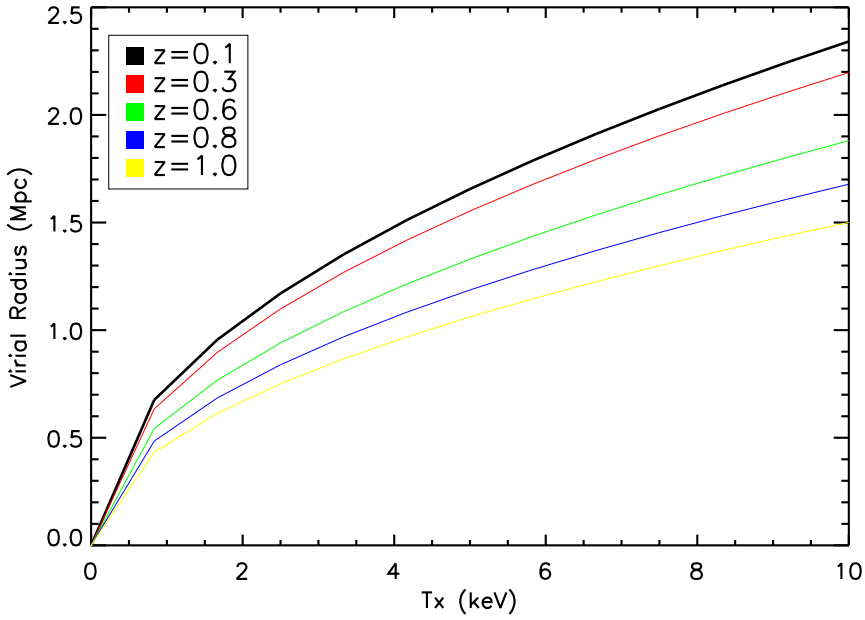

Figure 7.1 Four examples of how the virial radius (R_{200}) changes with temperature for clusters at redshift z=0.1,0.3,0.8, 1.0)

7.3.2 Estimating $0.4L_*$

In order to compare the optical richnesses of clusters at varying redshifts, a magnitude limit must be set above which the number of red sequence galaxies are counted. Otherwise, clusters detected at lower redshifts will gain artificially high richness estimates, as more galaxies towards the fainter end of the cluster luminisity function can be detected and thus included in the richness estimate. Hence, a luminosity limit is used. Following the method of MaxBCG, we use a luminosity limit of $0.4L_*$, corresponding to a magnitude limit of M_*+1. Hence, applying this magnitude cut to the limiting magnitude of a galaxy catalog then determines the redshift range over which cluster richnesses can be measured.

We choose to apply this magnitude cut to galaxies detected in the z-band. This filter is used as the 4000Å break does not enter the z-band until a redshift $z\sim$1.0. The spectrum of elliptical galaxies redward of the 4000Å break is relatively flat. Therefore any fluctuations in luminosity will be inherent to the galaxy cluster, as opposed to spectral features moving across the z-band filter (Koester et al., 2007b).

Similar to MaxBCG, we adopt the cluster characteristic absolute magnitude of M_*^r=-20.75 as measured for rich clusters at z=0.1 (Eisenstein et al., 2001). This r-band magnitude is converted into a z-band magnitude using the Bruzual & Charlot population synthesis models. These models are parametised to match those used by the empirical

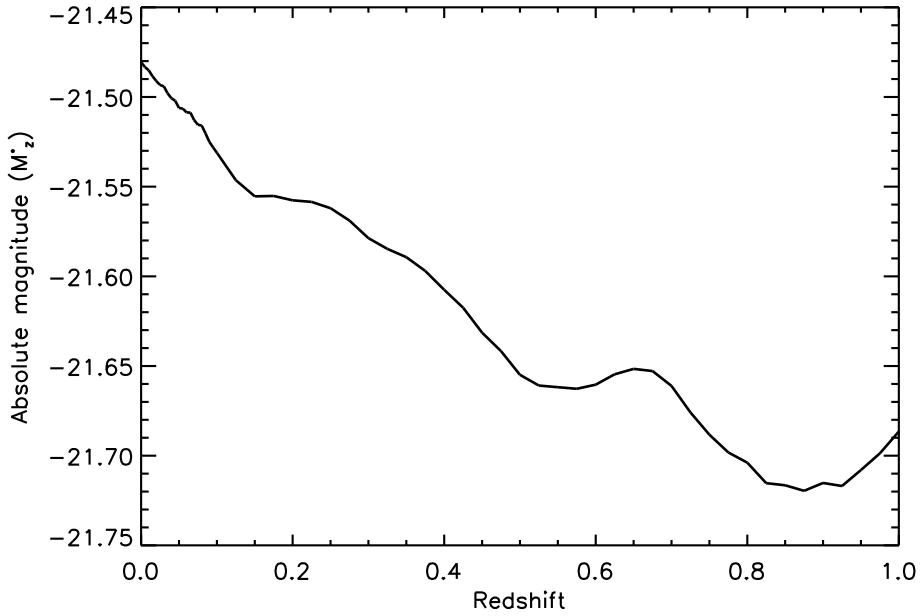

Figure 7.2 Illustration of the k- and evolution corrected characteristic absolute magnitude with redshift as measured in the z-band (M^z_*) based on the Bruzual & Charlot population synthesis models and the characteristic absolute magnitude of M^r_*=-20.75 as measured for rich clusters at z=0.1 (Eisenstein et al., 2001)

red sequence model defined in Section 5.2.3, *i.e.* a passively evolving galaxy with solar metalicity, formed from a 1Gyr burst of star formation at a redshift of z_f=2.5. As a result of this model, we obtain the corresponding characteristic z-band absolute magnitude of M^z_*=-21.53 at z=0.1, as well as the evolution of M^z_* with redshift (shown in Figure 7.2).

Therefore using this model, the absolute magnitude of M^z_*+1 is calculated for each cluster, given its redshift. This absolute magnitude is then converted into an apparent magnitude using the luminosity distance formula (§1.2). The k- and evolution corrected apparent magnitude of M^z_*+1 with redshift is shown in Figure 7.3. All galaxies within the galaxy catalogue brighter than this apparent magnitude are then included when determining the optical richness of each cluster.

7.4 Applying XCSRedSeqN$_{200}$ to NXS

Of the 314 XCS candidates detected as clusters by NXS (§5.6), 108 were detected with sufficient X-ray counts to gain an X-ray temperature measurement. By imposing a luminosity cut of $0.4L_*$ to the survey depth, a redshift limit is set to which the optical richnesses of clusters can be measured. Since the depth of each NXS-field varied across the survey

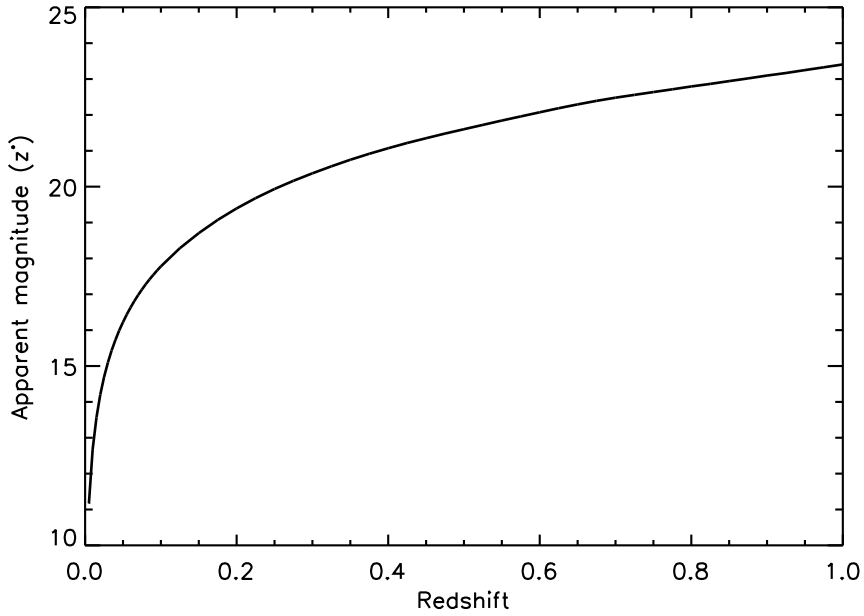

Figure 7.3 Illustration of the k- and evolution corrected apparent magnitude of M_*^z+1 with redshift based on the Bruzual & Charlot population synthesis models and the characteristic absolute magnitude of M_*^r=-20.75 as measured for rich clusters at z=0.1 (Eisenstein et al., 2001)

(§4.4), depending on exposure times, seeing conditions and sky levels at the telescope, a depth had to be determined for each individual NXS-field (using the method described below) hosting a cluster. A field-dependent redshift limit was then determined using the model in Section 7.3.2. However, we note that applying a $0.4L_*$ cut to the typical depth of the NXS survey, results in a typical redshift limit of z =0.8 to which N_{200} values could be measured. Of the 108 clusters with a T_X measurement, 102 had redshifts below z=0.8, so this sample (of 108) was reduced to 102 clusters.

Determining the depth of NXS-fields

In order to estimate the completeness of each NXS-field and hence measure the field dependant redshift limit, we used an estimate of peak in the number density versus magnitude distribution derived fom the galaxy catalogs extracted from the corresponding image. As can be seen in Figure 7.4, the number density (typically) drops steadily beyond the peak, rather than increasing at a slower rate of growth. Therefore, this method is adequate as we only wish to acquire an estimate of the completeness (to the 95% level) of each field. This is because the N_{200} estimates are more sensitive to variations in the field background

number density as discussed in Section 7.9.

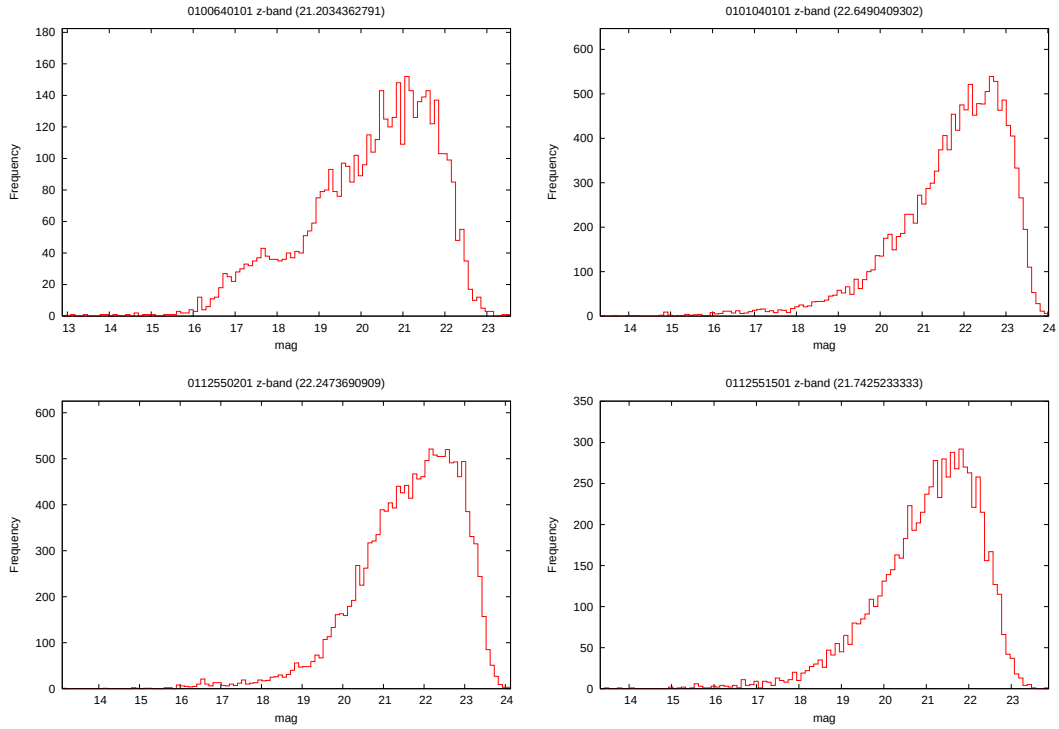

Figure 7.4 Four examples of the galaxy number density versus z'-band magnitude for the NXS-fields NXS0100640101, NXS0101040101, NXS0112550201 and 0112551501

NXS Cluster galaxy sample

For each cluster, a sample of cluster galaxies were extracted from the NXS galaxy catalogues as outlined in Section 5.2.1, with the exception that galaxies were selected from within the estimated virial radius (R_{200}) of the cluster, rather than twice the XAPA X-ray extent. R_{200} was estimated according to Section 7.3. NXS is not a contigous survey, but a survey made up of individual 0.38 deg^2 fields. As such, a given cluster may, in part, be located off the edge of an NXS-field. If the virial radius of the cluster was deemed to be located beyond the edge of an NXS-field then an Edge-flag was assigned. In these cases, the optical richnesses of the cluster could not be accurately measured.

NXS Field Galaxy Sample

A local field sample for each cluster was constructed using galaxies derived from within the same NXS-field as outlined in Section 5.2.2. However, unlike in Section 5.2.2, when constructing an image mask to exclude potential cluster galaxies in the field sample, we

use the virial radius of the cluster in question as opposed to the angular extent defined by XAPA. The regions of the remaining cluster candidates within that field were then masked using a set radius of 0.15 deg (as in §5.2.2).

NXS N_{200} Estimates

XCSRedSeqN$_{200}$ was run on 102 NXS clusters, analysing each cluster in turn. Using the redshift of the cluster, an apparent magnitude limit was calculated corresponding to $0.4L_*$ for the cluster NXS-field in question. The number of galaxies within the cluster and field samples were then cut, to only include galaxies brighter than this magnitude limit. These cluster and field galaxy samples were subjected to the E/S0 ridgeline likelihood fit to produce an optical richness estimate. In this manner, N_{200} values were obtained for 62 NXS clusters (the remaining 40 clusters were not complete to $0.4L_*$ based on the seeing and depth of their respective images).

7.5 Applying XCSRedSeqN$_{200}$ to SDSS

Of the 851 XCS candidates detected as clusters by XCSRedSeq in SDSS, 197 were detected with sufficient counts to measure an X-ray temperature. The SDSS catalogue is measured to have a mean 95% completeness limit of z=20.5 (Abazajian et al., 2004). Therefore, imposing a luminosity cut of $0.4L_*$ to this limiting magnitude (using the model defined in §7.3.2), sets a redshift limit of $z\sim$0.3 to which optical richnesses in SDSS can be measured. This redshift cut was applied to the sample of clusters in SDSS with measured temperatures, which resulted in a sample of 107 clusters from which we can gain an optical richness estimate.

SDSS Cluster and Field Galaxy Samples

For each cluster, a cluster galaxy sample was extracted from the SdssDR7 database as outlined in Section 6.2.1, with the exception that galaxies were extracted from within the cluster virial radius (R_{200}), as opposed to twice the X-ray extent defined by XAPA. R_{200} was estimated according to Section 7.3.1. As SDSS is a largely contiguous survey, an Edge-flag was not assigned to clusters partially located off the edge of the survey area, as had been the case with NXS 7.4. Instead, colour-composite images covering the extent of the virial radius for each cluster were eyeballed. If complete survey coverage was present, then an accurate optical richness measurement could be obtained. If not, they were excluded

from the sample. A universal field galaxy sample was then used for each cluster, following the procedure outlined in Section 6.2.2.

SDSS N_{200} Estimates

XCSRedSeqN$_{200}$ was run on this sample of 107 XCS-SDSS clusters, in the same manner as for NXS (§7.4). Consequently, N_{200} values were obtained for 92 SDSS clusters.

7.6 XCS ClusterZoo II

Before optical to X-ray scaling relations can be produced from the NXS and SDSS clusters with T_{200} and N_{200} values, the samples must be cleaned of spurious cluster detections. This was attempted by creating additional ClusterZoo's, similar to that described in Section 2.9, for the NXS (§7.6.1) and SDSS (§7.6.2) subsamples. The classification criteria was altered slightly from XCS-SDSS ClusterZoo I , however the catogory types *Gold*, *Silver*, *Bronze* remained the same. The classification criteria, used by NXS ClusterZoo and XCS-SDSS ClusterZoo II, are stated in Appendix B.

7.6.1 The NXS ClusterZoo

In 2010, an XCS-NXS ClusterZoo was created to classify XCSDR1, XCSDR2 and XCSDR3 cluster candidates observed by the NXS survey, designated NXS ClusterZoo. Only NXS clusters with measured T_X and N_{200} values were included in the Zoo[1]. Clusters were classified by eye based on NXS colour-composite images including information on the seeing and depth of the image (§4.4), as well as X-ray images and information. To aid in the classification process, NXS ClusterZoo included red sequence redshift information, colour-magnitude plots, and illustrations of the likelihood fit (*i.e.* figures similar to those presented in Section 5.5). The XCS images used in NXS ClusterZoo were created by Mark Hosmer, and the website created and hosted by Ben Hoyle.

Each candidate recieved an average of 1.6 classifications and was assigned its lowest classification. In this manner, 52 XCS candidates surveyed by NXS were classified as either a *Gold* or *Silver* Cluster. These clusters were then used in measuring NXS–XCS Optical to X-ray scaling relations (see §7.7).

[1]XCS aims to subject the entire NXS sample to NXS ClusterZoo at a later date.

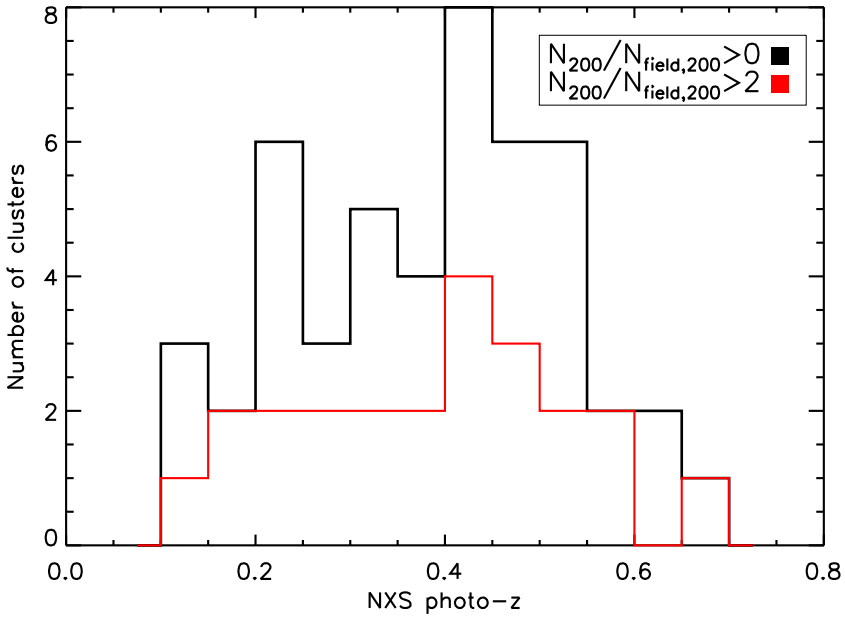

Figure 7.5 Redshift distribution of the NXS cluster sample with N_{200} estimates.

7.6.2 XCS-SDSS ClusterZoo II

In 2010, a second XCS-SDSS ClusterZoo was created and designated XCS-SDSS ClusterZooII. This was very similar to XCS-SDSS ClusterZooI (§2.9). It was used to classify 197 XCSDR3 cluster candidates with measured T_X and N_{200} values falling within the survey regions of SDSSDR7[2]. Classification was based on public SDSSDR7 colour-composite images, and XCS images created by Mark Hosmer. The website was created and hosted by Ben Hoyle.

Each candidate recieved an average of 1.6 classifications and was assigned it's lowest classification. In this manner, 141 XCSDR3 candidates were classified as either a *Gold* or *Silver* cluster. These clusters were then used in measuring SDSS–XCS Optical to X-ray scaling relations (§7.8).

7.7 Optical to X-ray Scaling Relations for NXS

Optical richnesses were estimated for 62 NXS clusters, of which 52 were classified as *Gold* or *Silver* clusters by NXS ClusterZoo. The distribution in redshift and N_{200} of this clean sample is shown in Figures 7.5 and 7.6 respectively.

Figures 7.7 and 7.8 show the pre-Zoo and post-Zoo N_{200}–T_X relations for the NXS

[2]XCS aims to subject the entire XCSDR3-v2 cluster sample falling within SDSS regions to XCS-SDSS ClusterZoo II at a later date.

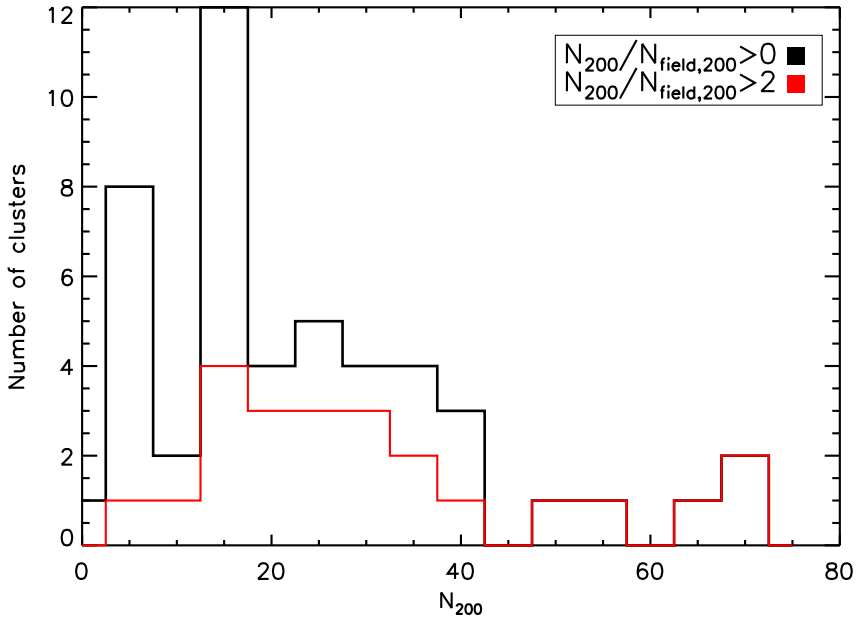

Figure 7.6 Richness distribution of NXS cluster sample with N_{200} estimates.

sample. The intensity of the points are scaled by the relative size of temperature errors (darkest points representing smaller temperature errors). As can be seen in Figure 7.8, a suggested relation exists amongst systems with smaller temperature errors (represented by the darker points). These Figures illustrate the need for ClusterZoo, as made evident by the reduced scatter (identifiable by eye) in the inferred optical scaling relation once spurious cluster detections are removed. This reduced scatter is noticable at the low temperature, low richness end of the sample.

Furthermore, it is reasonable to assume that clusters detected with small numbers of galaxies (N_{200}) compared to the background field sample ($N_{field,200}$) are likely to have their N_{200} values more heavily influenced by variations in the background field sample. Therefore, we decide to treat the N_{200} values obtained from these systems with caution. Consequently, we choose to adopt a minimum threshold upon the number of red sequence galaxies detected by XCSRedSeqN$_{200}$ compared to the estimated field sample $N_{field,200}$. In this manner, we choose to implement a N_{200} to $N_{field,200}$ ratio cut of $N_{200}/N_{field,200}$=2 to identify systems detected with uncertain N_{200} values and represent these values as lower limits only (see Figure 7.9). Subjecting the clean sample of 52 clusters to this $N_{200}/N_{field,200}$ threshold cut, resulted in a sample of 23 remaining clusters with more reliable N_{200} values.

As can be seen in the Figure 7.9, most of the outliers on the inferred N_{200}–T_X scaling

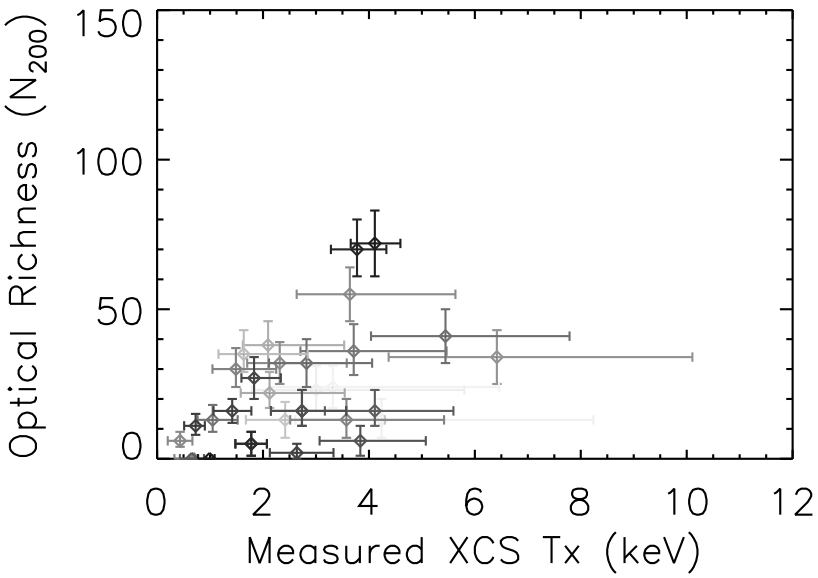

Figure 7.7 The N_{200}–T_X relation for NXS sample prior to classification using NXS ClusterZoo. Darker points represent those clusters with smaller measured temperature errors.

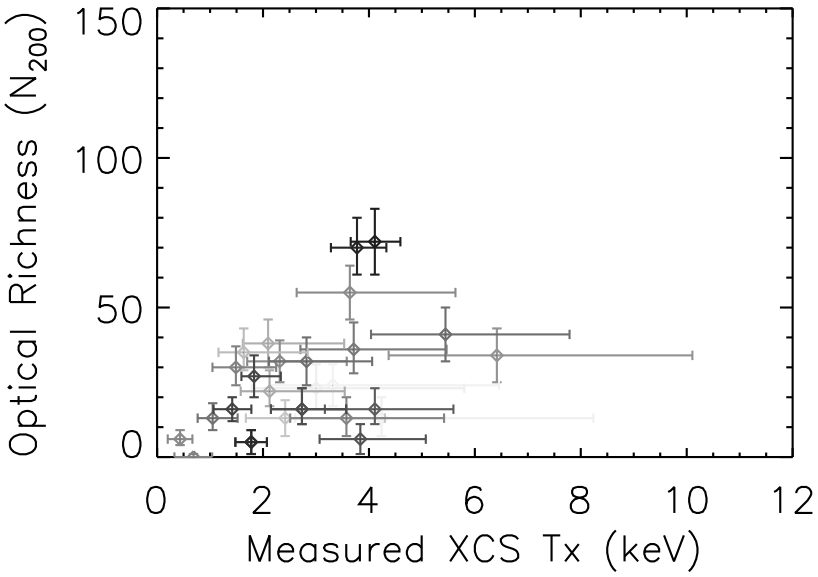

Figure 7.8 The N_{200}–T_X relation for NXS confirmed clusters. Darker points represent those clusters with smaller measured temperature errors.

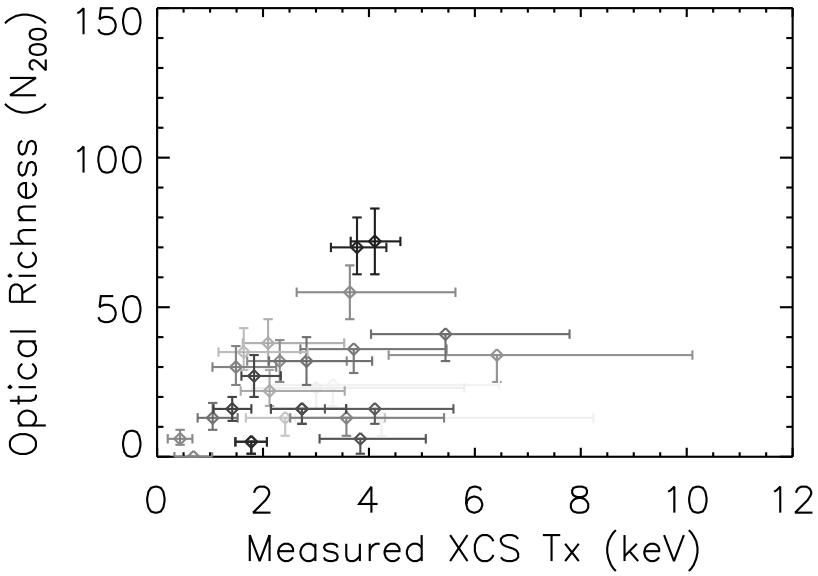

Figure 7.9 The N_{200}–T_X relation for NXS confirmed clusters. Darker points represent those clusters with smaller measured temperature errors. Clusters where the N_{200} value was detected with a $N_{200}/N_{field,200}$ ratio less than 2 are shown as upper limits only.

relation, are clusters that have been detected with a low $N_{200}/N_{field,200}$ ratio. These clusters tend to be located at the higher temperature end of the sample. For clarity, we remove these low level cluster detections from our scaling relation, illustrated in Figure 7.10. The clusters in 7.10 show much reduced scatter (identifiable by eye) compared to that in Figure 7.9.

Assuming that these low level cluster detections are providing uncertain N_{200} values, we thus chose to fit for an N_{200}–T_X scaling relation only using the clean sample of clusters, detected with a $N_{200}/N_{field,200}$ ratio of at least 2. The resulting scaling relation and fit paramters (determined by Ed Lloyd-Davies) is shown in Figure 7.11. As can be seen in the Figure, for these NXS clusters, a power law N_{200} – T_X scaling relation is obtained with a slope and normalisation given by 1.05±0.11 and 1.15±0.04 respectively.

7.8 Optical to X-ray Scaling Relations for SDSS

The process described in Section 7.7 was repeated for the XCS-SDSS sample.

Optical richnesses were estimated for 92 SDSS clusters, of which 66 were classified as *Gold* or *Silver* clusters by XCS-SDSS ClusterZoo II. The distribution in redshift and N_{200} of this clean sample is shown in Figures 7.12 and 7.13 respectively.

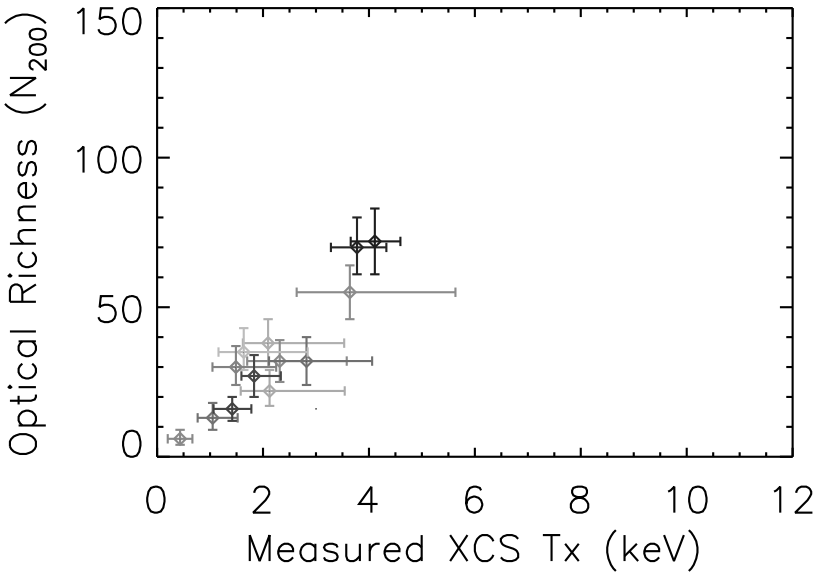

Figure 7.10 The N_{200}–T_X relation for NXS confirmed clusters detected with a $N_{200}/N_{field,200}$ ratio greater than 2. Darker points represent those clusters with smaller measured temperature errors.

Figures 7.14 and 7.15 show the pre-Zoo and post-Zoo optical richness to X-ray temperature scaling relations for the SDSS sample. The removal of spurious cluster detections via XCS-SDSS ClusterZoo II, shows an improvement in the scatter observed in Figure 7.14 (identified by eye). This improvement is most noticable at the low temperature, high richness end of the SDSS cluster sample (Figure 7.15). We decide to subject the SDSS sample to the same N_{200} to $N_{field,200}$ ratio cut of $N_{200}/N_{field,200}$=2 as implemented for the NXS sample. Clusters detected below this threshold are represented only as upper limits in Figure 7.16 and are removed completely in 7.17. The obtained fit to the SDSS N_{200}–T_X scaling relation (determined by Ed Lloyd-Davies) is illustrated in 7.18. As can be seen in Figure 7.11, a power law N_{200} – T_X scaling relation is obtained for SDSS clusters, with a slope and normalisation given by 1.11±0.11 and 1.14±0.05 respectively. Moreover, this relation is consistant, within the estimated errors, to that obtained by NXS.

7.9 Discussion

In this chapter, we have discussed the development of XCSRedSeqN$_{200}$, the adopted method of assigning optical richness, N_{200}, to XCS clusters, using the red sequence technique. Applying XCSRedSeqN$_{200}$ to confirmed clusters with XCS measured tempera-

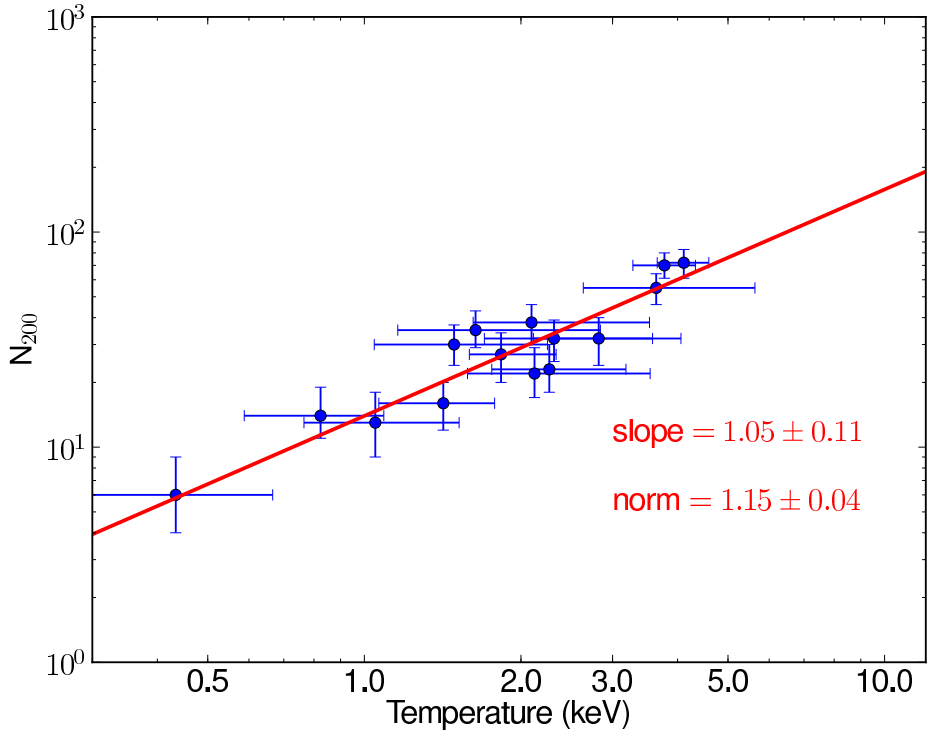

Figure 7.11 The inferred scaling relation for NXS confirmed clusters detected with a $N_{200}/N_{field,200}$ ratio greater than 2. Values for the slope and normalisation of the scaling relation fit are shown.

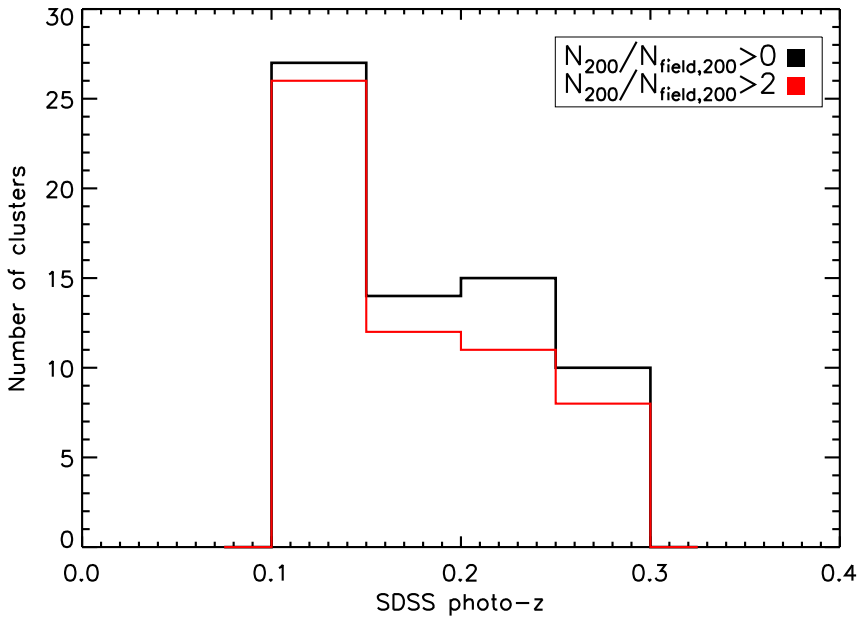

Figure 7.12 Redshift distribution of the SDSS cluster sample with N_{200} estimates.

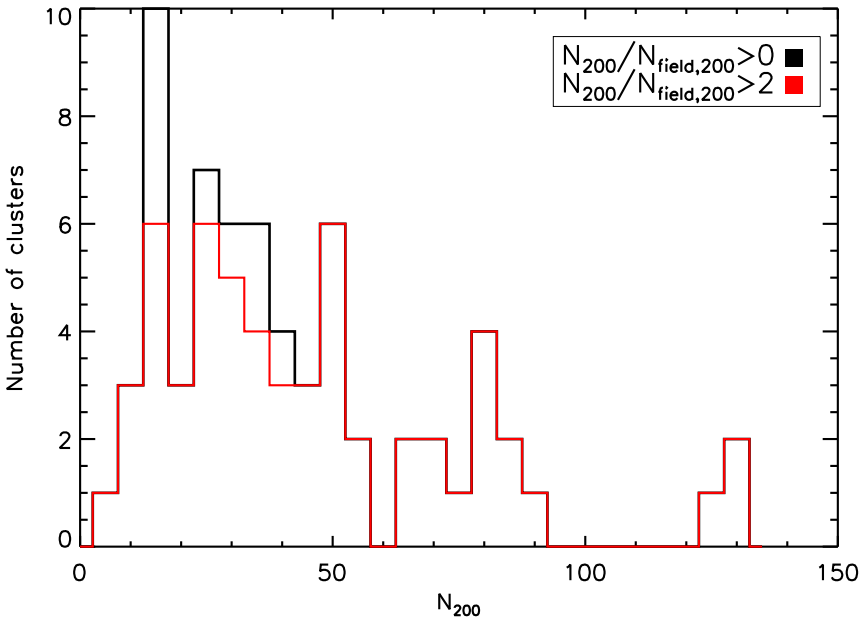

Figure 7.13 Richness distribution of SDSS cluster sample with N_200 estimates

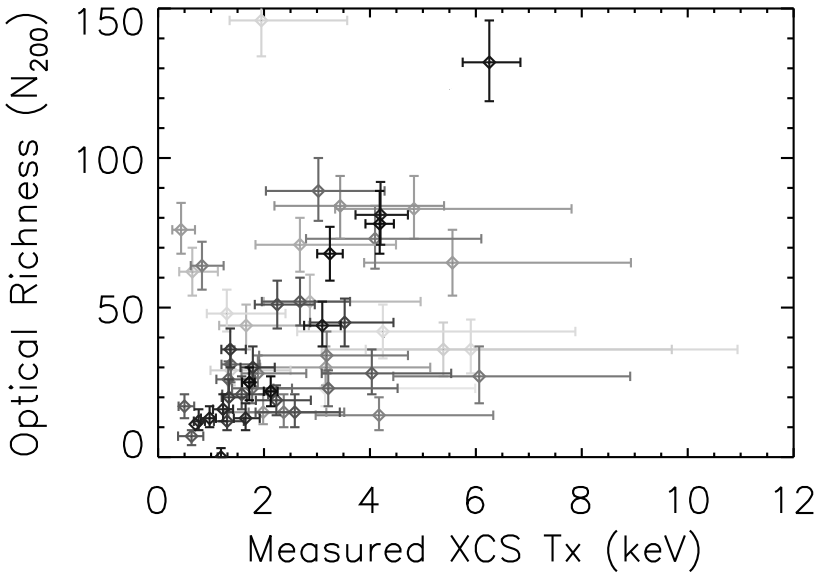

Figure 7.14 The N_{200}–T_X relation for SDSS sample prior to classification using XCS-SDSS ClusterZoo II. Darker points represent those clusters with smaller measured temperature errors.

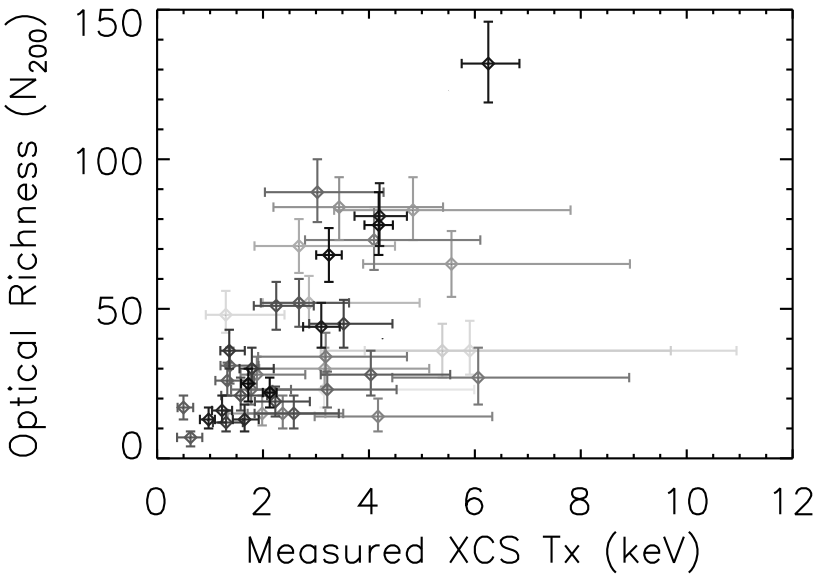

Figure 7.15 The N_{200}–T_X relation for SDSS confirmed clusters. Darker points represent those clusters with smaller measured temperature errors.

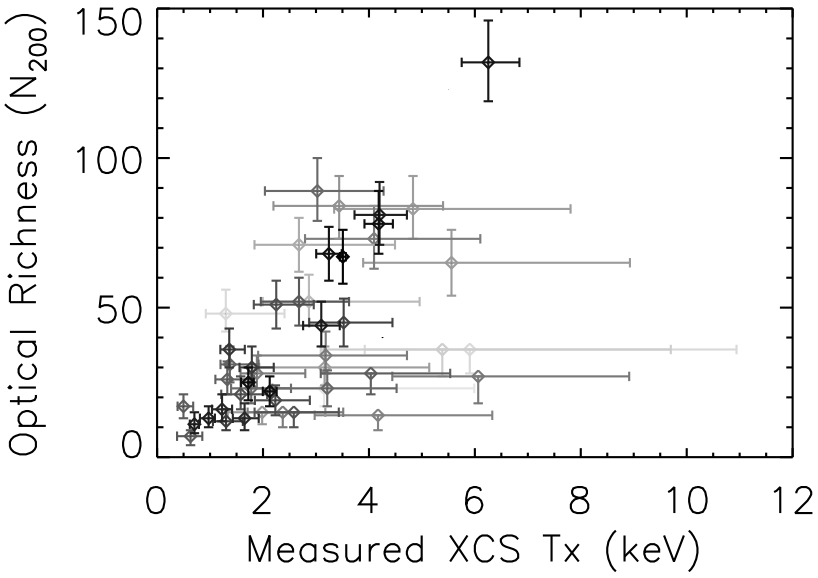

Figure 7.16 The N_{200}–T_X relation for SDSS confirmed clusters. Darker points represent those clusters with smaller measured temperature errors. Clusters where the N_{200} value was detected with a N_{200} to $N_{field,200}$ ratio of less than 2 are shown as upper limits only

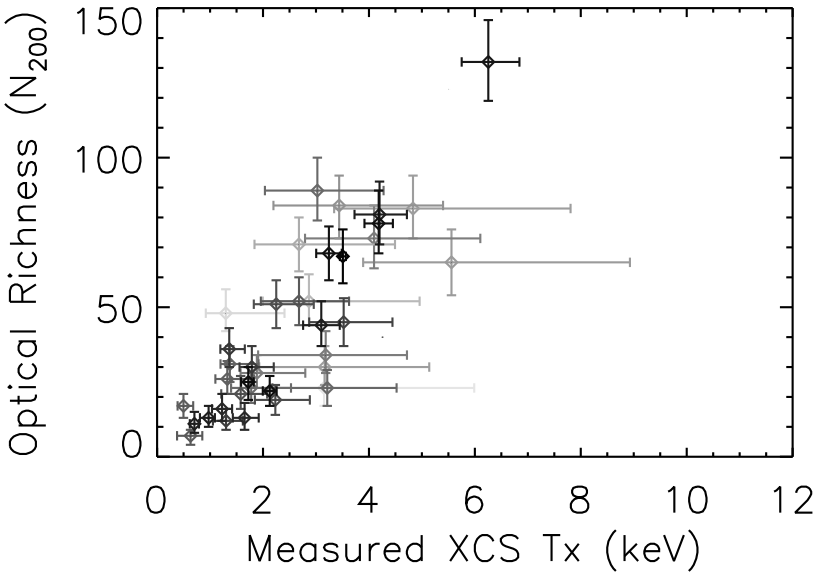

Figure 7.17 The N_{200}–T_X relation for SDSS confirmed clusters detected with a N_{200} to $N_{field,200}$ ratio greater than 2. Darker points represent those clusters with smaller measured temperature errors.

tures in both the NXS and SDSS samples, generated N_{200} estimates for 52 and 66 XCS clusters respectively. Optical scaling relations were then fitted for the sample of clusters, in which the number of galaxies falling on the red sequence relation, *i.e* the value of N_{200}, was twice the number estimated from the background field distribution, *i.e.* the value of $N_{field,200}$. The resulting fits implied a power law scaling relation between optical richness and X-ray temperature for XCS clusters. Morever, the power law slope and zeropoint for both the NXS and SDSS cluster samples were consistent within the estimated errors.

Our results compare favourably to previous work in this field. For example Yee and Ellingson (2003) predict the slope of the richness to temperature relation to be roughly unity, as we have found (although a more thorough comparison with their work, especially with regard to richness determination, is required before firm conclusions can be made). The redshift range of our scaling relation is similar to that presented in Hicks et al. (2006), $0.17 \leq z \leq 0.55$, based on CNOC and Chandra re-observations of EMSS X-ray clusters. However, their conclusions were based on only 14 systems, whereas we have more than 100. In Hicks et al. (2008), a higher redshift comparison to the 2006 work was presented, in which they presented Chandra observations of ten RCS clusters (redshifts $0.6 < z < 1$). Our sample does not yet probe to the depth of Hicks et al. (2008), however, this should

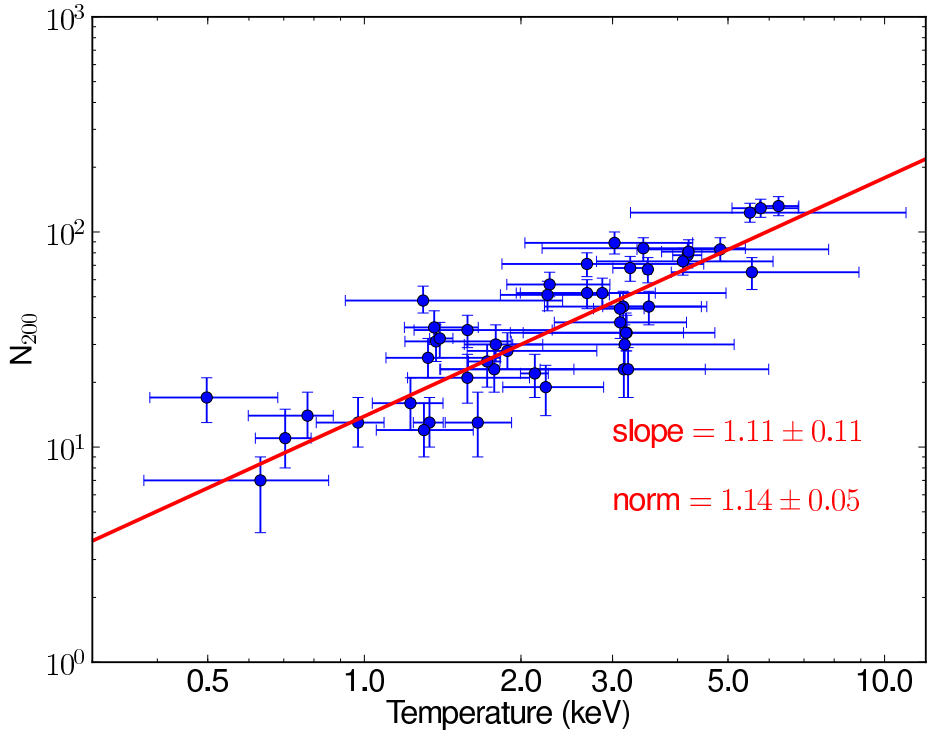

Figure 7.18 The inferred scaling relation for SDSS confirmed clusters detected with a N_{200} to $N_{field,200}$ ratio greater than 2. Values for the slope and normalisation of the scaling relation fit are shown.

be possible with the addition of deep XCS follow-up photometry.

The emergence of an optical to X-ray scaling relation from XCS adds weight to the claim made by the DES project that precision cosmology can be derived from DES cluster samples. Although these samples will be richness selected, by bootstrapping from optical to X-ray scaling relations, such as that derived from XCS, DES will be able place its clusters into mass bins and hence measure cosmological parameters. For example Wu et al. (2010), presented a scheme whereby the "Dark Energy Figure of Merit" (Albrecht et al., 2009) can be maximised via an optimised strategy of X-ray or SZ follow-up. Importantly, a large portion of the X-ray follow-up they proposed is in fact already available from XCS.

Furthermore, we can use our derived scaling relation to predict T_X, and hence mass values for clusters with optical photometry. As can be seen from Figure 7.10, for a given N_{200} value, a T_X can be estimated to within $\sim$2 keV, if the low detection systems are excluded. Thus, we can predict which clusters, for example in MaxBCG, will have sufficiently high temperatures to be detectable by Planck, even when X-ray follow-up is not available. Similarly, for XCS clusters with well determined N_{200} values, but only a few soft counts, a strong case can be made for additional XMM and Chandra follow-up in order to secure sufficient T_X measurements for the purposes of DES mass calibrations.

Importance of XCS Cluster Zoo

We draw attention to the role that Cluster Zoo has played in the determination of the preliminary optical to X-ray scaling relations from XCS. Subjecting the SDSS sample to XCS-SDSS ClusterZoo II, resulted in $\sim$30% of the XCS candidates being classed as spurious cluster detections. Whereas, $\sim$16% of the NXS sample subjected to NXS ClusterZoo, were classes as spurious cluster detections. The NXS zoo results are comparable to those found by XCS-SDSS ClusterZoo I for the 300 count sample. This discrepancy may be the result of eyeballing NXS targets prior to optical follow-up. In addition, it was based on clusters derived from the XCSDR1 and XCSDR2 lists, whereas XCS-SDSS ClusterZoo II, included the uncorrected version of XCSDR3. However, we note that classifications were conservative and each candidate only recieved 1.6 classifications. This result will be tested further upon the inclusion of the entire NXS and SDSS samples (with no soft count restrictions), along with the inclusion of XCSDR3-v2. Furthermore, we note that by only using *Gold* and *Silver* classed clusters in the fit, we may be artificially biasing the sample toward rich, centrally concentrated systems (See **Potential Selection Bias** below).

Ideally one would not use eye-ball classifications, as these may fold significant biases

into the selection function which cannot be modelled. Therefore, we plan to use statistical, rather than eye-ball, techniques to remove clusters with systematic errors in their derived properties (*i.e.* redshift, T_X, N_{200}) from the optical to X-ray scaling relations. For example, a cluster with high levels of AGN contamination would be removed from the fit. The results of ClusterZoo will be very useful in determining statistical thresholds upon which to clean these cluster samples.

Potential Selection Bias

As can be seen in Figures 7.9 and 7.16, most of the outliers on the relation are clusters with N_{200} to $N_{field,200}$ ratios. Therefore, they may have a higher optical richness that could not be detected by XCSRedSeqN$_{200}$. Thus in theory, these clusters may have higher richnesses and could lie on the observed relation. In which case, this relation may be one intrinsic to clusters.

However, these outliers generally have higher temperatures than the majority of the sample. Therefore this apparent relation may in fact be a selection effect. This is because hotter clusters have larger virial radii and as a consequence, the field contamination within R_{200} will be higher. This increased field contamination may inhibit XCSRedSeqN$_{200}$ from measuring a cluster signal. Consequently, it may be that XCSRedSeqN$_{200}$ is restricted to measuring the N_{200} values for only low temperature, and/or rich systems. In order to test the presence of a selection effect, a selection function should be determined. However, this is more difficult for cluster galaxy observables than it is for cluster X-ray observables (§2.6), as the galaxy distribution is more complex than a simple β-model. One approach however, would be to test the recovery rates and derived N_{200} values of mock clusters placed into NXS or SDSS images over a grid of T_X and z.

One drawback of our current sample is the lack of high temperature clusters with well determined T_X values. One way to test whether the problems at the high T_X end are due to the X-ray, or to the optical data, or to the N_{200} measurement technique, would be to use XMM targetted clusters. These are clusters specifically targetted by XMM, rather than serendipitous detections and are therefore not in XCS. These targetted clusters are generally detected with much higher counts than the XCS cluster sample. Moreover, they tend to be higher temperature than the average population because they are usually selected for follow-up from less sensitive surveys, such as RASS.

If a significant selection bias against high temperature, and/or poor systems is confirmed, then XCS may consider using a different richness estimator, for example the Bgc

method adopted by RCS (§1.6.3). This is because Bgc uses a smaller radius and folds in the spatial distribution of clusters into its estimate.

N_{gal} within a fixed aperture ($N_{gal,500kpc}$)

As mentioned in the discussion point 'Potential Selection Bias' higher redshift clusters suffer from increasing levels of field contamination within their virial radius (R_{200}), as the number density of background field galaxies gets larger. In an attempt to limit the field contamination for these systems, it may be prudent to use a fixed aperture concentrated in the central region of the cluster core, rather than one scaled to the larger virial radius. This may also help reduce any potential selection bias that may occour from throwing out systems detected with low numbers of cluster galaxies relative to the background field sample. Importantly, using a fixed aperture removes the need for a priori knowledge on the mass and therefore radius of the cluster. This makes the inferred scaling relation of greater use to the scientific community as a tool to attribute a mass to optically detected clusters using optical data alone.

For this reason, we have decided to measure the number of galaxies to within a fixed radius of the central 500kpc for each cluster. To do this, we use the algorithm XCSRedSeqN$_{500kpc}$, which is exactly the same as XCSRedSeqN$_{200}$ but uses the fixed radius 500kpc, instead of the virial radius R_{200}. XCSRedSeqN$_{500kpc}$ was run on the NXS and SDSS XCSDR3 sub-samples of ClusterZoo confirmed clusters to produce $N_{gal,500}$ values for 33 and 56 clusters respectively. The results of $N_{gal,500}$ versus X-ray temperature are shown for the NXS and SDSS samples in Figures 7.19 and 7.20, along with their inferred scaling relations. No cuts have been made on the number of cluster galaxies compared to the number of field galaxies detected on the red sequence relation in order to reduce any potential selection bias; however, only systems with temperature errors less than 100% have been used in the comparison.

Both Figures 7.19 and 7.20, show a relation between $N_{gal,500kpc}$ and X-ray temperature, however, the scatter in these relations are much larger (identified by eye) compared to their respective relations using N_{200} as a richness measure (shown in Figures 7.11 and 7.18). In addition, the inferred slopes of 1.15±0.25 and 0.64±0.15 for the respective NXS and SDSS samples are inconsistent within the errors. In an attempt to reduce the scatter in these scaling relations, we cut on all systems with measured temperature errors greater than 50%. These resulting scaling relations for the NXS and SDSS samples are shown in Figures 7.21 and 7.22 respectively. Only including systems with temperature errors less

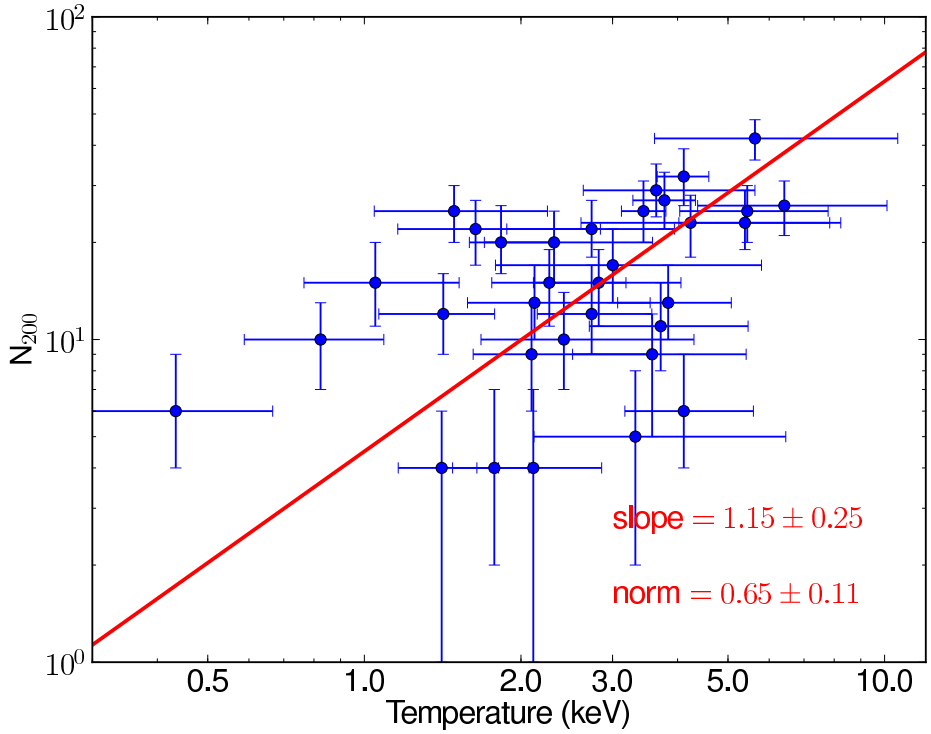

Figure 7.19 The inferred scaling relation of $N_{ga,500kpc}$ versus X-ray temperature for 33 NXS confirmed clusters. Values for the slope and normalisation of the scaling relation fit are shown.

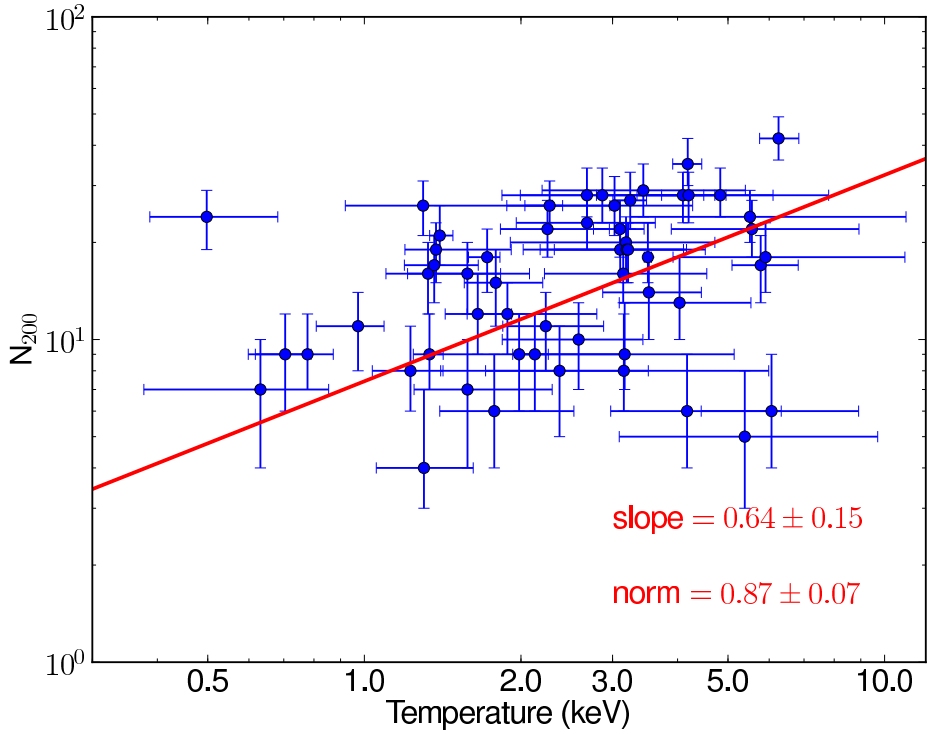

Figure 7.20 The inferred scaling relation of $N_{gal,500kpc}$ versus X-ray temperature for 56 SDSS confirmed clusters. Values for the slope and normalisation of the scaling relation fit are shown.

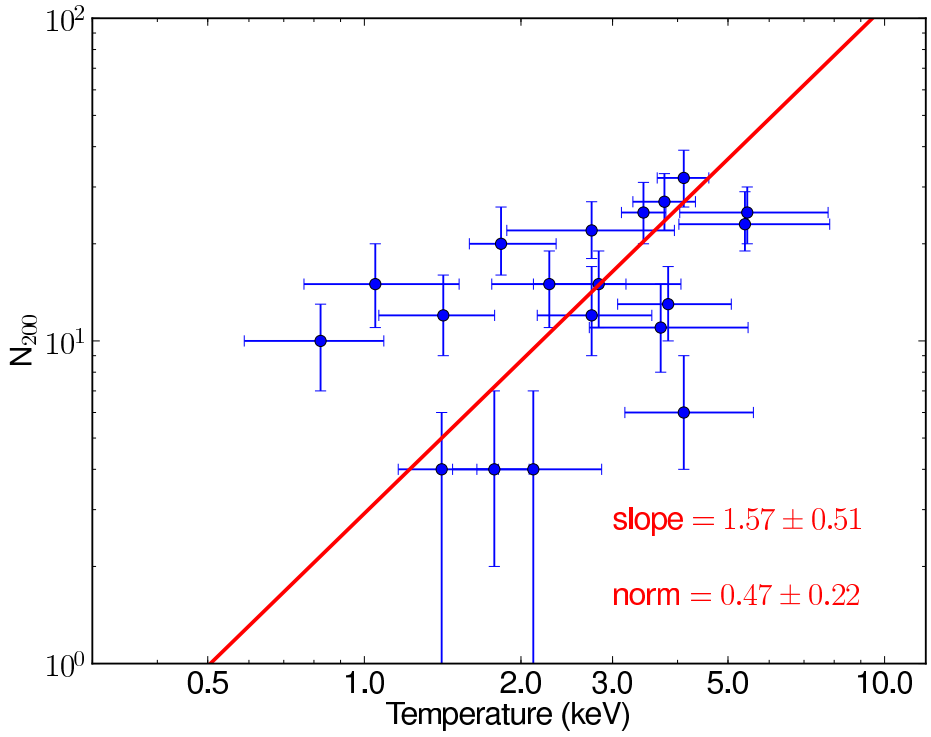

Figure 7.21 The inferred scaling relation of $N_{ga,500kpc}$ versus X-ray temperature for 19 NXS confirmed clusters with measured temperatures having errors less than 50%. Values for the slope and normalisation of the scaling relation fit are shown.

than 50% has improved the scatter for the SDSS sample but has failed to improve that of the NXS sample. Furthermore, the inferred scaling relations of 1.57±0.51 and 0.78±0.17 for the NXS and SDSS samples respectively, are inconsistent within the errors. As such, these scaling relations are of limited use as an optical richness to X-ray temperature scaling relation at this time.

Impact of Photo-z Errors

It should be noted that the effect of cluster photometric redshift errors have not been taken into account in our scaling relation fits. Whilst redshift errors do not alter the size of the colour cuts on the observed red sequence relation, they greatly impact the estimated temperature of the cluster, which in turn impacts the assumed virial radius and as a consequence, the number of red sequence galaxies included in the N_{200} estimate.

We can explore the impact of photometric redshift errors on the optical to X-ray scaling relations by using the subsample of clusters that have estimated redshifts from both XCSRedSeq and from one or more other source, *e.g.* the literature. We can also use

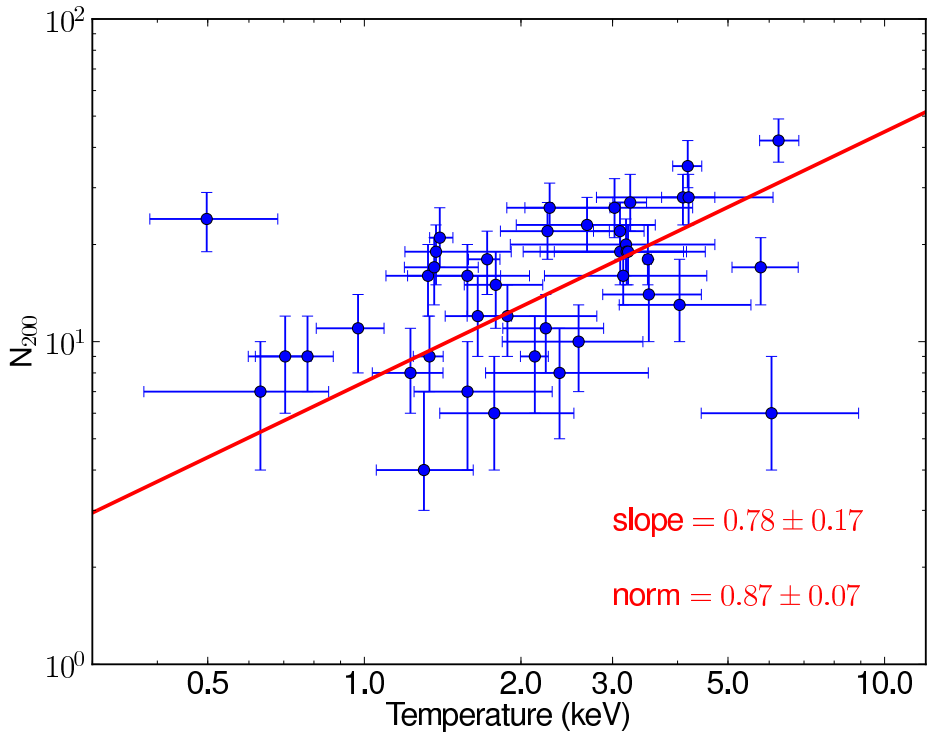

Figure 7.22 The inferred scaling relation of $N_{gal,500kpc}$ versus X-ray temperature for 42 SDSS confirmed clusters with measured temperatures having errors less than 50%. Values for the slope and normalisation of the scaling relation fit are shown.

those clusters that have multiple XCSRedSeq redshifts, *e.g.* those in SDSS regions that overlap with NXS. For these clusters we can compare the T_X and N_{200} values produced from the different redshift estimates to determine the scale of the effect. The addition of spectroscopic follow-up to XCS clusters would be of benefit to this investigation as uncertainties in redshifts would become negligible. However, it is unlikely more than a fraction of the clusters with XCSRedSeq redshifts (from NXS or SDSS) will be followed up with spectroscopy. Several proposals to carry out such follow-up have been submitted, however, none have been successful.

Extending the Cluster Sample

One could expand the cluster sample by applying an $L_X - T_X$ relation to those clusters which have insufficient counts for a T_X measurement, but sufficient counts for an L_X measurement. This has the potential to bring hundreds more clusters into our analysis, because we have so far not fully exploited the SDSS data that overlaps XCSDR3 (to date we have only examined those candidates with sufficient counts for T_X measurements). An initial investigation into an $N_{200} - T_{X,L-T}$ relation using XCSDR1 (Figure 7.23) shows this method has potential. Indeed Figure 7.23 even shows hints of two populations; one following a possible power law scaling relation, similar to that described above, and an additional, less steeply rising relation. No detection threshold cuts (*i.e* a minimum $N_{200}/N_{field,200}$ ratio) have been implemented on this sample, however, this second relation may be the result of low N_{200} to $N_{field,200}$ detections. In addition to expanding the number of low redshift clusters in the fit using SDSS, we could also increase the number of higher redshift clusters in the fit by extending the analysis to sample both Stripe82 and NXS clusters with less than 300 counts. One possible advantage (to expanding the sample size) of using an $L_X - T_X$ relation to estimate the virial radius is that we could adopt an iterative approach to measuring the red sequence redshift used to select the colour of the red sequence galaxies in the N_{200} estimate; rather than using a fixed aperture of twice the XAPA extent, we could use something more physical (*i.e.* an approach similar to that adopted to extract literature redshifts from NED, §2.8.1).

Alternatively, one could request additional photometry for clusters with good T_X measurements, but insufficient imaging to obtain a reliable N_{200} value. However, most imagers cover large field of views and are not designed to follow up individual (arcminute sized) objects. It would only be worthwhile to obtain such photometry for particularly interesting systems, for example those expected to be at redshift $z > 1$ and/or have $T_X > 6$ keV (the

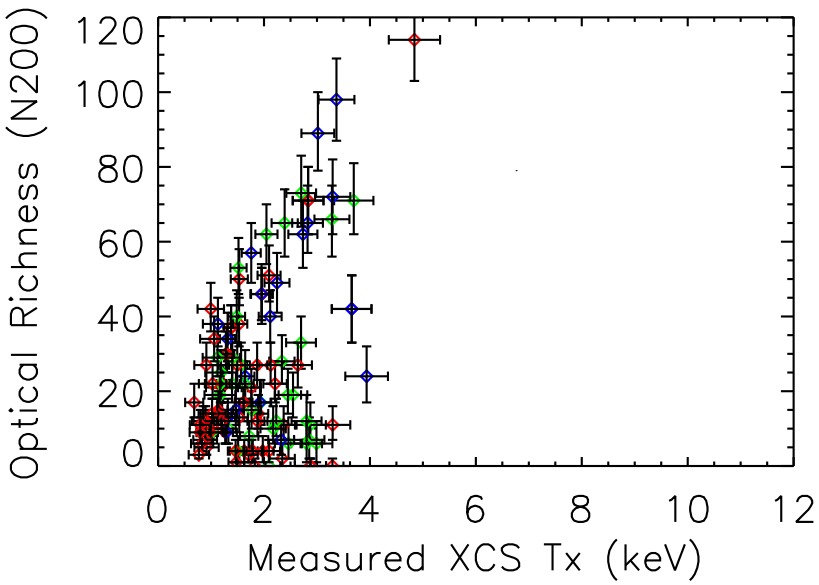

Figure 7.23 The N_{200}–T_X relation for the XCSDR3 sample falling in SDSS prior to classification using SDSS ClusterZoo II. Temperatures are estimated from the XCS $L_X - T_X$ relation. Red points represent clusters between $0.1<z<0.17$, green points represent clusters between $0.17<z<0.24$, blue points represent clusters between $0.24<z<0.3$. No cut has been made on a minimum $N_{200}/N_{field,200}$ value.

latter being the types of systems accessible to the current generation of SZ surveys). In the medium future, a large fraction of the XCS candidates will have been observed by DES. At that time, one will be able to rerun XCSRedSeqN$_{200}$ to the depths of Stripe82 over large contiguous regions. Moreover, DES provides several colours and this may enhance our ability to remove background contamination.

With an expanded sample we can begin to look for trends in the optical to X-ray scaling relation. For example, we can investigate the presence of any evolution in the $N_{200} - T_X$ scaling relation. Furthermore, it would also be interesting to examine the effect of X-ray properties, such as cool cores, on the inferred optical to X-ray relation. One would expect the scatter in the derived relation to be less for the cool core systems as these are assumed to be relaxed. In addition, we could make more use of the X-ray spectroscopy. XAPA-2 produces X-ray spectral fits to all XCS clusters with redshifts, under the assumption that the dominant emission mechanism is thermal bremstrahlung. By comparing the goodness of fit for a thermal spectrum to one dominated by power law emission, one might be able to pick out clusters suffering from high levels of AGN contamination before including them in the optical to X-ray scaling relation fit.

Summary of the Main Successes in this Thesis

- Acquisition and reduction of 38 nights of 4m MOSAIC imaging (covering 628 XCS cluster targets).
- Design of a red sequence redshift algorithms (XCSRedSeq) that is accurate to Δz=0.04 (SDSS) and Δz=0.07 (NXS).
- Measurement of 473 NXS redshifts (0.1<z< 1).
- Measurement of 603 SDSS redshifts (0.1<z<0.5).
- Measurement of 100 Stripe82 redshifts (0.1<z<0.8).
- Design of red sequence N_{gal} algorithm (XCSRedSeqN$_{200}$).
- Measurement of 92 NXS N_{200} values.
- Measurement of 62 SDSS N_{200} values.
- Production of a preliminary Optical to X-ray scaling relation from >100 XCS clusters.

- Facilitation of other XCS science (by supplying extra redshifts), e.g. the $L_X - T_X$ relation derived from > 500 XCS clusters.

Bibliography

Abazajian, K., Adelman-McCarthy, J. K., Agüeros, M. A., Allam, S. S., Anderson, K., Anderson, S. F., Annis, J., Bahcall, N. A., Baldry, I. K., Bastian, S., Berlind, A., Bernardi, M., Blanton, M. R., Bochanski, Jr., J. J., Boroski, W. N., Briggs, J. W., Brinkmann, J., Brunner, R. J., Budavári, T., Carey, L. N., Carliles, S., Castander, F. J., Connolly, A. J., Csabai, I., Doi, M., Dong, F., Eisenstein, D. J., Evans, M. L., Fan, X., Finkbeiner, D. P., Friedman, S. D., Frieman, J. A., Fukugita, M., Gal, R. R., Gillespie, B., Glazebrook, K., Gray, J., Grebel, E. K., Gunn, J. E., Gurbani, V. K., Hall, P. B., Hamabe, M., Harris, F. H., Harris, H. C., Harvanek, M., Heckman, T. M., Hendry, J. S., Hennessy, G. S., Hindsley, R. B., Hogan, C. J., Hogg, D. W., Holmgren, D. J., Ichikawa, S., Ichikawa, T., Ivezić, Ž., Jester, S., Johnston, D. E., Jorgensen, A. M., Kent, S. M., Kleinman, S. J., Knapp, G. R., Kniazev, A. Y., Kron, R. G., Krzesinski, J., Kunszt, P. Z., Kuropatkin, N., Lamb, D. Q., Lampeitl, H., Lee, B. C., Leger, R. F., Li, N., Lin, H., Loh, Y., Long, D. C., Loveday, J., Lupton, R. H., Malik, T., Margon, B., Matsubara, T., McGehee, P. M., McKay, T. A., Meiksin, A., Munn, J. A., Nakajima, R., Nash, T., Neilsen, Jr., E. H., Newberg, H. J., Newman, P. R., Nichol, R. C., Nicinski, T., Nieto-Santisteban, M., Nitta, A., Okamura, S., O'Mullane, W., Ostriker, J. P., Owen, R., Padmanabhan, N., Peoples, J., Pier, J. R., Pope, A. C., Quinn, T. R., Richards, G. T., Richmond, M. W., Rix, H., Rockosi, C. M., Schlegel, D. J., Schneider, D. P., Scranton, R., Sekiguchi, M., Seljak, U., Sergey, G., Sesar, B., Sheldon, E., Shimasaku, K., Siegmund, W. A., Silvestri, N. M., Smith, J. A., Smolčić, V., Snedden, S. A., Stebbins, A., Stoughton, C., Strauss, M. A., SubbaRao, M., Szalay, A. S., Szapudi, I., Szkody, P., Szokoly, G. P., Tegmark, M., Teodoro, L., Thakar, A. R., Tremonti, C., Tucker, D. L., Uomoto, A., Vanden Berk, D. E., Vandenberg, J., Vogeley, M. S., Voges, W., Vogt, N. P., Walkowicz, L. M., Wang, S., Weinberg, D. H., West, A. A., White, S. D. M., Wilhite, B. C., Xu, Y., Yanny, B., Yasuda, N., Yip, C., Yocum, D. R., York, D. G., Zehavi, I., Zibetti, S., and Zucker, D. B. (2004). The Second Data Release of the Sloan Digital Sky Survey. *AJ*, 128:502–512. Cited on 53, 129, 165

Abazajian, K. N., Adelman-McCarthy, J. K., Agüeros, M. A., Allam, S. S., Allende Prieto, C., An, D., Anderson, K. S. J., Anderson, S. F., Annis, J., Bahcall, N. A., Bailer-Jones, C. A. L., Barentine, J. C., Bassett, B. A., Becker, A. C., Beers, T. C., Bell, E. F., Belokurov, V., Berlind, A. A., Berman, E. F., Bernardi, M., Bickerton, S. J., Bizyaev, D., Blakeslee, J. P., Blanton, M. R., Bochanski, J. J., Boroski, W. N., Brewington, H. J., Brinchmann, J., Brinkmann, J., Brunner, R. J., Budavári, T., Carey, L. N., Carliles, S., Carr, M. A., Castander, F. J., Cinabro, D., Connolly, A. J., Csabai, I., Cunha, C. E., Czarapata, P. C., Davenport, J. R. A., de Haas, E., Dilday, B., Doi, M., Eisenstein, D. J., Evans, M. L., Evans, N. W., Fan, X., Friedman, S. D., Frieman, J. A., Fukugita, M., Gänsicke, B. T., Gates, E., Gillespie, B., Gilmore, G., Gonzalez, B., Gonzalez, C. F., Grebel, E. K., Gunn, J. E., György, Z., Hall, P. B., Harding, P., Harris, F. H., Harvanek, M., Hawley, S. L., Hayes, J. J. E., Heckman, T. M., Hendry, J. S., Hennessy, G. S., Hindsley, R. B., Hoblitt, J., Hogan, C. J., Hogg, D. W., Holtzman, J. A., Hyde, J. B., Ichikawa, S.-i., Ichikawa, T., Im, M., Ivezić, Ž., Jester, S., Jiang, L., Johnson, J. A., Jorgensen, A. M., Jurić, M., Kent, S. M., Kessler, R., Kleinman, S. J., Knapp, G. R., Konishi, K., Kron, R. G., Krzesinski, J., Kuropatkin, N., Lampeitl, H., Lebedeva, S., Lee, M. G., Lee, Y. S., Leger, R. F., Lépine, S., Li, N., Lima, M., Lin, H., Long, D. C., Loomis, C. P., Loveday, J., Lupton, R. H., Magnier, E., Malanushenko, O., Malanushenko, V., Mandelbaum, R., Margon, B., Marriner, J. P., Martínez-Delgado, D., Matsubara, T., McGehee, P. M., McKay, T. A., Meiksin, A., Morrison, H. L., Mullally, F., Munn, J. A., Murphy, T., Nash, T., Nebot, A., Neilsen, E. H., Newberg, H. J., Newman, P. R., Nichol, R. C., Nicinski, T., Nieto-Santisteban, M., Nitta, A., Okamura, S., Oravetz, D. J., Ostriker, J. P., Owen, R., Padmanabhan, N., Pan, K., Park, C., Pauls, G., Peoples, J., Percival, W. J., Pier, J. R., Pope, A. C., Pourbaix, D., Price, P. A., Purger, N., Quinn, T., Raddick, M. J., Fiorentin, P. R., Richards, G. T., Richmond, M. W., Riess, A. G., Rix, H.-W., Rockosi, C. M., Sako, M., Schlegel, D. J., Schneider, D. P., Scholz, R.-D., Schreiber, M. R., Schwope, A. D., Seljak, U., Sesar, B., Sheldon, E., Shimasaku, K., Sibley, V. C., Simmons, A. E., Sivarani, T., Smith, J. A., Smith, M. C., Smolčić, V., Snedden, S. A., Stebbins, A., Steinmetz, M., Stoughton, C., Strauss, M. A., Subba Rao, M., Suto, Y., Szalay, A. S., Szapudi, I., Szkody, P., Tanaka, M., Tegmark, M., Teodoro, L. F. A., Thakar, A. R., Tremonti, C. A., Tucker, D. L., Uomoto, A., Vanden Berk, D. E., Vandenberg, J., Vidrih, S., Vogeley, M. S., Voges, W., Vogt, N. P., Wadadekar, Y., Watters, S., Weinberg, D. H., West, A. A., White, S. D. M., Wilhite, B. C., Wonders, A. C., Yanny, B., Yocum, D. R., York, D. G.,

Zehavi, I., Zibetti, S., and Zucker, D. B. (2009). The Seventh Data Release of the Sloan Digital Sky Survey. *ApJS*, 182:543–558. Cited on 44

Albrecht, A., Amendola, L., Bernstein, G., Clowe, D., Eisenstein, D., Guzzo, L., Hirata, C., Huterer, D., Kirshner, R., Kolb, E., and Nichol, R. (2009). Findings of the Joint Dark Energy Mission Figure of Merit Science Working Group. *ArXiv e-prints*. Cited on 177

Alexander, D. M., Bauer, F. E., Brandt, W. N., Schneider, D. P., Hornschemeier, A. E., Vignali, C., Barger, A. J., Broos, P. S., Cowie, L. L., Garmire, G. P., Townsley, L. K., Bautz, M. W., Chartas, G., and Sargent, W. L. W. (2003). The Chandra Deep Field North Survey. XIII. 2 Ms Point-Source Catalogs. *AJ*, 126:539–574. Cited on 23

Allen, S. W., Schmidt, R. W., and Fabian, A. C. (2002). Cosmological constraints from the X-ray gas mass fraction in relaxed lensing clusters observed with Chandra. *MNRAS*, 334:L11–L15. Cited on 8

Andreon, S. (2006). The build-up of the red sequence in the galaxy cluster ms1054-0321 at z=0.831. Cited on 17

Andreon, S. (2007). The history of mass assembly of faint red galaxies in 28 galaxy clusters since z=1.3. Cited on 17

Arnaud, M. and Evrard, A. E. (1999). The L_X-T relation and intracluster gas fractions of X-ray clusters. *MNRAS*, 305:631–640. Cited on 11

Baldry, I. K., Balogh, M. L., Bower, R. G., Glazebrook, K., Nichol, R. C., Bamford, S. P., and Budavari, T. (2006). Galaxy bimodality versus stellar mass and environment. Cited on 16

Balogh, M. L., Pearce, F. R., Bower, R. G., and Kay, S. T. (2001). Revisiting the cosmic cooling crisis. *MNRAS*, 326:1228–1234. Cited on 11

Becker, A. C., Rest, A., Stubbs, C., Miknaitis, G. A., Miceli, A., Covarrubias, R., Hawley, S. L., Aguilera, C., Smith, R. C., Suntzeff, N. B., Olsen, K., Prieto, J. L., Hiriart, R., Garg, A., Welch, D. L., Cook, K. H., Nikolaev, S., Clocchiatti, A., Minniti, D., Keller, S. C., and Schmidt, B. P. (2004). The supermacho microlensing survey. Cited on 53, 56

Becker, M. R., McKay, T. A., Koester, B., Wechsler, R. H., Rozo, E., Evrard, A., Johnston, D., Sheldon, E., Annis, J., Lau, E., Nichol, R., and Miller, C. (2007). The Mean

and Scatter of the Velocity Dispersion-Optical Richness Relation for maxBCG Galaxy Clusters. *ApJ*, 669:905–928. Cited on 19

Beers, T. C., Flynn, K., and Gebhardt, K. (1990). Measures of location and scale for velocities in clusters of galaxies - A robust approach. *AJ*, 100:32–46. Cited on 106

Bell, E. F., Wolf, C., Meisenheimer, K., Rix, H.-W., Borch, A., Dye, S., Kleinheinrich, M., Wisotzki, L., and McIntosh, D. H. (2004). Nearly 5000 distant early-type galaxies in combo-17: a red sequence and its evolution since z$\tilde{1}$. Cited on 16

Bertin, E. and Arnouts, S. (1996). SExtractor: Software for source extraction. *AAS*, 117:393–404. Cited on 80

Bialek, J. J., Evrard, A. E., and Mohr, J. J. (2001). Effects of Preheating on X-Ray Scaling Relations in Galaxy Clusters. *ApJ*, 555:597–612. Cited on 12

Bildfell, C., Hoekstra, H., Babul, A., and Mahdavi, A. (2008). Resurrecting the red from the dead: Optical properties of bcgs in x-ray luminous clusters. Cited on 13

Boehringer, H., Schuecker, P., Pratt, G. W., Arnaud, M., Ponman, T. J., Croston, J. H., Borgani, S., Bower, R. G., Briel, U. G., Collins, C. A., Donahue, M., Forman, W. R., Finoguenov, A., Geller, M. J., Guzzo, L., Henry, J. P., Kneissl, R., Mohr, J. J., Matsushita, K., Mullis, C. R., Ohashi, T., Pedersen, K., Pierini, D., Quintana, H., Raychaudhury, S., Reiprich, T. H., Romer, A. K., Rosati, P., Sabirli, K., Temple, R. F., Viana, P. T. P., Vikhlinin, A., Voit, G. M., and Zhang, Y. Y. (2007). The representative xmm-newton cluster structure survey (rexcess) of an x-ray luminosity selected galaxy cluster sample. Cited on 58

Bower, R. G., Lucey, J. R., and Ellis, R. S. (1992). Precision photometry of early-type galaxies in the Coma and Virgo clusters: A test of the universality of the colour-magnitude relation. I - The data. II. Analysis. *MNRAS*, 254:589–613. Cited on 14

Brown, M. J. I., Dey, A., Jannuzi, B. T., Lauer, T. R., Tiede, G. P., and Mikles, V. J. (2003). Red Galaxy Clustering in the NOAO Deep Wide-Field Survey. *ApJ*, 597:225–238. Cited on 63

Bruzual, G. and Charlot, S. (2003). Stellar population synthesis at the resolution of 2003. *MNRAS*, 344:1000–1028. Cited on 100

Cash, W. (1979). Parameter estimation in astronomy through application of the likelihood ratio. *ApJ*, 228:939–947. Cited on 110

Clowe, D., Bradac, M., Gonzalez, A. H., Markevitch, M., Randall, S. W., Jones, C., and Zaritsky, D. (2006). A direct empirical proof of the existence of dark matter. Cited on 4

Collins, C. A., Guzzo, L., Nichol, R. C., and Lumsden, S. L. (1995). The EDSGC - VII: The Edinburgh-Milano Cluster Redshift Survey. *ArXiv Astrophysics e-prints*. Cited on 9, 14

Collins, C. A., Stott, J. P., Hilton, M., Kay, S. T., Stanford, S. A., Davidson, M., Hosmer, M., Hoyle, B., Liddle, A., Lloyd-Davies, E., Mann, R. G., Mehrtens, N., Miller, C. J., Nichol, R. C., Romer, A. K., Sahlen, M., Viana, P. T. P., and West, M. J. (2009). Early assembly of the most massive galaxies. *Nature*, 458:603. Cited on 17, 33, 42

Cowie, L. L., Songaila, A., Hu, E. M., and Cohen, J. G. (1996). New insight on galaxy formation and evolution from keck spectroscopy of the hawaii deep fields. *Astronomical Journal*, 112:839. Cited on 17

Dahle, H., Pedersen, K., Lilje, P. B., Maddox, S. J., and Kaiser, N. (2003). Weak Gravitational Lensing by a Sample of X-Ray-luminous Clusters of Galaxies. III. Serendipitous Weak Lensing Detections of Dark and Luminous Mass Concentrations. *ApJ*, 591:662–676. Cited on 7

Davidson, M. (2005). A serendipitous survey of galaxy clusters with xmm-newton. *Ph.D. Thesis*. Cited on 23, 24

De Lucia, G. and Blaizot, J. (2007). The hierarchical formation of the brightest cluster galaxies. Cited on 15, 17

De Lucia, G., Poggianti, B. M., Aragón-Salamanca, A., Clowe, D., Halliday, C., Jablonka, P., Milvang-Jensen, B., Pelló, R., Poirier, S., Rudnick, G., Saglia, R., Simard, L., and White, S. D. M. (2004). The Buildup of the Red Sequence in Galaxy Clusters since z $\sim$ 0.8. *ApJL*, 610:L77–L80. Cited on 17

De Lucia, G., Poggianti, B. M., Aragon-Salamanca, A., White, S. D. M., Zaritsky, D., Clowe, D., Halliday, C., Jablonka, P., von der Linden, A., Milvang-Jensen, B., Pello', R., Rudnick, G., Saglia, R. P., and Simard, L. (2006). The build-up of the colour-magnitude relation in galaxy clusters since z$\sim$0.8. Cited on 17

de Propris, R., Stanford, S. A., Eisenhardt, P. R., Dickinson, M., and Elston, R. (1999).

The K-Band Luminosity Function in Galaxy Clusters to Z ˜1. *AJ*, 118:719–729. Cited on 15

Demarco, R., Wilson, G., Muzzin, A., Lacy, M., Surace, J., Yee, H. K. C., Hoekstra, H., Blindert, K., and Gilbank, D. (2010). Spectroscopic Confirmation of Three Red-sequence Selected Galaxy Clusters at z = 0.87, 1.16, and 1.21 from the SpARCS Survey. *ApJ*, 711:1185–1197. Cited on 16

Dilday, B., Smith, M., Bassett, B., Becker, A., Bender, R., Castander, F., Cinabro, D., Filippenko, A. V., Frieman, J. A., Galbany, L., Garnavich, P. M., Goobar, A., Hopp, U., Ihara, Y., Jha, S. W., Kessler, R., Lampeitl, H., Marriner, J., Miquel, R., Molla, M., Nichol, R. C., Nordin, J., Riess, A. G., Sako, M., Schneider, D. P., Sollerman, J., Wheeler, J. C., Ostman, L., Bizyaev, D., Brewington, H., Malanushenko, E., Malanushenko, V., Oravetz, D., Pan, K., Simmons, A., and Snedden, S. (2010). Measurements of the Rate of Type Ia Supernovae at Redshift z ˜0.3 from the SDSS-II Supernova Survey. *ArXiv e-prints*. Cited on 35, 129

Donahue, M., Mack, J., Scharf, C., Lee, P., Postman, M., Rosati, P., Dickinson, M., Voit, G. M., and Stocke, J. T. (2001). Distant Cluster Hunting: A Comparison Between the Optical and X-Ray Luminosity Functions from an Optical/X-Ray Joint Survey. *ApJL*, 552:L93–L96. Cited on 20

Donahue, M., Scharf, C. A., Mack, J., Lee, Y. P., Postman, M., Rosati, P., Dickinson, M., Voit, G. M., and Stocke, J. T. (2002). Distant Cluster Hunting. II. A Comparison of X-Ray and Optical Cluster Detection Techniques and Catalogs from the ROSAT Optical X-Ray Survey. *ApJ*, 569:689–719. Cited on 18

Dressler, A. (1980). Galaxy morphology in rich clusters - Implications for the formation and evolution of galaxies. *ApJ*, 236:351–365. Cited on 14

Dressler, A., Oemler, A., Couch, W. J., Smail, I., Ellis, R. S., Barger, A., Butcher, H., Poggianti, B. M., and Sharples, R. M. (1997). Evolution since z = 0.5 of the morphology-density relation for clusters of galaxies. *The Astrophysical Journal*, 490:577. Cited on 17

Eisenstein, D. J., Annis, J., Gunn, J. E., Szalay, A. S., Connolly, A. J., Nichol, R. C., Bahcall, N. A., Bernardi, M., Burles, S., Castander, F. J., Fukugita, M., Hogg, D. W., Ivezic, Z., Knapp, G. R., Lupton, R. H., Narayanan, V., Postman, M., Riechart, D. E., Richmond, M., Schneider, D. P., Schlegel, D. J., Strauss, M. A., Subbarao, M., Tucker,

D. L., Berk, D. V., Vogeley, M. S., Weinberg, D. H., and Yanny, B. (2001). Spectroscopic target selection for the sloan digital sky survey: The luminous red galaxy sample. *ASTRON.J*, 2267. Cited on 37, 161, 162, 163

Ellis, R. S., Smail, I., Dressler, A., Couch, W. J., Oemler, Jr., A., Butcher, H., and Sharples, R. M. (1997). The Homogeneity of Spheroidal Populations in Distant Clusters. *ApJ*, 483:582–+. Cited on 14

Gal, R. R. (2006). Optical Detection of Galaxy Clusters. *ArXiv Astrophysics e-prints*. Cited on 14

Gilbank, D. G. and Balogh, M. L. (2008). Tracking down a critical halo mass for killing galaxies through the growth of the red-sequence. Cited on 17, 18

Gilbank, D. G., Bower, R. G., Castander, F. J., and Ziegler, B. L. (2004). Exploring the selection of galaxy clusters and groups: an optical survey for X-ray dark clusters. *MNRAS*, 348:551–580. Cited on 20

Gilbank, D. G., Yee, H. K. C., Ellingson, E., Gladders, M. D., Loh, Y.-S., Barrientos, L. F., and Barkhouse, W. A. (2008). The Red-Sequence Luminosity Function in Galaxy Clusters since z ˜ 1. *ApJ*, 673:742–751. Cited on 13, 17

Girardi, M., Giuricin, G., Mardirossian, F., Mezzetti, M., and Boschin, W. (1998). Optical Mass Estimates of Galaxy Clusters. *ApJ*, 505:74–95. Cited on 8, 18

Gladders, M. D. and Yee, H. K. C. (2000a). A new method for galaxy cluster detection i: The algorithm. *Astronomical Journal*, 120:2148. Cited on 2

Gladders, M. D. and Yee, H. K. C. (2000b). A new method for galaxy cluster detection i: The algorithm. *Astronomical Journal*, 120:2148. Cited on 14, 16, 36, 45, 99, 100

Gladders, M. D. and Yee, H. K. C. (2004). The red-sequence cluster survey i: The survey and cluster catalogs for patches rcs0926+37 and rcs1327+29. Cited on 7, 100

Gladders, M. D., Yee, H. K. C., Majumdar, S., Barrientos, L. F., Hoekstra, H., Hall, P. B., and Infante, L. (2007). Cosmological Constraints from the Red-Sequence Cluster Survey. *ApJ*, 655:128–134. Cited on 9

Gwyn, S. D. J. (2008). MegaPipe: The MegaCam Image Stacking Pipeline at the Canadian Astronomical Data Centre. *PASP*, 120:212–223. Cited on 96

Hansen, S. M., McKay, T. A., Wechsler, R. H., Annis, J., Sheldon, E. S., and Kimball, A. (2005). Measurement of Galaxy Cluster Sizes, Radial Profiles, and Luminosity Functions from SDSS Photometric Data. *ApJ*, 633:122–137. Cited on 19

Helsdon, S. F. and Ponman, T. J. (2000). Are X-ray properties of loose groups different from those of compact groups? *MNRAS*, 319:933–938. Cited on 11

Hicks, A. K., Ellingson, E., Bautz, M., Cain, B., Gilbank, D. G., Gladders, M. G., Hoekstra, H., Yee, H. K. C., and Garmire, G. (2008). Chandra X-Ray Observations of the 0.6 $<z<$ 1.1 Red-Sequence Cluster Survey Sample. *ApJ*, 680:1022–1041. Cited on 19, 175

Hicks, A. K., Ellingson, E., Hoekstra, H., and Yee, H. K. C. (2006). Multiwavelength Mass Comparisons of the z˜0.3 CNOC Cluster Sample. *ApJ*, 652:232–248. Cited on 19, 175

Hilton, M. (2006). The optical properties of galaxies in x-ray selected clusters. *Ph.D. Thesis*. Cited on 104

Hilton, M., Collins, C. A., Stanford, S. A., Lidman, C., Dawson, K. S., Davidson, M., Kay, S. T., Liddle, A. R., Mann, R. G., Miller, C. J., Nichol, R. C., Romer, A. K., Sabirli, K., Viana, P. T. P., and West, M. J. (2007). The XMM Cluster Survey: The Dynamical State of XMMXCS J2215.9-1738 at z = 1.457. *ApJ*, 670:1000–1009. Cited on 33, 35

Hilton, M., Stanford, S. A., Stott, J. P., Collins, C. A., Hoyle, B., Davidson, M., Hosmer, M., Kay, S. T., Liddle, A. R., Lloyd-Davies, E., Mann, R. G., Mehrtens, N., Miller, C. J., Nichol, R. C., Romer, A. K., Sabirli, K., Sahlén, M., Viana, P. T. P., West, M. J., Barbary, K., Dawson, K. S., Meyers, J., Perlmutter, S., Rubin, D., and Suzuki, N. (2009). The XMM Cluster Survey: Galaxy Morphologies and the Color-Magnitude Relation in XMMXCS J2215.9 - 1738 at z = 1.46. *ApJ*, 697:436–451. Cited on 33, 35

Hoessel, J. G. and Schneider, D. P. (1985). CCD observations of Abell clusters. IV - Surface photometry of 175 brightest cluster galaxies. *AJ*, 90:1648–1664. Cited on 13

Hogg, D. W., Blanton, M. R., Brinchmann, J., Eisenstein, D. J., Schlegel, D. J., Gunn, J. E., McKay, T. A., Rix, H., Bahcall, N. A., Brinkmann, J., and Meiksin, A. (2004). The Dependence on Environment of the Color-Magnitude Relation of Galaxies. *ApJL*, 601:L29–L32. Cited on 18

Hogg, D. W., Finkbeiner, D. P., Schlegel, D. J., and Gunn, J. E. (2001). A photometricity and extinction monitor at the apache point observatory. *Astronomical Journal*, 122:2129. Cited on 129

Holden, B. P., Stanford, S. A., Eisenhardt, P., and Dickinson, M. (2004). Evolution in the color-magnitude relation of early-type galaxies in clusters of galaxies at z≐1. *Astronomical Journal*, 127:2482. Cited on 17

Hosmer, M. A. (2009). The xmm cluster survey: A new cluster candidate sample and detailed selection function. *Ph.D. Thesis*. Cited on 24

Hoyle, B. (2008). Building a mass function and testing gravity using galaxy clusters. *Ph.D. Thesis*. Cited on 36

Jarosik, N., Bennett, C. L., Dunkley, J., Gold, B., Greason, M. R., Halpern, M., Hill, R. S., Hinshaw, G., Kogut, A., Komatsu, E., Larson, D., Limon, M., Meyer, S. S., Nolta, M. R., Odegard, N., Page, L., Smith, K. M., Spergel, D. N., Tucker, G. S., Weiland, J. L., Wollack, E., and Wright, E. L. (2010). Seven-Year Wilkinson Microwave Anisotropy Probe (WMAP) Observations: Sky Maps, Systematic Errors, and Basic Results. *ArXiv e-prints*. Cited on 4, 7

Jenkins, A., Frenk, C. S., White, S. D. M., Colberg, J. M., Cole, S., Evrard, A. E., Couchman, H. M. P., and Yoshida, N. (2001). The mass function of dark matter haloes. *MNRAS*, 321:372–384. Cited on 7

Johnston, D. E., Sheldon, E. S., Wechsler, R. H., Rozo, E., Koester, B. P., Frieman, J. A., McKay, T. A., Evrard, A. E., Becker, M. R., and Annis, J. (2007). Cross-correlation Weak Lensing of SDSS galaxy Clusters II: Cluster Density Profiles and the Mass–Richness Relation. *ArXiv e-prints*. Cited on 19

Kaiser, N. (1986). Evolution and clustering of rich clusters. *MNRAS*, 222:323–345. Cited on 10

Knop, R. A., Aldering, G., Amanullah, R., Astier, P., Blanc, G., Burns, M. S., Conley, A., Deustua, S. E., Doi, M., Ellis, R., Fabbro, S., Folatelli, G., Fruchter, A. S., Garavini, G., Garmond, S., Garton, K., Gibbons, R., Goldhaber, G., Goobar, A., Groom, D. E., Hardin, D., Hook, I., Howell, D. A., Kim, A. G., Lee, B. C., Lidman, C., Mendez, J., Nobili, S., Nugent, P. E., Pain, R., Panagia, N., Pennypacker, C. R., Perlmutter, S., Quimby, R., Raux, J., Regnault, N., Ruiz-Lapuente, P., Sainton, G., Schaefer, B.,

Schahmaneche, K., Smith, E., Spadafora, A. L., Stanishev, V., Sullivan, M., Walton, N. A., Wang, L., Wood-Vasey, W. M., and Yasuda, N. (2003). New Constraints on Ω_M, Ω_Λ, and w from an Independent Set of 11 High-Redshift Supernovae Observed with the Hubble Space Telescope. *ApJ*, 598:102–137. Cited on 8

Kodama, T. and Arimoto, N. (1997). Origin of the colour-magnitude relation of elliptical galaxies. *AA*, 320:41–53. Cited on 15

Kodama, T., Arimoto, N., Barger, A. J., and Arag'on-Salamanca, A. (1998). Evolution of the colour-magnitude relation of early-type galaxies in distant clusters. *AA*, 334:99–109. Cited on 15, 16

Kodama, T., Tanaka, I., Kajisawa, M., Kurk, J., Venemans, B., De Breuck, C., Vernet, J., and Lidman, C. (2007). The first appearance of the red sequence of galaxies in proto-clusters at 2 ˜ z ˜ 3. *MNRAS*, 377:1717–1725. Cited on 14

Koester, B. P., McKay, T. A., Annis, J., Wechsler, R. H., Evrard, A., Bleem, L., Becker, M., Johnston, D., Sheldon, E., Nichol, R., Miller, C., Scranton, R., Bahcall, N., Barentine, J., Brewington, H., Brinkmann, J., Harvanek, M., Kleinman, S., Krzesinski, J., Long, D., Nitta, A., Schneider, D. P., Sneddin, S., Voges, W., and York, D. (2007a). A MaxBCG Catalog of 13,823 Galaxy Clusters from the Sloan Digital Sky Survey. *ApJ*, 660:239–255. Cited on 101

Koester, B. P., McKay, T. A., Annis, J., Wechsler, R. H., Evrard, A. E., Rozo, E., Bleem, L., Sheldon, E. S., and Johnston, D. (2007b). MaxBCG: A Red-Sequence Galaxy Cluster Finder. *ApJ*, 660:221–238. Cited on 7, 19, 100, 157, 161

Kron, R. G. (1980). Photometry of a complete sample of faint galaxies. *ApJS*, 43:305–325. Cited on 81

Landolt, A. U. (1992). UBVRI photometric standard stars in the magnitude range 11.5-16.0 around the celestial equator. *AJ*, 104:340–371. Cited on 53

Lin, Y., Mohr, J. J., and Stanford, S. A. (2004). K-Band Properties of Galaxy Clusters and Groups: Luminosity Function, Radial Distribution, and Halo Occupation Number. *ApJ*, 610:745–761. Cited on 158

Lintott, C. J., Schawinski, K., Slosar, A., Land, K., Bamford, S., Thomas, D., Raddick, M. J., Nichol, R. C., Szalay, A., Andreescu, D., Murray, P., and den Berg, J. V. (2008).

Galaxy zoo : Morphologies derived from visual inspection of galaxies from the sloan digital sky survey. Cited on 37

Loh, Y., Ellingson, E., Yee, H. K. C., Gilbank, D. G., Gladders, M. D., and Barrientos, L. F. (2008). The Color Bimodality in Galaxy Clusters since z ˜ 0.9. *ApJ*, 680:214–223. Cited on 16

Loh, Y.-S. and Strauss, M. A. (2006). The bright end of the luminosity function of red sequence galaxies. *MNRAS*, 366:373–386. Cited on 16

Lopes, P. A. A., de Carvalho, R. R., Kohl-Moreira, J. L., and Jones, C. (2009). NoSOCS in SDSS - I. Sample definition and comparison of mass estimates. *MNRAS*, 392:135–152. Cited on 18

López-Cruz, O., Barkhouse, W. A., and Yee, H. K. C. (2004). The Color-Magnitude Effect in Early-Type Cluster Galaxies. *ApJ*, 614:679–691. Cited on 14, 112

Mantz, A., Allen, S. W., Rapetti, D., and Ebeling, H. (2009). The Observed Growth of Massive Galaxy Clusters I: Statistical Methods and Cosmological Constraints. *ArXiv e-prints*. Cited on 8, 10, 42

Markevitch, M. (1998). The L X-T Relation and Temperature Function for Nearby Clusters Revisited. *ApJ*, 504:27–+. Cited on 11

Maughan, B. J. (2007). The $L_X - Y_X$ Relation: Using Galaxy Cluster X-Ray Luminosity as a Robust, Low-Scatter Mass Proxy. *ApJ*, 668:772–780. Cited on 32, 33, 39

McInnes, R. N., Menanteau, F., Heavens, A. F., Hughes, J. P., Jimenez, R., Massey, R., Simon, P., and Taylor, A. (2009). First lensing measurements of SZ-detected clusters. *MNRAS*, 399:L84–L88. Cited on 8

McMahon, R. G., Walton, N. A., Irwin, M. J., Lewis, J. R., Bunclark, P. S., and Jones, D. H. (2001). The INT wide field imaging survey (WFS). *New Astronomy Review*, 45:97–104. Cited on 45

Mei, S., Holden, B. P., Blakeslee, J. P., Ford, H. C., Franx, M., Homeier, N. L., Illingworth, G. D., Jee, M. J., Overzier, R., Postman, M., Rosati, P., van der Wel, A., and Bartlett, J. G. (2009). Evolution of the color-magnitude relation in galaxy clusters at z $\tilde{1}$ from the acs intermediate redshift cluster survey. Cited on 14, 17

Mei, S., Holden, B. P., Blakeslee, J. P., Rosati, P., Postman, M., Jee, M. J., Rettura, A., Sirianni, M., Demarco, R., Ford, H. C., Franx, M., Homeier, N. L., and Illingworth, G. D. (2006). Evolution of the color-magnitude relation in high-redshift clusters: Early-type galaxies in the lynx supercluster at z$\tilde{1}$.26. *The Astrophysical Journal*, 644:759. Cited on 14

Metcalfe, N., Shanks, T., Fong, R., and Jones, L. R. (1991). Galaxy number counts. II - CCD observations to B = 25 mag. *MNRAS*, 249:498–522. Cited on 92, 97

Miller, C. J., Nichol, R., Reichart, D., Wechsler, R., Evrard, A., Annis, J., McKay, T., Bahcall, N., Bernardi, M., Boehringer, H., Connolly, A., Goto, T., Kniazev, A., Lamb, D., Postman, M., Schneider, D., Sheth, R., and Voges, W. (2005). The c4 clustering algorithm: Clusters of galaxies in the sloan digital sky survey. *ASTRON.J*, 968. Cited on 7, 104

Monet, D. and et al. (1998). A catalogue of astrometric standards. *VizieR Online Data Catalog*, 1252:0–+. Cited on 68

Muanwong, O., Kay, S. T., and Thomas, P. A. (2006). Evolution of X-Ray Cluster Scaling Relations in Simulations with Radiative Cooling and Nongravitational Heating. *ApJ*, 649:640–648. Cited on 11

Pacaud, F., Pierre, M., Adami, C., Altieri, B., Andreon, S., Chiappetti, L., Detal, A., Duc, P., Galaz, G., Gueguen, A., Le Fèvre, J., Hertling, G., Libbrecht, C., Melin, J., Ponman, T. J., Quintana, H., Refregier, A., Sprimont, P., Surdej, J., Valtchanov, I., Willis, J. P., Alloin, D., Birkinshaw, M., Bremer, M. N., Garcet, O., Jean, C., Jones, L. R., Le Fèvre, O., Maccagni, D., Mazure, A., Proust, D., Röttgering, H. J. A., and Trinchieri, G. (2007). The XMM-LSS survey: the Class 1 cluster sample over the initial 5 deg^2*anditscosmologicalmodelling.*$MNRAS, 382 : 1289 - -1308.$*Citedon* $7, 8, 9, 39$

Pen, U. (1997). Measuring the universal deceleration using angular diameter distances to clusters of galaxies. *New Astronomy*, 2:309–317. Cited on 8

Percival, W. J., Reid, B. A., Eisenstein, D. J., Bahcall, N. A., Budavari, T., Frieman, J. A., Fukugita, M., Gunn, J. E., Ivezic, Z., Knapp, G. R., Kron, R. G., Loveday, J., Lupton, R. H., McKay, T. A., Meiksin, A., Nichol, R. C., Pope, A. C., Schlegel, D. J., Schneider, D. P., Spergel, D. N., Stoughton, C., Strauss, M. A., Szalay, A. S., Tegmark, M., Vogeley, M. S., Weinberg, D. H., York, D. G., and Zehavi, I. (2009). Baryon acoustic oscillations in the sloan digital sky survey data release 7 galaxy sample. Cited on 4

Perlmutter, S., Aldering, G., Goldhaber, G., Knop, R. A., Nugent, P., Castro, P. G., Deustua, S., Fabbro, S., Goobar, A., Groom, D. E., Hook, I. M., Kim, A. G., Kim, M. Y., Lee, J. C., Nunes, N. J., Pain, R., Pennypacker, C. R., Quimby, R., Lidman, C., Ellis, R. S., Irwin, M., McMahon, R. G., Ruiz-Lapuente, P., Walton, N., Schaefer, B., Boyle, B. J., Filippenko, A. V., Matheson, T., Fruchter, A. S., Panagia, N., Newberg, H. J. M., Couch, W. J., and The Supernova Cosmology Project (1999). Measurements of Omega and Lambda from 42 High-Redshift Supernovae. *ApJ*, 517:565–586. Cited on 4, 5

Peterson, J. R. and Fabian, A. C. (2006). X-ray spectroscopy of cooling clusters. *Phys. Rept.*, 427:1–39. Cited on 11

Pimbblet, K. A., Smail, I., Kodama, T., Couch, W. J., Edge, A. C., Zabludoff, A. I., and O'Hely, E. (2002). The las campanas/aat rich cluster survey - ii. the environmental dependence of galaxy colours in clusters at z˜0.1. *mnras*, 331:333–350. Cited on 18, 105, 106, 109, 110

Poggianti, B. M., Fasano, G., Bettoni, D., Cava, A., Dressler, A., Vanzella, E., Varela, J., Couch, W. J., D'Onofrio, M., Fritz, J., Kjaergaard, P., Moles, M., and Valentinuzzi, T. (2009). The evolution of spiral, s0 and elliptical galaxies in clusters. Cited on 17

Poggianti, B. M., von der Linden, A., De Lucia, G., Desai, V., Simard, L., Halliday, C., Aragon-Salamanca, A., Bower, R., Varela, J., Best, P., Clowe, D. I., Dalcanton, J., Jablonka, P., Milvang-Jensen, B., Pello, R., Rudnick, G., Saglia, R., White, S. D. M., and Zaritsky, D. (2005). The evolution of the star formation activity in galaxies and its dependence on environment. Cited on 17, 18

Ponman, T. J., Sanderson, A. J. R., and Finoguenov, A. (2003). The Birmingham-CfA cluster scaling project - III. Entropy and similarity in galaxy systems. *MNRAS*, 343:331–342. Cited on 11

Popesso, P., Biviano, A., Böhringer, H., and Romaniello, M. (2007). RASS-SDSS galaxy cluster survey. V. The X-ray-underluminous Abell clusters. *AA*, 461:397–410. Cited on 20

Postman, M., Lubin, L. M., Gunn, J. E., Oke, J. B., Hoessel, J. G., Schneider, D. P., and Christensen, J. A. (1996). The Palomar Distant Clusters Survey. I. The Cluster Catalog. *AJ*, 111:615–+. Cited on 100, 102

Pratt, G. W., Croston, J. H., Arnaud, M., and Böhringer, H. (2009). Galaxy cluster X-ray luminosity scaling relations from a representative local sample (REXCESS). *AA*, 498:361–378. Cited on 11

Predehl, P., Boehringer, H., Brunner, H., Brusa, M., Burwitz, V., Cappelluti, N., Churazov, E., Dennerl, K., Freyberg, M., Friedrich, P., Hasinger, G., Kendziorra, E., Kreykenbohm, I., Schmid, C., Wilms, J., Lamer, G., Meidinger, N., Muehlegger, M., Pavlinsky, M., Robrade, J., Santangelo, A., Schmitt, J., Schwope, A., Steinmetz, M., Strueder, L., Sunyaev, R., and Tenzer, C. (2010). eROSITA on SRG. *ArXiv e-prints*. Cited on 24

Press, W. H. and Schechter, P. (1974). Formation of Galaxies and Clusters of Galaxies by Self-Similar Gravitational Condensation. *ApJ*, 187:425–438. Cited on 6

Reiprich, T. H. and Böhringer, H. (2002). The Mass Function of an X-Ray Flux-limited Sample of Galaxy Clusters. *ApJ*, 567:716–740. Cited on 8, 10

Reyes, R., Mandelbaum, R., Hirata, C., Bahcall, N., and Seljak, U. (2008). Improved optical mass tracer for galaxy clusters calibrated using weak lensing measurements. *MNRAS*, 390:1157–1169. Cited on 8, 20

Riess, A. G., Macri, L., Casertano, S., Sosey, M., Lampeitl, H., Ferguson, H. C., Filippenko, A. V., Jha, S. W., Li, W., Chornock, R., and Sarkar, D. (2009). A redetermination of the hubble constant with the hubble space telescope from a differential distance ladder. Cited on 4

Romer, A. K., Viana, P. T. P., Liddle, A. R., and Mann, R. G. (2001). A Serendipitous Galaxy Cluster Survey with XMM: Expected Catalog Properties and Scientific Applications. *ApJ*, 547:594–608. Cited on 2, 7, 21, 23

Rosati, P., Borgani, S., and Norman, C. (2002). The Evolution of X-ray Clusters of Galaxies. *ARA&A*, 40:539–577. Cited on 23

Roseboom, I. G., Pimbblet, K. A., Drinkwater, M. J., Cannon, R. D., De Propris, R., Edge, A. C., Eisenstein, D. J., Nichol, R. C., Smail, I., Wake, D. A., Hawthorn, J. B., Bridges, T. J., Carson, D., Colless, M., Couch, W. J., Croom, S. M., Driver, S. P., Hewett, P. C., Loveday, J., Ross, N., Schneider, D. P., Shanks, T., Sharp, R. G., and Weilbacher, P. (2006). The 2df-sdss lrg and qso survey: The star formation histories of luminous red galaxies. Cited on 13

Rozo, E., Rykoff, E. S., Evrard, A., Becker, M., McKay, T., Wechsler, R. H., Koester, B. P., Hao, J., Hansen, S., Sheldon, E., Johnston, D., Annis, J., and Frieman, J. (2009). Constraining the Scatter in the Mass-richness Relation of maxBCG Clusters with Weak Lensing and X-ray Data. *ApJ*, 699:768–781. Cited on 8

Rozo, E., Rykoff, E. S., Koester, B. P., McKay, T., Hao, J., Evrard, A., Wechsler, R. H., Hansen, S., Sheldon, E., Johnston, D., Becker, M., Annis, J., Bleem, L., and Scranton, R. (2008). An Improved Cluster Richness Estimator. *ArXiv e-prints*. Cited on 19

Rozo, E., Wechsler, R. H., Rykoff, E. S., Annis, J. T., Becker, M. R., Evrard, A. E., Frieman, J. A., Hansen, S. M., Hao, J., Johnston, D. E., Koester, B. P., McKay, T. A., Sheldon, E. S., and Weinberg, D. H. (2010). Cosmological Constraints from the Sloan Digital Sky Survey maxBCG Cluster Catalog. *ApJ*, 708:645–660. Cited on 9, 18

Rykoff, E. S., McKay, T. A., Becker, M. R., Evrard, A., Johnston, D. E., Koester, B. P., Rozo, E., Sheldon, E. S., and Wechsler, R. H. (2008). Measuring the Mean and Scatter of the X-Ray Luminosity-Optical Richness Relation for maxBCG Galaxy Clusters. *ApJ*, 675:1106–1124. Cited on 8, 10, 19

Sahlén, M., Viana, P. T. P., Liddle, A. R., Romer, A. K., Davidson, M., Hosmer, M., Lloyd-Davies, E., Sabirli, K., Collins, C. A., Freeman, P. E., Hilton, M., Hoyle, B., Kay, S. T., Mann, R. G., Mehrtens, N., Miller, C. J., Nichol, R. C., Stanford, S. A., and West, M. J. (2009). The XMM Cluster Survey: forecasting cosmological and cluster scaling-relation parameter constraints. *MNRAS*, 397:577–607. Cited on 8, 10, 32, 33, 39, 42, 51, 160

Salpeter, E. E. (1955). The Luminosity Function and Stellar Evolution. *ApJ*, 121:161–+. Cited on 104

Sandage, A. and Visvanathan, N. (1978). The color-absolute magnitude relation for E and S0 galaxies. II - New colors, magnitudes, and types for 405 galaxies. *ApJ*, 223:707–729. Cited on 14, 16

Sasaki, S. (1996). A New Method to Estimate Cosmological Parameters Using the Baryon Fraction of Clusters of Galaxies. *PASJ*, 48:L119–L122. Cited on 8

Schechter, P. (1976). An analytic expression for the luminosity function for galaxies. *ApJ*, 203:297–306. Cited on 13

Schlegel, D. J., Finkbeiner, D. P., and Davis, M. (1998). Maps of Dust Infrared Emission for Use in Estimation of Reddening and Cosmic Microwave Background Radiation Foregrounds. *ApJ*, 500:525–+. Cited on 92, 132

Schwope, A. D., Lamer, G., de Hoon, A., Kohnert, J., Boehringer, H., Dietrich, J. P., Fassbender, R., Mohr, J., Muehlegger, M., Pierini, D., Pratt, G. W., Quintana, H., Rosati, P., Santos, J., and Suhada, R. (2010). XMMU J100750.5+125818: A strong lensing cluster at z=1.082. *ArXiv e-prints*. Cited on 34

Sheldon, E. S., Johnston, D. E., Scranton, R., Koester, B. P., McKay, T. A., Oyaizu, H., Cunha, C., Lima, M., Lin, H., Frieman, J. A., Wechsler, R. H., Annis, J., Mandelbaum, R., Bahcall, N. A., and Fukugita, M. (2009). Cross-correlation Weak Lensing of SDSS Galaxy Clusters. I. Measurements. *ApJ*, 703:2217–2231. Cited on 18

Short, C. J., Thomas, P. A., Young, O. E., Pearce, F. R., Jenkins, A., and Muanwong, O. (2010). The evolution of galaxy cluster X-ray scaling relations. *ArXiv e-prints*. Cited on 12

Sijacki, D., Springel, V., Di Matteo, T., and Hernquist, L. (2007). A unified model for AGN feedback in cosmological simulations of structure formation. *MNRAS*, 380:877–900. Cited on 12

Smith, J. A., Tucker, D. L., Kent, S., Richmond, M. W., Fukugita, M., Ichikawa, T., Ichikawa, S.-i., Jorgensen, A. M., Uomoto, A., Gunn, J. E., Hamabe, M., Watanabe, M., Tolea, A., Henden, A., Annis, J., Pier, J. R., McKay, T. A., Brinkmann, J., Chen, B., Holtzman, J., Shimasaku, K., and York, D. G. (2002). The u'g'r'i'z' Standard-Star System. *AJ*, 123:2121–2144. Cited on 53, 54, 85

Stanek, R., Evrard, A. E., Böhringer, H., Schuecker, P., and Nord, B. (2006). The X-Ray Luminosity-Mass Relation for Local Clusters of Galaxies. *ApJ*, 648:956–968. Cited on 10

Stanford, S. A., Eisenhardt, P. R., and Dickinson, M. (1998). The Evolution of Early-Type Galaxies in Distant Clusters. *ApJ*, 492:461–+. Cited on 14, 15

Stanford, S. A., Romer, A. K., Sabirli, K., Davidson, M., Hilton, M., Viana, P. T. P., Collins, C. A., Kay, S. T., Liddle, A. R., Mann, R. G., Miller, C. J., Nichol, R. C., West, M. J., Conselice, C. J., Spinrad, H., Stern, D., and Bundy, K. (2006). The XMM Cluster Survey: A Massive Galaxy Cluster at z = 1.45. *ApJL*, 646:L13–L16. Cited on 33, 35, 44

Stott, J. P., Edge, A. C., Smith, G. P., Swinbank, A. M., and Ebeling, H. (2008). Near-infrared evolution of brightest cluster galaxies in the most x-ray luminous clusters since z=1. *MNRAS*, 384:1502. Cited on 16

Stott, J. P., Pimbblet, K. A., Edge, A. C., Smith, G. P., and Wardlow, J. L. (2009). The evolution of the red sequence slope in massive galaxy clusters. Cited on 17, 18

Stott, J. P., Smail, I., Edge, A. C., Ebeling, H., Smith, G. P., Kneib, J. P., and Pimbblet, K. A. (2007). An increase in the faint red galaxy population in massive clusters since z$\tilde{0}$.5. *ASTROPHYS.J*, 95. Cited on 17

Stubbs, C. W. and Tonry, J. L. (2006). Toward 1% photometry: End-to-end calibration of astronomical telescopes and detectors. Cited on 56

Tody, D. (1993). IRAF in the Nineties. In R. J. Hanisch, R. J. V. Brissenden, & J. Barnes, editor, *Astronomical Data Analysis Software and Systems II*, volume 52 of *Astronomical Society of the Pacific Conference Series*, pages 173–+. Cited on 63

Valdes, F. G. (1998). The IRAF Mosaic Data Reduction Package. In R. Albrecht, R. N. Hook, & H. A. Bushouse, editor, *Astronomical Data Analysis Software and Systems VII*, volume 145 of *Astronomical Society of the Pacific Conference Series*, pages 53–+. Cited on 63

Vanderlinde, K., Crawford, T. M., de Haan, T., Dudley, J. P., Shaw, L., Ade, P. A. R., Aird, K. A., Benson, B. A., Bleem, L. E., Brodwin, M., Carlstrom, J. E., Chang, C. L., Crites, A. T., Desai, S., Dobbs, M. A., Foley, R. J., George, E. M., Gladders, M. D., Hall, N. R., Halverson, N. W., High, F. W., Holder, G. P., Holzapfel, W. L., Hrubes, J. D., Joy, M., Keisler, R., Knox, L., Lee, A. T., Leitch, E. M., Loehr, A., Lueker, M., Marrone, D. P., McMahon, J. J., Mehl, J., Meyer, S. S., Mohr, J. J., Montroy, T. E., Ngeow, C., Padin, S., Plagge, T., Pryke, C., Reichardt, C. L., Rest, A., Ruel, J., Ruhl, J. E., Schaffer, K. K., Shirokoff, E., Song, J., Spieler, H. G., Stalder, B., Staniszewski, Z., Stark, A. A., Stubbs, C. W., van Engelen, A., Vieira, J. D., Williamson, R., Yang, Y., Zahn, O., and Zenteno, A. (2010). Galaxy Clusters Selected with the Sunyaev-Zel'dovich Effect from 2008 South Pole Telescope Observations. *ArXiv e-prints*. Cited on 7

Vikhlinin, A., Allen, S. W., Arnaud, M., Bautz, M., B%ouml, ringer, H., Bonamente, M., Burns, J., Evrard, A., Henry, J. P., Jones, C., McNamara, B. R., Nagai, D., Rapetti, D.,

and Reiprich, T. (2009a). Cosmological studies with a large-area X-ray telescope. In *astro2010: The Astronomy and Astrophysics Decadal Survey*, volume 2010 of *Astronomy*, pages 304–+. Cited on 24

Vikhlinin, A., Kravtsov, A. V., Burenin, R. A., Ebeling, H., Forman, W. R., Hornstrup, A., Jones, C., Murray, S. S., Nagai, D., Quintana, H., and Voevodkin, A. (2009b). Chandra Cluster Cosmology Project III: Cosmological Parameter Constraints. *ApJ*, 692:1060–1074. Cited on 8, 42

Visvanathan, N. and Sandage, A. (1977). The color-absolute magnitude relation for E and S0 galaxies. I - Calibration and tests for universality using Virgo and eight other nearby clusters. *ApJ*, 216:214–226. Cited on 14

Voit, G. M., Kay, S. T., and Bryan, G. L. (2005). The baseline intracluster entropy profile from gravitational structure formation. *MNRAS*, 364:909–916. Cited on 10

Wake, D. A., Collins, C. A., Nichol, R. C., Jones, L. R., and Burke, D. J. (2005). The Environmental Dependence of Galaxy Colors in Intermediate-Redshift X-Ray-selected Clusters. *ApJ*, 627:186–202. Cited on 18

Wake, D. A., Sheth, R. K., Nichol, R. C., Baugh, C. M., Bland-Hawthorn, J., Cannon, R., Colless, M., Couch, W. J., Croom, S. M., De Propris, R., Drinkwater, M. J., Edge, A. C., Loveday, J., Lam, T. Y., Pimbblet, K. A., Roseboom, I. G., Ross, N. P., Schneider, D. P., Shanks, T., and Sharp, R. G. (2008). The 2df-sdss lrg and qso survey: evolution of the clustering of luminous red galaxies since z = 0.6. Cited on 13

Wilson, G., Muzzin, A., Yee, H. K. C., Lacy, M., Surace, J., Gilbank, D., Blindert, K., Hoekstra, H., Majumdar, S., Demarco, R., Gardner, J. P., Gladders, M. D., and Lonsdale, C. (2009). Spectroscopic Confirmation of a Massive Red-Sequence-Selected Galaxy Cluster at z = 1.34 in the SpARCS-South Cluster Survey. *ApJ*, 698:1943–1950. Cited on 16

Wu, H., Rozo, E., and Wechsler, R. H. (2010). Annealing a Follow-up Program: Improvement of the Dark Energy Figure of Merit for Optical Galaxy Cluster Surveys. *ApJ*, 713:1207–1218. Cited on 177

Yanny, T. S.-I. S. C., Rockosi, C., Newberg, H. J., and Knapp, G. R. (2009). Segue: A spectroscopic survey of 240,000 stars with g=14-20. *ASTRON.J*, 4377. Cited on 129

Yee, H. K. C. and Ellingson, E. (2003). Correlations of Richness and Global Properties in Galaxy Clusters. *ApJ*, 585:215–226. Cited on 19, 175

Yee, H. K. C., Gladders, M. D., Gilbank, D. G., Majumdar, S., Hoekstra, H., Ellingson, E., and the RCS-2 Collaboration (2007). The Red-Sequence Cluster Surveys. *ArXiv Astrophysics e-prints*. Cited on 100

Yee, H. K. C., Gladders, M. D., and Lopez-Cruz, O. (1999). The color-magnitude relation of early-type galaxies: A tool for cluster finding and redshift determination. Cited on 19

Zhang, Y., Finoguenov, A., Böhringer, H., Kneib, J., Smith, G. P., Czoske, O., and Soucail, G. (2007). Scaling relations and mass calibration of the X-ray luminous galaxy clusters at redshift ˜0.2: XMM-Newton observations. *AA*, 467:437–457. Cited on 10

Zhang, Y., Okabe, N., Finoguenov, A., Smith, G. P., Piffaretti, R., Valdarnini, R., Babul, A., Evrard, A. E., Mazzotta, P., Sanderson, A. J. R., and Marrone, D. P. (2010). LoCuSS: A Comparison of Cluster Mass Measurements from XMM-Newton and SubaruTesting Deviation from Hydrostatic Equilibrium and Non-thermal Pressure Support. *ApJ*, 711:1033–1043. Cited on 8, 18

Appendix A

A description of the XCS Spectral and Surface brightness fitting

A.1 Spectral fitting

The spectral fitting was carried out using version 12.5.0ac of the XSpec X-ray spectral fitting package. The models were simultaneously fitted to the spectra for the available observations and cameras using the maximum likelihood Cash statistic. The spectral bins were grouped such that there was a minimum number of counts per bin. This minimum number of counts was based on the number of counts in the spectrum and varied from 1 for spectra with 250 counts and below up to 5 for spectra with 850 counts and above, scaling as a powerlaw with an index of 0.75 for values in between. This scaling of the minimum number of counts per bin was derived from simulations of spectral fitting EPIC data and is designed to minimise the bias in the derived parameters while also minimising the errors. Data between 0.3 and 7.9 keV were used for the fitting in order to maximise the signal-to-noise.

Four different models were fitted to the data. All the models included a photoelectric absorption component (WABS) to simulate the absorption from the neutral gas in our galaxy and a hot plasma component (MEKAL) to simulate the X-ray emission from the intracluster medium (ICM). The first model involved fitting these components with the hydrogen column and ICM metallicity frozen (at the galactic radio column for the hydrogen column and the canonical value of 0.3 for the metallicity). The second model was the same as the first except that the hydrogen column and metallicity were allowed to vary. The third model included an extra powerlaw component to simulate a potential contaminating point sources, and the fourth model had two MEKAL components rather than one in

order to simulate the case where there is a significant cool core in the cluster. The best fitting model was used to derive the luminosity and temperature of the cluster.

A.1.1 Background Subtraction

The background subtraction from the spectral fitting was done using an in-field method, since XCS clusters do not have large angular sizes. The background spectra were taken from an annulus around the source (in the case of sources very near the edge of the field of view an ellipse perpendicular to the direction of the centre of the field of view with a circular region centred on the cluster excluded, was used instead). The outer edge of the annulus in 1.5 times the maximum radius identified for the source by XAPA and the inner edge is at 1.05 times that radius.

A.2 Surface brightness fitting

The surface brightness fitting was performed by simultaneously fitting a model to the individual images for each camera and observation of the source. The model was convolved with the 1-dimensional "Extended Accuracy" XMM-Newton point spread function model, multiplied by the exposure map and have a background map added before being compared with the data. The maximum likelihood Cash statistic was used for the comparison and the MINUIT package of minimisation algorithms was used to find the best fit. The main function used the characterise the shape of the clusters was a a 1-dimensional King profile consisting of a core with a powerlaw decline outside that. Three different models were fitted to the data. First a simple King model with β frozen at the canonical value of $\frac{2}{3}$. Second a King model with β allowed to vary. Thirdly a King model by with an inner powerlaw cusp where inside a certain radius (usually of the order of the core radius) the surface brightness increase as a powerlaw into the centre. The best fitting model was used to calculate the scaling of the luminosity from the extraction region to r_{500}.

A.2.1 Background Subtraction

The same background regions were used for the surface brightness fitting as were used for the spectral fitting. However in addition to . Since the background can be considered as two components, an 'X-ray' component that is focused (and so vignetted) by the telescope mirrors and a 'particle' component that is not. In reality the 'X-ray' component includes soft protons that are focused by the mirrors and the 'particle' component includes high energy photons that are created as the result of particle collisions with the telescope

structure. These need to be treated separately as their spatial variation is different. To calculate the 'particle' component which should be approximately constant across the field of view the number of counts and effective exposure time is measured for two regions with significantly different off-axis angles. The comparison of these quantities allows the 'particle' background rate to be calculated. Using the total rate estimated from the annular background region and the exposure map, background map can then be constructed consisting of the sum of the constant 'particle' background and the spatially varying X-ray background.

A.3 X-ray redshifts

For sources with high numbers of counts it should be possible to place constraints on the redshift using the X-ray spectra. However the quality of the constraints will depend on a number of factors including the number of counts in the spectra, the temperature of the cluster and how well the spectra is represented by the fitted model. High cluster temperatures will degrade the constraints since the spectra will be more dominated by the Bremstrallung continuum rather than emission lines. Typically a single temperature MEKAL model is used, convolved with a photoelectric absorption model to represent the galactic hydrogen column, since the number of free parameters must be kept to a minimum. If this model does not represent the cluster spectra well however because it is significantly multi-temperature (cool core) has significant non-thermal emission (AGN). To futher reduce the number of parameters that it is necessary to fit the normalisation and temperature can be reduced to a single parameter by assuming that the cluster lies on an L-T relation.

In order to produce these constraints the XSpec spectral fitting package is used to scan through redshift space. At each of a set of redshifts the model is fitted to the spectra with the normalisation being the only free parameters. The hygrogen column is set to the galactic radio value and the metallicity is set to the canonical value of 0.3 Solar. The Cash statistic for the best fit is stored at each redshift and is then used to find the best fitting redshift and the 1-sigma limits around it. Where there are several minima in redshift space the best fit is not always used if it has a temperature that is unphysical for a galaxy cluster. For some sources no best fit can be found if there are not enough counts or one of the other problems mentioned above is too severe.

Figure A.1 shows two comparison plots of redshifts estimated from optical data and measured X-ray redshifts with uncertainties of less than 2.5 percent and 20 percent respec-

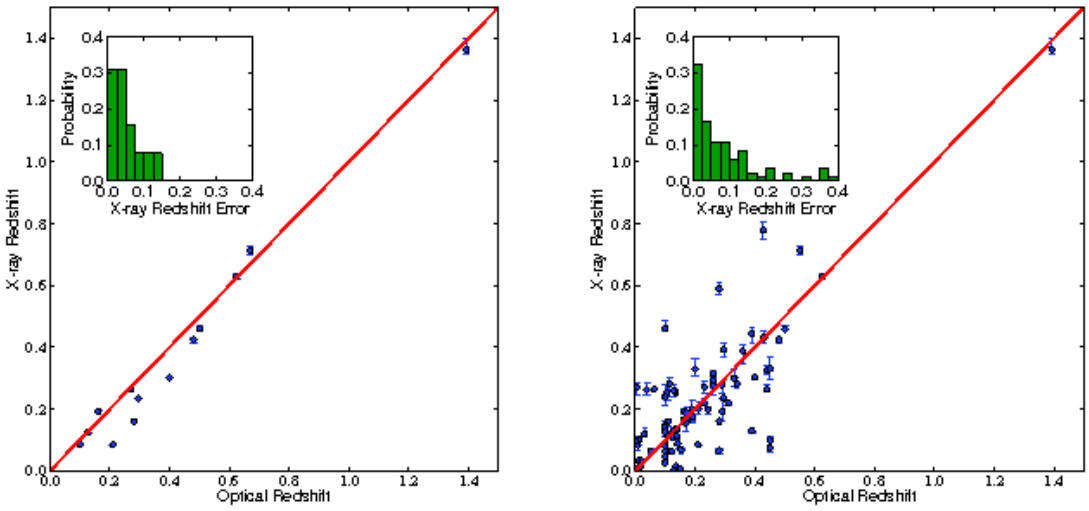

Figure A.1 Measured X-ray redshifts plotted against optically determined redshifts. The solid line shows the one-to-one relationship. Left panel: X-ray redshifts with statistical uncertainties of 2.5 percent or less. Right panel: X-ray redshifts with statistical uncertainties of 20 percent or less. Inserts show histograms of the difference between the X-ray redshifts and optically determined redshifts. [Figure and caption credit: Ed Lloyd-Davies

tively. The relations demonstrate the efficacy of the measured X-ray redshifts provided the statistical uncertainties on the measured X-ray redshifts are low.

Appendix B

NXS summary observing logs

Table B.1. Summary of NXS-fields observed during Run2

XCS ObsID	R.A (J2000)	Dec.(J2000)	r'-band	z'-band	XCSRelease	DR1 (XCS500)	DR2 (XCS500)	comments
0044350201	20:07:46.4	-11:07:19.4	x2	x3	DR1	1 (0)	0 (0)	2
0103060101	21:29:06.5	-15:37:38.7	x2	x3	DR1	1 (0)	0 (0)	2
0106660601	22:15:37.1	-17:44:56.6	x2	x3	DR1	9 (1)	0 (0)	2
0151450101	22:38:39.4	-20:36:29.4	x2	x3	DR1	2 (0)	0 (0)	2
0125910301	23:56:46.3	-24:24:34.0	x2	x3	DR1	1 (0)	0 (0)	2
0125920201	00:33:48.3	-12:06:32.7	x2	x3	DR1	1 (0)	0 (0)	2
0109520601	02:22:45.2	-04:31:11.1	x2	x3	DR1	4 (0)	0 (0)	2
0037982601	02:20:34.8	-03:28:50.4	x2	x3	DR1	3 (1)	0 (0)	2
0152360101	13:15:22.5	-16:43:55.2	x2	x2	DR1	3 (2)	0 (0)	2
0100240801	15:32:20.5	-08:30:27.2	x2	x3	DR1	2 (0)	0 (0)	2
0081341001	19:31:04.2	-72:38:09.3	x2	x3	DR1	1 (0)	0 (0)	2
0088020201	21:27:30.1	-44:47:50.4	x2	x3	DR1	2 (0)	0 (0)	2
0152670101	21:57:24.6	-69:41:58.0	x2	x3	DR1	3 (0)	0 (0)	2
0093640701	23:16:03.0	-42:34:11.7	x2	x3	DR1	1 (0)	0 (0)	2
0125310101	00:00:23.5	-25:06:05.4	x2	x3	DR1	4 (1)	0 (0)	2
0148960101	00:35:40.5	-43:18:48.2	x2	x3	DR1	6 (3)	0 (0)	2

Table B.1 (cont'd)

XCS ObsID	R.A (J2000)	Dec.(J2000)	r'-band	z'-band	XCSRelease	DR1 (XCS500)	DR2 (XCS500)	comments
0067170101	01:12:41.9	-45:32:53.1	x2	x3	DR1	2 (1)	0 (0)	2
0146510401	02:49:39.6	-31:12:25.8	x2	x3	DR1	2 (1)	0 (0)	2
0148650101	04:54:24.5	-53:22:20.1	x2	x3	DR1	3 (1)	0 (0)	2
0152360101	13:15:22.5	-16:43:55.2	x0	x1	DR1	3 (2)	0 (0)	2
0110980601	13:19:22.6	-14:52:15.8	x2	x3	DR1	4 (0)	0 (0)	2
0112380101	15:56:27.7	-23:39:23.9	x2	x3	DR1	2 (0)	0 (0)	2
0083210101	20:54:13.2	-15:54:37.8	x2	x3	DR1	2 (0)	0 (0)	2
0062940401	21:52:06.9	-27:32:50.7	x2	x3	DR1	4 (0)	0 (0)	2
0100440101	22:28:24.7	-05:17:55.5	x2	x3	DR1	7 (0)	0 (0)	2
0110960101	22:40:24.3	+03:22:25.2	x2	x3	DR1	2 (0)	0 (0)	2
0055990301	23:40:00.3	-12:18:23.2	x2	x3	DR1	2 (0)	0 (0)	2
0112300101	01:52:55.0	-13:43:19.4	x2	x3	DR1	2 (0)	0 (0)	2
0037981601	02:23:14.3	-02:48:56.3	x2	x3	DR1	2 (0)	0 (0)	2
0108062301	03:32:35.0	-27:48:54.9	x2	x1	DR1	6 (1)	0 (0)	2
0164570401	15:17:03.7	-16:09:52.7	x2	x3	DR1	2 (0)	0 (0)	1
0111510101	20:41:57.3	-32:27:05.7	x2	x3	DR1	1 (0)	0 (0)	1

Table B.1 (cont'd)

XCS ObsID	R.A (J2000)	Dec.(J2000)	r'-band	z'-band	XCSRelease	DR1 (XCS500)	DR2 (XCS500)	comments
0124930601	21:58:58.3	-30:14:28.7	x2	x3	DR1	2 (1)	0 (0)	1

Table B.2. Summary of NXS-fields observed during Run3

XCS ObsID	R.A (J2000)	Dec.(J2000)	r'-band	z'-band	XCSRelease	DR1 (XCS500)	DR2 (XCS500)	comments
0125300101	10:44:34.2	-01:26:41.3	x2	x3	DR1	4 (0)	0 (0)	1
0124110101	12:21:33.0	+75:17:03.9	x2	x1	DR1	3 (1)	0 (0)	1
0134920901	03:53:47.5	-00:06:04.1	x2	x3	DR1	2 (0)	0 (0)	2
0094790201	03:57:16.9	+01:12:11.9	x2	x2	DR1	2 (2)	0 (0)	2
0112880801	07:34:35.2	+31:53:50.6	x2	x0	DR1	5 (0)	0 (0)	2
0110070401	07:55:08.1	+21:58:32.5	x2	x3	DR1	5 (0)	0 (0)	2
0112620101	08:41:27.4	+70:52:00.0	x2	x3	DR1	2 (0)	0 (0)	2
0200730101	09:26:33.9	+30:56:44.9	x2	x3	DR1	0 (0)	0 (0)	2
0041170201	10:00:39.1	+25:16:00.8	x2	x3	DR1	5 (1)	0 (0)	2
0143500201	12:10:32.5	+39:22:39.1	x0	x2	DR1	9 (3)	0 (0)	2
0056020301	02:56:37.9	+00:04:59.7	x2	x3	DR1	3 (0)	0 (0)	1
0094790201	03:57:16.9	+01:12:11.9	x0	x1	DR1	2 (2)	0 (0)	2
0103863001	04:51:36.2	-03:47:17.7	x2	x0	DR1	1 (0)	0 (0)	1
0111220201	06:15:16.9	+71:03:06.0	x3	x3	DR1	2 (0)	0 (0)	1
0025540301	08:38:25.5	+25:43:40.0	x2	x3	DR1	1 (0)	0 (0)	1
0203361801	09:59:25.2	+02:14:14.2	x2	x2	DR1	1 (0)	0 (0)	1

Table B.2 (cont'd)

XCS ObsID	R.A (J2000)	Dec.(J2000)	r'-band	z'-band	XCSRelease	DR1 (XCS500)	DR2 (XCS500)	comments
0102040201	11:31:08.8	+31:15:48.0	x2	x3	DR1	1 (0)	0 (0)	1
0104860501	12:21:37.1	+28:04:33.6	x2	x3	DR1	3 (0)	0 (0)	1
0056020901	12:41:32.9	+32:48:40.1	x1	x2	DR1	2 (0)	0 (0)	1
0093641001	01:43:07.6	+13:37:32.3	x1	x1	DR1	2 (0)	0 (0)	1
0084140501	02:08:45.1	+35:22:09.9	x2	x0	DR1	12(0)	0 (0)	1
0107460601	11:06:35.1	+72:32:49.5	x0	x1	DR1	3 (0)	0 (0)	1
0093641001	01:43:07.6	+13:37:32.3	x1	x0	DR1	2 (0)	0 (0)	1

Table B.3. Summary of NXS-fields observed during Run4

XCS ObsID	R.A (J2000)	Dec.(J2000)	r'-band	z'-band	XCSRelease	DR1 (XCS500)	DR2 (XCS500)	comments
0058940301	14:04:15.4	-34:00:35.7	x2	x3	DR1	3 (0)	0 (0)	1
0148520101	14:49:29.3	+08:58:18.3	x2	x3	DR1	5 (1)	0 (0)	1
0202890101	15:35:50.7	-14:11:34.4	x2	x3	DR2	0 (0)	1 (1)	1
0200360201	20:07:49.9	-44:33:37.0	x2	x3	DR2	0 (0)	4 (1)	1
0204310101	21:55:06.9	-09:23:29.1	x2	x3	DR2	0 (0)	2 (1)	1
0135980201	22:57:02.7	-36:27:03.2	x2	x3	DR1	1 (0)	0 (0)	1
0203240201	23:54:36.3	-15:14:03.6	x2	x3	DR2	0 (0)	3 (1)	1
0204670101	00:13:05.8	-27:12:26.1	x2	x3	DR2	0 (0)	6 (2)	1
0148961401	00:33:41.1	-43:18:17.4	x2	x3	DR1	5 (1)	0 (0)	1
0203170301	12:32:44.3	+00:08:29.7	x2	x3	DR2	0 (0)	2 (1)	1
0032141201	13:05:11.8	-10:19:22.0	x2	x3	DR1	5 (0)	0 (0)	1
0002940101	13:07:04.7	-23:38:51.3	x2	x3	DR1	1 (0)	0 (0)	1
0021540101	15:06:27.4	+01:37:55.2	x2	x3	DR1	2 (0)	0 (0)	1
0203020201	20:42:11.2	-35:14:03.4	x2	x3	DR2	0 (0)	4 (2)	2
0083210101	20:54:13.2	-15:54:37.8	x2	x3	DR1	2 (0)	0 (0)	1
0103060401	21:51:49.2	-30:26:53.4	x2	x2	DR1	1 (0)	0 (0)	1

Table B.3 (cont'd)

XCS ObsID	R.A (J2000)	Dec.(J2000)	r'-band	z'-band	XCSRelease	DR1 (XCS500)	DR2 (XCS500)	comments
0202060201	11:29:15.6	-04:22:24.3	x2	x0	DR2	0 (0)	5 (1)	1
0200430801	13:34:38.2	-23:25:05.4	x2	x2	DR2	0 (0)	1 (1)	2
0058940301	14:04:15.4	-34:00:35.7	x2	x3	DR1	3 (0)	0 (0)	2
0200430801	13:34:38.2	-23:25:05.4	x2	x3	DR2	0 (0)	1 (1)	2
0147670201	13:37:38.3	-12:55:45.8	x2	x3	DR1	6 (0)	0 (0)	2
0148520101	14:49:29.3	+08:58:18.3	x2	x3	DR1	5 (1)	0 (0)	2
0201902201	20:14:55.4	-24:31:37.7	x2	x3	DR2	0 (0)	1 (0)	2
0203020201	20:42:11.2	-35:14:03.4	x0	x3	DR2	0 (0)	4 (2)	2
0081340501	20:13:23.2	-41:46:19.7	x2	x3	DR1	1 (0)	0 (0)	2
0012440301	22:05:04.3	-01:54:19.1	x2	x3	DR1	2 (0)	0 (0)	2
0111790101	22:35:40.4	-26:01:50.8	x2	x3	DR1	4 (0)	0 (0)	2
0055990301	23:40:00.3	-12:18:23.2	x2	x3	DR1	2 (0)	0 (0)	2
0112880201	11:01:52.2	-34:44:07.5	x4	x6	DR1	5 (1)	0 (0)	1
0101040401	13:49:17.2	-30:16:57.6	x4	x6	DR1	1 (0)	0 (0)	1
0201830301	14:13:16.3	-03:14:06.6	x6	x7	DR2	0 (0)	0 (0)	1
0103060401	21:51:49.2	-30:26:53.4	x2	x3	DR1	1 (0)	0 (0)	1

Table B.3 (cont'd)

XCS ObsID	R.A (J2000)	Dec.(J2000)	r'-band	z'-band	XCSRelease	DR1 (XCS500)	DR2 (XCS500)	comments
0200020301	22:11:09.4	-17:04:25.8	x2	x3	DR2	0 (0)	2 (0)	1
0206060101	23:55:13.3	+05:55:54.3	x2	x3	DR2	0 (0)	1 (1)	1
0112880101	11:31:55.1	-34:34:39.6	x4	x6	DR1	2 (1)	0 (0)	1
0027340101	11:51:01.6	-28:46:36.5	x4	x6	DR1	4 (0)	0 (0)	1
0110890101	13:25:18.2	-38:23:14.7	x4	x6	DR1	4 (1)	0 (0)	1
0147920701	18:47:34.6	-78:32:18.2	x0	x6	DR1	1 (0)	0 (0)	1
0109463201	20:08:47.1	-65:26:19.2	x2	x3	DR1	1 (0)	0 (0)	1
0200780301	21:31:54.8	-42:51:41.1	x2	x3	DR2	0 (0)	1 (0)	1
0201150101	21:42:56.1	+06:55:19.5	x0	x3	DR2	0 (0)	1 (0)	1
0090050601	22:23:55.1	-02:07:11.3	x2	x3	DR1	2 (0)	0 (0)	2
0081340901	22:51:43.3	-17:51:27.0	x2	x3	DR1	6 (0)	0 (0)	2
0200270101	00:13:22.4	-19:29:04.5	x2	x3	DR2	0 (0)	4 (0)	2

Table B.4. Summary of NXS-fields observed during RUN5

XCS ObsID	R.A (J2000)	Dec.(J2000)	r'-band	z'-band	XCSRelease	DR1 (XCS500)	DR2 (XCS500)	comments
0150610201	21:14:47.1	+06:08:44.9	x2	x4	DR1	1 (0)	0 (0)	1
0203050601	21:01:25.4	+10:53:47.9	x2	x3	DR2	0 (0)	3 (0)	2
0110960101	22:40:24.3	+03:22:25.2	x2	x3	DR1	2 (0)	0 (0)	2
0205180101	00:29:21.3	+34:55:41.1	x3	x3	DR2	0 (0)	2 (0)	2
0200430301	01:16:13.9	+33:04:17.2	x2	x3	DR2	0 (0)	2 (0)	2
0109520101	02:23:25.2	-04:11:07.5	x2	x3	DR1	5 (0)	0 (0)	2
0202100301	17:36:50.3	+66:01:01.9	x2	x3	DR2	0 (0)	3 (1)	1
0102041201	17:23:17.8	+34:19:33.8	x2	x0	DR1	1 (0)	0 (0)	1
0090050601	22:23:55.1	-02:07:11.3	x2	x3	DR1	2 (0)	0 (0)	2
0201090401	01:25:38.1	+32:07:17.7	x2	x3	DR2	0 (0)	4 (1)	1
0203610201	01:11:06.2	+33:08:21.5	x2	x3	DR2	0 (0)	1 (0)	2
0202770301	01:57:16.9	+28:50:40.3	x2	x3	DR2	0 (0)	3 (0)	2
0112680501	02:23:54.6	-04:29:00.0	x2	x3	DR1	1 (0)	0 (0)	2
0037980301	02:25:25.7	-03:50:59.2	x2	x0	DR1	2 (1)	0 (0)	1
0203720201	18:42:33.3	+79:44:57.3	x2	x3	DR2	0 (0)	1 (0)	1
0102041201	17:23:17.8	+34:19:33.8	x0	x3	DR1	1 (0)	0 (0)	1

Table B.4 (cont'd)

XCS ObsID	R.A (J2000)	Dec.(J2000)	r'-band	z'-band	XCSRelease	DR1 (XCS500)	DR2 (XCS500)	comments
0200430201	22:06:56.3	+10:15:02.1	x2	x3	DR2	0 (0)	5 (0)	1
0112170101	23:03:22.1	+08:51:55.5	x2	x3	DR1	4 (0)	0 (0)	1
0202520101	01:11:44.2	+39:05:25.0	x2	x3	DR2	0 (0)	2 (0)	1
0205390201	02:06:55.7	+29:31:47.2	x2	x3	DR2	0 (0)	2 (1)	1
0112371701	02:17:07.0	-04:38:02.1	x2	x3	DR1	3 (0)	0 (0)	1
0037980301	02:25:25.7	-03:50:59.2	x2	x3	DR1	2 (1)	0 (0)	1
0147110201	02:20:35.1	-02:49:00.0	x3	x4	DR1	3 (0)	0 (0)	2
0202100401	17:24:40.1	+66:37:31.6	x2	x3	DR2	0 (0)	0 (0)	1
0111971601	19:49:17.0	+77:42:48.4	x0	x1	DR1	1 (0)	0 (0)	1
0150600101	21:23:19.5	-05:48:59.5	x2	x0	DR1	1 (0)	0 (0)	1
0203390101	01:20:08.6	+14:20:42.9	x2	x3	DR2	0 (0)	1 (0)	2
0153030701	01:56:27.3	+05:36:05.5	x1	x2	DR2	0 (0)	1 (0)	2
0111110501	02:22:34.0	-05:09:02.9	x2	x3	DR1	1 (0)	0 (0)	2
0036540101	03:38:34.1	+00:20:41.6	x1	x0	DR1	1 (0)	0 (0)	1

Table B.5. Summary of NXS-fields observed during Run6

XCS ObsID	R.A (J2000)	Dec.(J2000)	r'-band	z'-band	XCSRelease	DR1 (XCS500)	DR2 (XCS500)	comments
0150800101	08:06:20.5	+15:29:08.8	x1	x0	DR1	4(1)	0(0)	2
0148740101	08:57:26.3	+09:02:09.6	x2	x3	DR1	2(0)	0(0)	2
0070940101	09:53:39.6	+01:36:31.8	x2	x3	DR1	1(1)	0(0)	2
0093640301	10:20:01.7	+08:11:56.0	x2	x3	DR1	2(1)	0(0)	2
0112880201	11:01:52.2	-34:44:07.4	x2	x3	DR1	5(1)	0(0)	2
0110890101	13:25:18.2	-38:23:14.7	x2	x3	DR1	4(1)	0(0)	2

The XCS ClusterZoo II Classification Criteria

The classification types and corresponding criteria for XCS ClusterZoo II are as stated below:

- Gold Cluster/Group: *Both optical and X-ray properties are compelling could it be high-z? click on High redshift candidate flag too.*
- Silver Cluster/Group: *One of optical or X-ray properties is compelling (see Gold) and the other one is OK could it be high-z? click on High redshift candidate flag too.*
- Bronze Cluster/Group: *Both optical and X-ray are OK, but neither are compelling could it be high-z? click on High redshift candidate flag too.*
- Other: *One or both of the optical or X-ray properties is not-OK (use flags to indicate why) could it be high-z? click on High redshift candidate flag too.*

Compelling in optical :clear over density of galaxies coincident with an X-ray source

Compelling in X-rays : Obviously an extended source, i.e. rather than a blend of point sources. Note that occasionally point sources will fall inside the extended source, but as long as the point sources have been found by XAPA and do not dominate the emission, these candidates can still be classed as compelling.

OK in optical : One of more of: a) there are some galaxies around and these could in principle be in a cluster; b) there isn't much of anything in SDSS, but it could be high-z.

OK in X-rays : Both of: a) I can believe this is an extended source, although more data might expose it as a blend; b) there aren't any artifact issues to worry about (chip gaps, chip edges, background, masking)

Not-OK in optical : One or more of: a) this is likely not to be a cluster e.g. there is a nearby (z¡0.02) galaxy coincident with the X- ray source; or this is an obvious AGN. b) even if this was a cluster we could never know e.g. it is in a dense star field or close to a v. bright star.

Not-OK in X-rays : One or more: of a) this is likely not to be a cluster e.g. it looks like XAPA has blended two point sources; b) even if this was a cluster, the point source contamination is too high to extract information from the extended emission without a

Chandra image; c) even if this was a cluster, there are artifacts that require more XMM data to solve (e.g. candidate is on a chip gap/edge or the background seems very high); d) there seems to be a problem with the masking.

High-z : Don't worry about using this flag too often. High-z clusters are precious, be inclusive rather than conservative. Anything you flag up will be checked by an expert. High-z clusters may well look like X-ray point sources, so don't discount blends, e.g. if one of the hot spots happens to coincide with a very faint red galaxy on SDSS. High-z clusters will look unremarkable in the SDSS, so its unlikely (but not impossible) that a Gold cluster will also be a high-z candidate.